DOE/MC/28135 -- 5258
(DE96011352)

Fracture Detection, Mapping, and Analysis of Naturally Fractured Gas Reservoirs Using Seismic Technology

Final Report
November 1995

October 1995

Work Performed Under Contract No.: DE-AC21-92MC28135

For
U.S. Department of Energy
Office of Fossil Energy
Morgantown Energy Technology Center
Morgantown, West Virginia

By
Coleman Research Corporation
301 Commercial Road, Suite B
Golden, Colorado 80401

Disclaimer

DOE/MC/28135 -- 5258
(DE96011352)
Distribution Category UC-101

Fracture Detection, Mapping, and Analysis of Naturally Fractured Gas Reservoirs Using Seismic Technology

Final Report
November 1995

Work Performed Under Contract No.: DE-AC21-92MC28135

For
U.S. Department of Energy
Office of Fossil Energy
Morgantown Energy Technology Center
P.O. Box 880
Morgantown, West Virginia 26507-0880

By
Coleman Research Corporation
Corporate Center
301 Commercial Road, Suite B
Golden, Colorado 80401

October 1995

ABSTRACT

Many basins in the Rocky Mountains contain naturally fractured gas reservoirs. Production from these reservoirs is controlled primarily by the shape, orientation and concentration of the natural fractures. The detection of gas filled fractures prior to drilling can, therefore, greatly benefit the field development of the reservoirs. The objective of this project was to test and verify specific seismic methods to detect and characterize fractures in a naturally fractured reservoir. The Upper Green River tight gas reservoir in the Uinta Basin, Northeast Utah was chosen for the project as a suitable reservoir to test the seismic technologies.

Knowledge of the structural and stratigraphic geologic setting, the fracture azimuths, and estimates of the local in-situ stress field, were used to guide the acquisition and processing of approximately ten miles of nine-component seismic reflection data and a nine-component Vertical Seismic Profile (VSP). Three sources (compressional P-wave, inline shear S-wave, and cross-line, shear S-wave) were each recorded by 3-component (3C) geophones, to yield a nine-component data set. Evidence of fractures from cores, borehole image logs, outcrop studies, and production data, were integrated with the geophysical data to develop an understanding of how the seismic data relate to the fracture network, individual well production, and ultimately the preferred flow direction in the reservoir. The multi-disciplinary approach employed in this project is viewed as essential to the overall reservoir characterization, due to the interdependency of the above factors.

Seismic anisotropy was observed in both the VSP and the reflection seismic data sets, and this anisotropy is considered to be a characteristic feature of the fractured reservoir under study. A clear relation was observed between fracture density, dominant fracture azimuth, and P-wave and S-wave seismic properties, in the fractured Upper Green River gas reservoirs.

From the S-wave seismic, the fracture azimuth was inferred from the fast shear wave (S1 after rotation) direction, N40W, which indicates the stiff direction within a rock. The 9-C VSP revealed that no change in the orientation of the principal axes of the S-wave anisotropy was detected from 2,800-8,650 ft (through the target reservoir zone at 6,500-8,650 ft): the dominant fast direction is N40W and the slow direction is N50E. The S1 direction, calculated independently for the VSP and the surface S-wave data, gave similar results to within 15°. The average S1 direction was consistent with geologic evidence of the dominant open fracture strike and the local maximum horizontal compressive stress direction for this reservoir. Relative fracture density was estimated from the travel time anisotropy in the split shear wave data. Also, amplitude variations in the S2 shear wave component correlated with known fractured gas production.

Differences in the P-wave amplitude variation with offset and azimuth (AVOA) for gas-producing intervals known from wells were observed for the two seismic lines. Where the P-wave line direction was perpendicular to the fracture strike, AVO sensed the gas-filled fractures, whereas on the P-wave line the direction of which was parallel to the fracture

strike, the AVO was insensitive to the gas-filled fractures, sensing only the rock matrix properties. Most of the P-wave observations of low Poisson ratio intervals, i.e., intervals that indicate a presence of gas in the rock, correlate with the S-wave indications of high fracture density. Thus it is inferred that for these locations, the gas is in open fractures. P-wave observations of low Poisson ratio that correlate with little or no S-wave anisotropy suggest the presence of gas in matrix porosity. Strong S-wave anisotropy with no corresponding P-wave AVO gas response was observed for brine-filled fractures, or gas-filled fractures when the P-wave line direction is parallel to fractures.

The good correlation between the P-wave and S-wave results documents that P-wave AVO data can be used to evaluate the potential for gas in naturally fractured reservoirs, when the acquisition line is perpendicular to the fracture strike. However, the combination of P-wave and S-wave data adds a degree of certainty to the extraction of fracture characteristics from the seismic data. This work is being extended to 3-D P-wave surveys, such that a 3-D P-wave grid acquired along the principal azimuths (i.e., parallel and perpendicular to the gas-filled fracture strike), may be used to map high-fracture intensity zones within the 3-D survey area, using P-wave AVOA (amplitude variation with offset and azimuth). The calibration of the principal azimuths in depth with an S-wave VSP is strongly recommended.

ACKNOWLEDGMENTS

We gratefully acknowledge the Department of Energy Morgantown Energy Technology Center for this project's major funding, and in particular Royal Watts, DOE Project Manager, for his valuable guidance and insight. We are grateful to Pennzoil Exploration and Production Company for their financial and technical commitment as Industry Partner, especially Mike Layman, Ron Schneider, and Noel Putscher for countless useful discussions and for their geologic and geophysical support. We commend the good work of Lockhart Geophysical, Denver, and Bay Geophysical, who acquired the 9C reflection seismic data, and Schlumberger, Calgary, who acquired the 9C VSP. We thank Amoco Production Company, especially Allan Skorpen, for the use of the Amoco S-wave vibrators with the rotatable base plates. In addition, we thank Peter Cary, Rob Wiens, and Gary Lorenz of Pulsonic Geophysical, Calgary, for superbly rising to the challenge of processing of the nine-component seismic reflection data. Mike Jones and Allan Campbell at Schlumberger Calgary aided us considerably by accomplishing the 9-C VSP processing. The pseudo-shear log and initial AVO model were calculated by Dick Angerer of Associated Geophysical Analysts. Mike Schoenberg, Colin Sayer and James Rickett at Schlumberger Cambridge Research contributed essential input to the anisotropic elastic modeling. We thank Don Robinson for the MIRA software used in the seismic stratigraphic and AVO analysis, and Stewart Squires for his valued assistance in the AVO work.

We proudly point out that all of the results achieved in this project were obtained by using commercially available products and services. No proprietary code or equipment was used. Therefore, we acknowledge our significant dependence upon the oil and gas industry's communal infrastructure and marketplace of commercially available services.

C. Richard Bates, Ph.D., Co-principal Investigator, Coleman Research Corporation-Blackhawk Geosciences Division

Heloise B. Lynn, Ph.D., Principal Investigator, Lynn, Inc.

Pieter Hoekstra, Ph.D., Program Manager, Coleman Research Corporation-Blackhawk Geosciences Division

Michelle K. Simon, Project Investigator, Lynn, Inc.

David R. Phillips, Project Investigator, Coleman Research Corporation-Blackhawk Geosciences Division

TABLE OF CONTENTS

LIST OF TABLES

FIGURE CAPTIONS

Figure 4-1. Location map of Uinta Basin. Bluebell-Altamont Field is located along the basin axis and north-central portion of the basin.

Figure 4-2a. Uinta Basin Generalized Stratigraphic column.

Figure 4-2b. Gamma Ray and Sonic logs in the Upper Green River showing high sonic velocity and clean sandstone.

Figure 4-3. Structure map, T/UGR Formation, showing low-relief nature of the top reservoir.

***Figure 4-4a.** Net SP Isopach, TG2-Z Interval, represents the net reservoir sandstone in this interval. The thick near the axial crest of the anticline indicates a possible structural/stratigraphic trap.

Figure 4-4b. Northwest-Southeast structural dip section shows the marginal-lacustrine wedge of sediments prograding from north to south.

Figure 4-5a. Schematic diagram of raypaths in fractured medium.

Figure 4-5b. 3-D Elastic modeling of an azimuthally anisotropic medium beneath an isotropic medium (from Allen and Peddy, 1993).

***Figure 5-1a.** Results of fractures mapped from outcrop show orthogonal distribution, N30W and N60E.

***Figure 5-1b.** Orthogonal fracture set, dominant N42W (compass reading) with N45E subdominant fractures terminating at NW fracture.

***Figure 5-2a.** Orthogonal fracture set, compass setting N45W and N45E (magnetic north). The arrow on the compass points north; the left-hand edge of the compass mounting is aligned with the fracture and has heading N42W.

***Figure 5-2b.** View South along Line 1.

Figure 5-3. Local maximum horizontal stress directions interpreted from borehole elongations recorded in four-arm caliper and FMS logs, and the fracture azimuths from Formation Microscanner (FMS) logs and from oriented core at seismic line tie.

***Figure 5-4.** Well B2: FMS log interpretation: NW pattern of fractures in Upper Green River (6,500-7,500 ft) EW in Lower Green River (+9,000 ft). Strike and Dip graph shows that fractures are vertical to subvertical.

***Figure 5-5.** Well B2: FMS image shows thinly-bedded Upper Green River strata as light (sandier) and dark (shalier) horizontal bands. The irregular dark sinusoid which is traced on all 4 image strips is a fracture cutting the borehole, at average depth 6,295 ft. Apparent dip about 85 degrees (subvertical); apparent strike is N20W.

***Figure 5-6.** Well B2: 4-arm caliper log from Upper Green River Formation showing consistent borehole elongation in the NE direction. Shaded track on right indicates calipers oriented NE-SW measured borehole axis in NE-SW direction is 1-2 inches longer than NW-SE measured borehole axis.

Figure 5-7. Gilsonite veins (dashed lines) and major faults (solid heavy lines) in Upper Cretaceous and Tertiary rock of the Uinta Basin (from Fouch et al., 1991).

Figure 8-21a. S1 sections for Line 1 (left) and Line 2 (right) spliced at line tie, show differences in amplitudes of T/UGR and Z events attributed to SH and SV (source and receiver polarization) considerations.

Figure 8-21b. S1 sections for Line 2 (left) and Line 1 (right) spliced at line tie, show difference in amplitudes of T/UGR and Z events attributed to SH and SV (source and receiver polarization) considerations.

Figure 8-22a. S2 section for Line 1 (left) and Line 2 (right) spliced at line tie, amplitude differences are less apparent on S2 sections than on S1 sections.

Figure 8-22b. S2 sections for Line 2 (left) and Line 1 (right) spliced at line tie, amplitude differences are less apparent on S2 sections than on S1 sections.

Figure 8-23. Line 1: Average S-wave anisotropy within the five stratigraphic intervals analyzed for Line 1. These show the variation in percent S-wave anisotropy, which can be taken as equivalent to the average fracture density within the interval. Positive values indicate S1 polarized N30W is the first-arriving S-wave (NW-trending fractures); negative values indicate S2 polarized N60E arrived first (NE-trending fractures). All graphs have smoothing of 500 ft moving average applied. Error range plotted on T/UGR-Z applies to all intervals.

Figure 8-24. Line 2: Average S-wave anisotropy within the five stratigraphic intervals for Line 2. These show the variation in percent S-wave anisotropy, which can be taken as equivalent to the average fracture density within the interval. Positive values indicate S1 polarized N30W is the first-arriving S-wave (NW-trending fractures); negative values indicate S2 polarized N60E arrived first (NE-trending fractures). All graphs have smoothing of 500 ft moving average applied. Error range plotted on T/UGR-Z applies to all intervals.

Figure 8-25. VP/VS ratios for Line 2 and Line 2, datum to Uinta interval (uppermost interval). On Line 1, VP/VS1 and VP/VS2 are separated at the NW end of the line, indicating azimuthal anisotropy, but come together at the SE end of the line, where azimuthal anisotropy is greatly reduced. This is discussed under S-wave Refraction Statics in the section on Data Processing.

Figure 8-26. VP/VS ratios for four stratigraphic intervals from Uinta-M.B., Line 1.

Figure 8-27. VP/VS ratios for four stratigraphic intervals from Uinta-M.B., Line 2.

Figure 8-28. (A) Variation of VP/VS with rock properties. Increase in sand percentage, introduction of gas, and increase in depth of burial all cause decrease in VP/VS. (From Tatham and McCormack, 1991). (B) Calculated values of VP/VS versus porosity for gas and brine saturated solids with four different proportions of spherical pores (aspect ratio 1.0), and flat cracks (aspect ratio of 0.01). (From Tatham and McCormack, 1991.) For gas-saturated rock, VP/VS decreases with increased percentage of flat cracks.

Figure 8-29. Comparison of near-offset stacks (offsets less than 5,989 ft) of Line 1 and Line 2 at tie point , shows very close similarity in reflector amplitudes on the two lines.

Figure 8-30. Comparison of far-offset stacks (offsets greater than 5,989 ft) of Line 1 and Line 2 at tie point , shows differences in reflector amplitudes on the two lines at far offsets, indicating an azimuthal difference in AVO response.

Figure 8-31a. Reproduced from Rutherford and Williams, 1989. Zoeppritz P-wave reflection coefficients for a shale-gas sand interface for a range of R_0 values. The Poisson's ratio and density of the shale were assumed to be 0.38 and 2.4 g/cm^3, respectively. The Poisson's ratio and density of the gas sand were assumed to be 0.15 and 2.0 g/cm^3, respectively.

Figure 8-41b. Positive AVO gradients (+3693 and +5270) at Line 2, CDPs 369 and 370, line tie and 1 CDP west, time .928, T/UGR gas sand. Positive AVO gradients on both lines indicate an isotropic AVO response to the interval which flowed gas on DST. (Note: there is a static shift of 10 msec. between the gathers of the two lines, which was corrected for after stack).

Figure 8-42. AVO response of Line 1 (left) and Line 2 (right), spliced together at line tie. Shading is Castagna Parameter [(AVO Gradient + AVO Intercept)/2] where positive values only are shaded; wiggle trace is near-offset stack. Note difference at Z reflector; the cause of the anisotropic AVO response is interpreted as NW-trending gas-filled fractures.

Figure 8-43a. Negative AVO gradients (-5665 and -5412) at Line 1, CDPs 477 and 478, 1 CDP south of line tie and line tie location, time .984 sec, Z reflector.

Figure 8-43b. Positive AVO gradients (+6842 and +10117) at Line 2, CDPs 369 and 370, 1 CDP (75 ft) east of line tie and line tie location, time .992 and .990 sec., Z reflector. AVO gradients of opposite signs on Lines 1 and 2 show dependence of AVO gradient on line direction.

Figure 8-44. Schematic representation of anisotropic AVO response, showing P-wave particle motion on Lines 1 and 2 with respect to dominant NW fracture trend: P-waves on line 1 are insensitive to fractures because source to receiver raypaths are parallel to fractures, while P-waves on Line 2 have raypaths which cross the fractures and do sense the fractures and their fluid or gas fill.

Figure 8-45a. Negative (-6975) and positive (+3166) AVO gradients at Line 1, CDPs 477 and 478, 1 CDP south of line tie and line tie location, time 1.160 and 1.158 sec., M.B. reflector.

Figure 8-45b. Positive AVO gradients (+5977 and +4923) at Line 2, CDPs 369 and 370, 1 CDP east of line tie and line tie location, time 1.166 and 1.164 sec., M.B. reflector. Positive AVO gradients correspond to low Poisson's ratio in the medium below the M.B. reflector. Different AVO gradients on Line 1 and Line 2 indicate variation with line direction, although Line 1 AVO gradient fluctuates near the line tie location.

Figure 8-46a. Sonic and gamma ray logs over portion of Well G where a DST test did not flow.

Figure 8-46b. Flat AVO gradient (+82) corresponding to top sand at left.

Figure 8-47a. Negative AVO gradients (-4097 and -2603) at Line 1, CDPs 324 and 325, 1 CDP south of Well N and Well N location, time .940 sec., T/UGR reflector. Negative gradients represent increase in Poisson's ratio beneath reflector. The T/UGR is water-wet in this well.

Figure 8-47b. Near-zero AVO gradients (+1689 and -1185) at Line 2, CDPs 468 and 469, 1 CDP east of Well B2 and B2 location, time .926 sec., T/UGR reflector. The T/UGR is water-wet in this well.

Figure 8-48. Range of AVO gradients observed on Line 1 (a), and Line 2 (b) gas-producing sands and non-gas sands in Upper Green River, calibrated to wells closest to line. Gas pay and non-pay sands show overlap in AVO gradients and intercepts for Line 1 and distinct separation for Line 2.

Figure 8-49. Composite Anomaly Map, T/UGR - Z Interval: P-wave AVO anomalies: stars denote positive AVO gradient at T/UGR shale/sand interface; (--) denote positive AVO gradient at second Upper Green River shale/sand reflection (sand in TG2.2-TG2.3). S-wave anisotropy shown by density/orientation of line shading.

Figure 8-50. Composite Anomaly Map, Z - TN1 Interval: P-wave AVO anomalies at Z-Peak denoted by stars; S-wave anisotropy shown by density/orientation of line shading.

Figure 8-51. Cost in percent of each facet of the project.

1.0 EXECUTIVE SUMMARY

The detection of gas-filled fractures using seismic methods represents a potentially important aid to gas production in many low-permeability reservoirs. The primary objective of this project was to detect and characterize fractures in a naturally fractured tight gas reservoir using seismic methods. The project consisted of planning, acquiring, processing and interpreting seismic data sets specifically designed to evaluate a naturally fractured tight gas reservoir. Information from four main categories were sought, to develop an understanding of the relation between the fracture network, the seismic response, the in situ stresses, and the preferred flow direction, in fractured Upper Green River gas reservoirs of the Bluebell-Altamont Field, in the Uinta Basin, Utah. The importance of such a multi-disciplinary approach is emphasized because of the interdependency of the above factors.

The four main types of information that were integrated in the analysis of the naturally fractured reservoir, were:

1. The geology: fractures, stratigraphy, and structural setting;
2. The seismic response: Compressional (P-) wave amplitude variation with offset and azimuth; and Shear (S-) wave velocity anisotropy (normalized difference in travel times between fast and slow arriving shear waves) and amplitude differences with azimuth;
3. The local in-situ stress field determination, because the open fracture direction is often parallel or subparallel to the maximum horizontal stress direction;
4. The preferred flow direction (the maximum horizontal permeability direction), dominantly parallel to the open fracture set.

In this project, both P-wave and S-wave data were used, because both types of data respond in different ways to vertical gas-filled fractures. The seismic program was acquired based on considerations of the structural and stratigraphic geologic setting, and on evidence of fractures from cores, formation micro-scanner (FMS) logs and surface mapping. The hypothesis is offered that the maximum horizontal permeability direction is consistent with the fast shear wave azimuth, in that the open fractures controlling the seismic response act as flow conduits within the reservoirs. Unfortunately, there was no evidence of horizontal permeability direction in the reservoir, because no two wells within interference range were simultaneously on-line from which Upper Green River pressure communication or flow data would have been available.

1.1 Seismic Acquisition

Approximately ten miles of nine-component reflection seismic data and a nine-component VSP were acquired, targeting the fractured Upper Green River reservoirs, at depths of 6,000 ft-8,500 ft. Fractures in outcrop were mapped which, together with fracture data interpreted from cores and FMS logs, were used to plan the geometry of the seismic acquisition. The source-receiver azimuths for both surface seismic and VSP were aligned with the suspect principal natural axes in the rocks (parallel and perpendicular to the dominant fracture strike) in order to yield the most easily interpretable seismic data. The 9-C VSP was acquired with a Schlumberger, magnetically clamped, five-stage 3-C geophone sonde in a cased borehole. The compressional, crossline shear and inline shear sources were oriented so as to allow each S-wave source's energy to split into S1 and S2. This geometry facilitated an independent analyses of the shear wave anisotropy, together with a combined 4-component rotation analysis. The nine-component VSP is of excellent data quality, with 3 octaves of S-wave reflection signal (6 Hz - 48 Hz) recorded. The P-P (vertical component) of the nine-component reflection seismic, and the final S-wave surface reflection sections are considered very good quality.

1.2 Seismic Processing

The 9-C VSP was processed by Schlumberger in Calgary. The P, S1 and S2 corridor stacks tied the reflection data very well. Pulsonic Geophysical in Calgary processed the 9-C reflection seismic. The P-wave processing was straightforward and the signal to noise ratio is very good on the stack and good on the gathers. The S-wave processing was more complex due to difficult S-wave statics, but the processing of both the 9C VSP and 9C reflection seismic yielded very good final results, which simplified the interpretation of the seismic data.

1.3 Seismic Interpretation

The seismic data sets were interpreted for fracture characteristics, after first accounting for lateral changes in stratigraphy. These lateral stratigraphic changes were interpreted by comparison of all components of the reflection seismic lines to cross-sectional seismic models, or 2-D synthetic seismograms along the seismic lines. The fracture interpretation was based to a large degree of observations of *seismic anisotropy*, where the value of the property measured depends upon the azimuth in which the measurement is made. Both the S-wave and the P-wave data exhibited anisotropic responses, which were interpreted in terms of fracture azimuth and relative fracture density.

1.3.1 S-wave Anisotropy

A medium that will transmit only two differently polarized vertically propagating S-waves is termed azimuthally anisotropic or birefringent. In rocks with vertically aligned fractures, gives rise to two differently polarized shear waves, which travel at different speeds: the first-arriving, or S1 component, polarized parallel to the stiff direction of the rock, and the second-arriving, or S2 component, polarized parallel to the compliant direction within the rock. S-wave splitting occurs when one S-wave of arbitrary polarization enters an anisotropic medium: the incident S-wave splits into the two S-waves allowed by the medium. The shear wave VSP and reflection data sets were processed independently for estimation of the S1 directions. The results showed a consistent S1 direction from the two data sets, to within 15°. The average S1 direction agreed with geological evidence of a principal fracture strike, and the local maximum horizontal compressive stress direction from borehole breakout, and FMS fracture analyses. The velocity anisotropy observed in the shear wave data was interpreted to be proportional to the relative fracture density. The S-wave anisotropy along the line was compared to well performance: gas production was established in zones with increased S-wave anisotropy. The S2, or slow shear wave component, showed amplitude variations believed to be indicative of enhanced fracture intensity zones.

1.3.2 P-wave Anisotropy

A marked dependence of P-wave AVO response on line azimuth was observed in the surface seismics. The dependence indicates that the seismic line perpendicular to the fracture strike is sensitive to gas-filled fractures, while the seismic line parallel to the fracture strike is insensitive to these open fractures. This azimuthal anisotropy in AVO was not accompanied by any significant P-wave stacking velocity anisotropy.

The AVO response is governed by the *contrast* in P- and S-wave velocities, as a function of the angle of incidence, at a boundary. When vertically aligned fractures exist, there are two S velocities: S1 and S2 (fast and slow).

The P-wave AVO dependence on line direction is consistent with the fracture model inferred from the shear wave data, in that the line direction perpendicular to fractures (Line 2) is P-S2, and thus sensitive to the relative fracture density and fracture contents; while the line direction parallel to the fractures is P-S1, and thus not sensitive to the relative fracture density or the fracture contents. This correlation between the P-wave and S-wave data provides a measure of confidence in the use of P-wave data to characterize fractured reservoirs. However, it is the use of a combination of P-wave and S-wave data sets that reduces potential ambiguity in the interpretation of fracture characteristics from the seismic data.

1.4 Conclusions

A clear relationship between fracture azimuth, fracture density, and P and S-wave seismic properties was observed in a naturally fractured gas reservoir. These specific features could be used as diagnostic tools for characterization of similar reservoirs elsewhere. The P-wave reflection data were interpreted for zones of high fracture density and gas saturation using AVO anisotropy. This interpretation was supported by S-wave velocity anisotropy. A gas recompletion prospect based on this interpretation was recommended to the industry partner.

The conclusion from this work is that P-wave AVO is a suitable tool for detection of gas in vertically aligned fractures, in the setting of a naturally fractured gas reservoir, provided that the seismic line direction is perpendicular to the open fracture azimuth. Water-filled fractures with no gas present are shown in this report to be clearly distinguishable, using P-wave AVO, from gas-filled fractures: the S-wave reflection data detected the high fracture density, and the P-wave AVO is interpreted to indicate what is in the fractures. If the fracture azimuth is not known, then multi-azimuth P-wave data will be diagnostic to reveal fracture azimuth, relative fracture density and presence of gas. As in all gas-detection P-wave AVO studies, the percent gas saturation may range between a few percent and 100 percent. Domenico (1976) showed that the first 10% of gas in a rock provides the bulk of the change in P-wave velocity (VP), while later authors (for example, Tatham and McCormack, 1991, among others) have indicated that the first few percent of gas in a rock provide the bulk of the change in P-wave velocity.

Although this project was limited to two crossing reflection lines and a 9C VSP, it is clear that the work can be extended to 3-D P-wave surveys. This would require P-wave 3-D seismic data to be acquired in the principal azimuths, parallel and perpendicular to dominant fracture strike. With such a survey, it should be possible to map zones of high fracture density and gas saturation within the 3-D survey area, using the P-wave AVO and/or other observed P-wave anomalies, such as azimuthal variation of stacking velocities, frequency content, travel times, etc. Furthermore, it is strongly recommended that the principal azimuths be calibrated with shear wave data, using a multi-component VSP. The P-wave AVO response that indicates the presence of gas has been observed in conjunction with a significant network of high density connected open fractures conducive to flow; we believe that a system of low density isolated gas-filled cracks would not give rise to the P-wave AVO gas-response.

2.0 INTRODUCTION

Characterization of a naturally fractured reservoir is necessarily an integrated study, analyzing data from different disciplines. In this project, information from the following categories has been examined and correlated:

The Geologic Setting. Extensive, detailed knowledge of the structural setting and the stratigraphy, as well as estimated values of the porosity and permeability, are essential.

The Seismic Anisotropy. In reservoirs with nearly vertically aligned fractures, S-wave and P-wave seismic data acquired under certain limiting conditions, and properly processed, may exhibit anisotropic responses, which can be interpreted as characteristic features of the reservoirs. Many field cases and laboratory studies are now documented where these anisotropic responses are observed.

The Stress Field. The local in situ horizontal stress is one of the major factors influencing open fracture direction, and thus horizontal permeability within the reservoir.

The Production Data. Individual well production is enhanced by high fracture intensity, and preferred flow direction may be indicated from well interference data, when available.

In this report the seismic anisotropy is analyzed in terms of the physical and geologic reservoir attributes. No new theoretical relations are invoked, rather, empirical data is used to characterize fractures within established seismic theory and previously documented field case histories. The project, therefore, consists of technology demonstration and technology transfer.

Shear waves provide the most reliable seismic data for fracture characterization, and so despite the increased cost of acquisition, shear wave data are more directly applicable to fractured reservoir characterization than conventional P-wave data. Crampin (1984, 1985) established the link between shear wave anisotropy and internal rock structure, and further showed that fracture orientation and relative fracture density could be estimated from shear wave anisotropic quantities. Lynn and Thomsen (1990) and Mueller (1991) have documented the use of reflection shear wave data to estimate fracture characteristics, by means of velocity anisotropy and azimuthal amplitude variations. Queen and Rizer (1990), evaluated fracture-related shear wave anisotropy in light of extensive geological studies, providing evidence of a correlation between fast shear wave (S1) direction, stress, dominant open fracture orientation, and preferred fluid flow direction.

Whereas shear waves carry information about the rock's matrix or internal structure, P-waves respond to the combination of rock matrix plus pore fluid.

The relations between P-wave anisotropy and fractures are less well-understood than those between S-wave anisotropy and fractures; nonetheless, azimuthally varying P-wave AVO response has been modeled by Allen and Peddy (1993) and successfully used to position gas wells in a naturally fractured gas reservoir by Johnson (1995). Garotta (1989) documented azimuthal anisotropy of P-wave stacking velocities in a 3-D survey, which was correlated with fracture strike. Mallick and Fraser (1991) have published model seismic data to show that the P-wave seismic response to a fractured medium depends upon the line direction relative to the fracture azimuth.

3.0 PROJECT OBJECTIVES

The objectives of this project were to detect and characterize fractures in the naturally fractured Upper Green River tight gas reservoirs of the Bluebell-Altamont field, Uinta Basin, Utah, using surface seismic and VSP methods, borehole imaging logs, and in-situ stress field data. Furthermore, the project aimed to evaluate the various seismic methods as to their potential as tools for fracture characterization of tight gas reservoirs prior to drilling.

This project is a field case history documenting the relation between the response observed in multi-component seismic data, and the fracture characteristics obtained from geologic sources: outcrop, cores and logs. Stress field data were also incorporated, where available.

4.0 BACKGROUND

4.1 SUMMARY

The Bluebell-Altamont field produces commercial hydrocarbons from naturally fractured reservoirs in predominantly marginal-lacustrine facies of the Paleocene/Eocene Wasatch Formation (oil and associated gas), lacustrine to marginal-lacustrine facies of the Eocene Lower Green River Formation (oil and associated gas), and marginal lacustrine facies of the Eocene Upper Green River Formation (gas). The gas was first discovered in the Green River Formation in 1987 when a shut-in well ruptured its casing and blew out with a very high volume of gas from the Upper Green River formation. Since then several wells have been completed solely for the Upper Green River gas, and several others have flowed gas during drilling or drill stem testing. The limits of the Upper Green River gas accumulation are currently not well-defined.

4.1.1 Geological Setting

The project site is Bluebell-Altamont field, in the Uinta Basin, northeastern Utah (Figure 4-1). The Uinta Basin is an asymmetric east-west trending basin with a steep north flank bounded by a thrust and a gently sloping (1-2 degree) south flank. The geologic history of the basin is summarized here for its relevance to the stress history and fracture formation:

During Cretaceous times, the basin was situated on the stable continental shelf of an epicontinental seaway which covered much of the central part of the United States and Canada. The Laramide orogeny, beginning during latest Cretaceous, uplifted the highlands surrounding the basin, and the remaining depression became a vast inland lake with central open-lacustrine sedimentation surrounded by laterally equivalent marginal-lacustrine and alluvial deposits. The Tertiary Upper Green River formation represents the last major lacustrine deposition within the Uinta Basin, before renewed uplift of the Laramide highlands brought about a change to predominantly alluvial deposition at the end of the Eocene. (See generalized stratigraphic column, Figure 4-2a). The youngest sediments now present are terriginous rocks of the Duchesne River formation deposited in the early Oligocene. Significant erosion of these sediments has created a highly developed badlands type terrain, with steep, rough and broken surfaces. It is estimated that approximately 15,000 ft of sediments were deposited before erosion began to strip off the upper layers. Widespread fracturing of the reservoirs is thought to be caused by extension during maximum burial and throughout subsequent uplift (Narr and Currie, 1982).

The trapping mechanism for the Upper Green River gas reservoirs is a combination of structural and stratigraphic factors: The Top of Upper Green River (T/UGR) structure map, Figure 4-3, shows an east-west trending anticlinal

LOCATION MAP
D.O.E Study Area

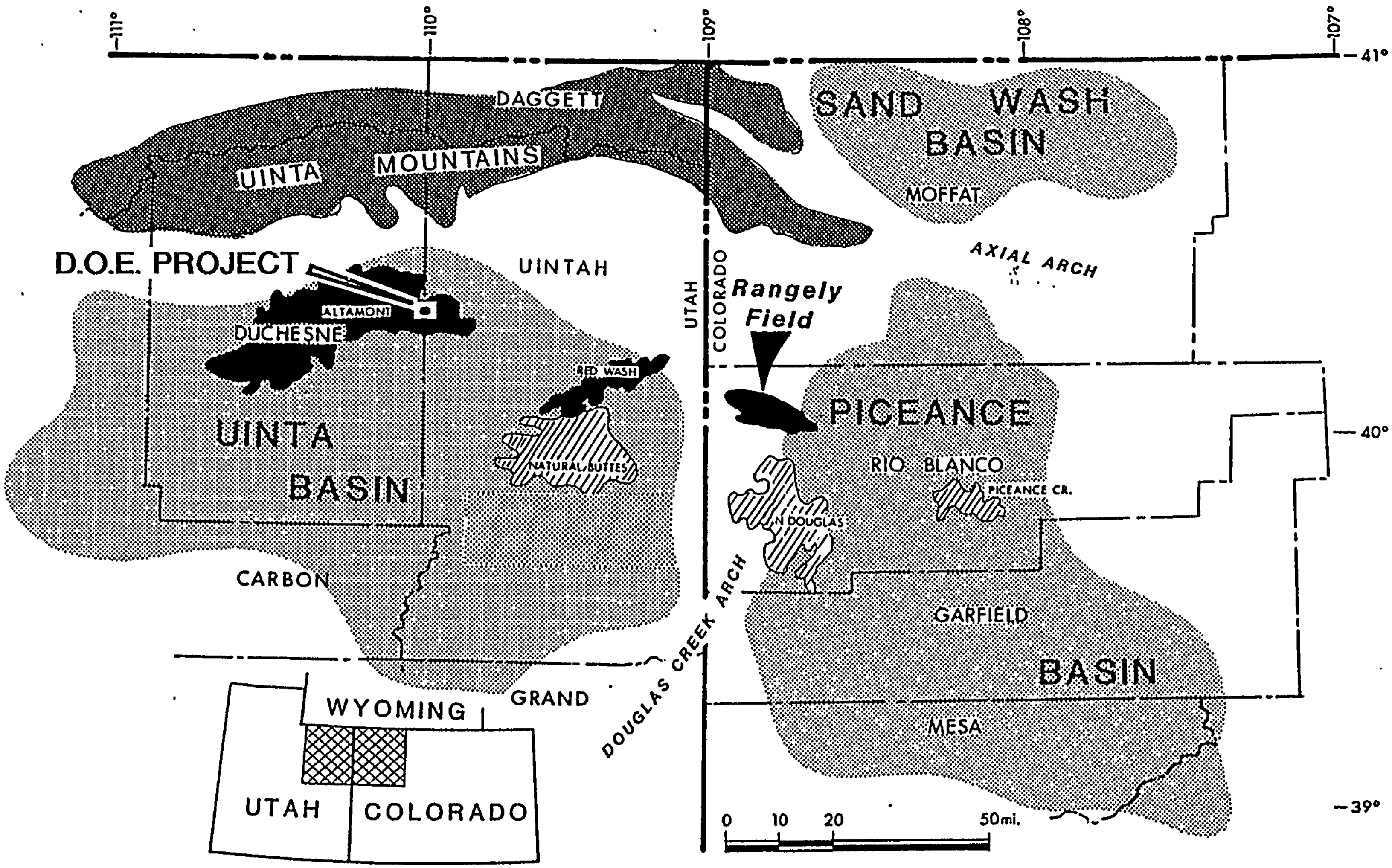

FIGURE 4-1

Location map of Uinta Basin. Bluebell-Altamont Field is located along the basin axis and north-central portion of the basin.

A)

UINTA BASIN
Generalized Stratigraphic Column

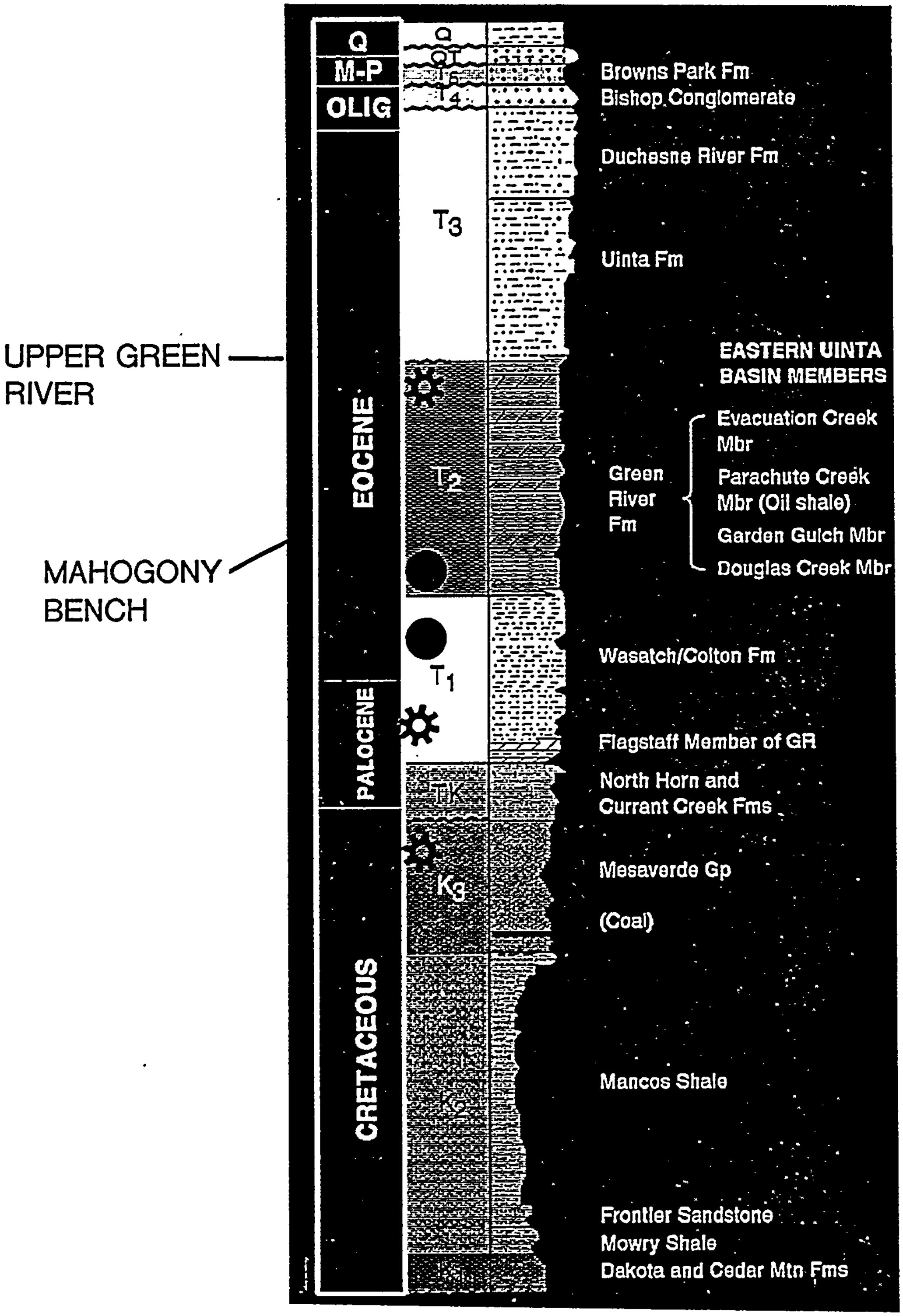

A) Uinta Basin Generalized Stratigraphic Column.

FIGURE 4-2A

B)

9C VSP WELL

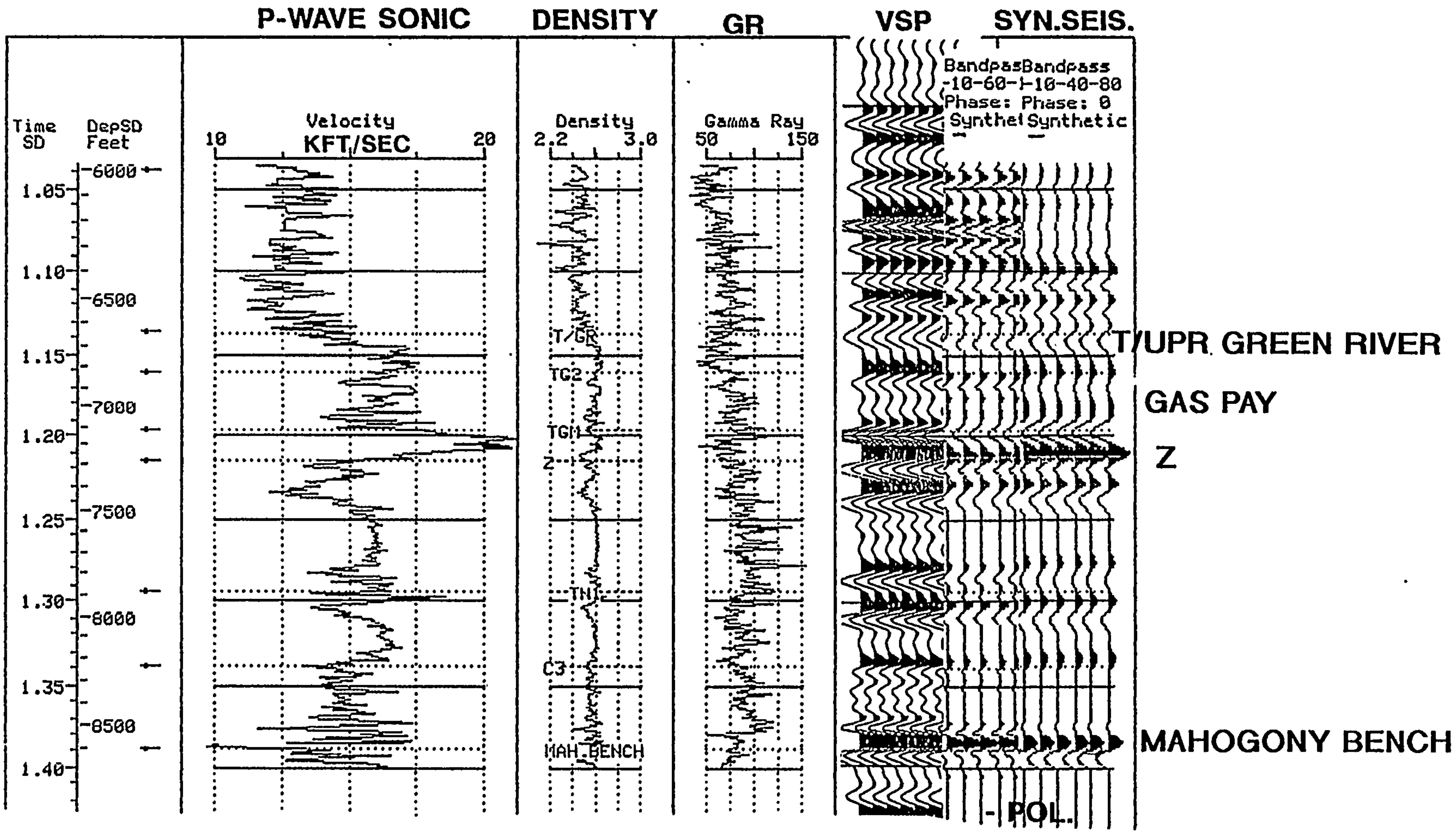

(B) Gamma Ray and Sonic Logs in the Upper Green River showing high sonic velocity and clean sandstone.

FIGURE 4–2B

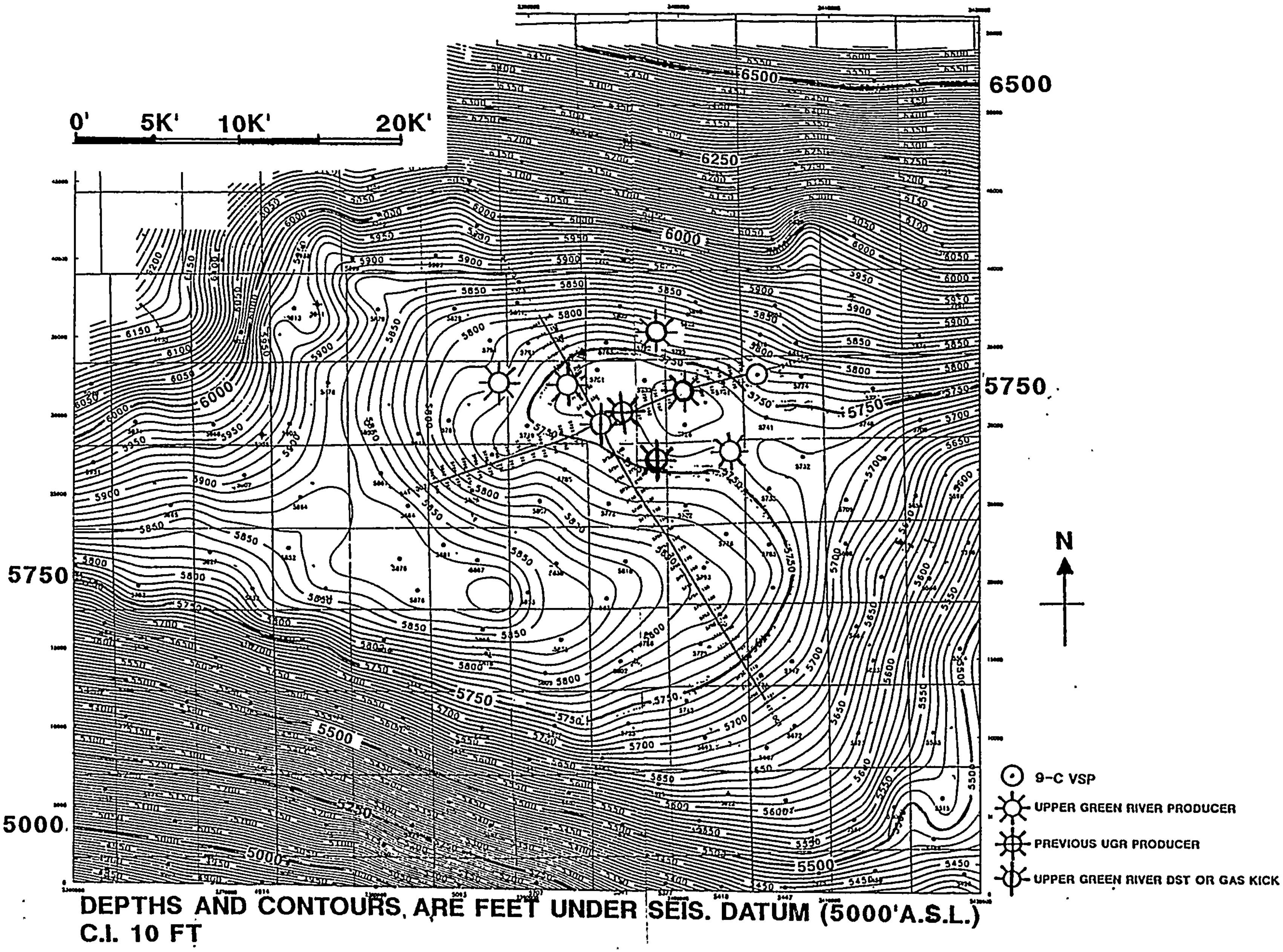

FIGURE 4-3

Structure map, Top Green River Formation, showing low-relief nature of the top reservoir.

nose with about 50 ft of structural closure. Gas reservoirs within the field are trapped by updip pinchouts of the prograding lake margin. Producing intervals consist of fractured lake-margin sandstones encased by tight shales and carbonates of the lacustrine deposits. The isopach of the upper reservoir interval shows stratigraphic thickening over the axial crest of the anticline, which has been interpreted as shoaling of the sands (Figure 4-4a). Geological work by Pennzoil shows that there is a marginal lacustrine wedge of sediments prograding from north to south along structural dip (Figure 4-4b). Sandstone reservoirs have been mapped by Pennzoil using both SP and gamma ray logs, the SP deflection taken to indicate sandstone of reservoir quality either because of porosity or fracturing, and the gamma ray log representing cleanness of the sand, with gamma ray less than 25 API representing very clean sandstone. The individual sandstones are about 5 to 20 ft thick, sometimes stacking to give the appearance of thicker sands, up to 80 ft thick. These sandbodies are very limited in the east-west or strike direction. The cleanest sands usually correspond to very fast sonic velocities, ranging from 15,000 to 18,000 ft/sec. (Figure 4-2b).

The nature of this reservoir setting, with very fast sandstones interbedded with lacustrine shales, gives rise to strong reflectivities in the seismic data. This allows a high confidence level in identifying and correlating the marker horizons.

4.1.2 Nature Of Upper Green River Gas Production

Natural gas is being produced from the Upper Green River Formation in the Bluebell-Altamont field at depths of 6,500-8,500 ft. Production rates from these zones range from 100 million cubic foot per day (MCFPD) to over 5,000 MCFPD. The sandstones which produce gas have matrix porosity of less than 8 percent and permeability less than 1 md. Production has been enhanced in several wells with hydraulic sand fracturing. Several wells have producing rates that are much higher than would be possible if only the matrix were effective. Cores, FMS and sonic logs, and mudlog samples have shown natural fractures which are the likely cause of high production rates in the several wells. Sandstones in non-fractured wellbores are capable of producing at rates of 100-300 MCFPD whereas wells from naturally or artificially fractured wellbores produce at rates from 1000-5000 MCFPD.

4.1.3 Fracture-Related Seismic Response

The effect of vertically aligned fractures upon shear waves has been documented in the literature for many years (Nur and Simmons, 1969; Nur, 1971; Crampin, 1985; Lynn, 1986; Crampin and Lynn, 1989; Lynn, 1989). However, compressional (P) waves (most commercial seismic data) have not been as widely used for investigations of fractured rocks. In this project, the known characteristics of both S-waves and P-waves were applied to detect

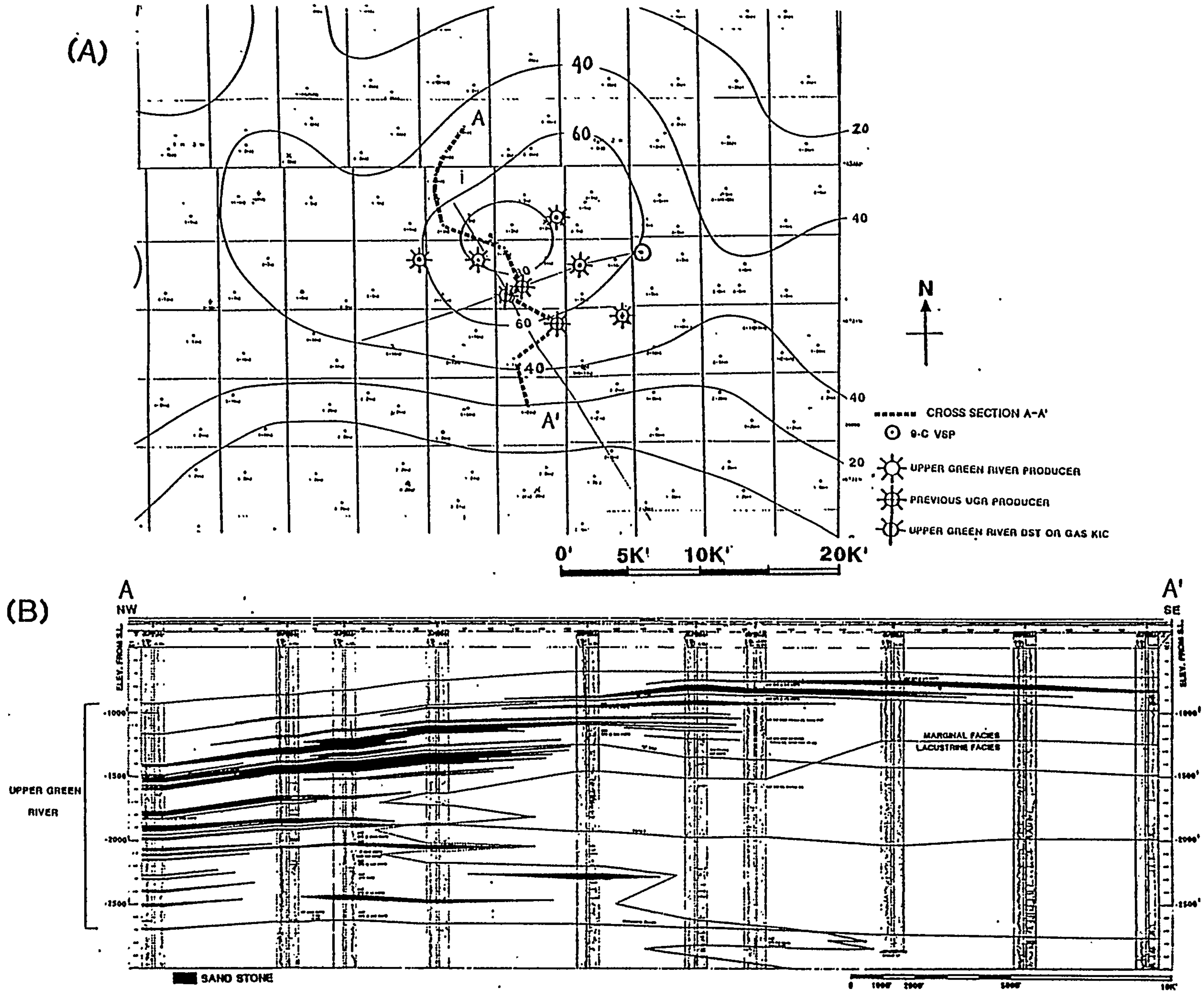

(A) Net SP Isopach, TG2-Z interval, represents the net reservoir sandstone in this interval. The thick near the axial crest of the anticline indicates a possible structural/stratigraphic trap.
(B) Northwest-Southeast structural dip section shows marginal-lacustrine wedge of sediments prograding from north to south.

FIGURE 4–4

relative fracture density and potential gas in the Bluebell-Altamont Upper Green River gas reservoirs.

In a medium with vertically aligned fractures, the shear wave splits into two vertically propagating shear waves: the shear wave polarized parallel to the fractures (S1 which travels at the faster velocity) and the shear wave polarized perpendicular to the fractures (S2, which travels at the slower velocity). S1 travels at the uncracked rock's velocity, to a first-order approximation, while the velocity of S2 is a function of fracture density (Lynn and Thomsen, 1990). These two directions, parallel and perpendicular to the fractures, are often referred to as the principal directions, or axes, of the anisotropic medium. When a shear wave polarized intermediate between the principal axes propagates within the fractured medium, the shear wave will split into the two polarization directions. The amplitudes of the split shear waves are a geometrical decomposition of the incident shear wave's amplitude (Thomsen, 1986, 1988). The presence of unequal horizontal stresses can also result in shear wave birefringence, since the cracks perpendicular to the maximum horizontal stress are relatively more closed, while the cracks perpendicular to the minimum horizontal stress are relatively more open. Crampin (1985) has maintained that all shear-wave birefringence is directly attributable to vertical stress-aligned fluid-filled cracks.

4.1.4 Time Delays Between the S1 and S2 Arrivals

From the S1-S1 and S2-S2 migrated stacks, the magnitude of the time delay between correlative S1 and S2 reflections (i.e., the magnitude of the birefringence) can be determined for all events of interest at all common mid point (CMP) locations. The time delay between the S1 and the S2 reflections to the top of the zone of interest documents the magnitude of the azimuthal anisotropy in the formations overlying the target formation. In the zone of interest, the normalized time delay is the S-wave anisotropy. The lateral differences in S-wave anisotropy reveal the lateral changes in relative fracture density. The magnitude of the birefringence attributable to a given interval of rock is considered to be directly proportional to the magnitude of the fracturing within the interval studied. The relative fracture density will govern the interval velocity of the S2 waves in the target formation.

4.1.5 S-wave Reflection Amplitudes

The relative fracture density in the subsurface target formation will govern the interval velocity of the S2 waves (the second arriving shear waves, which are polarized perpendicular to the fractures) in the target formation, the S2-S2 reflection coefficients at the top and base of the target, and the time delay between the S1 and S2 reflections from the base of the zone of interest.

4.1.6 P-wave Reflection Amplitudes

The relative fracture density will also govern the P-wave reflection coefficients on the mid- to far-offsets on the reflection profiles perpendicular to the fractures, and the amplitude of the P-S upgoing mode-converted arrivals. The reason that relative fracture density governs the P-wave AVO (amplitude variation with offset) response on the lines perpendicular to the fractures is that "SV" on those lines is "S2" (Some of the energy in a P-wave impinging upon an acoustic boundary is reflected as an inline-polarized S-wave. When the inline direction is perpendicular to the open fracture strike, this P-SV mode conversion is P-S2).

Figure 4-5a is a schematic representation of the P-P and the P-S (converted waves) corresponding to P-S1 and P-S2 depending upon line orientation with respect to fracture azimuth. Figure 4-5b is the Allen and Peddy (1993) AVOA model data.

Allen and Peddy (1993) modeled the P-wave AVO response in an isotropic layer over an azimuthally anisotropic medium, corresponding to a shale (low impedance) over a gas-filled fractured Austin Chalk (high impedance). Their 3-D elastic modeling used the opposite polarity convention than the one used at Bluebell-Altamont. In Allen and Peddy, a low-to-high impedance contrast gives a trough (negative reflection). To compare Allen and Peddy's model data to the field data in this report, imagine the polarity reversed. Now, the P-P AVO response on the line parallel to cracks will have a flat AVO gradient, and the P-P AVO response on the line perpendicular to cracks will have a positive gradient (a trough reducing in amplitude), which is the gas-response AVO recorded in the Bluebell-Altamont field data at the T/UGR, when the seismic line (source-receiver azimuth) is perpendicular to gas-filled cracks.

Model parameters are taken from a well through the Taylor Shale over unfractured Austin Chalk, gas-filled, coin-shaped cracks were inserted in the Austin Chalk with a radius of 1.65 ft (0.5 m) and an aspect ratio (thickness/diameter, or width/height) of 0.01. The crack density is 0.1. Crack density is defined as Na^3/v, where N is the number of cracks of radius in volume v. Water-filled cracks do not produce strong azimuthally-dependent changes for this model.

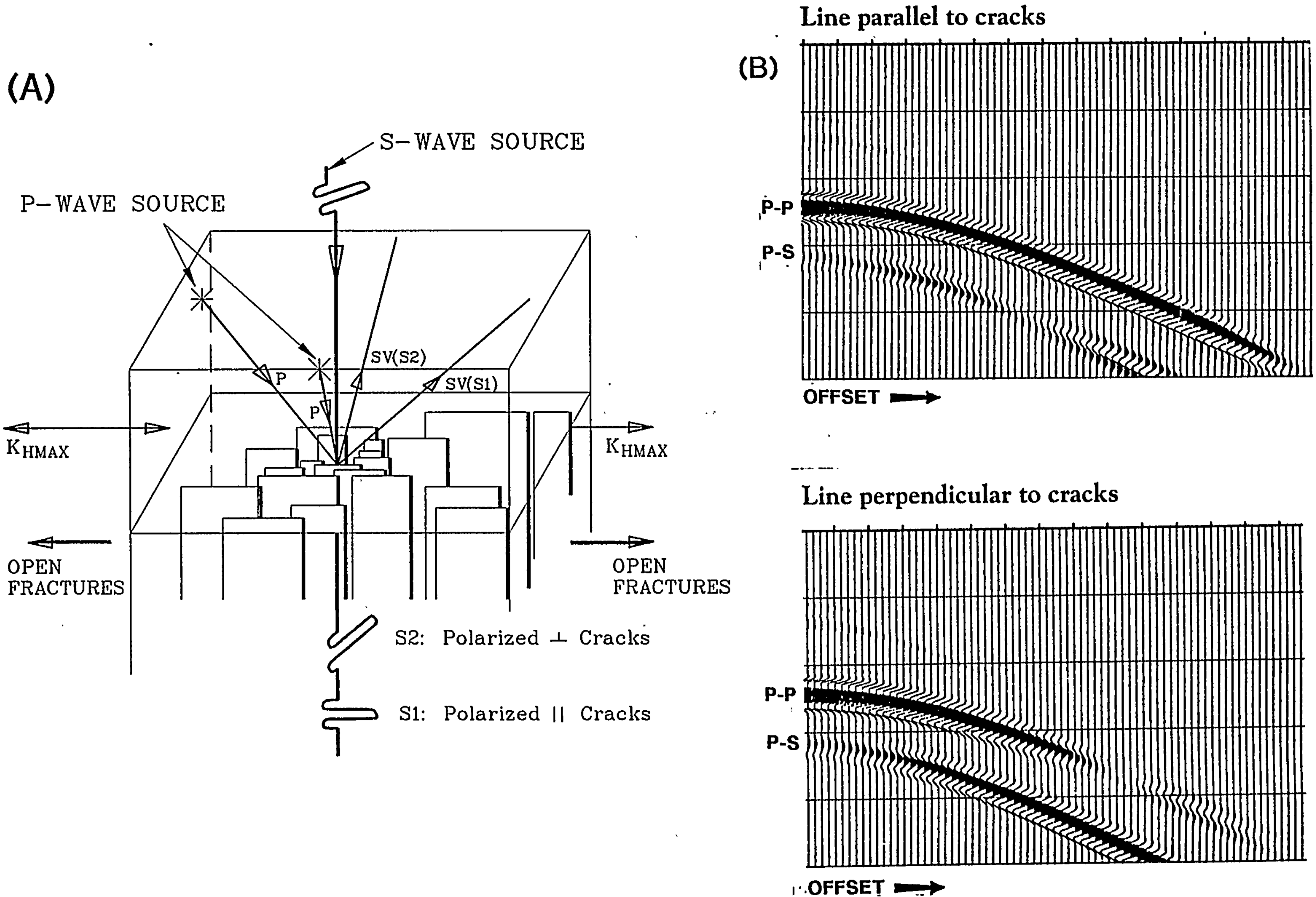

(A) Schematic diagram of raypaths in fractured medium.
(B) 3-D Elastic modeling of an azimuthally anisotropic medium beneath an isotropic medium. (From Allen and Peddy, 1993).

FIGURE 4–5

5.0 GEOLOGIC DATA

5.1 SURFACE MAPPING

5.1.1 Fracture Azimuths Exposed in Outcrops Near or on the Seismic Lines and Initial Shear-wave Seismic Work (Shallow Refraction and Reflection)

During the planning stages of surface seismic acquisition (July 1993), the field site was visited and fracture and joint orientations on outcrops were recorded. The joints and fractures were predominantly vertical and closed with little indication of movement. A dominant NW/SE and NE/SW orientation was evident. The pattern of fracture orientations mapped from outcrops is shown in Figure 5-1a. The fractures observed were typically vertical, in the more competent units exposed in rocky hills, cliffs, or pavements. Measurements of fracture azimuths and locations of good outcrops on and near the proposed seismic lines have been detailed in prior reports (DOE report 6801-000, 1994). Examples of the orthogonal fracture sets observed are shown in the photos, Figures 5-1b and 5-2. The terrain was fairly brushy with the more competent units containing the fractures being ridge formers. The sandier units are less resistant to erosion.

Also prior to the main survey, two high-resolution shallow shear-wave reflection and refraction data sets were acquired adjacent to the proposed line locations. These indicated that the near surface is azimuthally anisotropic (birefringent to shear waves) and that the natural shear wave polarization directions (after shear-wave splitting) in the near surface are NW/SE and NE/SW. Both sites showed the shear wave refraction arrival to be polarized NW/SE or NE/SW. Also, at one site, a split-shear wave reflection at 0.120 - 0.150 sec was recorded. The NMO or normal move-out velocity was calculated at 1,189 ft/sec, and the depth at ~70 ft. The split shear wave reflection shows particle motion displacements with S1, the fast shear wave, polarized NW/SE. These seismic data verified that the proposed NW/SE and NE/SW line directions are aligned with the principal axes of the anisotropy in the near surface. In addition, these directions are parallel to the local maximum horizontal stress directions in the Upper Green River based upon borehole breakout information (wireline logs).

5.1.2 Conclusions from Initial Field Work

Orthogonal fracture sets were seen in outcrops adjacent to the proposed seismic lines. The dominant strikes of the fracture sets are N40-60W and N30-40E. There was scatter among the fracture azimuths as observed in the field, but the NW and NE fracture sets were predominant. The shallow layers were azimuthally anisotropic, with S1 being polarized NW/SE. Thus, it was

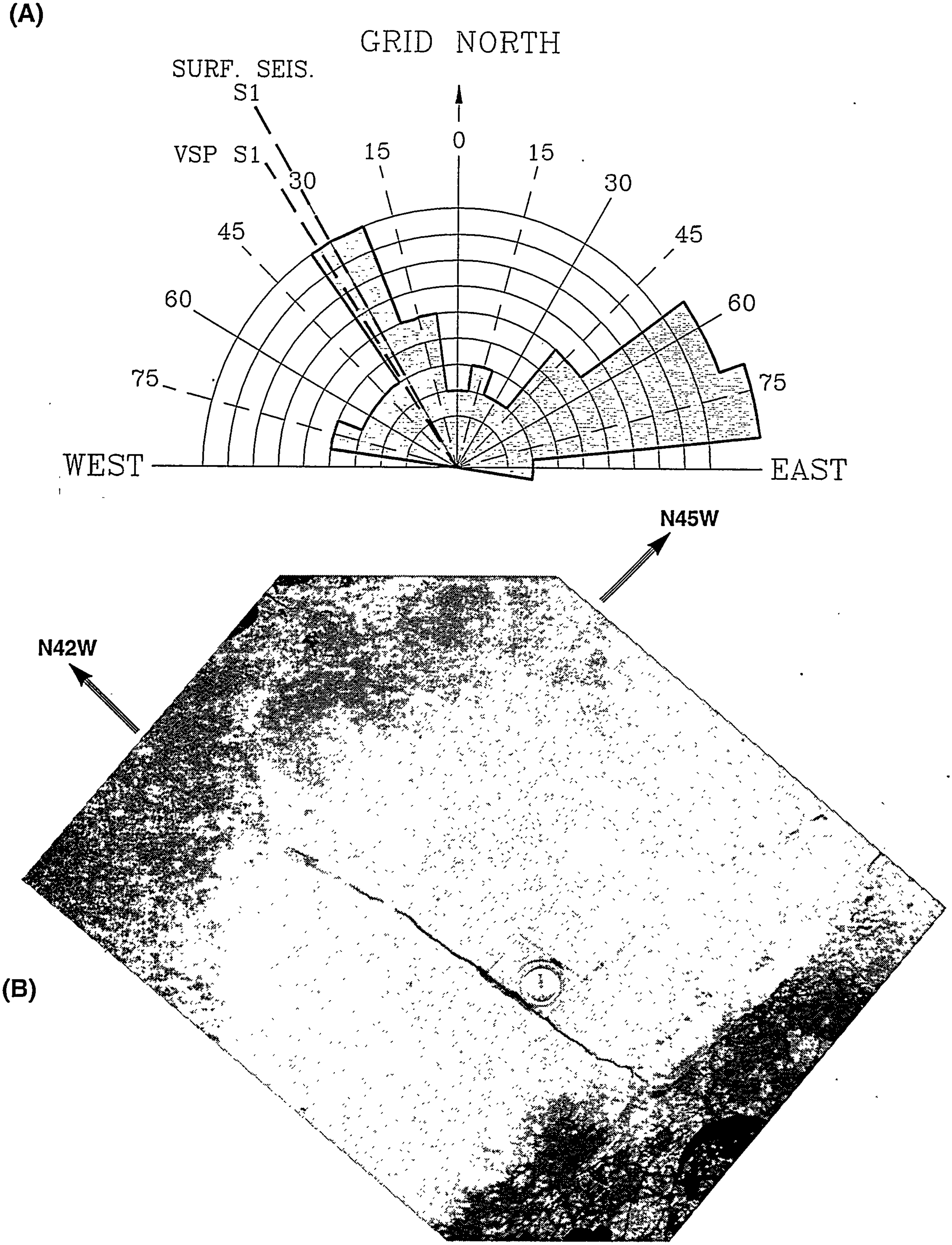

Figure 5-1

(A) Results of fractures mapped from outcrops show orthogonal distribution N30W and N60E.
(B) Orthogonal fracture set, dominant N42W (compass reading) with N45E subdominant fractures terminating at NW fracture.

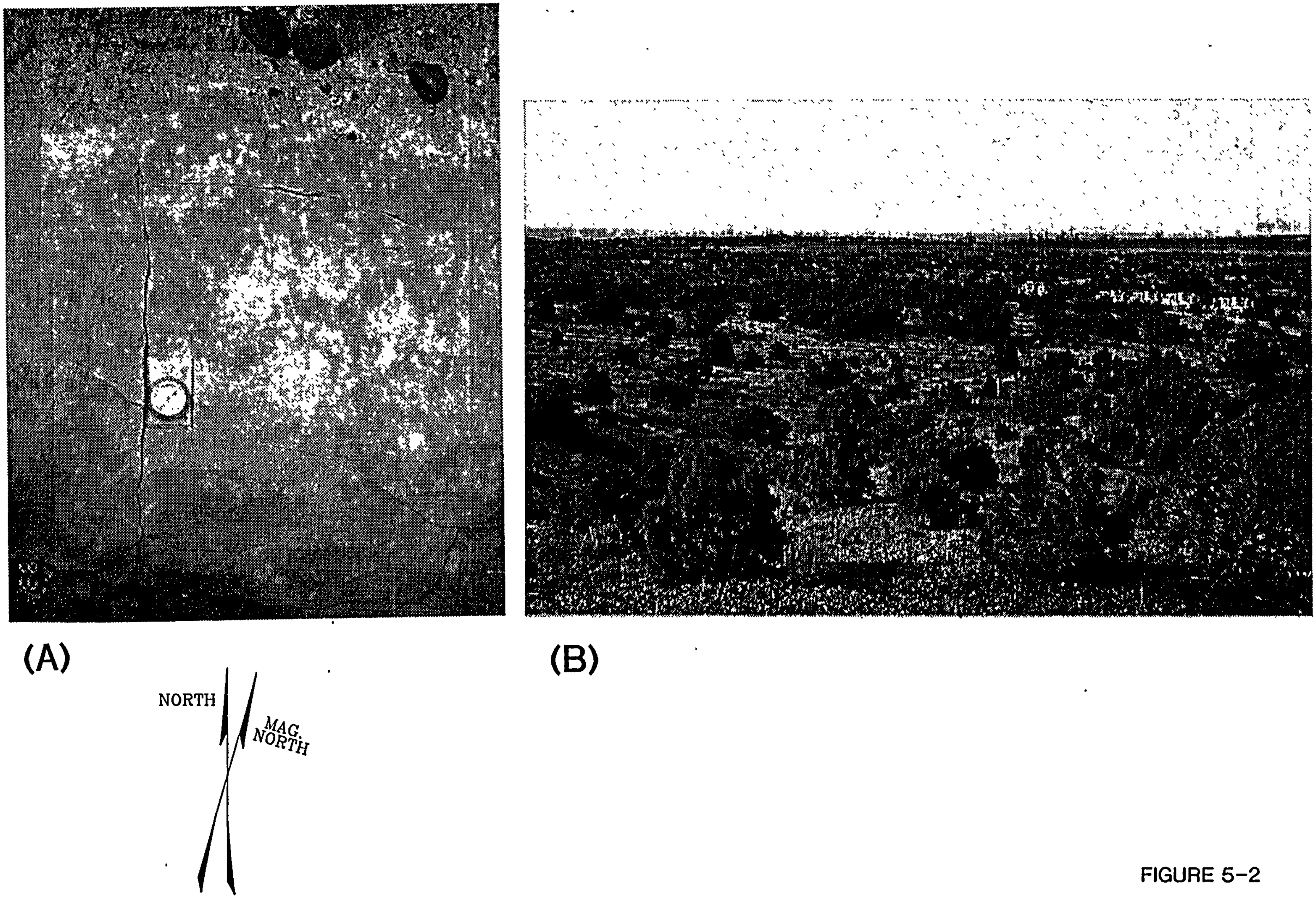

FIGURE 5–2

(A) Orthogonal fracture set, N 30° W, N 60° E.
(B) Veiw South along line 1.

considered reasonable and appropriate to orient the seismic lines with the initially proposed NE and NW orientations.

5.2 Borehole Image Log Data

Two FMS (Formation Micro Scanner) logs were available from Wells B2 and G (see Figure 5-3). The FMS logs are oriented logs which provide very high-resolution resistivity images of the borehole walls. Changes in resistivity are often associated with both structural features such as fractures and faults, and stratigraphic features such as scour marks, cross bedding, etc. The image logs also show borehole breakouts, that is, collapses into the borehole wall due to release of stress during drilling. These have been used by others to indicate the minimum horizontal stress direction.

On the image data, the highest fracture density was noted at logged depths corresponding to the Green River formation (approx. 6,600 - 10,890 ft). The logs show a dominant fracture orientation of N20-30W in the B2, and multiple orientations (NW and NE) in the G. The FMS fracture orientations are shown on the map in Figure 5-3. The Upper Green River fractures were recorded as natural, induced, or a mixture thereof. It is also noteworthy that most of the fractures imaged were vertical to subvertical. The FMS data in the B2 well are described in some detail below.

5.2.1 Well B2 Fracture Images

The strike histogram and the azimuth plots in Figure 5-4 clearly show the two fracture sets observed in this well. Note that the strike histogram represents all fractures sampled from 6,490-10,890 ft which includes both the upper and Lower Green River Formations. The Lower Green River (below 10,000 ft) appears to be more heavily fractured than the Upper Green River (6,600-8,700 ft) in this well, and the dominant fracture strike changes by about 44° between the upper and Lower Green River. The azimuth plot shows that in the Upper Green River, above 7,500 ft, the dominant fracture direction is NW-SE, and in the Lower Green River, below 10,000 ft, the fracture trend is E-W.

An example of a NW-striking Upper Green River imaged fracture is shown in Figure 5-5. In this figure, the thinly-laminated beds which characterize the Upper Green River are seen as light (sandier) and dark (shalier) horizontal bands. The irregular dark sinusoid which is traced on all 4 image strips is a fracture cutting the borehole. The fracture dip, given by the azimuth at the bottom of the sinusoid, is about 85° (subvertical), and its strike is N20W.

5.3 Stress Field

Several lines of evidence were used to document the local and regional stress fields in the Bluebell-Altamont area. Although the data are sparse, the stress field study was aimed at interpreting the most likely direction of the open

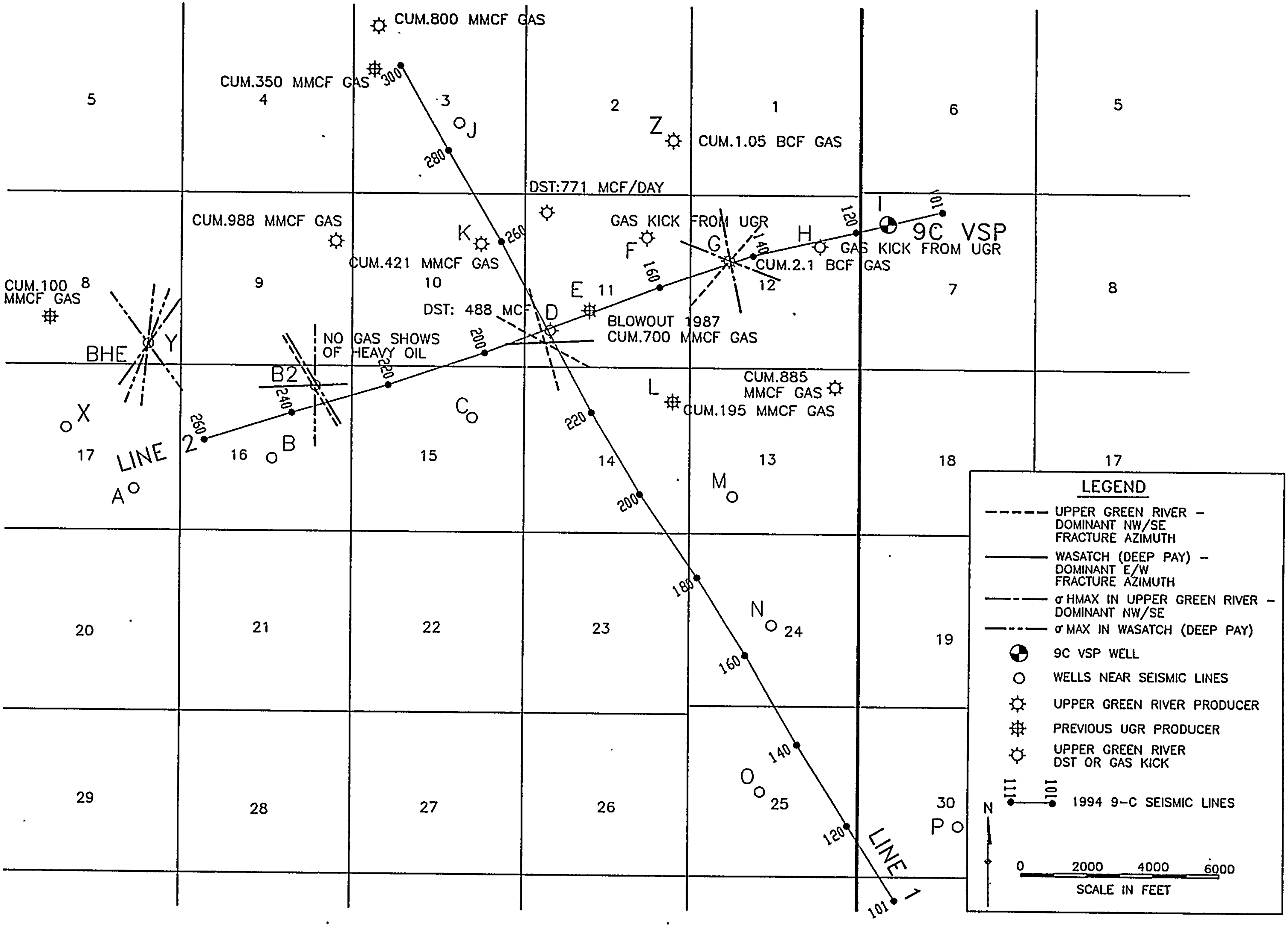

FIGURE 5-3

Local maximum horizontal stress directions interpreted from borehole elongations recorded in four-arm caliper and FMS logs, and the fracture azimuths from FMS logs and from oriented core at seismic line tie.

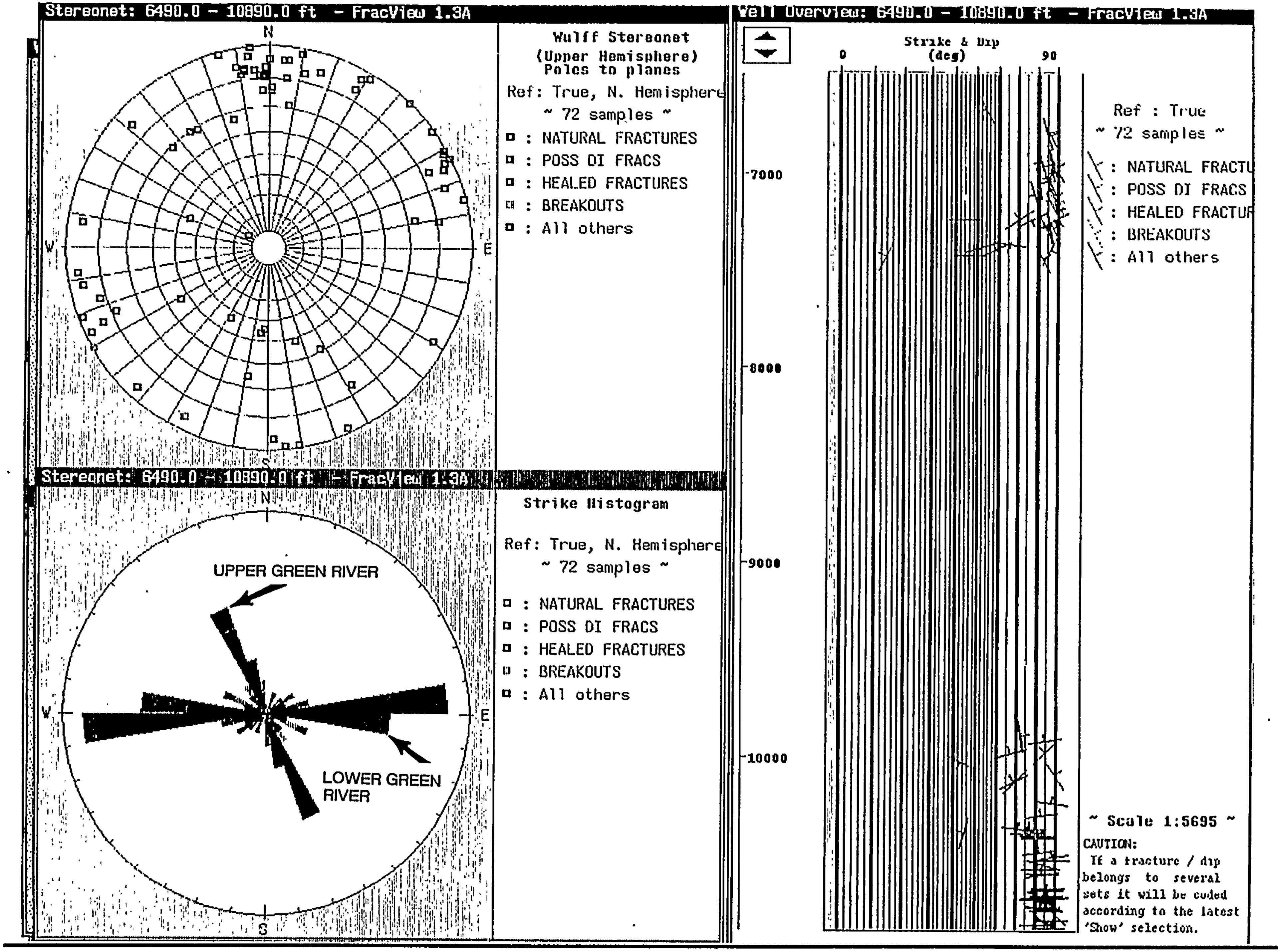

CAUTION:
If a fracture / dip belongs to several sets it will be coded according to the latest 'Show' selection.

Well B2: FMS log interpretation: NW pattern of fractures in Upper Green River (6,500-7,500 ft) EW in Lower Green River (+9,000 ft). Strike and Dip graph shows that fractures are vertical to subvertical.

FIGURE 5-4

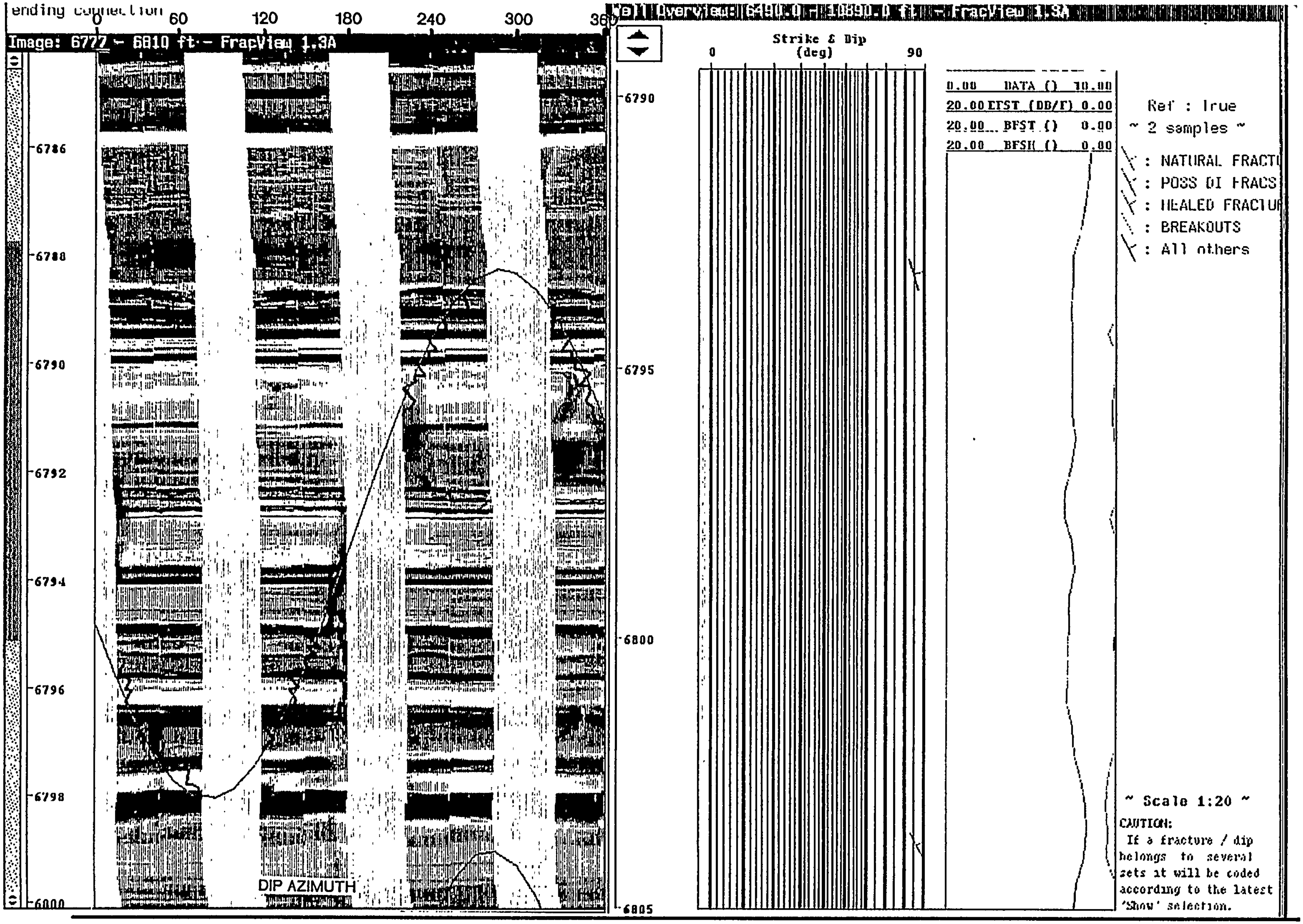

CAUTION:
If a fracture / dip belongs to several sets it will be coded according to the latest 'Show' selection.

Well B2: FMS image shows thinly-bedded Upper Green River strata as light (sandier) and dark (shalier) horizontal bands. The irregular dark sinusoid which is traced on all 4 image strips is a fracture cutting the borehole, at average depth 6,295 ft. Apparent dip about 85 degrees (subvertical); apparent strike is N20W.

FIGURE 5-5

fractures. All of the sources investigated led to the conclusion of NW or NNW-trending open fractures. The sources used in this project to determine the local stress field included:

5.3.1 Local Stress Field

Borehole elongation data from wells in the field have been used to indicate the local in-situ minimum horizontal stress by the long axis of the elliptical borehole.

5.3.2 Regional Stress Field

1. A review of pertinent literature, including published regional stress maps and modeling studies was conducted. The regional stress map of the continental United States (Zoback and Zoback, 1990) documented stresses from a variety of indicators including earthquake focal mechanisms, stress-induced borehole enlargement, young fault slip and volcanic alignments. This study found that the northernmost Colorado Plateau, containing the Uinta Basin study area, is characterized by a NNW maximum horizontal stress. Other, local studies of the Uinta Basin (Narr and Currie, 1982; Harthill and Bates, 1995) have used fracture distribution patterns and evidence of tectonism to argue that the stress history of the basin can be used to predict NW-trending open fractures.
2. Gilsonite veins, emplaced as natural hydrofracturing events in Cenozoic times, parted the most recent rocks covering the basin in long veins that strike NW in outcrops nearest the project area. Some workers have interpreted these as paleo stress indicators, which coincidentally have the same orientation as the local present-day stress field (see Figure 5-7).
3. The most recent earthquake in the Uinta Basin area occurred in 1977 about 34 miles west of Bluebell-Altamont field. The two largest shocks of that sequence had tension axes of N70E and N80E and compression axes of N10W and N20W (Carver et. al, Seismological Society of America bulletin, 1983). These findings indicate that the current in-situ stresses at the earthquake focal depths of approximately 6 km (20,000 ft) and at the earthquake focus (40°28′ N, 110°28′W, about 34 miles west of the field) are likely to be:
    - minimum horizontal stress σ_3 N70E-N80E;
    - maximum horizontal stress σ_2 N10W-N20W;
    - maximum principal stress σ_1 vertical.

5.3.3 Borehole Elongation Data

Borehole elongation data was obtained from four-arm caliper logs in two wells in the project area, the B2 and the Y. Gough and Bell (1982) and Zoback et al (1985), have interpreted ellipticity in boreholes as an indicator of the regional stress field with the long axis of the ellipse parallel to the minimum local horizontal stress (Figure 5-6). The four arm caliper logs in the field were interpreted in a similar manner for stress orientation, which is posted on the map in Figure 5-3. Following is an example of the interpretation of the borehole ellipticity data for the B2 well.

5.3.4 B2 Borehole Ellipticity Interpretation

The two orthogonal caliper sets consistently showed elongation of the borehole in the NE direction within the Upper Green River, log depths 6,670 ft-7,030 ft, indicating NE minimum horizontal stress direction, thus implying that the maximum horizontal stress direction, which governs the strike direction of the open fractures, is NW. Figure 5-6 shows a portion of the caliper log where the borehole elongation azimuth ranges from approximately N50W to N20W. The shaded area on the right-hand side of the figure shows that the greatest difference between long and short borehole axes is about 2 inches, at 6,910 ft-6,920 ft log depth.

Borehole failure images on the FMS log were also seen in the NE direction within the Upper Green River, providing an analysis of the stress direction which is independent from the 4-arm caliper logs.

5.3.4 Gilsonite Veins

Gilsonite Veins near the field area also provide evidence for the paleo stress field. Gilsonite or uintahite is a black to green shiny asphalite found almost uniquely in veins in Utah. The veins are from inches to 10-20 ft wide and can propagate for miles as continuous events. Fouch et al, (1992) have postulated that the veins form subsequent to hydrofracture of the rock perpendicular to the minimum horizontal stress. This natural hydrofracturing is thought to have occurred due to formation water expulsion from the Lower Green River, followed by expulsion of the viscous precursor of the gilsonite. In the project area, the veins have rotated from the dominant NW-SE orientation to NNW-SSE. Figure 5-7 shows the orientation of gilsonite veins near the project area.

5.3.6 Fracture Formation Models

Narr and Currie (1982) used observations of orthogonal joint sets observed on outcrops in the central and southern parts of the field, together with mono-directional fractures in cores, to develop a stress history model of fracture formation by failure in extension, after burial to maximum depth and continuing throughout subsequent uplift. The model is supported with geological evidence

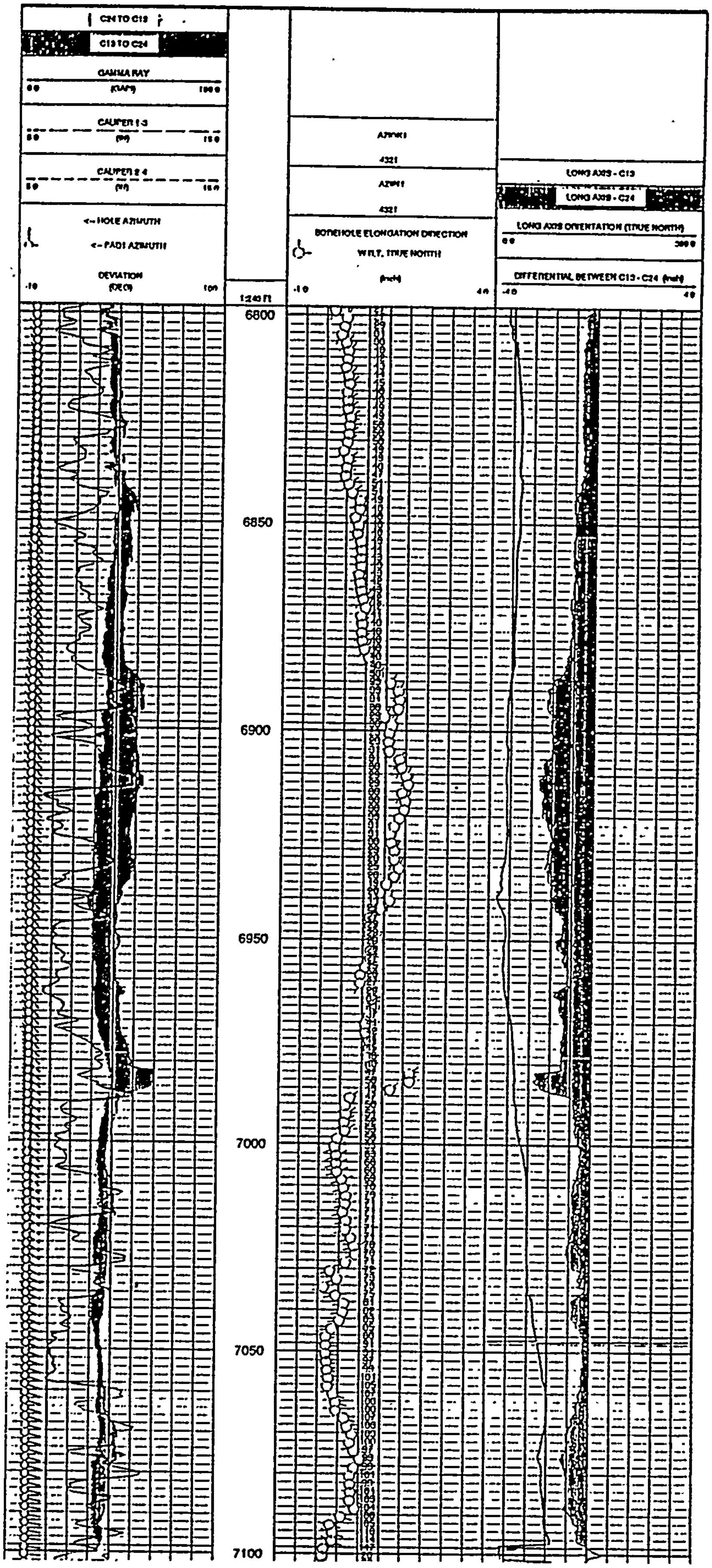

Well B2: 4-arm caliper log from Upper Green River Formation showing consistent borehole elongation in the NE direction. Shaded track on right indicates calipers oriented NE-SW measured borehole axis in NE-SW direction is 1-2 inches longer than NW-SE measured borehole axis.

FIGURE 5-6

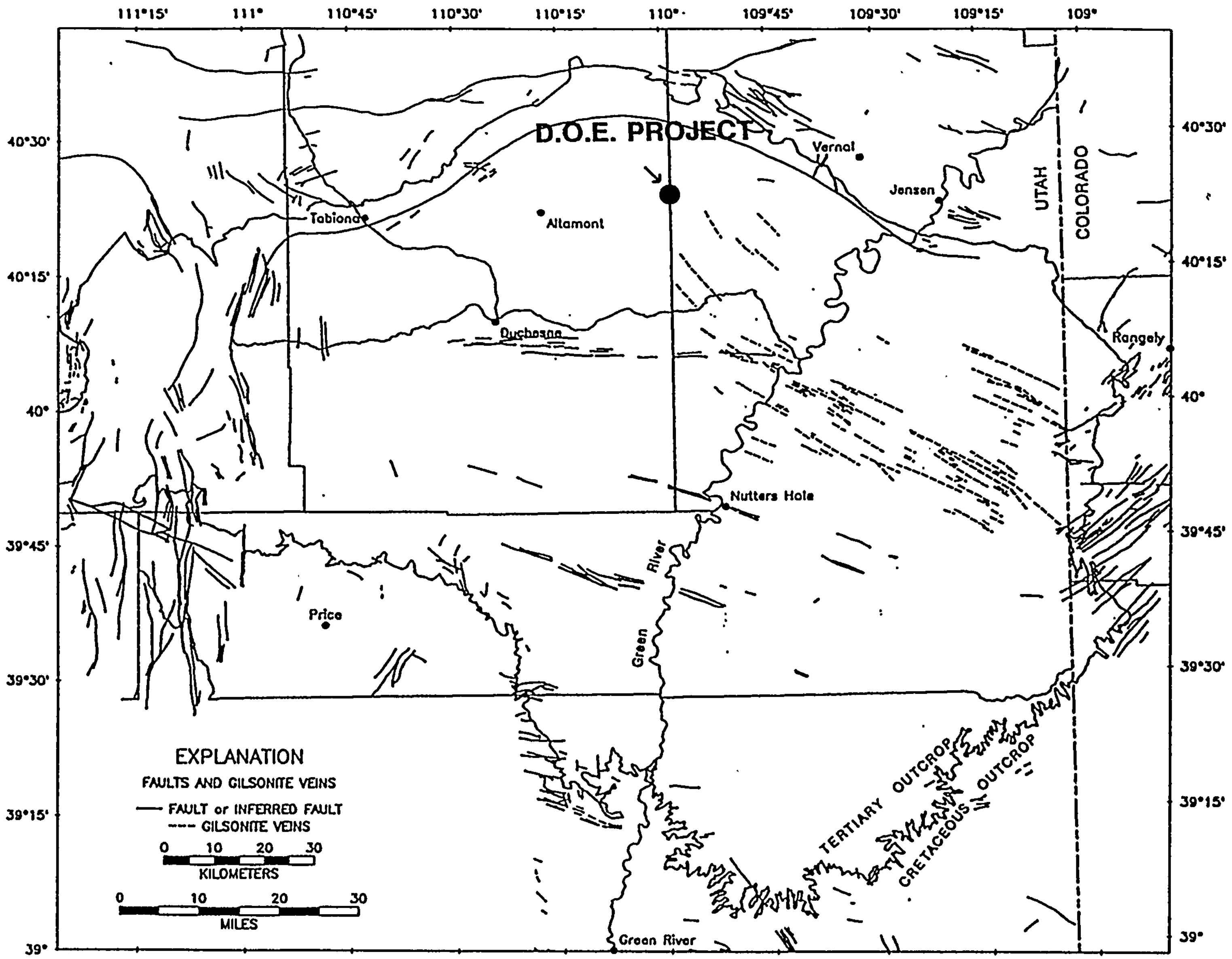

Gilsonite veins (dashed lines) and major faults (solid heavy lines) in Upper Cretaceous and Tertiary rock of the Uinta Basin (from Fouch et al, 1991)

FIGURE 5-7

including fluid inclusion studies, which suggested that fluids filled and partially filled the fractures throughout gradual removal of the overburden. Fractures seen in oriented cores from a well in the southern part of this DOE project area strike N20-N30W, parallel with the Uncompahgre uplift near the southeast perimeter of the basin. Normal faults occurring near the periphery of the basin are commonly aligned with nearby regional uplifts bordering the basin. The extensional failure model is also suggested by plumose markings (associated with fracture formation in extensional regimes) whose preservation would not be expected if shearing across joint surfaces had occurred. Both hydrostatic and overpressured pore fluid pressure gradients were modeled, since high fluid pressures at great depths within the field have been documented by several authors (Lucas and Drexler, 1976; Bredehoeft et al, 1994). The stress modeling of Narr and Currie suggests that high fluid pressures may have played a significant role in development of fractures at depth in Bluebell-Altamont. However, the modeling indicated that the development of a system of extension fractures during uplift is similar whether or not abnormal pore pressures existed at great depth.

Other authors studying the Uinta Basin have invoked a left-lateral strike-slip framework for the tectonism of the surrounding uplifts (Harthill and Bates, 1995), to predict a N15W orientation for the open fracture strike in the basin.

In summary, there are four sources of information concerning the potential orientation of the open fractures: 1, Borehole elongation data, which document the <u>local</u> in-situ stress; 2, <u>regional</u> stress maps and stress/fracture history models based on observations of faulting and trends of Laramide uplifts, and supported by direct geologic evidence (fractures in oriented cores); 3, <u>Regional</u> Cenozoic-aged gilsonite dikes; and 4, focal mechanism of a recent earthquake in the Uinta Basin. The consistency of all these sources leads to a conclusion that the open fractures are characterized by NW to NNW strike. <u>Local</u> variations in the in-situ stress field are interpreted as being reflected in the changing S1 (shear wave fast component) direction and magnitude of S-wave anisotropy observed along the 9-C seismic lines.

5.4 Horizontal Permeability Anisotropy

The production data were examined for evidence of a preferred flow direction, or a preferred communication direction. No wells producing in the Upper Green River were close enough together and on-line at the right time to test the hypothesis that the split shear S1 direction is the preferred flow direction (the maximum horizontal permeability direction). Based upon prior work, it is believed that the rocks that exhibit anomalously high shear wave anisotropy contain additional ordered compliant members within the rocks: these additional ordered compliant members are the flow conduits.

5.5 Core Analysis

Cores from the three wells indicated in Figure 5-3 were analyzed for fracture characteristics and reservoir parameters by David K. Davies and Associates, Kingwood, Texas. Oriented core was available only in the **D** well, located at the seismic line tie. Fracture azimuths from this well are shown on Figure 5-3 together with the FMS fracture and the borehole ellipticity (BHE) stress azimuths.

The analyses performed by David K. Davies and Associates included detailed macroscopic examination and description, interpretation of depositional environments, and analyses of small samples using thin section, x-ray diffraction and Scanning Electron Microscope techniques. The following section summarizes the primary results of the Bluebell-Altamont core analysis, and includes core photos and example thin section photomicrographs in Figure 5-8.

5.5.1 General Setting

In all wells, the cored intervals consist of alternating layers of sandstone, limestone and clastic shale. The sediments were deposited in lacustrine environments, specifically lake deltas, beaches and offshore bars, nearshore swamps, oxygenated and anoxic lake bottoms. The lake was large, deep, the water column stratified and located relatively close to a source area characterized by active vulcanism.

Most of the environments represented in the cored intervals are of marginal lacustrine origin. Potentially productive sandstones represent deposition in delta channels and stream mouth bars that were associated with tidal flat/shoreline fine grained deposits. The fine grained deposits are dominantly clastic shale with kerogen (plant fragments) and limestone (micrite) with fragments of thin shelled pelecypods. These deposits are either finely laminated or bioturbated. The laminated deposits represent anoxic bottom conditions: the bioturbated deposits represent oxygenated bottom conditions. These deposits can be interbedded indicating periodic turnover of a stratified water column.

Water laid volcanic ash deposits are present in one well (Well Z). These have been extensively silicified resulting in a rock that consists of a complex mixture of chert (microcrystalline quartz), plagioclase feldspar, augite, biotite, oxyhornblende (lamprobalite) and calcite. The rocks are laminated and contain occasional thin, parallel laminae of carbonaceous shale.

5.5.2 Sandstone Composition

The sandstones are classified as quartz arenites. Detrital constituents are principally subangular to subround grains of detrital quartz. Minor detrital grains include chert, orthoclase feldspar, plagioclase feldspar and volcanic/hypabyssal acidic igneous rock fragments. The rocks contain variable proportions of intra-basinal rip-up clasts, commonly limestone and dolostone fragments, sandstone and shale clasts. Fossil fragments (calcite) and plant fragments are scattered

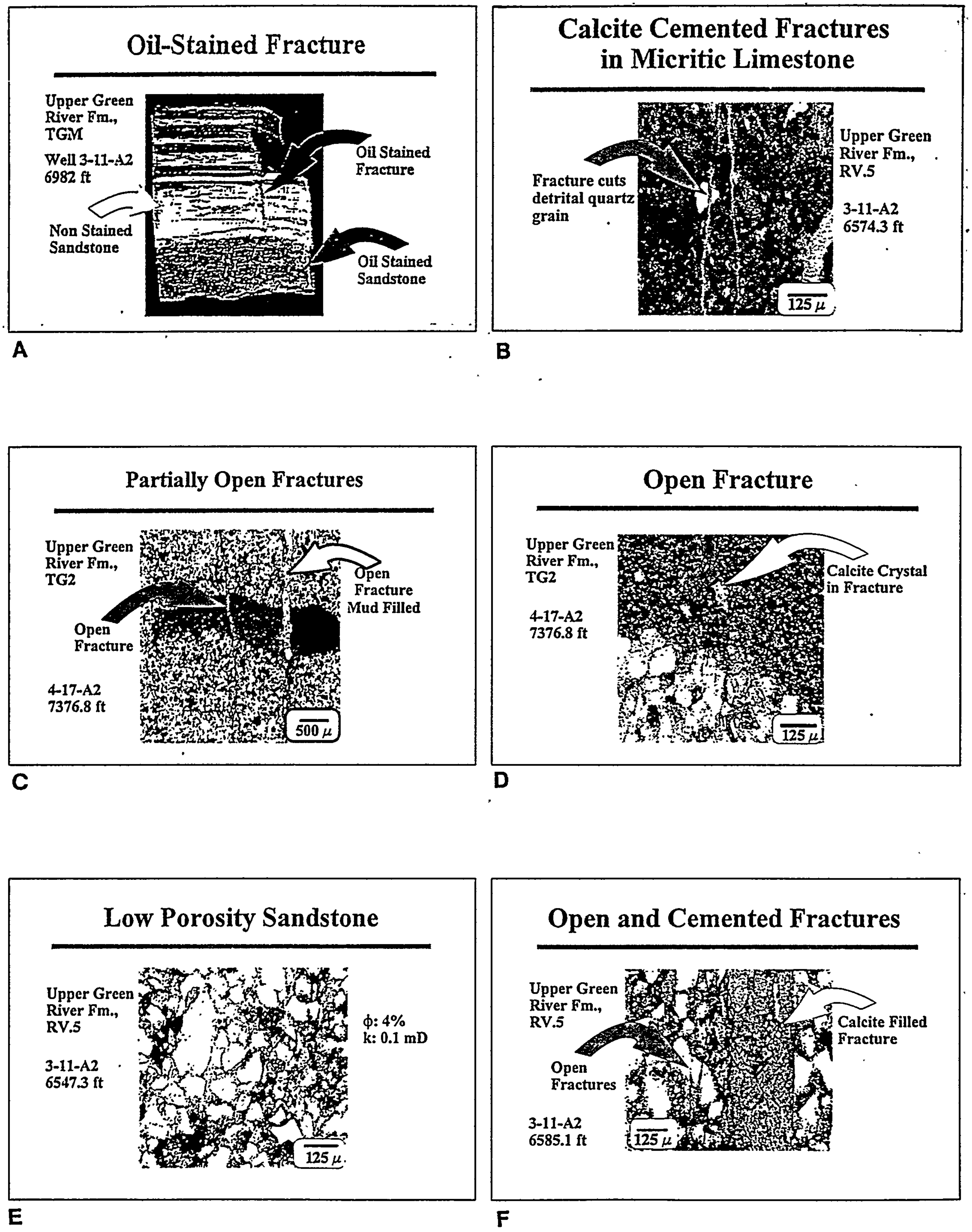

A Oil-Stained Fracture

B Calcite Cemented Fractures in Micritic Limestone

C Partially Open Fractures

D Open Fracture

E Low Porosity Sandstone

F Open and Cemented Fractures

FIGURE 5-8

Photomicrographs showing typical thin sections from Bluebell-Altamont throughout the rocks. Accessory (heavy) minerals include tourmaline and zircon (common) with rare augite and hornblende confined to volcanic ash deposits.

X-ray diffraction analysis reveals that the sandstones are clean (contain less than 5% clay minerals). Depositional shale (detrital matrix) occurs as occasional laminae and can also be dispersed between sand grains. X-ray diffraction analysis reveals that the principal components of the depositional shale are illite and illite-smectite.

Most samples are strongly cemented. The most abundant cements are dolomite, calcite and quartz. The dolomite occurs most commonly as an alteration of micrite that was deposited simultaneously with detrital quartz grains. This dolomitized micrite is fine grained and may contain minor volumes of dispersed depositional shale. Late stage, coarsely crystalline dolomite also occurs, but is volumetrically less important than the dolomitized micrite. Calcite cement is generally poikilotopic and can occur either in association with calcite fragments, or without the fragments. The calcite preserves loose packing in some samples (post-burial, pre-compactional cement), whereas in other samples it occurs in sandstones with moderate packing and tangentional grain contacts (syn- to post-compactional cement). Quartz occurs as silica overgrowths on detrital quartz grains and less commonly as microcrystals. Both varieties of quartz were precipitated during the early stages of compaction and are important because they preserve tangentional grain contacts.

Less common cements include authigenic clay (illite), rare zeolite, feldspar overgrowths and pyrite. All cement varieties can be well seen in the thin section and scanning electron microscope (SEM) photomicrographs.

Two samples of altered volcanoclastic sandstone were analyzed (6,976.8 ft and 6978.3 ft, Well D). These have been extensively silicified resulting in a rock that consists of a complex mixture of chert (microcrystalline quartz), plagioclase feldspar, augite, biotite, oxyhornblende (lamprobalite) and calcite.

5.5.3 Sandstone Texture

For the most part, the sandstones are very fine to fine grained, poorly to moderately well sorted and moderately tightly packed. Packing is a function of the cementation history of the rock. Sandstones with silica overgrowths and calcite cement are commonly characterized by tangential grain contacts and moderately tight packing. Sandstones that contain fine grained carbonate (dolomitized depositional micrite) in the intergranular areas exhibit tight packing. In these rocks, long grain contacts are dominant. Thus, authigenic precipitation of silica and calcite was restricted to sandstones that were devoid of depositional carbonate. In the strict sense, the fine grained dolomite represents the recrystallization of dispersed depositional calcareous matrix.

5.5.4 *Limestone Texture and Composition*

Limestones are common in the cored intervals. They are skeletal micrites. The skeletal fragments include thin shelled pelecypods and ostracods, together with algae. These rocks have very low values of porosity and permeability, and are not reservoir rocks.

5.5.5 *Controls On Matrix Porosity*

The volume of matrix porosity in the sandstones is low, most Thin Section derived porosity values are <10%. However, some sandstones have porosity values of 12 to 14%. The volume of matrix porosity is a function of the cementation history of the rock. Samples with fine grained dolomite have low values of porosity (generally <5%) due to tight packing. Compaction during burial resulted in grain rotation and slippage that ultimately led to the development of detrital grains with long contacts and intergranular areas filled with depositional carbonate matrix. Sandstones that were clean (matrix-free) at the time of deposition experienced cementation during burial compaction. The precipitation of silica overgrowths and patchy calcite during the early stages of burial and compaction imparted a degree of rigidity to the rock that resulted in the preservation of intergranular porosity in some sandstones. Obviously, too much cement precipitation resulted in the filling of intergranular pores, and a significant loss of porosity and permeability. Rocks with porosity values between 5 and 14% exhibit a delicate balance between the effects of cementation and burial compaction.

5.5.6 *Matrix Porosity and Permeability*

In general the potential reservoir rocks are characterized by low values of matrix porosity and permeability. Core measured values of porosity (for the samples analyzed petrographically) range from 2.6 to 9.7%. The core measured porosity values in Wells X and Z are, for the most part, lower than Thin Section derived values of porosity.

Table 5-1
Core Measured Porosity and Thin Section-measured Porosity
Well X

Depth (ft.)	Core Measured Porosity (%)	Thin Section Porosity (%)
7288.6	6.2	11
7294.8	3.0	11
7376.8	2.4	3
7517.8	6.1	6
7552.6	2.8	3

Table 5-2 Core-measured Porosity and Thin Section-measured Porosity Well Z		
Depth (Ft)	**Core Measured Porosity (%)**	**Thin Section Porosity (%)**
7038	7.1	10
7056.8	7.5	12
7060.2*	2.6	3
7073.7*	9.7	12
7092.2	5.4	12
7099.8*	5.6	4
7117.6*	9.6	14
7135.6	9.7	8

* Thin Section was taken from the same inch of rock as core plug. Remaining samples are from the same foot of rock. The precise core plug location was not known in these instances.

Note: Core measured values are from whole core analysis (several inches of whole core). Thin Section values are from small samples removed from the core.

This type of discrepancy is highly unusual. Thin Sections tend to underestimate core measured porosity because Thin Section values report visible porosity (generally pores larger than a few microns). Core measured porosity determines the volume of all interconnected pores, irrespective of their size.

The discrepancies in porosity values may reflect either: 1) rapid changes in porosity over very short distances, inches or less, or 2) inadequate core cleaning prior to core analysis resulting in pessimistically low values of core measured porosity. The uniformity of oil stain in some of cores from the X Well indicates uniformity of porosity over several inches of core. Log derived values of porosity (PHID) from this well indicate that the core measured values of porosity are low (see Table 5-1). Thin Section and log data suggest that porosity values are higher than those measured in core analysis. This leads us to suspect that there may be some problem with the core analysis data. This may be related to inadequate core cleaning in oil-stained samples.

The same sort of comparison between cores, logs and Thin Sections cannot be undertaken for the Z Well (there is no density porosity log) and the core analysis was carried out on whole core pieces (see Table 5-2). However, the same problem may occur in this well.

These results suggest that the routine core data should be used only with great caution. Some of the measured core analysis data may not be correct, it may significantly underestimate matrix porosity.

Oil staining occurs irregularly throughout the sandstones (see Figure 5-8a). Oil staining is associated with rocks with the highest porosity.

5.5.7 Fracture Porosity and Permeability

All cores contain evidence of some natural fracturing (see Figure 5-8a, b, c, d and f, and Figure 5-9). Calcite crystals observed within some fractures, as in Figure 5-8d, is interpreted as evidence of the fractures' natural origin. The degree of fracturing is not extensive. Most of the fractures are relatively short (<1 ft vertical length as seen in core). They are vertical and represent a fracture system in which the individual fractures are relatively widely separated from one another. As a result, fractures occur most commonly as single vertical cracks in the rock, not as multiple side-by-side fractures. A core photograph from Well D, in Figure 5-9, shows an example of such a single vertical fracture. In the opinion of David K. Davies and Associates, these cores do not represent a highly fractured reservoir.

Natural fractures in these rocks generally contain calcite cement. Some of the fractures are completely cemented by calcite (they are "healed") while others contain discontinuous calcite cement and are, therefore, open. These open fractures can be 10 microns wide (as determined from the size of the calcite crystals in the fracture system). Some of the fractures in the rocks contain drilling mud.

There is no doubt that natural fracturing enhances the porosity and permeability (particularly the permeability) of the matrix system. Hydraulic fracturing of the rocks will be effective because it will link the widely separated fractures that characterize the rocks. The natural and hydraulically induced fractures will effectively drain the matrix pore system.

WELL D

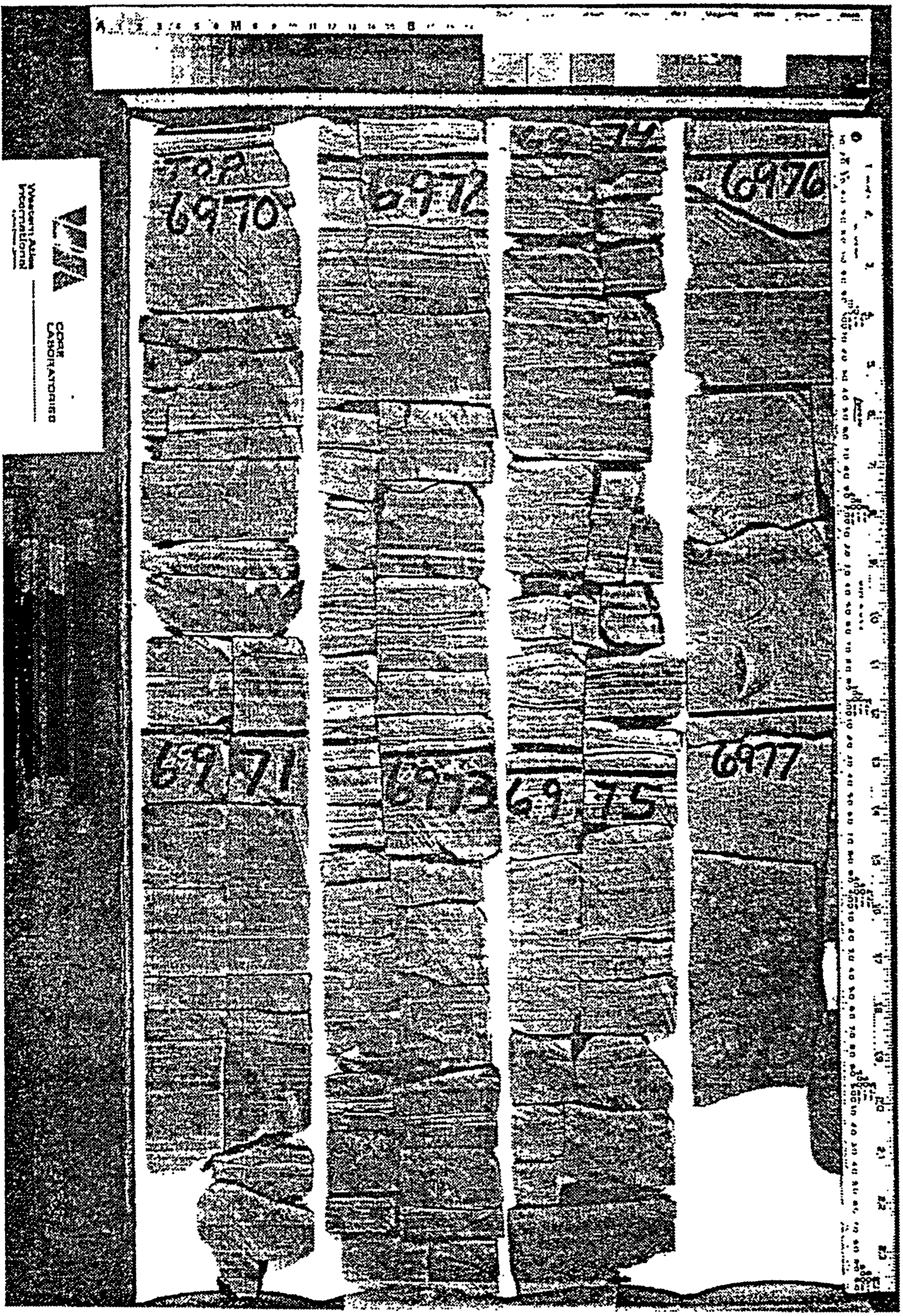

6970 - 6977 FT.
NOT TESTED

GRTGM FM.

FIGURE 5-9

Core photograph from Well D showing vertical fracture.

6.0 SEISMIC ACQUISITION

6.1 Summary

Seismic acquisition (VSP and Surface Seismics) were completed during the period April 8-24, 1994. Ten miles of surface seismics were collected using the parameters outlined in Table 6-1.

Locating the multi-component seismic lines in the field was a critical planning aspect of the project. For the P-wave AVO studies it was important that the seismic lines were set out both parallel and perpendicular to the open fractures. The line orientations were based on fracture and joint outcrop studies, literature reviews and analysis of the borehole data, as outlined in Section 5. The final NW/SE and NE/SW orientation also facilitated the acquisition effort as the NW/SE line was parallel to the major drainage in the field site. As in with the field work described by, Lynn and Thomsen (1990), the drainage was influenced by the dominant crack azimuth. Easy access routes paralleled the drainage, and the vibrators stayed on or near the easy access.

The final acquisition parameters for the surface seismics were determined during a wave test program at the beginning of acquisition. At this time, impact studies were conducted to determine the recording system polarity.

The S-wave reflection data were acquired simultaneously with the P-wave reflection data, using 3-component geophones. Because P-wave and S-wave data have different inherent characteristics requiring different acquisition geometries for optimum interpretation, compromises had to be made in the acquisition phase of the project. The most important criterion for the P-wave data was to have source-receiver offsets sufficiently long for AVO analysis; in order to record P-waves with incidence angles up to 30°, it was determined that a maximum offset of 9,000 ft was desirable. However, for S-wave data, near-vertical travel paths are considered more interpretable. The S-wave data on offsets from 0-6,000 ft were judged the most useful. Therefore, a decision was made to acquire the 3-component seismic data to record offsets out to 9,000 ft, in order to obtain the data necessary for P-wave AVO, at the expense of reducing the fold of the useable S-wave data (offsets greater than 6,000 ft were not stacked into the final S-wave sections). For this reason, the fold of the final S-wave sections is reduced from that of the P-wave sections.

The 9-C VSP was acquired prior to the 9-C reflection seismic, in order that the S-wave two-way time to target could be determined and used to set the surface field acquisition parameters.

The VSP field work was conducted by Schlumberger in Well I from April 8 to April 10, 1994. Four compressional wave vibrators were supplied by Lockhart Geophysical and four shear wave vibrators were supplied by Grant Geophysical for the VSP acquisition. The S-wave vibrators were the Amoco S-vibrators with rotatable baseplate. Seven source locations were used for the VSP to acquire 9-C VSP data from 8,650 ft below surface to 300 ft below surface (see Figure 6-1a). Data through the target zone were of good quality once problems associated with tube noise had been mitigated (the source was moved off the hill into a small valley).

After the 9C VSP was acquired, two days were spent testing for optimum receiver array length, source array, source sweeps, and polarity of recording system and of vibrators. The noise spread or wave test consisted of potting the geophones (1 string per receiver location) at a 15 ft receiver spacing for 48 ground locations. Hammer blows (P, inline shear, and crossline shear) were used to verify the polarity of phones and recording system. This was followed by tests with P and S-wave vibrators to measure the wavelength, frequency and velocity of ground roll and source-generated noise. An array length of 110 ft centered on the receiver location was determined to be acceptable for both P and S sources. The source tests included number of vibrators, number of sweeps, and swept frequencies. The chosen parameters are summarized in Table 6-1. The maximum source-receiver offset is about one-third greater than target depth, for the T/UGR, target depth 6,600 ft, maximum offset 8,950 ft). The offsets from 5,989 ft to 8,950 ft were the critical offsets for the P-wave AVO response.

The time of acquisition was fortunate, before spring irrigation of the agricultural land. Since the winter and spring had been relatively dry, access was good and damage by the vibrators small. Unfortunately, this also resulted in poor coupling between the source/receivers and surface loose sandy soil, despite an effort to bury the phones. It is thought that a great amount of energy can be lost through this surface zone and this appeared to be the case with this survey. This was also substantiated by the vibration monitoring which showed vibrations an order of magnitude less than USBM standards. It is recommended that future work be timed more closely with the potential for frozen or moist ground. The receiver coupling might also have been improved by drilling 1 ft auger holes down which the geophones would be planted and buried.

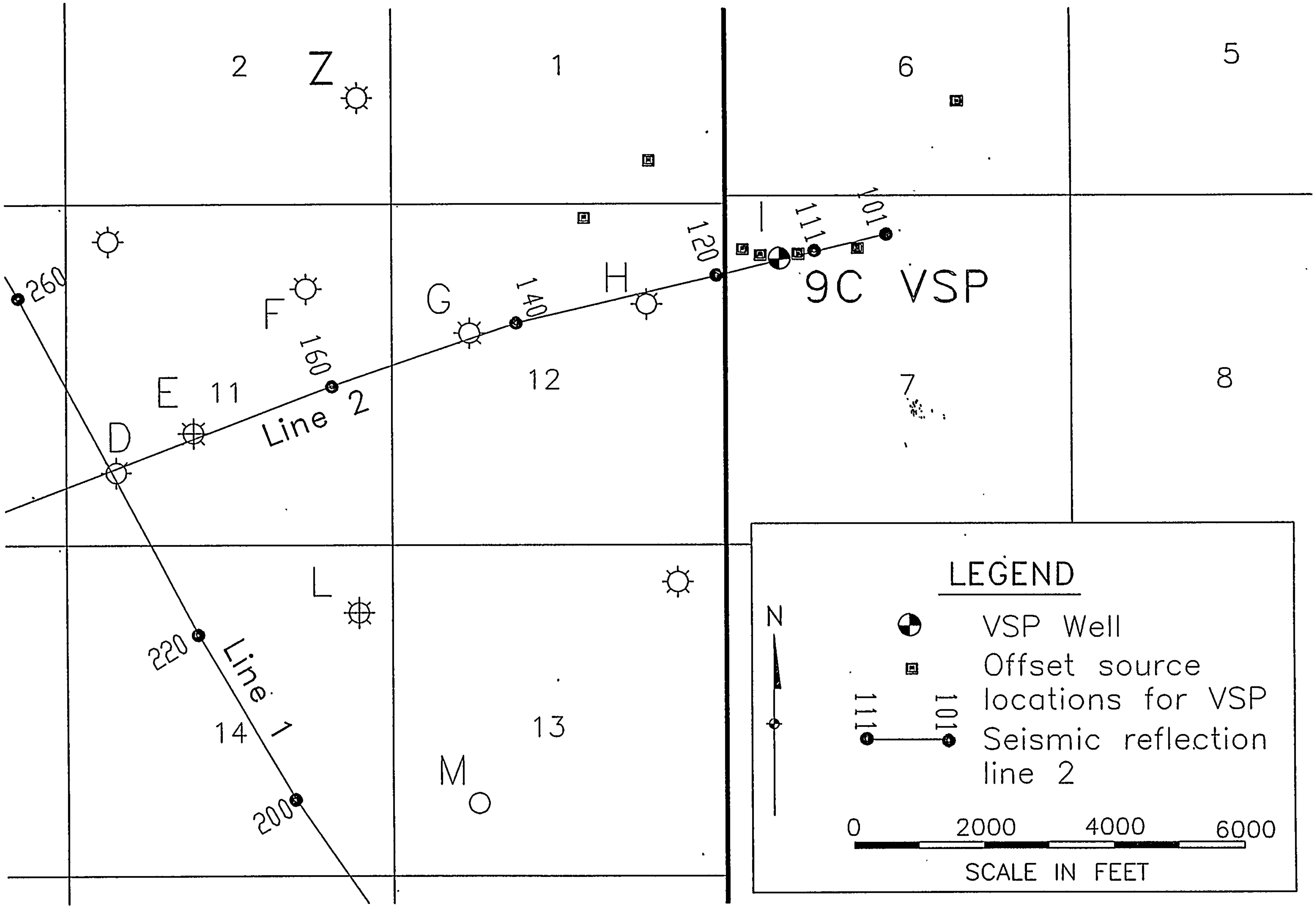

FIGURE 6-1A

Location map showing Well I (9C VSP well) and 9C surface reflection seismic line locations. Acquisition diagram for 9C VSP showing offset source configuration.

Table 6-1
Acquisition Parameters for P-wave and S-wave Surface Reflection Seismic

Instrument Type	DFS-V
Sample Rate Record Length	2 msec. 6000 msec.
Number of Traces	120
Recording System	3 DFS-Vs in master-slave arrangement
Gain	Instantaneous Floating Point
Geophone Type Geophone Frequency	OYO 3-C 10 Hertz
Geophones per string	12 at 5.5 ft separation
Group Interval	150 ft
Group Array Length	110 ft
Source Type	Mertz P/S Vibrators
Source Interval	300 ft
Nominal CDP Fold	30 fold
P-wave Sweep	16-96 Hz. nonlinear; 12-sweep sum
S-wave Sweep	Line 1: 10-64 Hz linear SP 101-239; 6-36 Hz. linear SP 240-286; Line 2: 6-36 Hz. linear (all SP)
Filter	out - 128 Hz
Environment	Pasture and Grassland

6.2 VSP

The 9C VSP was acquired in Well I (Figure 6-1a) from 8,650 ft to 300 ft. Seven source locations were used; four offset locations for P, crossline shear or tangential shear (SH), and radial shear (SV) , and three far offset P-wave locations.

6.3 Surface Seismics

6.3.1 Production Line 1

Line 1 was surveyed on April 14 to 18. The location of the line is shown on Figure 6-1b. Data quality was variable along the line with what appeared to be poor data quality on the field monitors to the south over the mixed agricultural land and improved quality to the north over the undisturbed terrain. During processing it became evident that the southern data were still quite usable. Wind noise was obvious during the first day of production survey and the

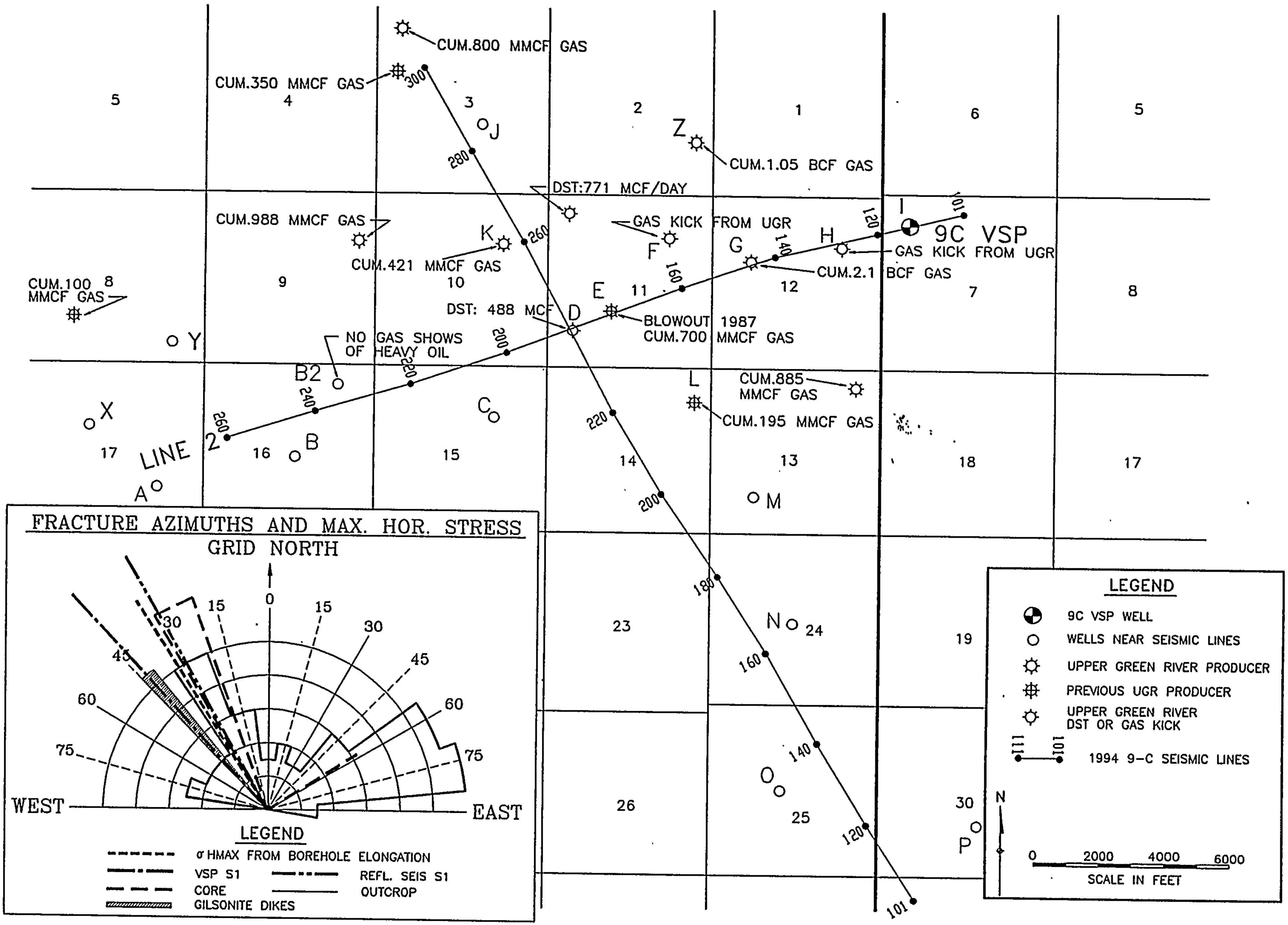

FIGURE 6-1B

Surface Seismic Line 1 and Line 2.

geophones were subsequently buried under a few inches of topsoil. The wind noise was most evident on the horizontal components. Field operations were shifted to the early morning hours to take advantage of the minimal wind noise in the mornings.

In the field a number of reflectors were clearly identified in the raw P-wave records. The most prominent of these were the T/UGR Formation and Mahogany Bench (MB) (Figure 6-2a); that is, the top and bottom of the zone of interest for this project.

The shear wave data did not show clear reflectors in the field apart from that of the MB (Figure 6-2b). However, it was evident from this reflector and its presence in cross components (i.e., shooting with crossline shear and recording inline shear) that anisotropy in shear waves was present in the section down to the MB. The magnitude of shear wave splitting can be estimated by the 100 msec time delay between crossline and inline reflectors - shown by the two sets of geophones in Figure 6-2b. The inline shear is within 20° of S1; that is, it behaves like S1 and the cross shear like S2 for this line. The lines are skewed approximately 20° to the natural coordinate system. A 4% anisotropy is observed at the MB reflector (~2.6 sec.). The interpreted open fracture direction from this is N25W. Since a typical background shear wave anisotropy in North America is approximately 2%, the 4% observed average anisotropy in the sedimentary column between surface and MB is significant.

6.3.2 Production Line 2

Line 2 was surveyed on April 19 to 24. Data quality was once again variable, although with little agricultural land traversed, was generally improved over Line 1. Logistical problems were compounded along Line 2 with the steep topography associated with crossing a major drainage. Wind noise was once again only a significant problem towards the late afternoon and early evening.

6.3.3 Surface Static Tests

A number of locations were chosen to conduct shallow static tests using point sources and receivers. At each location, single element geophone receivers were deployed at 10 ft intervals to 480 ft, and an impact source used at various offset distances. These data were used to supplement the reflection statics analysis. The results of the survey are summarized in Table 6-2 below.

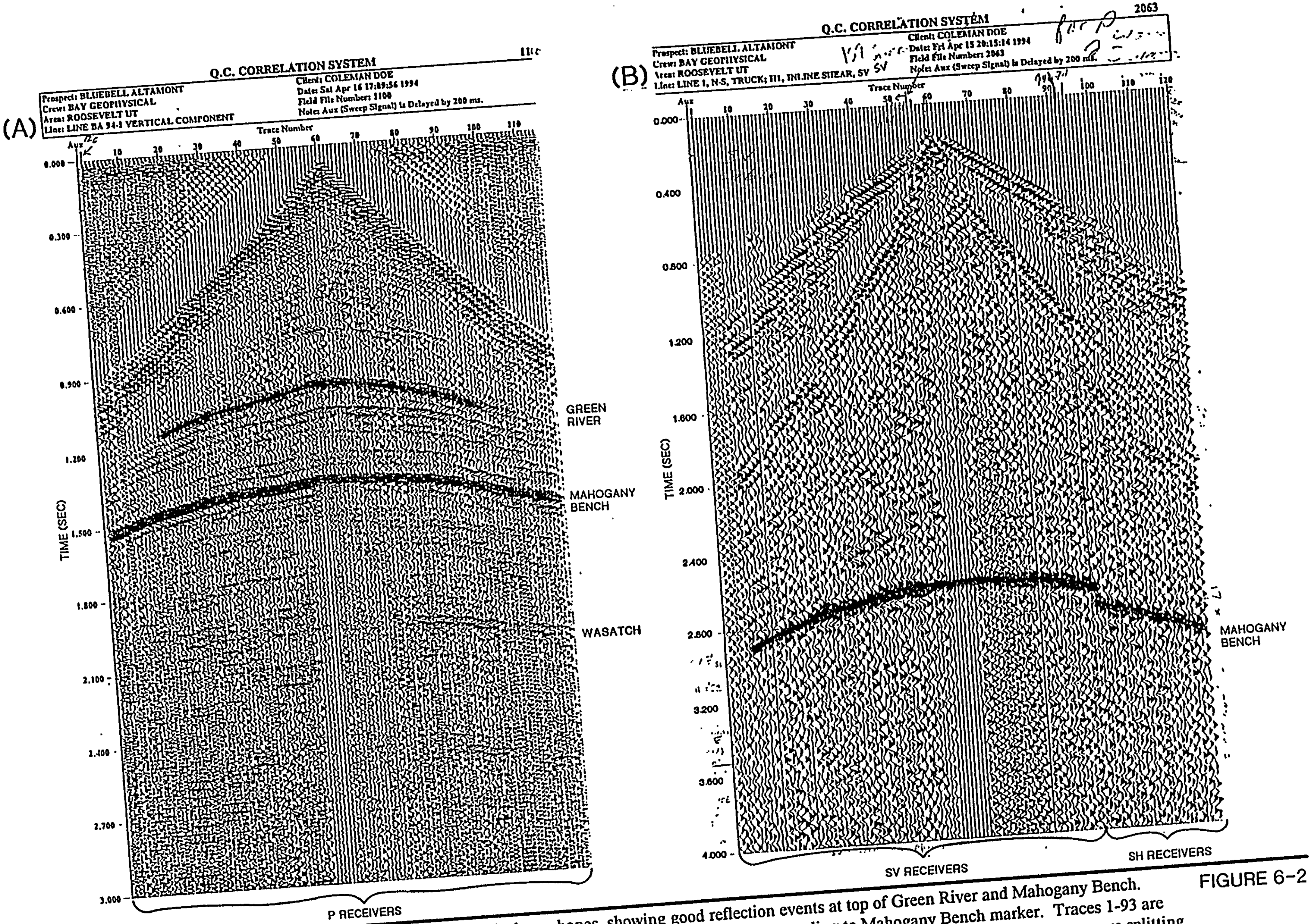

FIGURE 6-2

(A) Field record from P-wave source, vertical geophones, showing good reflection events at top of Green River and Mahogany Bench.
(B) Field record from S-wave inline source, showing strong reflection event corresponding to Mahogany Bench marker. Traces 1-93 are inline receivers, traces 94-120 are crossline receivers. Time delay between inline and crossline receivers indicates shear wave splitting.

Table 6-2
Shallow Refraction Statics

		Velocity (ft/sec)			Depth (ft)			
Record No.	Source/ Receiver Orientation	V1	V2	V3	Z1	Z2	Line Number	Location
SHOT TUBE								
2152	SV/SV		3000	4250		190	2	Crosspoint
2145	SV/SV		3000	4200		275	2	Crosspoint
3159	SH/SH		3375	4500		281	2	Crosspoint
3141	SH/SH		3563	4500		292	2	Crosspoint
1141	P/P		7941	9265		400		
1032	P/P		10200	11800		994		
HAMMER IMPACT								
34	SH/SH	650	3370		42		2	On Peninsula
37	SV/SV	833	2870		48		2	In Cotton Creek
	P/P	800	3700					
29	SV/SV	1000	4364		23		1	Up On Hill
3	SH/SH	1200	2824		26		1	
LARGE VIBRATORS								
3004	SH/SH	1875	4500	6000		189	2	Near Duncan
2012	SV/SV	1875	3750	5250		152	2	Near Duncan
VSV < VSH on L2 (SH ~ S1,SV ~ S2)								
3088	SH/SH	2625	4875	5625		230	2	Source @ STN 180
2085	SV/SV	2625	4875	5625		230	2	Source @ STN 180
	SH/SH	2250	4500	6000		286	1	Source @ STN 240
	SV/SV	3000	5250	6000		466	1	Source @ STN 240
	P/P		6750	9000		280	1	Source @ STN 240
JULY 1993 TESTING								
465	SV/SV	1440	4800		20		2	(T3)2^{ND} On W/EOL 2
458	SH/SH	1750	6000		29		2	(T3)2^{ND} On W/EOL 2
455	SH/SH	480	1500		14		2	(52)N-S 1
440	SH/SH	685	2400		32		2	1^{ST} On E (MID. Of L-2)
456	SV/SV		1142					
451	SH/SH	280	1100		4		2	
452	SV/SV	480	1371		5		2	

The static spreads were deployed parallel to both Line 1 and Line 2 with crossline (SH) source and receiver orientations perpendicular to the line, and inline (SV) source and receiver orientations parallel to the line.

The results show that:

1. The hammer impact study along Line 2 indicates SH/SH energy to be faster than SV/SV energy. The SV/SV hammer energy along Line 1 was faster than the SH/SH energy.
2. The SH/SH shot tube energy along Line 2 was faster than SV/SV.

These results suggest that an azimuthal anisotropy in shear wave velocity exists in the near surface to a depth of approximately 1,000 ft. The anisotropy is interpreted to result from cracks because the fast/slow directions reverse with line/polarization direction. Also it was noted that the dominant crack set seen in outcrops adjacent to the seismic line is NW/SE. These results were confirmed by analysis of the statics from the shear-wave reflection data (see Data Processing, Section 7).

6.3.4 Line Direction

The advantages and disadvantages of acquiring multi-component seismic data parallel and perpendicular to the rock's natural axes should be clearly understood. If the lines are acquired skewed to the natural coordinate system, each source's (SV and SH) S-waves split and the source-generated noise effects of SV vs. SH acquisition are minimized through four-component rotation (Alford rotation). In this case, the source-generated noise (SH or SV) is minimized. If, however, the lines are acquired parallel to the natural coordinate system, source-generated SV or SH noise is seen clearly on the S1 or S2 shot records. Therefore, comparing reflection amplitudes of S1 to S2 may be influenced by the source-generated SV or SH noise. In this project, shear wave splitting was observed, and the line directions estimated to be skewed by approximately 20° to the natural coordinates, as described above. Hence the influence of coherent noise is somewhat diminished. For the concurrently acquired P-wave data to be useful for the far-offset (AVO) analyses, the source-receiver azimuth was required to be nearly parallel or perpendicular to the strike of the open fracture set. A comparison of the seismic response of P-waves propagating nearly parallel and perpendicular to the open fracture strike, would be more clearly interpretable in terms of line azimuth with respect to open fracture strike, than that of P-waves propagating skewed to the natural coordinates.

6.3.5 Environmental Impact

The survey was conducted to the satisfaction of local authorities with no permanent habitat disturbances. No culturally significant artifacts were discovered along the acquisition lines and, therefore, no sites were nominated for the National Historic Register. Disturbances to the ground caused by the vibrator trucks were successfully remediated (graded and re-seeded) to the satisfaction of local land owners.

7.0 SEISMIC PROCESSING

7.1 Nine-Component VSP

The goals of the 9C VSP processing were: 1), to determine the time-depth-velocity relationships for P, S1 and S2; and 2), to calculate the corridor stack for P, S1 and S2. The corridor stack is the capture of the upgoing (reflected) wavefield close to the reflecting boundary. The corridor stack gives the seismogram in time and depth that is used to tie formation boundaries to reflection events.

7.1.1 P-wave

Median stacking of the seven P-wave source initiations, using the vertical component, was performed after manual editing of noisy traces. A polarization filter using X and Z (crossline and vertical components) estimated tube wave noise. A 10-100 hz filter was applied to the vertical channel. Amplitudes at each level are normalized to the same RMS value in a window of 150 msec, starting 40 msec before P wave arrival time. These data, the preprocessed vertical stacks, are shown in Figure 7-1a.

A velocity filter was used to separate the downgoing and upgoing wavefields: the downgoing wave field was time aligned, and an 11-level median filter enhanced the downgoing wave after frequency domain alignment of downgoing waves to first P arrival times. The downgoing wave is shown in Figure 7-1b. The median P downgoing wave is subtracted from the pre-processed Z stacks to create a difference file (the upgoing wavefield). A 7-level median filter was applied to the upgoing wavefield to enhance the upgoing waves, after frequency domain alignment of upgoing waves (Figure 7-1c).

Waveshaping of the P-wave wavelet was next performed. The input to the Wiener filter was the median downgoing P wavefields. A Wiener filter designed on the median downgoing wave at each level is applied to both the median downgoing and median upgoing wavefield. The input was 2,000 msec of downgoing wavefield, starting 40 msec before the first break. The desired output is the impulse response of a 6th order zero phase Butterworth 10-100 hz filter. White noise of .01 level was used. Then the data were filtered (10-100 hz). A gain function of Time exponent 2.3 (T**2.3) was then applied. The output was the waveshaped downgoing and waveshaped upgoing wavefields (Figures 7-1d, 7-1e).

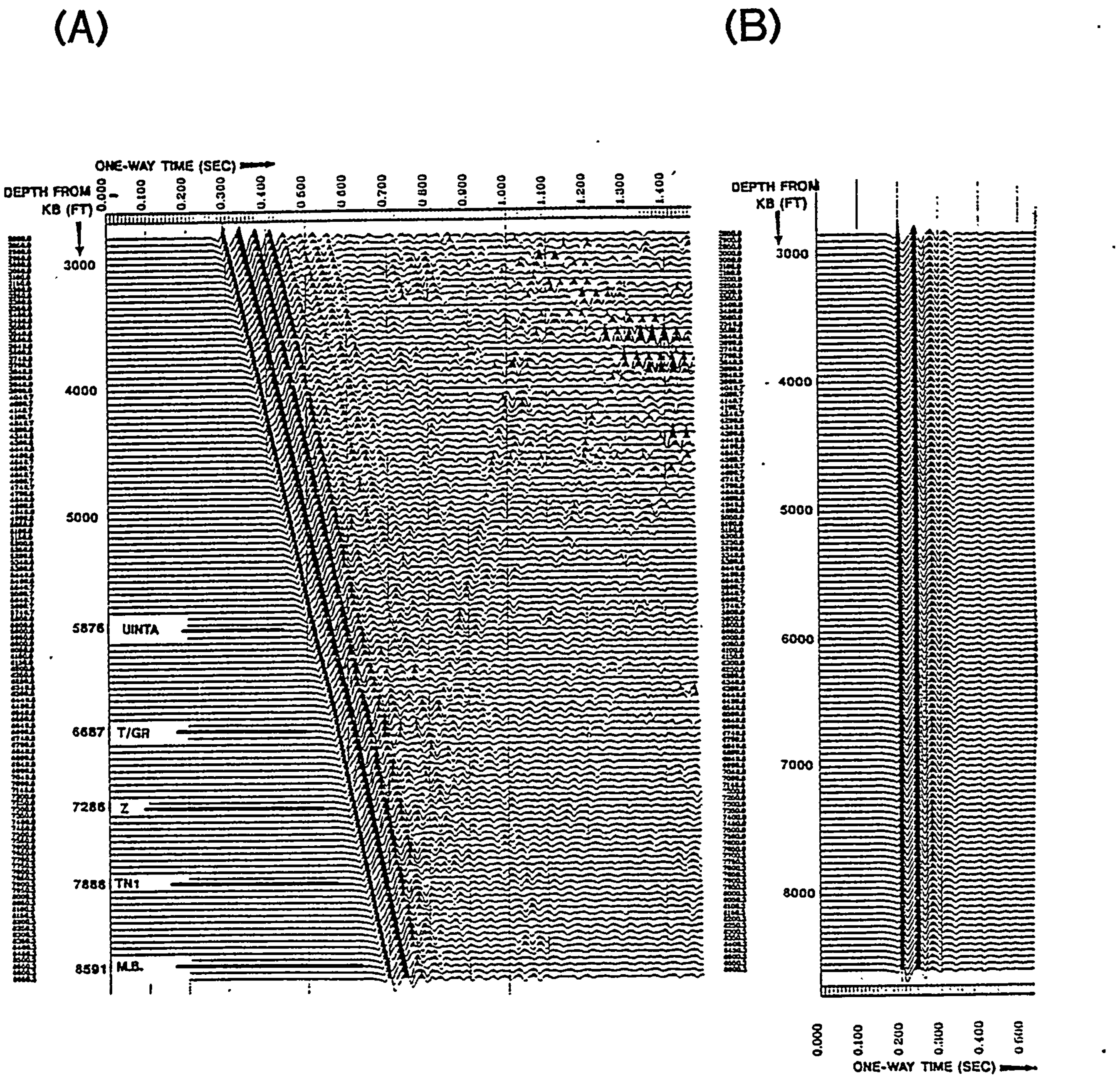

FIGURE 7-1 A-B

(A) P-wave VSP: Reprocessed stacks, vertical component.
(B) P-wave VSP: Downgoing wave, vertical component.

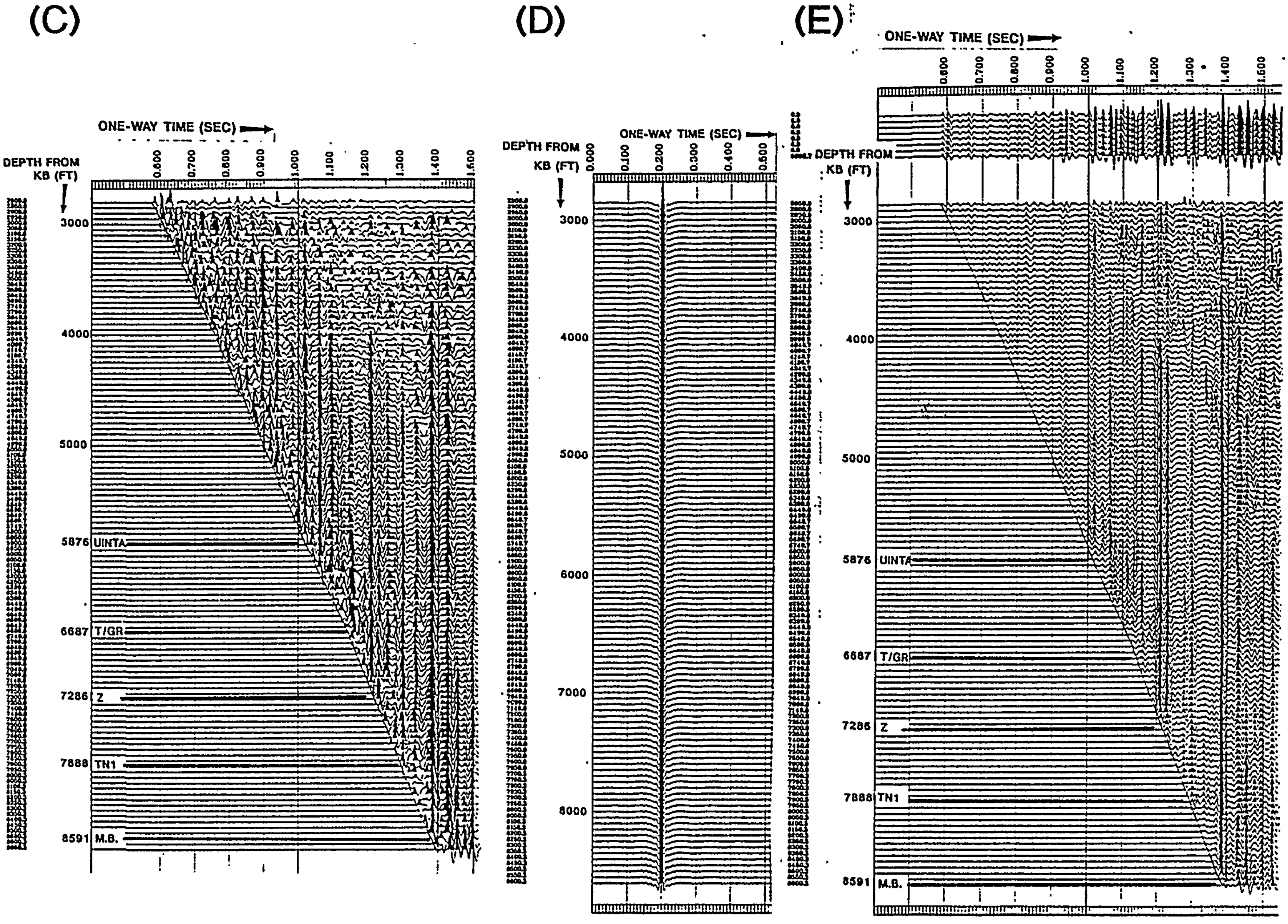

FIGURE 7-1 C–E

(C) P-wave VSP: Upgoing wave, vertical component.
(D) P-wave VSP: Vertical component, downgoing wave after waveshaping filter.
(E) P-wave VSP: Vertical component, upgoing wave after waveshaping filter.

7.1.2 S-wave

7.1.2.1 Source Offsets 550 ft West of Borehole

Processing included the following: Manual editing of noisy traces were performed on the raw data. Median stacking of the seven shear-wave source initiations, using both horizontal components, were performed for both SH and SV sources.

The toolspin corrections were achieved using the P-wave arrival from the far offset P-wave source (offset 3,050 ft at azimuth of N256.8E. Then the horizontal phones were rotated to be parallel to baseplate motion. The effective baseplate motion for SV is E/W; for SH, N/S. The SV data set was used as the reference data set. The SH data set was corrected by a static shift of -10 msec and a phase rotation of -30° in order to match the SV data set. The amplitudes of the SH and the SV vibrator data sets were balanced, since the four-component (Alford) rotation expects equal power in both sources: the SH data set had an amplitude reduction of 28%. The 4-component shear-wave input to the 4-C Rotation is shown in Figures 7-2a-d. A downgoing shear wave was observed on all four data sets. If only layer anisotropy were present, the receiver orthogonal to the source would have no energy. The conclusion is, therefore, that azimuthal anisotropy is present, and that the orientation of the cracks is skewed to the acquisition coordinates.

The hodograms from the SV (crossline) source are shown in Figure 7-3. The downgoing waves on both S1 and S2 were observed to be about equal in amplitude: the conclusion is, therefore, that the source to VSP wellbore azimuth was about 45° to the cracks. Furthermore, the S1 direction is clearly established as N43W from 2,800 ft to 8,650 ft, and the S1 does not change azimuth with depth, thus helping processing and interpretation.

The output from the 4-C rotation is shown in Figures 7-4a-d. The azimuth of S1 (Figure 7-4a) is N43W. The gain was set by the shallow S1 trace amplitude data, so that all other traces can be compared to it. The cross-component data are nearly quenched (7-4b and 7-4c), indicating that the S1-S2 source-receiver had nearly null energy, and likewise the S2-S1 source-receiver pair, thus demonstrating that the 4-C Rotation is correct. The S2 wave is observed to arrive at .646 sec (Figure 7-4d), while the S1 arrives at .618 sec (Figure 7-4a), so that a 28 msec delay exists between S1 and S2 at 2,850 ft depth (the top of this VSP). The percent azimuthal anisotropy (28 msec/618 msec) is 4.5%, which is attributed to the top 2,850 ft below ground level. In most other areas in which multi-component data have been gathered, the near surface has been more anisotropic than the indurated rock column. This area is thus like other areas in that the anisotropy is more significant in the near surface (0-2800 ft) than in the indurated rock column (2800 to 6650 ft). Below 6650 ft, there are zones with significantly increased shear-wave anisotropy related to high crack density.

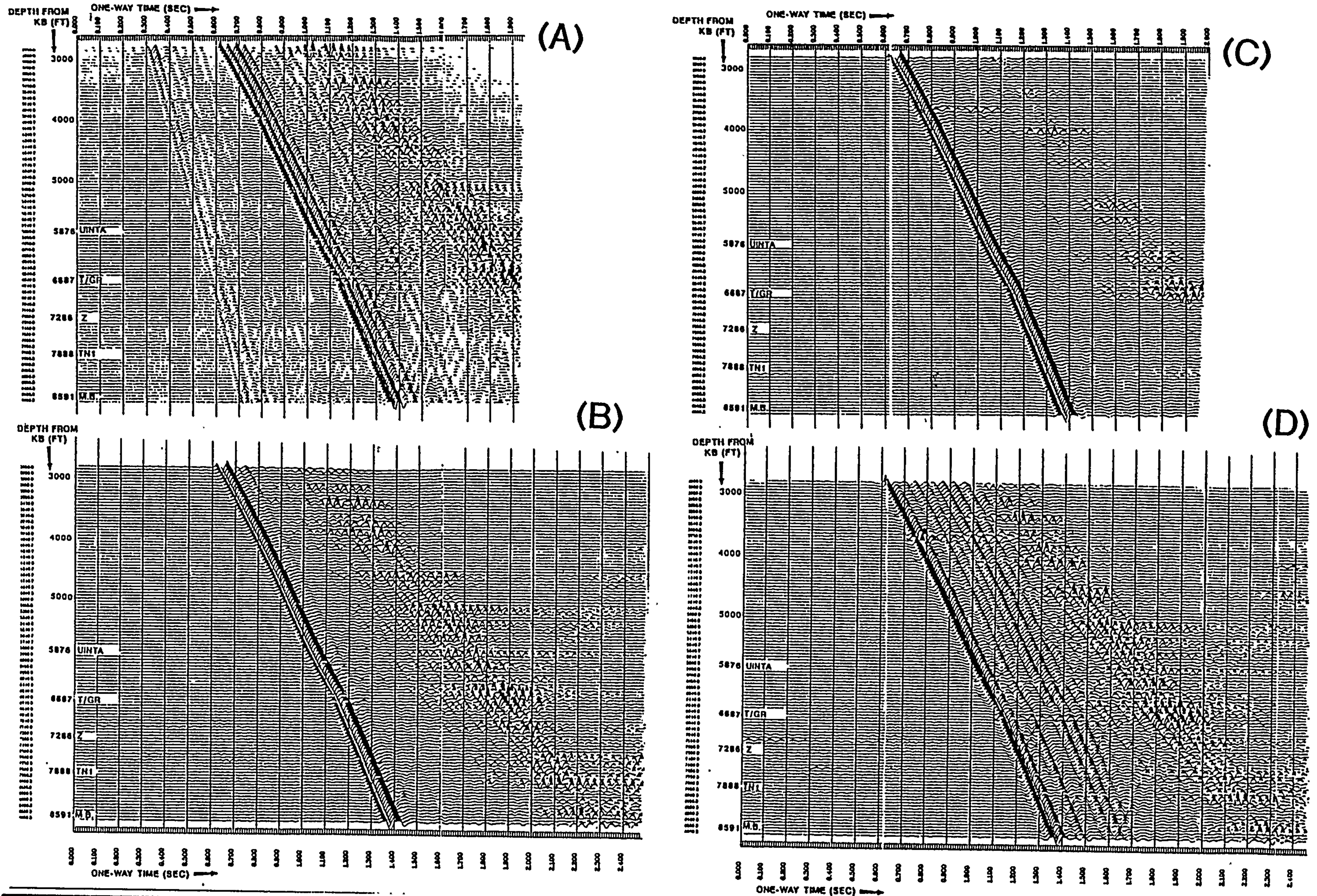

9C VSP: Shear components output from 4-component rotation. S1 azimuth is N43W. Note near-zero amplitudes on (B) and (C), the cross-components. 28-msec delay between S1 and S2 downgoing wave indicates 4.5% azimuthal anisotropy.

(A) S1 source, S1 receivers.
(B) S1 source, S2 receivers.
(C) S2 source, S1 receivers.
(D) S2 source, S2 receivers.

FIGURE 7-2

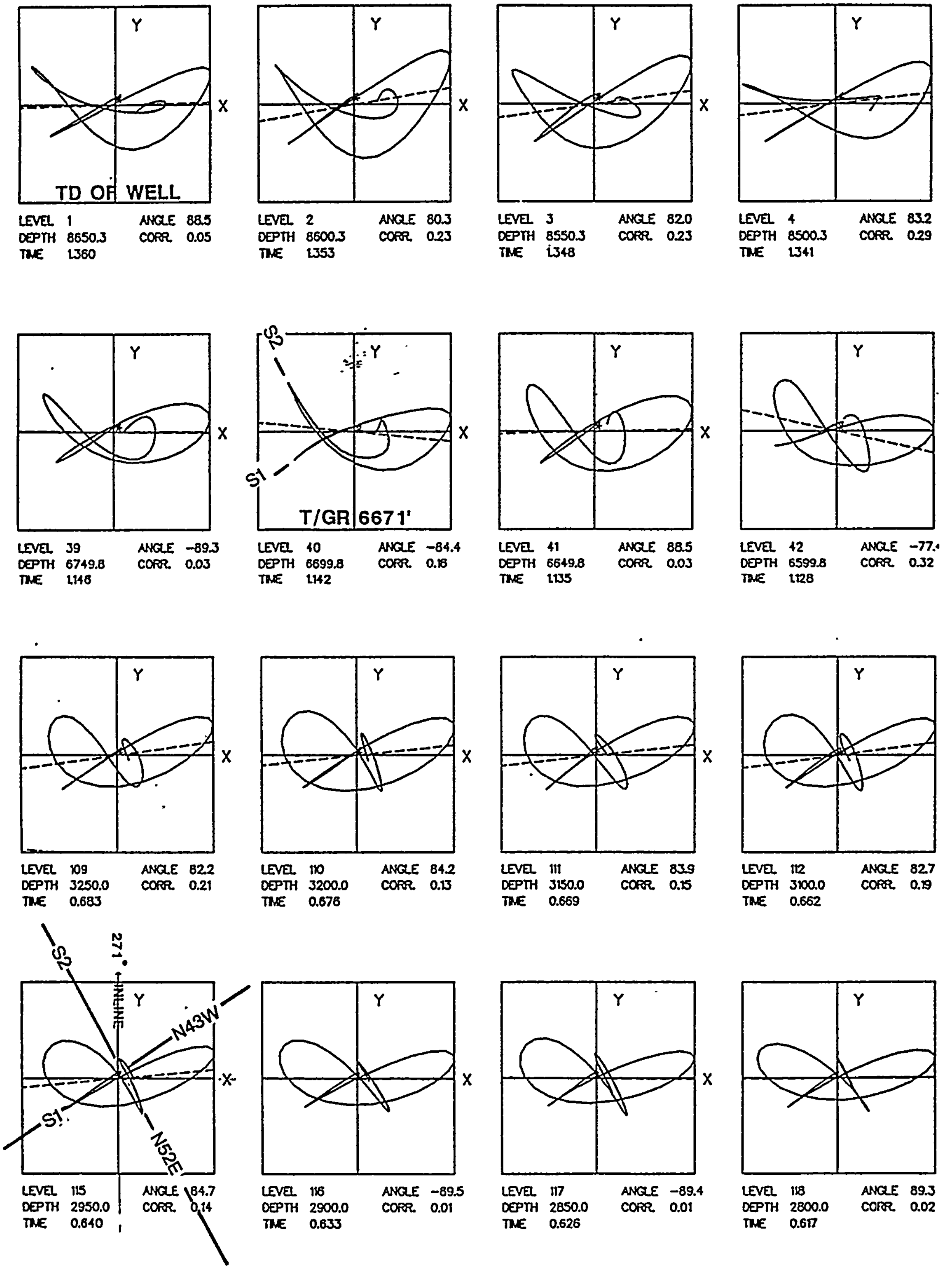

FIGURE 7-3

9C VSP: Hodograms (polarization diagrams within a time window). Each box corresponds to a depth level starting with 2800 ft. (lower right) and ending with 8650 ft. (upper left). S1 (fast shear) and S2 (slow shear) azimuths, indicated at lower left (depth 2950 ft.), do not change within the depth range 2800-9650 ft.

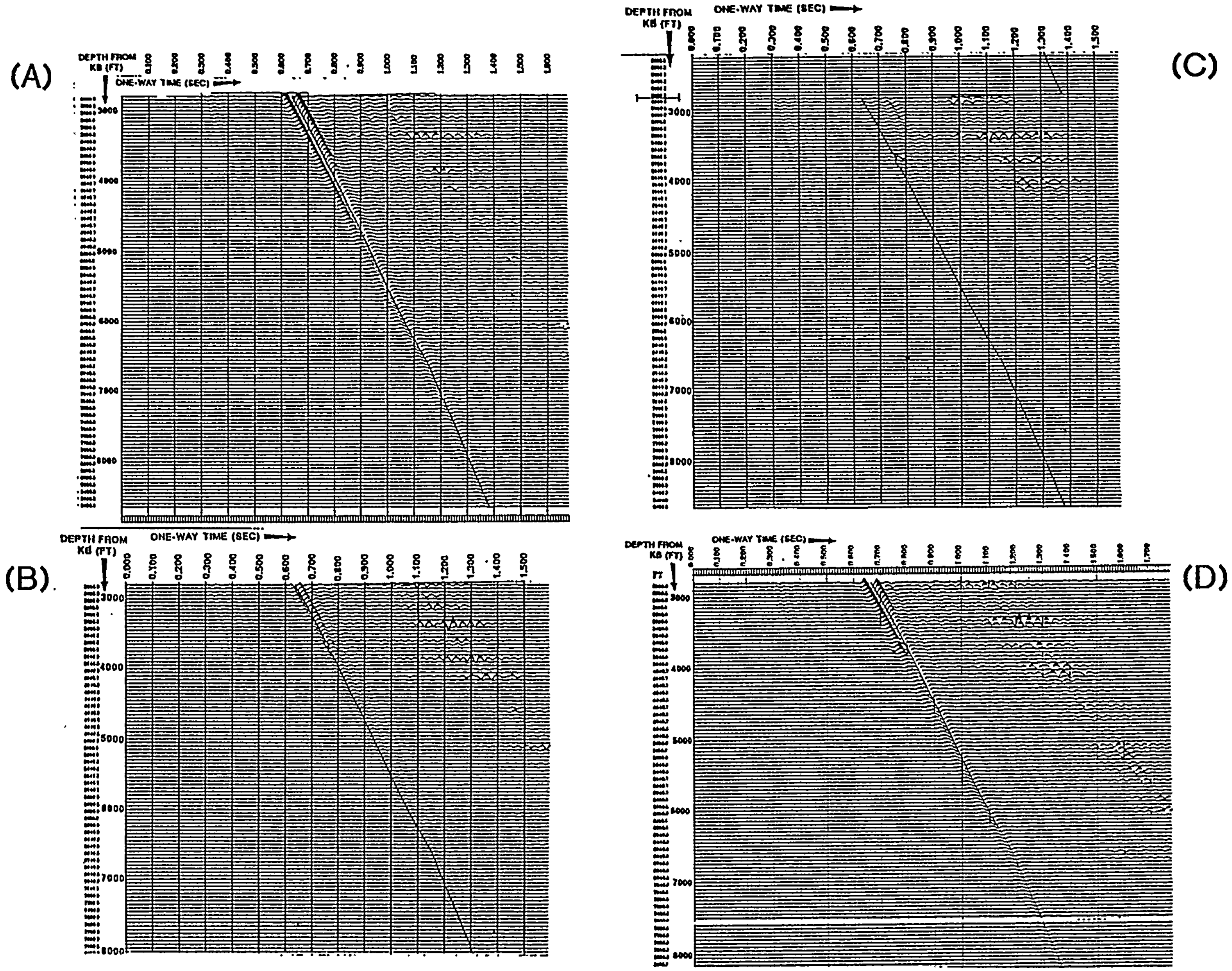

9C VSP: Shear components output to 4-component rotation. S1 azimuth is N43W. Note near-zero amplitudes on (B) and (C), the cross-components. 28-msec. delay between S1 and S2 downgoing wave indicates 4.5% azimuthal anisotropy.

(A) S1 source, S1 receivers.

(B) S1 source, S2 receivers.

(C) S2 source, S1 receivers.

(D) S2 source, S2 receivers.

FIGURE 7-4

A trace normalized display of the downgoing S1 and S2 after 4-C rotation is provided in Figure 7-5a and b. At the shallow depths, a similarity is seen in the S1 and S2 downgoing waveforms, but at the bottom of the hole, the trailing leg of S2 is quite attenuated. This is inferred to indicate that the S2 attenuation is different from the S1 attenuation.

The upgoing wavefields of S1 and S2, after 4-C rotation, are displayed in Figure 7-6a and b. Of note are the many good reflectors of S1, in contrast to the fewer, poorer reflectors on S2. These plots are trace normalized, so it is possible that the downgoing tube noise on the S2 is influencing the plot. However, similar results are observed when the SV and SH source data receivers were rotated into the natural coordinate system, as is shown in Figure 7-7a-d (SV-S1, SV-S2, SH-S1, SH-S2). Note especially that in the SH source data (Figures 7-7c-d), the tube wave noise is minimized, that the P-wave energy looks similar, and that the upgoing energy is better on S1 than on S2. In all of these cases, the S1 showed stronger amplitudes and better signal to noise ratio (S/N). What is also of interest is the increased magnitude of downgoing P in the SV data set (Figures 7-7a-b) than the SH data set (7-7c-d), as would be expected. In conclusion, it is most likely that the attenuation for S2 is greater than for S1. The hypothesis offered is that this attenuation difference is consistent with the S1 sensing the stiffer rock, with better transmission of seismic energy, while the S2, the slower shear wave, loses more energy from seismic transmission (into either friction as the rocks deform or as fluid is moved due to pressure changes).

The 2-C (geophone) rotation from the acquisition coordinates to the natural coordinates (N43W, N47E) for both SH and SV sources was used to compare the S1 and S2 travel times and downgoing wave shapes between the two vibrators. With such excellent quality data, the SH source static and the SH source phase correction were readily discerned.

The time delay between S1 and S2 for the SV vibrator is shown in Figure 7-8, using the parametric inversion algorithm of Schlumberger. The near surface (to 2,800 ft) exhibited a 28 msec delay, as mentioned above. An additional 5 msec of time delay to S2 is accumulated to the T/UGR (6,650 ft), over a 3,850 ft-thick interval. This correlates to ~1% azimuthal anisotropy. In the T/UGR, the interval containing the naturally fractured gas reservoir units adjacent to the borehole, the time delay sharply increases, correlating to a 5-12% increase, or an additional 6 msec over 2,000 ft. The conclusion from this plot is that the zone containing the fractured gas reservoir in adjacent boreholes does exhibit increased shear wave anisotropy, which is attributed to an increase in crack density. This anomaly in the VSP shear wave travel time difference which coincides with the top fractured gas reservoir formation is discussed in Lynn et al. (1995b).

Figure 7-9 shows the time delay (delta T) between the slow shear wave and the fast shear wave for the SV source, for different bandpass filters, and compared to the 4-C rotation. The low frequencies (5-10 hz) exhibit more shear wave

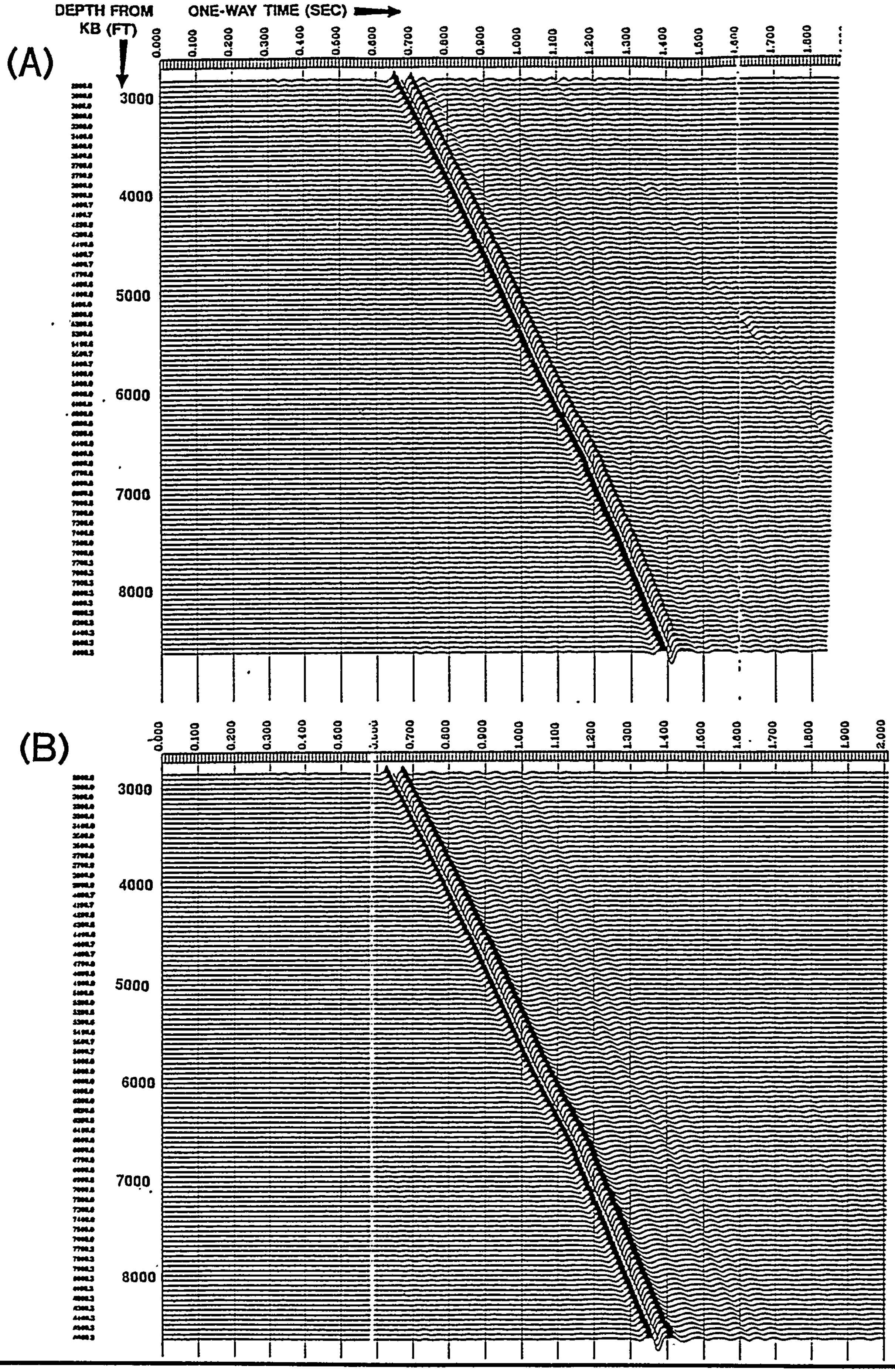

9C VSP: Downgoing shear wavefields after 4-component rotation (trace-normalized display).

(A) Downgoing S1. **(B)** Upgoing S2.

FIGURE 7-5

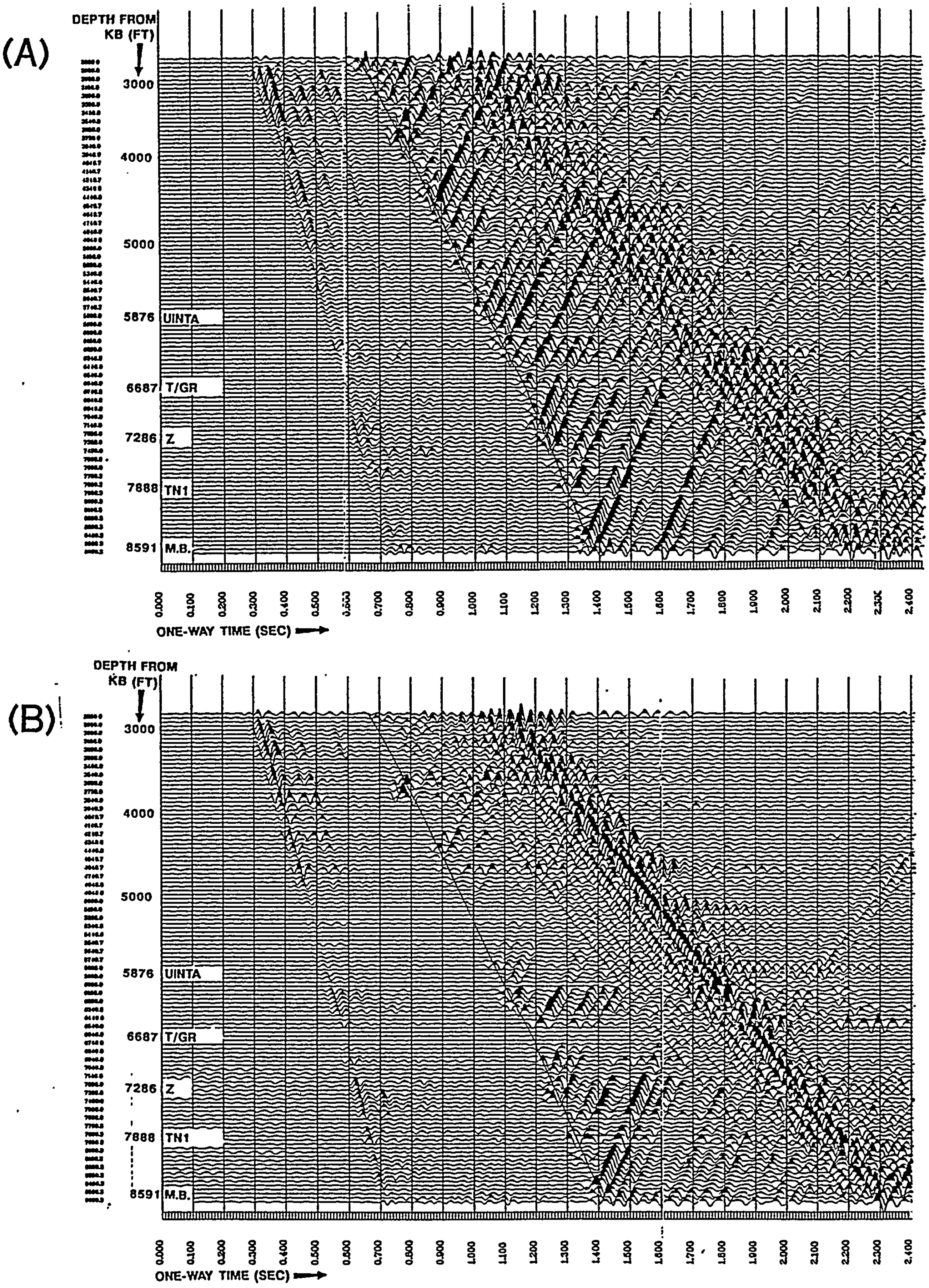

9C VSP: Upgoing shear wavefields after 4-component rotation (trace-normalized display).
(A) Upgoing S1 (B) Upgoing S2

FIGURE 7-6

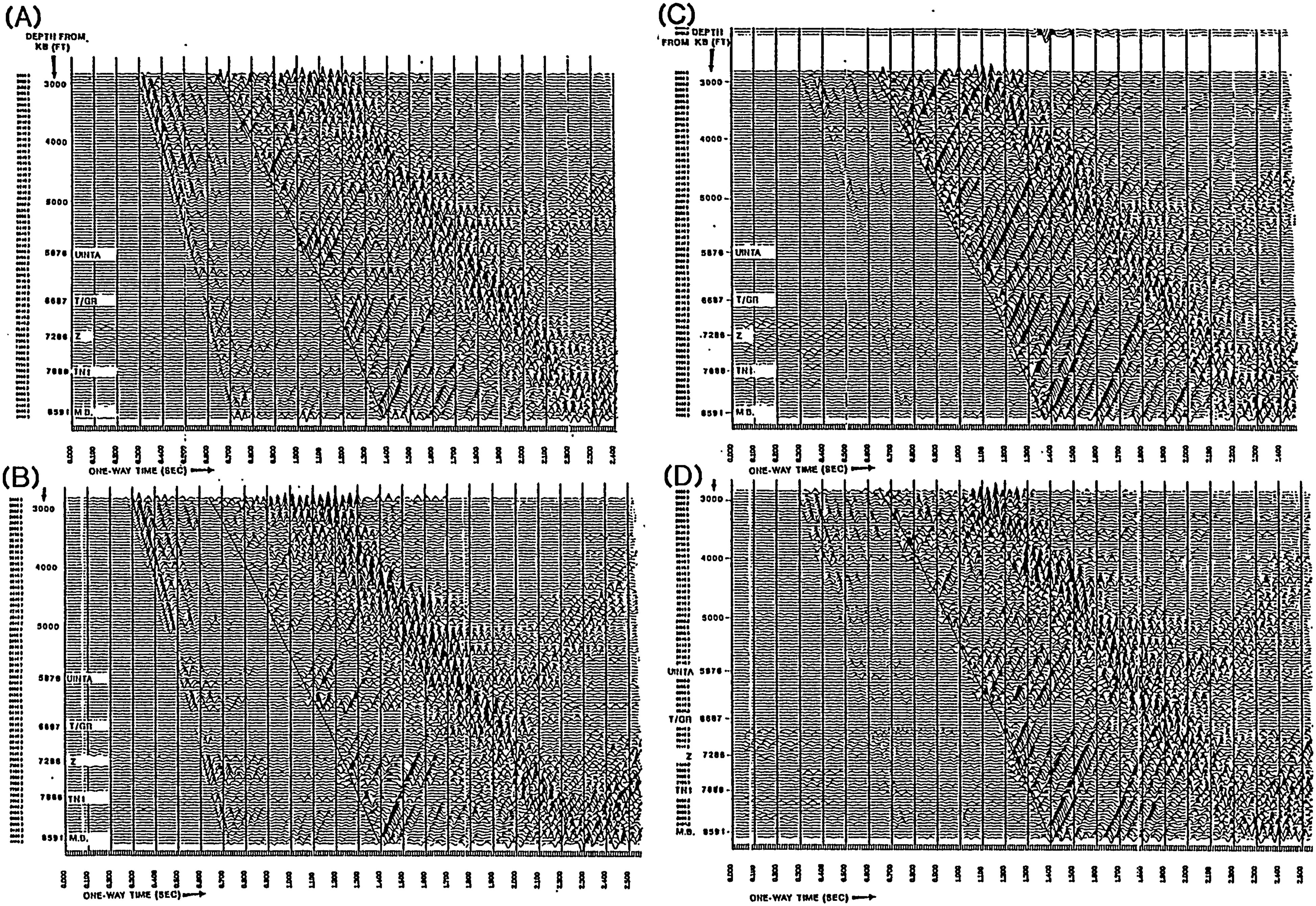

9C VSP: Shear wavefields with original source components, rotated receiver components. S1 components generally better S/N than S2 components.
(A) Inline (SV) source, S1 receivers.
(B) SV source, S2 receivers.
(C) Crossline (SH) source, S1 receivers.
(D) SH source, S2 receivers.

FIGURE 7-7

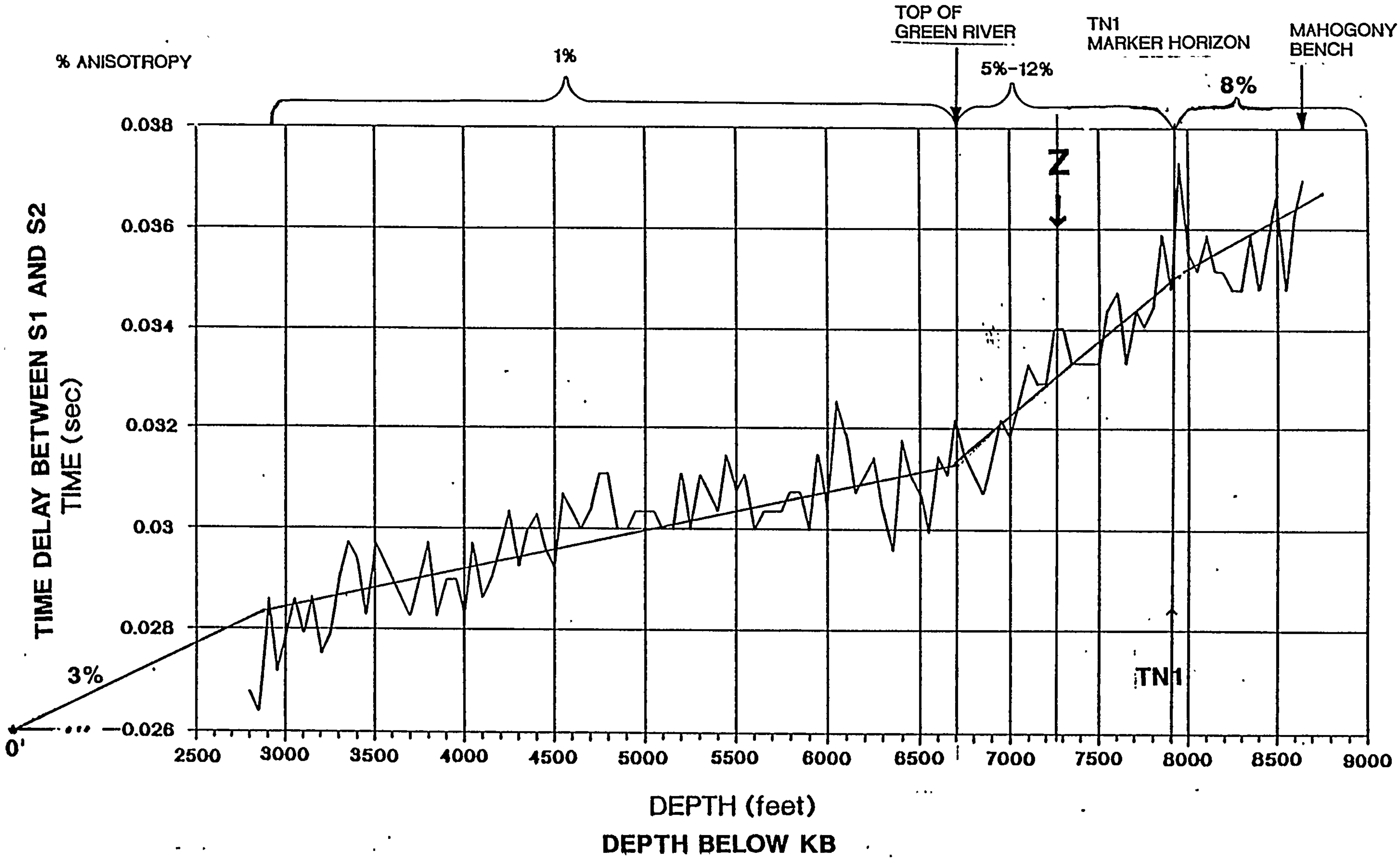

FIGURE 7-8

9C VSP: Time delay between S1 and S2 (SV source). Near surface (Ground level 2850 ft) anisotropy is 28 msec, or 4.5%. Change in slope occurs at 6,700 ft, or top of Green River (T/UGR).

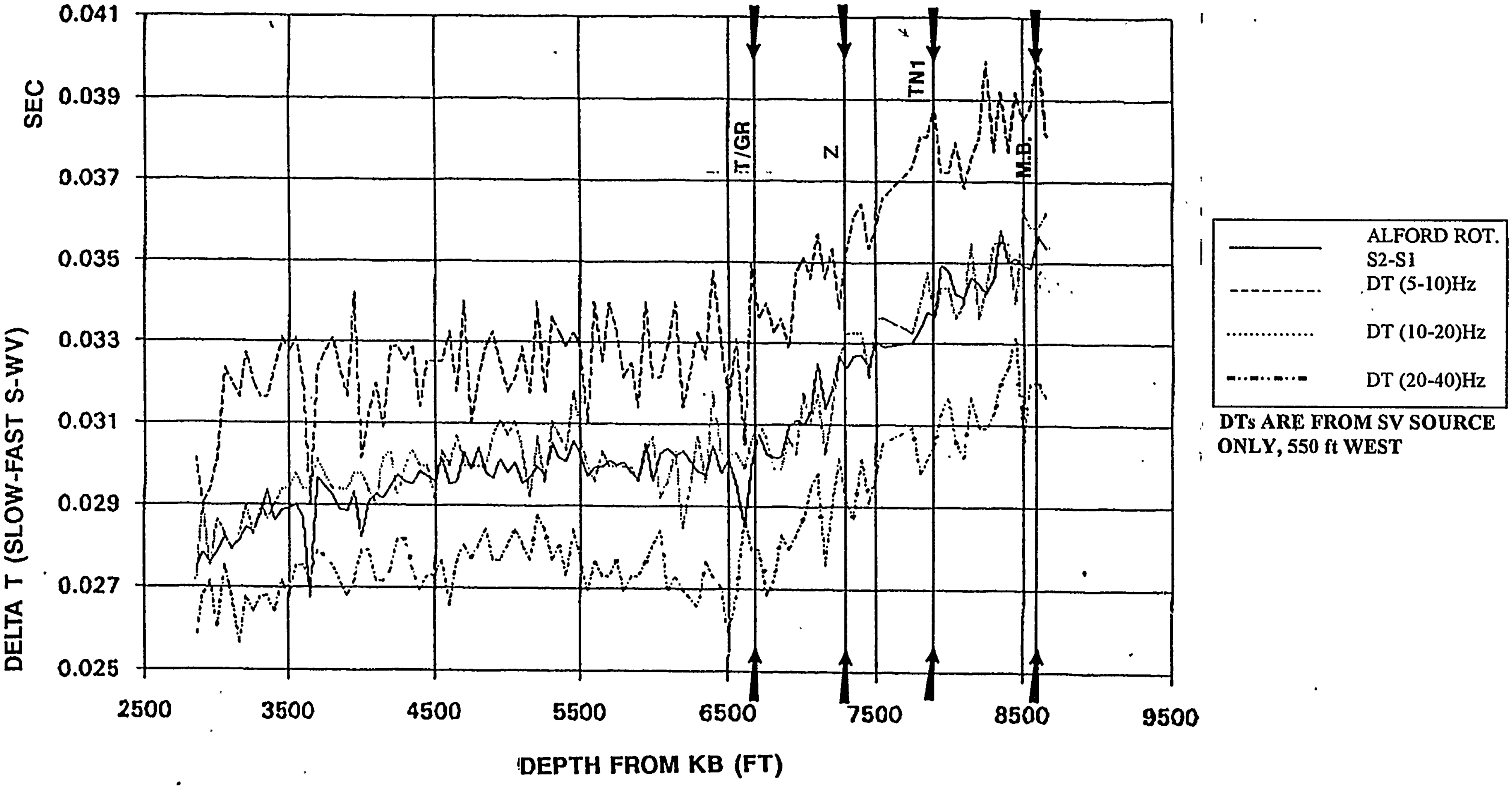

9C VSP: Time delay between S1 and S2 for various frequency passbands, showing that lower frequencies exhibit more anisotropy than higher frequencies.

FIGURE 7–9

splitting, while the high frequencies (20-40 hz) exhibit less shear wave splitting. The following interpretation is proposed: since the low frequencies have longer wavelengths compared to the higher frequencies, they encounter more cracks per wavelength for the longer wavelengths, and thus more shear wave splitting. The higher frequencies with their shorter wavelengths encounter fewer cracks per wavelength, and, therefore, exhibit less shear wave anisotropy. The apparent deciding factor for the amount of shear wave splitting is cracks per wavelength.

Figure 7-10 posts as a function of two way time (P-wave) from seismic datum, the interval P velocity, the interval S velocity, and the percent shear wave anisotropy for the 550 ft west 9C VSP data. This plot was generated from the arrival times of the downgoing P, S1, and S2 waves for the 550 ft-west 9C VSP. An interval of 200 ft was used, in order to smooth out rapid variation due to picking errors. At the T/UGR (0.93 sec), the sudden increase in VP and in VS, as well as an increase in the percent anisotropy, is observed.

Figure 7-10b posts as a function of two way P-wave travel time the VP/VS1 ratio, interval VP, interval VS1 and VS2. The VP/VS1 ratios here compare very well to the VP/VS ratios calculated from the surface seismic at the NE end of Line 2 (the location of the 9C VSP well).

7.1.2.2 Source Offsets 1,121 ft East of Borehole

The offset located 1,121 ft east of the VSP borehole had a similar processing flow to the 550 ft west VSP. Results similar to the ones described above are observed on the 1,121 ft east offset VSP. The processing flows for both VSPs are posted on the label of the Schlumberger processing flow provided on 8 mm tapes.

The identification of reflectors recorded in the VSPs and the ties between the VSPs and the surface seismic are discussed under Seismic Interpretation.

7.2 9-COMPONENT SURFACE SEISMIC

The surface reflection P-wave and S-wave seismic data were processed by Pulsonic Geophysical Ltd., Calgary.

7.2.1 P-wave Surface Seismic

The P-wave seismic data were processed as follows:

1. The data were demultiplexed, reformatted, and edited; the geometry was defined; spherical divergence correction was applied with a gain correction function derived from decay analysis of the raw data in both time and offset.

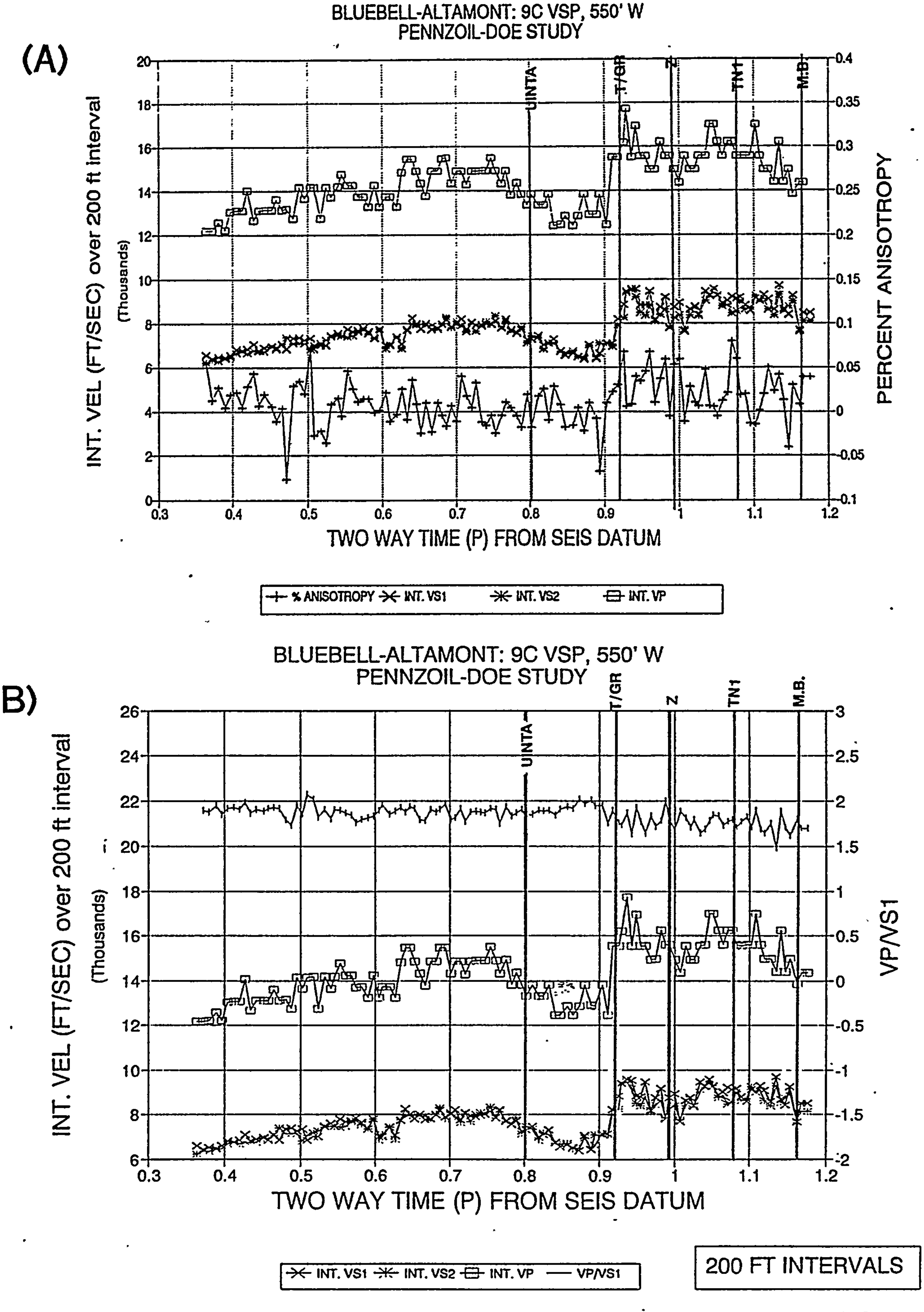

FIGURE 7-10

(A) 9C VSP, 550 ft west offset source. P- and S-wave internal velocities and percent S-wave anisotropy versus one-way P-wave time, showing abrupt increase in VP, VS and anisotropy at Top Upper Green River.
(B) VP/VS1 ratio, VP, internal VS1 and VS2.

2. A minimum-phase conversion filter which was derived from the source sweep was applied to the data, and the minimum-phase data were deconvolved with a surface-consistent designature deconvolution.
3. The data were sorted into Common Depth Points (CDPs); refraction statics were applied and referenced to datum at 5,000 ft. ASL, followed by automatic surface consistent statics.
4. The stacking velocities were picked approximately every 20 shotpoints (~3,000 ft) on the lines. Zero-phase spectral balancing was performed. A mute was applied down to 900 msec. at the nominal far offset (9,000 ft).
5. Automatic CDP consistent trim statics were applied, and the data were stacked and migrated, and a final filter and multiple gate trace balance scalar were applied.

Bulk Static Shift

A bulk static shift of 10 msec was necessary to tie P-wave Line 1 to Line 2: Line 1 is shifted up 10 msec. This shift is necessary because the reflection statics applied were different at the tie point, since each of the lines had reflection statics independently calculated.

The processed stacked P-wave sections for Line 1 and Line 2 show excellent signal to noise, as seen in Figures 7-11a and 7-11b.

P-wave Normal Move-out (NMO) Analysis

The stacking velocities applied to the P-wave reflection seismic were also analyzed at the intersection of the two lines.

7.2.1.1 Method

The P-wave velocity scans were analyzed. For each line, nine CDPs centered at the line intersection were summed to form supergathers. The displays provided by Pulsonic showed the original data (pre-NMO), then CDP gathers with nine different NMO functions, a coherence plot showing the contoured values (two-way time in seconds versus stacking velocity in ft/sec) and the machine picks, using all offsets to the mute (posted on the CDP gathers).

7.2.1.2 Observations

Line 2 had hyperbolic moveout to the applied mute on the far offsets, while Line 1 had non-hyperbolic moveout past 3,750 ft offset for events in the Uinta (0.84 sec) and the T/UGR (0.93 sec) (Figure 7-12).

Table 7-1 lists the zero offset time T_0, the offset used, the stacking velocity picked from the moved out gathers, the time on the far offset T_F, and the normal

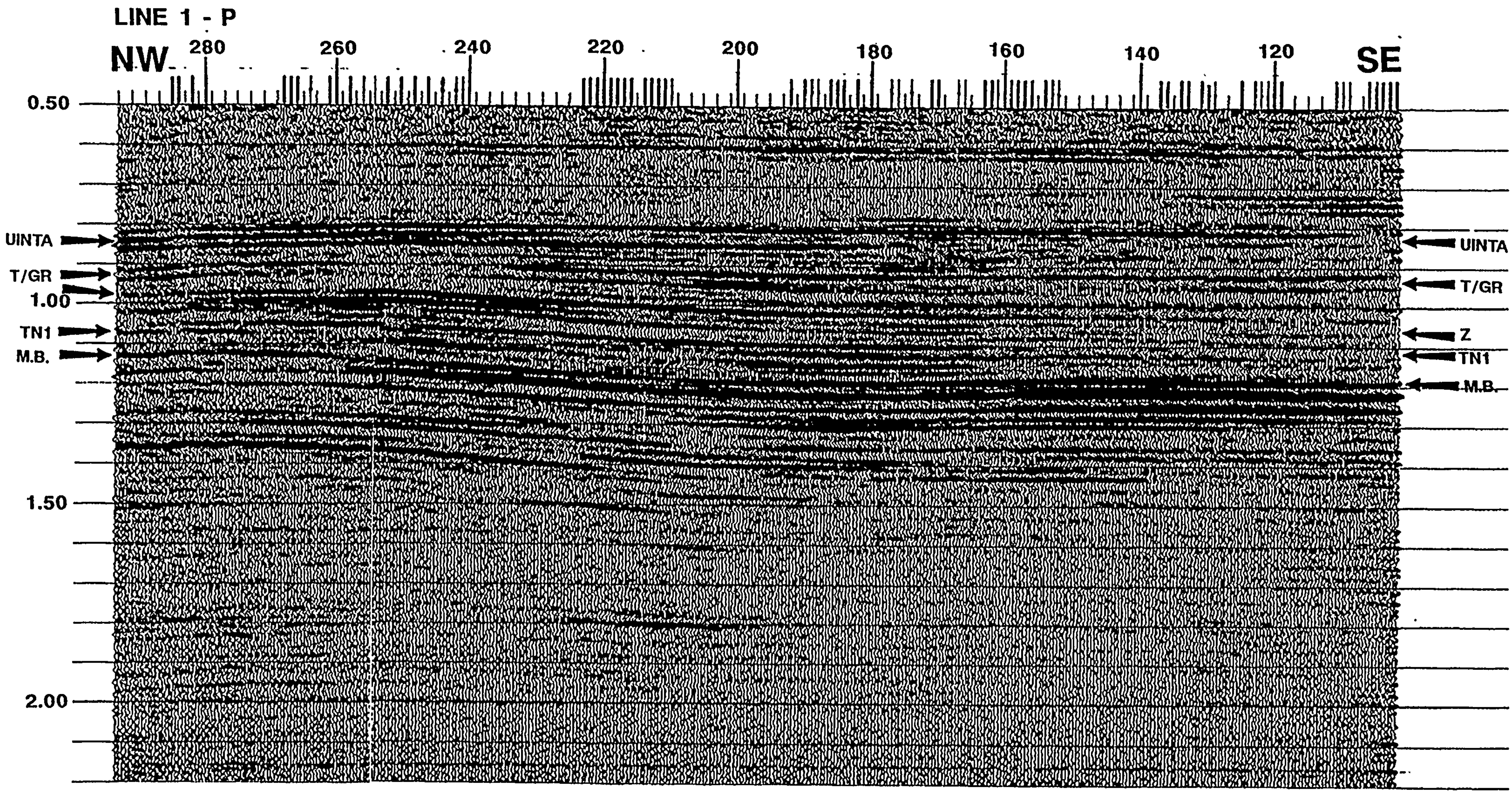

P-Wave Line 1 final stacked section.

FIGURE 7-11A

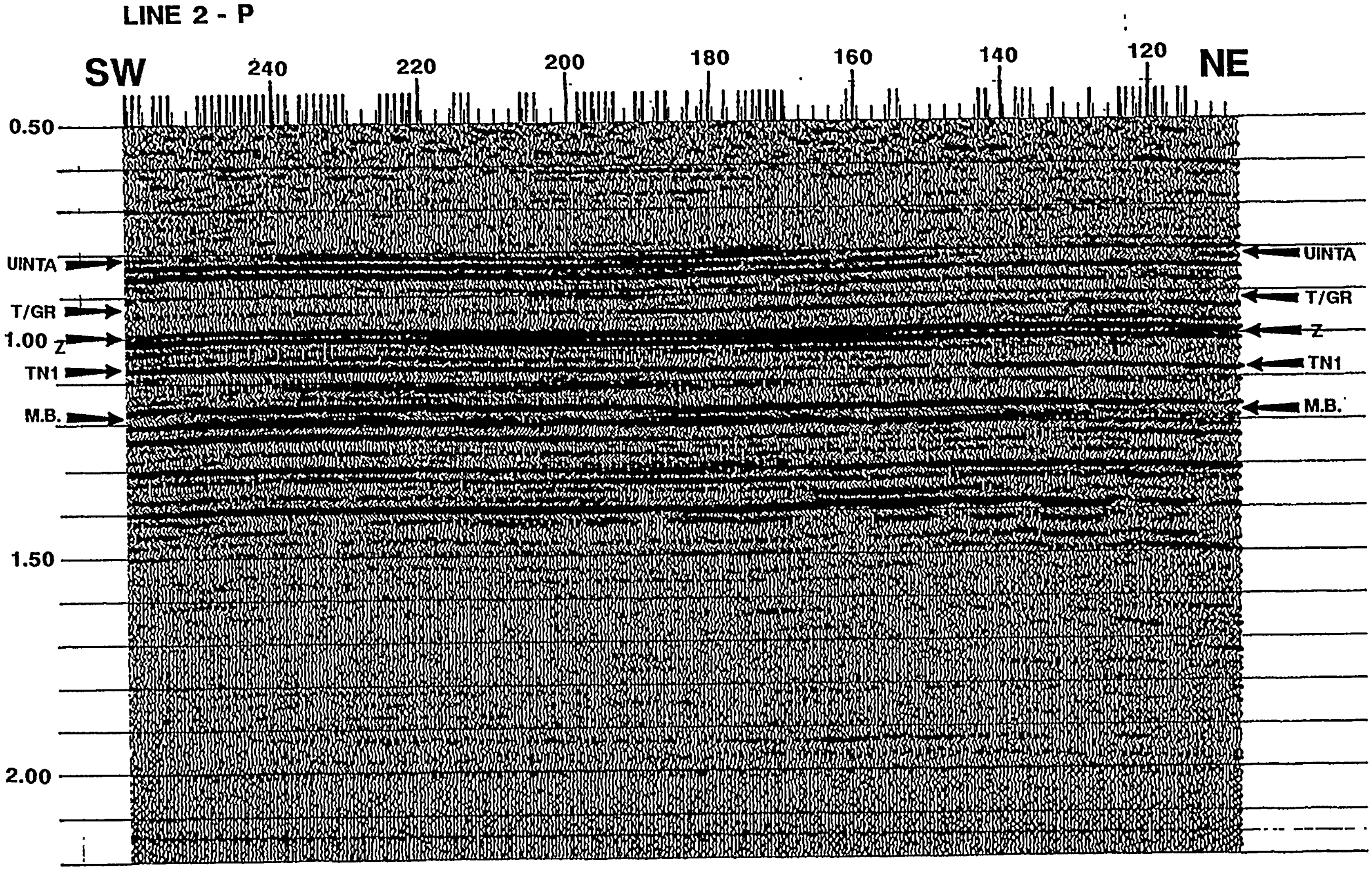

P-Wave Line 2 final stacked section.

FIGURE 7-11B

SUPERGATHERS FOR LINE 1 AND LINE 2 AT TIE POINT

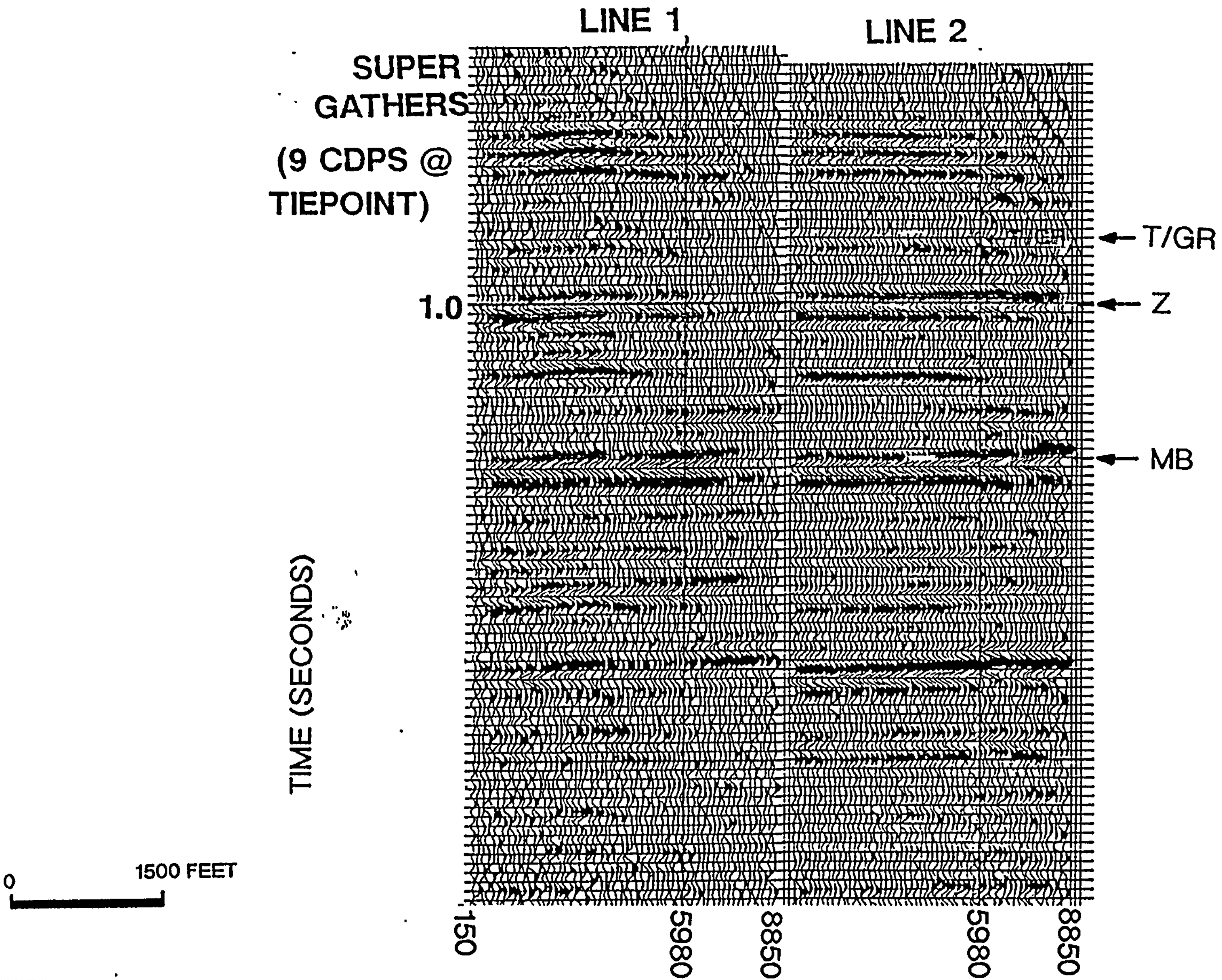

Supergathers (9 CDPs centered at a tiepoint) for line 1, left, and line 2, right, at the tiepoint of the two lines. Note increased amplitudes on far offsets on line 2, Z and MB reflectors, as opposed to decreased amplitudes on line 1.

FIGURE 7–12

moveout correction (NMO, or delta T) for Line 1 and Line 2 at the tie point. For Line 1, the additional quantity of the difference in the NMO (delta t, L2-L1) is posted, to show the difference at the usable far offset implied by the posted velocity. The bandwidth of the reflection signal is 10-60 hz, with the average frequency at the T/UGR of 30 hz., or period 33 msec. A difference of less than 4 msec. in delta T between the two lines is not significant; a difference of 5 msec. or more is considered significant.

Figure 7-13 shows the stacking velocity functions for Line 2 and Line 1 at the tie point. Also plotted is the vertical average P velocity from the VSP. The only significant difference in NMO is at 1.4 sec, where 8 msec difference on the far offset is observed. Line 2, perpendicular to the dominant open crack set trending NW, showed the faster velocity (14,771 ft/sec, compared to 14,300 ft/sec on Line 1).

7.2.1.3 Discussion

Theory predicts that the P-waves parallel to the fractures travel faster on the far offsets, while the P-waves perpendicular to the fractures travel slower on the far offsets.

The observed shallow (~0.4 sec) field data are in accord with theory. From the T/UGR (0.93 sec) through the Lower Green River, the line parallel to the open (NW) fractures shows slower moveout velocity than the line perpendicular to these fractures; thus, the observations are not in accord with theory. The differences in normal moveout range between 2 and 8 msec, with 5 msec differences being quite detectable with this data set's signal to noise ratio.

Table 7-1a
P-wave NMO Calculations
Line 1 at Tie Point

Dix V-INT ft/sec	T_0 sec	Offset ft.	Vstk ft./sec	T_F sec	NMO sec	Diff. in NMO (L2-L1), sec
5700	0.190	2300	5700	0.446	0.256	
14750	0.264	2300	9185	0.364	0.100	
15972	0.357	2300	11351	0.410	0.053	
15819	0.434	2300	12263	0.473	0.039	0.000
14464	0.614	3000	12947	0.656	0.042	0.000
14814	0.866	8850	13517	1.086	0.220	0.000
15332	1.016	8850	13800	1.201	0.185	-0.003
15607	1.206	8850	14100	1.360	0.154	-0.004
15435	1.409	8850	14300	1.539	0.130	-0.008
15665	1.967	8850	14700	2.057	0.090	-0.003
15863	2.360	8850	14900	2.434	0.074	-0.003
15954	1.968	8850	14850	2.056	0.088	-0.004

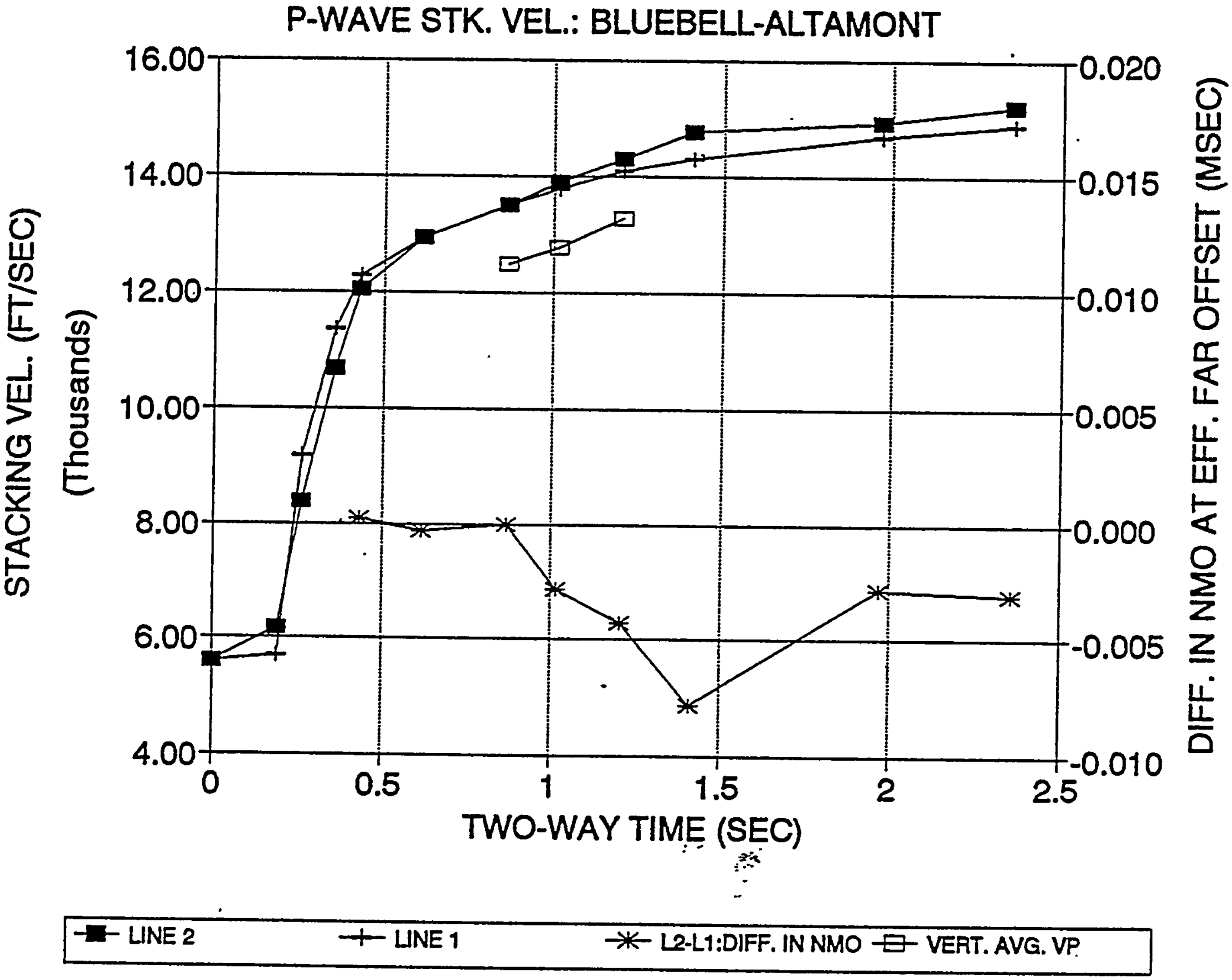

Stacking velocities versus two-way time for Line 1 and Line 2 at the tiepoint.

FIGURE 7–13

Table 7-1b
P-wave NMO Calculations
Line 2 at Tie Point

Dix V-INT ft/sec	T_0 sec	Offset ft	Vstk ft/sec	T_F sec	NMO sec	delta V-INT (L2-L1) ft/sec
6164	0.196	2300	6164	0.421	0.225	464
13702	0.250	2300	8387	0.371	0.121	-1048
15025	0.347	2300	10667	0.409	0.062	-947
15827	0.449	2300	12035	0.488	0.039	8
15093	0.619	3000	12947	0.661	0.042	629
14850	0.866	8850	13517	1.086	0.220	35 Uinta
16026	1.016	8850	13916	1.199	0.183	694 T/UGR
16284	1.206	8850	14315	1.355	0.149	6778 M.B.
17233	1.409	8850	14771	1.531	0.122	1798
15365	1.967	8850	14942	2.054	0.087	-299
16580	2.360	8850	15227	2.431	0.071	717

Dix V-INT	Dix Interval Velocity
T_0	Zero Intercept Time
Offset	Far Offset Distance
Vstk	Stacking Velocity
T_F	Far Offset Time
NMO	Normal Move-out
Diff in NMO	Difference Line 2-Line 1 in NMO

Line 2 is the strike line (topographically and geologically), having only 30 ft of elevation change in the 8,850 ft spread at the tie point location (see Table 7-2). Line 1 starts lower in the basin and ends in the upper hills (topographically). Line 1 has a change of 170 ft of elevation within the 8,850 ft spread at the tie point: northwest of the tie point, there is only 30 ft of elevation increase, but southeast of the tie point, the elevations decrease 140 ft in the 4,425 ft of spread length. Thus, the bulk of change in elevation is confined to one half of the spread (the southeastern spread from the tie point). If there were errors in going to datum (5,000 ft above sea level), Line 1 would be subject to more error, while Line 2 would have less.

Table 7-2
Elevation changes along Line 1 and Line 2

Line 1: Elevation	Shotpoint/Location
5,820 ft	264 NW
5,790 ft	239 tie point
5,650 ft	209 SE
Line 2: Elevation	**Shotpoint/Location**
5,800 ft	225 SW
5,790 ft	185 tie point
5,810 ft	165 NE

The conclusion from this comparison is that at the tie point of the two lines, the P-wave stacking velocities do not show reliable azimuthal anisotropy. It is thought that elevation changes along the lines may have more influence on the stacking velocities than azimuthal effects caused by vertical fractures.

Heterogeneity can play a role, also. There is less heterogeneity in the strike direction (Line 2), while more change in lithology in the dip direction (Line 1) in the Upper Green River section, based upon stratigraphic modeling. Therefore, Line 2 would be less influenced by heterogeneity than Line 1. Sonic logs above 5,800 ft are not available, so information above the Uinta marker is lacking. The section above the Uinta will influence the stacking velocities, so the preceding evaluation is unfortunately incomplete.

7.2.1.4 Attenuation of P-wave Data

The amplitude spectra of the two lines were compared at the line tie, Figure 7-14, to determine if there were differences associated with line azimuth. Theory predicts that in fractured media, attenuation of the P-waves will be greater for the waves propagating in the direction perpendicular to the fracture strike; this is the direction of Line 2. The attenuation is a ratio of dissipated energy to stored energy in the wave, and more energy is dissipated by a wave propagating across open fractures than along the strike of the fractures. Gelinsky and Shapiro (1995) showed that vertically aligned cracks caused permeability anisotropy, which in turn yielded strong anisotropic seismic attenuation.

Only slight differences in frequency content and amplitude were observed on the near-trace, migrated sections, between Line 1 and Line 2 at the tie point. (Near-trace stacks were compared so as not to introduce AVO into the comparison). The seismic traces from Line 1 and Line 2 at the tie point, displayed in the left of Figure 7-14, show marked similarity and no visible differences in attenuation are observed.

The reflection signal in the seismic traces is contained within the frequency band from about 10 to 60 hertz. The amplitude spectrum of Line 1 shows higher

P-WAVE SEISMIC AT LINE TIE

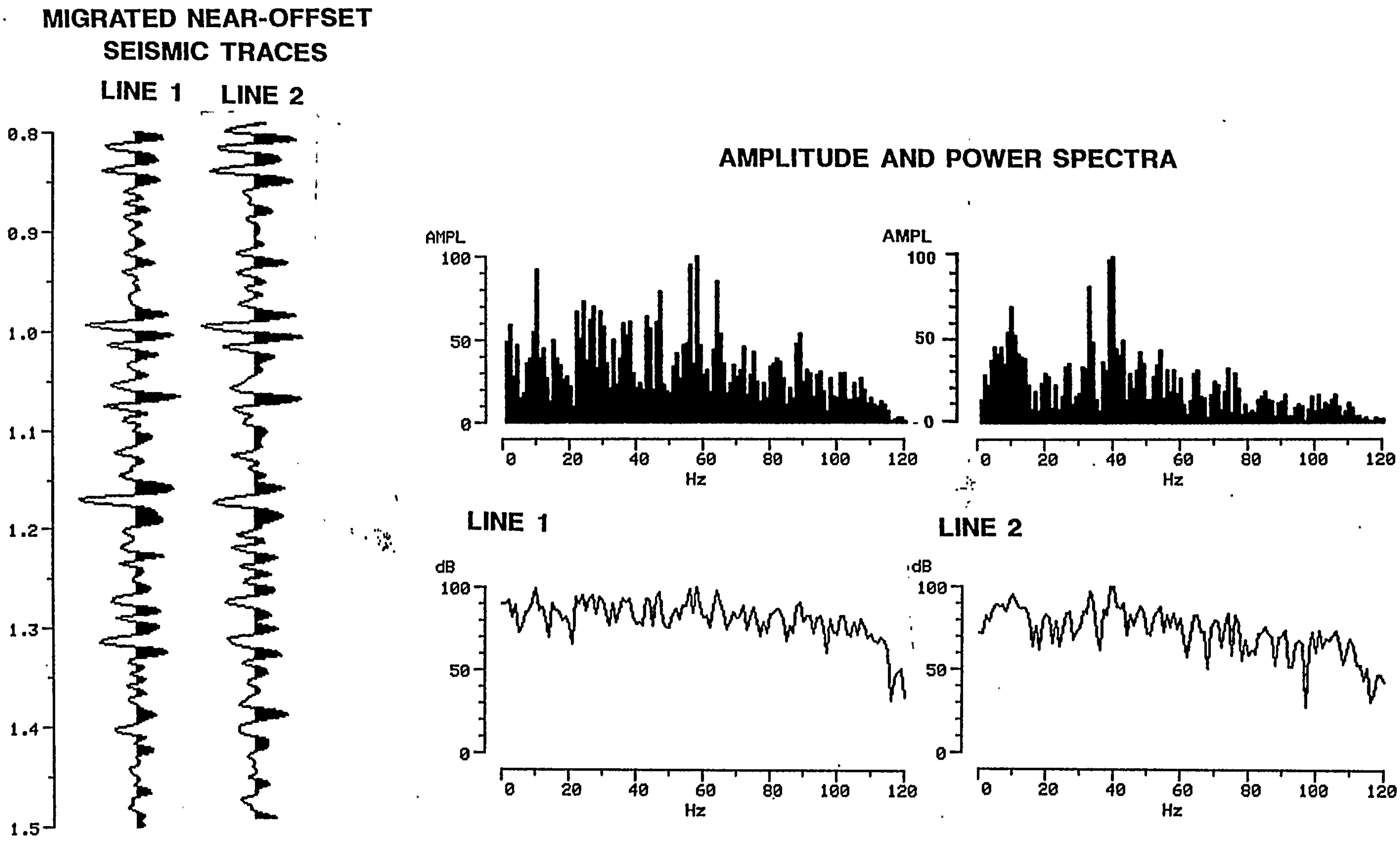

Seismic traces from near-offset stacked, migrated sections of line 1 and line 2 at the tiepoint, showing amplitude and power spectra computed within a window from 800-1500 msec (over the section of interest).

FIGURE 7–14

frequencies better preserved than on Line 2. The average amplitude in the signal band on Line 1 is from 10 to 20 percent higher than the average on Line 2. The difference observed is in the sense predicted by theory.

The power spectra of the traces from the two lines at the tie point show that the power on the high frequency end begins to drop off at lower frequencies on Line 2 than on Line 1. Since this dropoff occurs on both lines at frequencies higher than the reflection signal, it is insignificant to this study. According to these data, attenuation differences do not appear to be useful as an exploration strategy in this area.

7.2.2 S-wave Surface Seismic

The S-wave data processing flow is summarized below:

1. The data were demultiplexed, reformatted, and edited; geometry was created and the data were corrected for spherical divergence and gain corrected with a function derived from decay analysis of the raw data in both time and offset.
2. Alford rotation was performed which indicated that a rotation angle of 150° clockwise from grid north would rotate the data into a fast shear (S1) direction and a slow shear (S2) direction; S1 being N30W and S2 perpendicular to this.
3. A minimum phase conversion filter derived from the sweep was applied; these minimum phase data were then deconvolved using a 4-component surface consistent deconvolution algorithm.
4. The data were sorted into CDPs and refraction statics were applied. The refraction analysis was performed on the pre-rotated data. Statics were applied as shown below:

Line	Statics Calculated From
BA-94-1 S1	Inline source into H1 (inline) phones
BA-94-1 S2	Crossline source into H2 (crossline) phones
BA-94-2 S1	Inline source into H1 phones
BA-94-2 S2	Crossline source into H2 phones

5. Automatic surface consistent statics were run on the data. This was followed by preliminary velocity analysis. Shot and receiver stacks were formed and statics were hand picked. Detailed velocity analysis followed.
6. The data were normal moveout corrected and a mute was applied. Automatic CDP consistent trim statics were calculated and applied. The data were scaled with a 1000 msec Automatic Gain Control (AGC) operator and were corrected for dip moveout. Offsets to 6,000 ft were

stacked, although reflection signal is seen on offsets from 6,000-10,000 ft. The non-hyperbolicity of the far offsets made it difficult to correctly process these offsets and it was noted that the amplitudes of some events changed with offset. Stacks of 0-6,000 ft and 0-10,000 ft offset were compared and amplitude differences were noted. Because shear waves with near-vertical propagation are better understood than those propagating at wider angles, it was decided to use the 0-6,000 ft stacks.

The data were stacked and migrated, and a final filter of 3-6-25-30 hz. was applied.

7.2.2.1 Bulk Static Shifts

Bulk static shifts have been applied to 3 of the 4 S-wave stacks in order to maintain at the tie point the 63 msec difference in S1 and S2 traveltimes observed from ground level to the T/UGR in the 9C VSP (source offset 550 ft west). Rather large static shifts between the 4 sections were introduced by the refraction statics solutions. Refraction statics were necessary to start the solution of the statics problems.

Using the data from the nearest offset VSP (150 ft offset from the wellhead), the following bulk static shifts were applied to the shear wave reflection data.

Line - Component	Bulk Static Shift
L 1 - S 1	0 msec
L 1 - S 2	-137 msec
L 2 - S 1	-105 msec
L 2 - S 2	-147 msec

Line 1-S1 was not bulk shifted at all: it was used as the reference line, because it had the minimum time to any given reflector. It also had very good S/N and good correlation to the P-wave section.

Line 1-S2 had a -137 msec shift applied. This results in a 63 msec difference in S1 and S2 at the T/UGR reflector on Line 1, which is the difference in S1 versus S2 time as recorded in the VSP well (see Table 7-3 below, and discussion). The VSP showed that from ground level to T/UGR, the S-wave anisotropy results in a two-way time difference of 63 msec.

Line 2-S1 had a -105 msec shift applied, in order to tie Line 1 S1 and Line 2 S1 at the Uinta marker (the first good marker in the column). It is possible that the S1 time depends upon line direction and/or whether S1 travels more like an SH-wave or more like an SV-wave. This type of observation was observed in the VSP data as well, in that the SH source needed a source static to make the 550 ft offset S1s tie, and the 1,150 ft offset S1s tie. After the bulk shift of -105 msec was applied to the Line 2-S1 surface reflection line, a small (<10 msec) residual dynamic mistie was still observed on the deeper reflectors.

Line 2-S2 had a -147 msec shift applied. The result is that the S2 sections tie on all reflectors within 1 msec.

In order to examine the weathering layer velocities and birefringence, the 150 ft offset VSP was used. Table 7-3 lists the measured vertical travel times for S1 and S2 in the 9C VSP well.

Table 7-3
9C- VSP: 150 ft Offset (Near Offset)

Measured Depth ft	One Way Time S1 sec.	One Way Time S2 sec.	Avg. V S1 ft/sec	Avg. V S2 ft./sec	Avg. % Az. Anis.
850	0.328	0.342	2591	2465	4.2%
1000	0.355	0.372	2816	2688	4.8%
Interpolated Depth ft					
900 (datum)	0.338	0.354	2666	2539	4.7%

Avg. V S1	Average Velocity S1
Avg. V S2	Average Velocity S2
Avg. % Az. Anis.	Average Percentage Azimuthal Anisotropy

Upon inspection of the 9C VSP (150 ft source offset, that is, the nearest source offset), the first reliable data points are at 850 and 1,000 ft depth (below ground level). The 17 msec difference in S1 (one-way) time from S2 time at 1,000 ft depth indicates an average 4.8% azimuthal anisotropy (crack anisotropy) in the first 1,000 ft Therefore, a difference of ~32 msec (two way time) in the shift to seismic datum (5,000 ft above sea level) is expected between the two S-wave sections. The difference in applied time shift on Line 2 between S1 and S2 is 42 msec, very similar to that observed in the VSP.

At the 9C VSP location, the S1 and S2 corridor stacks were processed relative to ground level. From the strip chart above the film display of the reflection seismic, it is observed that a total static shift of 670 msec was applied at SP 125 (L2-S1), in the good data zone adjacent to the 9C VSP location. As already stated, this total static shift was determined by refraction statics, reflection statics, and the bulk shift determined by the appearance of the tie point.

The character correlation between the VSP S1 corridor stack and the S1 seismic section shows a 680 msec shift. The character correlation between the VSP S2 corridor stack and the S2 section also reveals a 680 msec shift, that is, a shift from the corridor stack's datum of ground level to the seismic datum of 5,000 ft above sea level.

As stated in the above paragraph, the one-way S1 time to seismic datum is 338 msec (one-way), or 676 msec, two way time. The concurrence of these three independent measurements of shift to datum is a *dramatic* confirmation of the statics techniques.

Final stacks of the shear wave post-rotation S1 and S2 components are shown in Figures 7-15 through 7-18. Figure 7-19 is a display of both the pure and the cross components for Line 1, arranged such that the columns are source components and rows are the receiver components. It is observed that the signal to noise ratio is substantially higher on the pure-mode sections. The 4C rotation has thus achieved the goal of determining the fast S-wave direction (N30W), and the signal has been rearranged onto the proper data sets.

7.2.2.2 Line 1 S-wave Refraction Statics

A comparison of the final total static correction applied to Line 1 S1 and Line 1 S2 revealed that there was a significant difference (an average of 25 msec.) in the static corrections to the two components northwest of the tie point, and that the difference in static corrections diminished in the southeast portion of the line. This difference in static corrections represents the difference in travel time needed to shift each component to the seismic datum of 5,000 ft above sea level. For most of the survey, ground level was between 5,700 ft to 5,900 ft above sea level. The S2 static corrections are in general greater than the S1 corrections, which is consistent with the S1 wave traveling faster. The fact that the S2 static shift is significantly larger than the S1 static shift in the northwest part of the line, and the two static shifts are approximately the same in the southeast part of the line, implies that the near surface rocks from ground level to datum are more azimuthally anisotropic near the northwest end of the line.

It should be borne in mind that Line 1 is a dip line whose northwest end is nearest the Uinta mountains, a thrust front, and whose southeast end is on a more stable plateau area, and thus the northwest end may be expected to show more azimuthal anisotropy. It is interesting to note that the S-wave travel time anisotropy observed on the stacks for the uppermost interval, from seismic datum to the Uinta marker at approximately 5,800 ft log depths, shows the same trend: significant anisotropy (7 percent) at the northwest part of Line 1, diminishing to 2 percent anisotropy at the southeast end of the line (Figure 8-22). Also, the VP/VS ratios for the seismic datum - Uinta interval (Figure 8-25) show a gradual increase and convergence from 1.70 and 1.80 for VP/VS1 and VP/VS2, respectively, at the northwest end of Line 1, to 1.90 for both VP/VS1 and VP/VS2 at the southeast end of the line. This increase and convergence of the two VP/VS ratios is interpreted as an increase in shale content and a decrease in crack anisotropy towards the basin in the southeast.

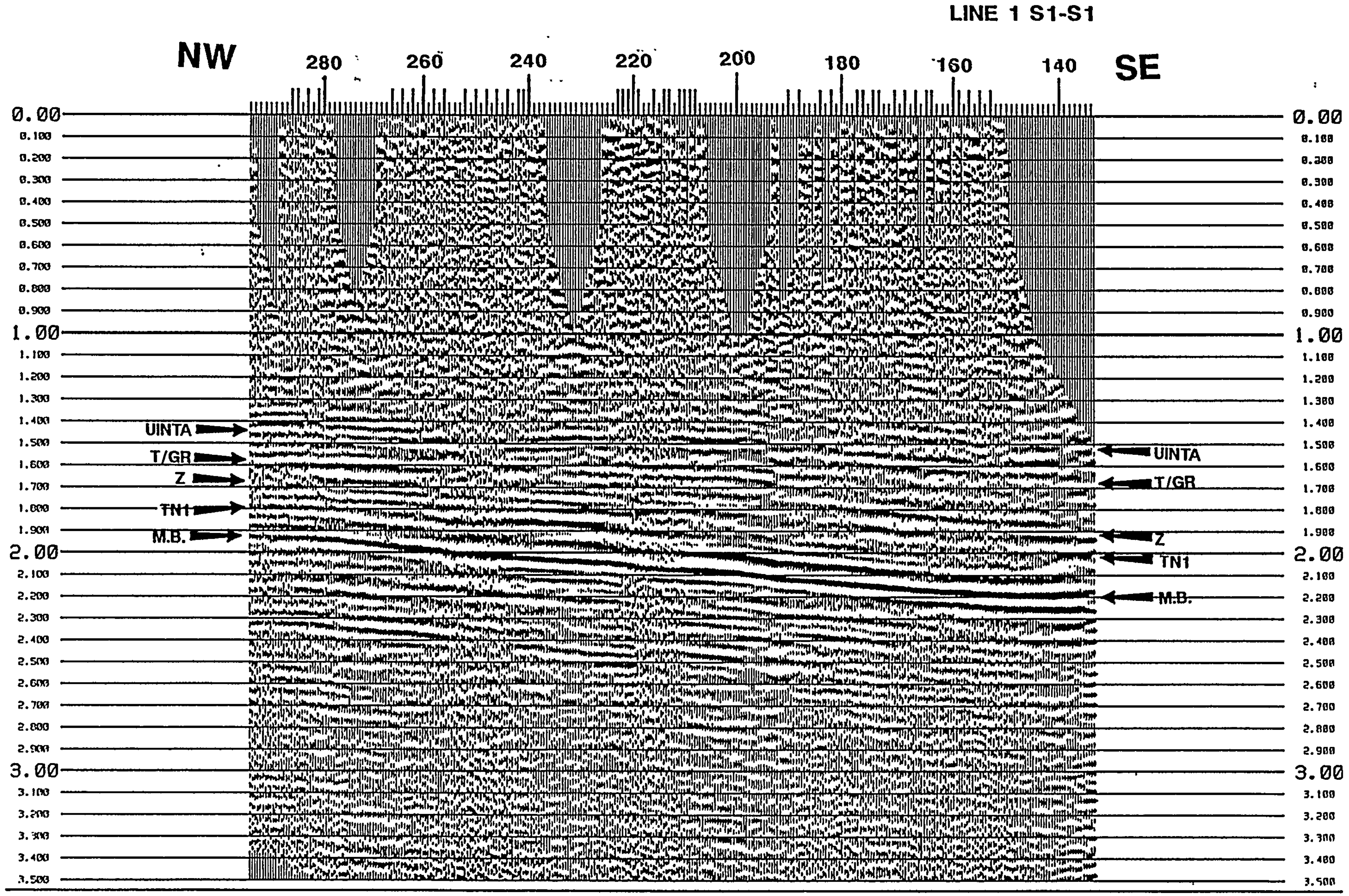

FIGURE 7–15

S-wave Line 1 final stack, post-rotation S1 component (fast S-wave).

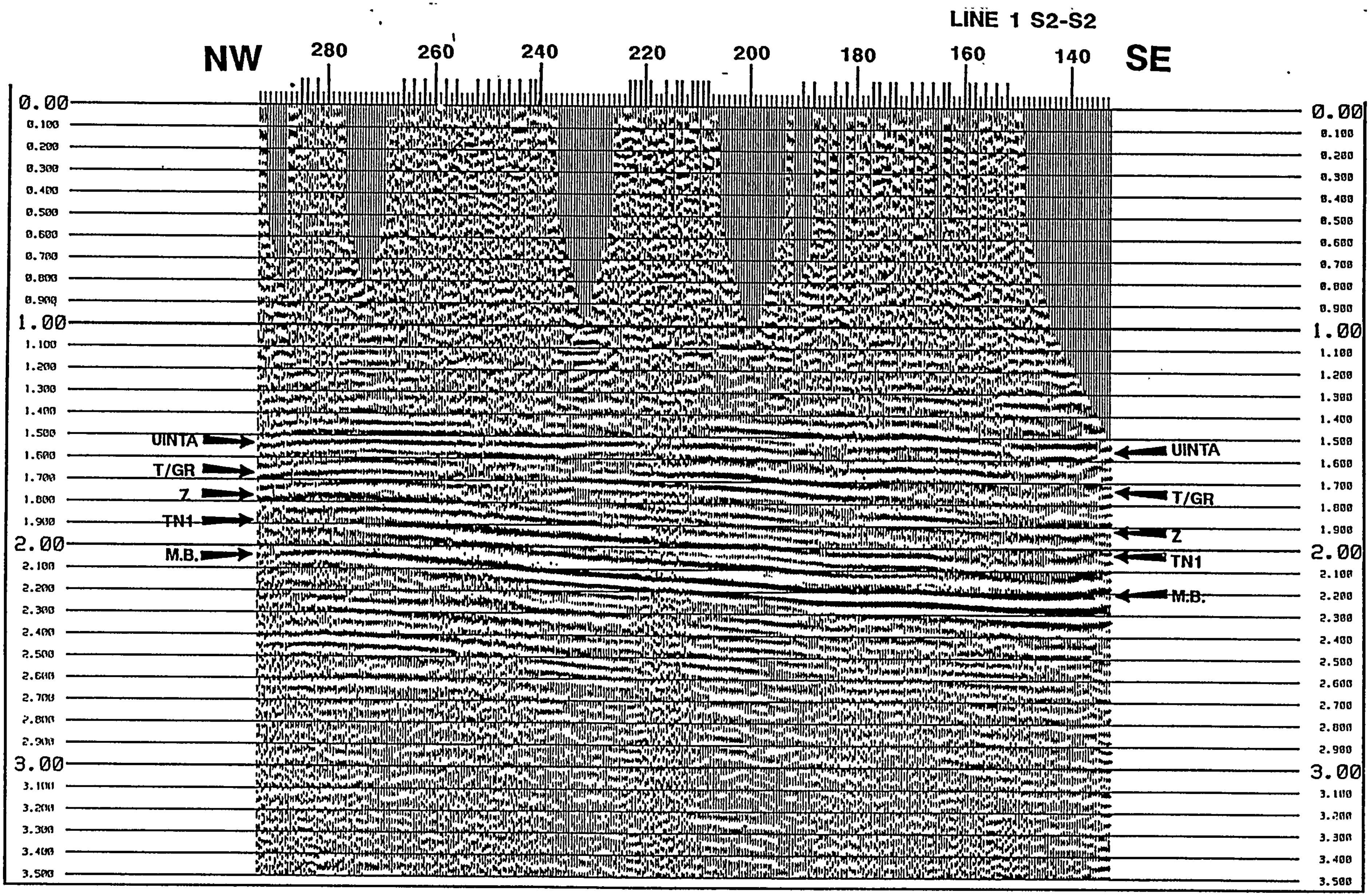

FIGURE 7–16

S-wave Line 1 final stack, post-rotation S2 component (slow S-wave).

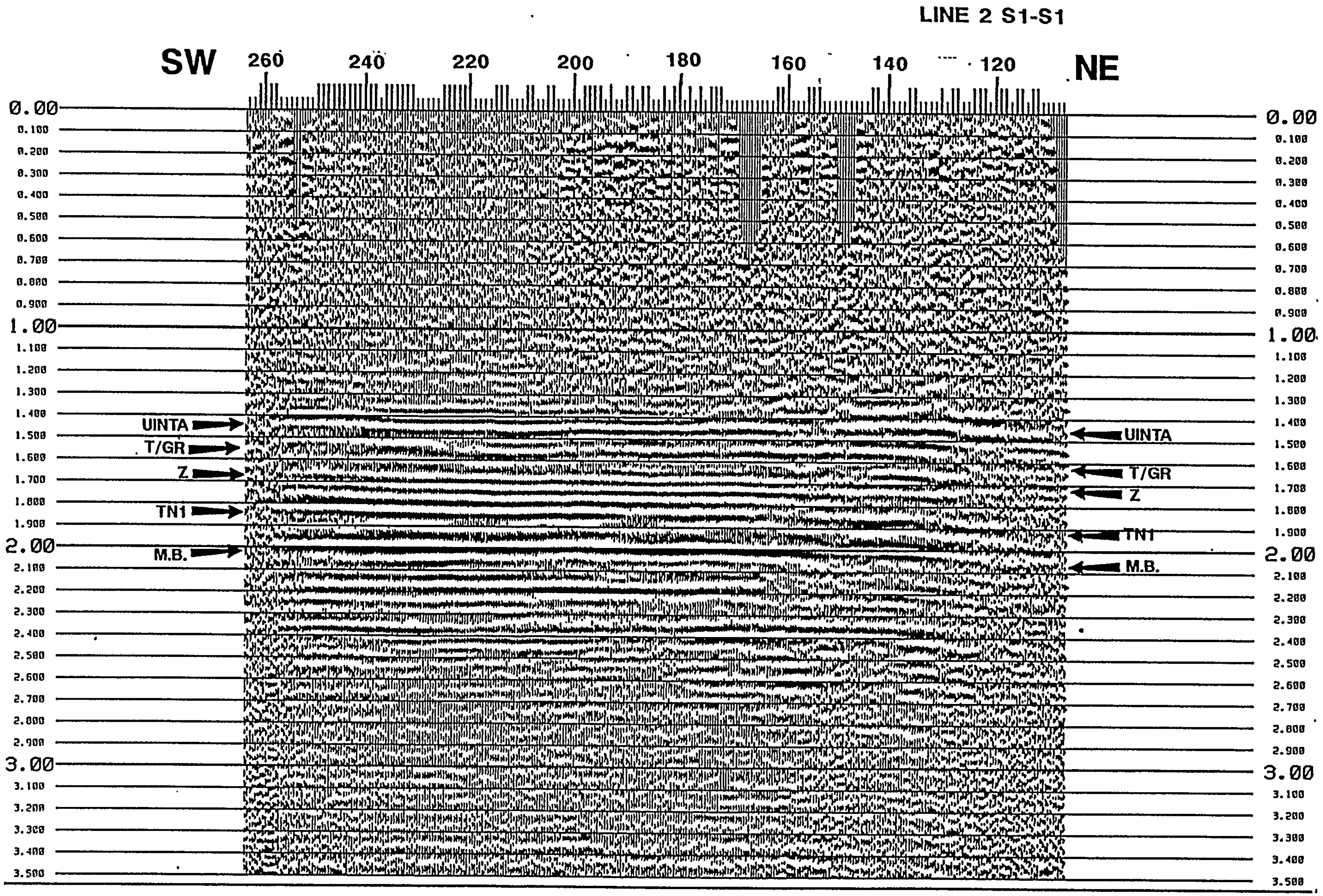

FIGURE 7–17

S-wave Line 2 final stack, post-rotation S1 component (fast S-wave).

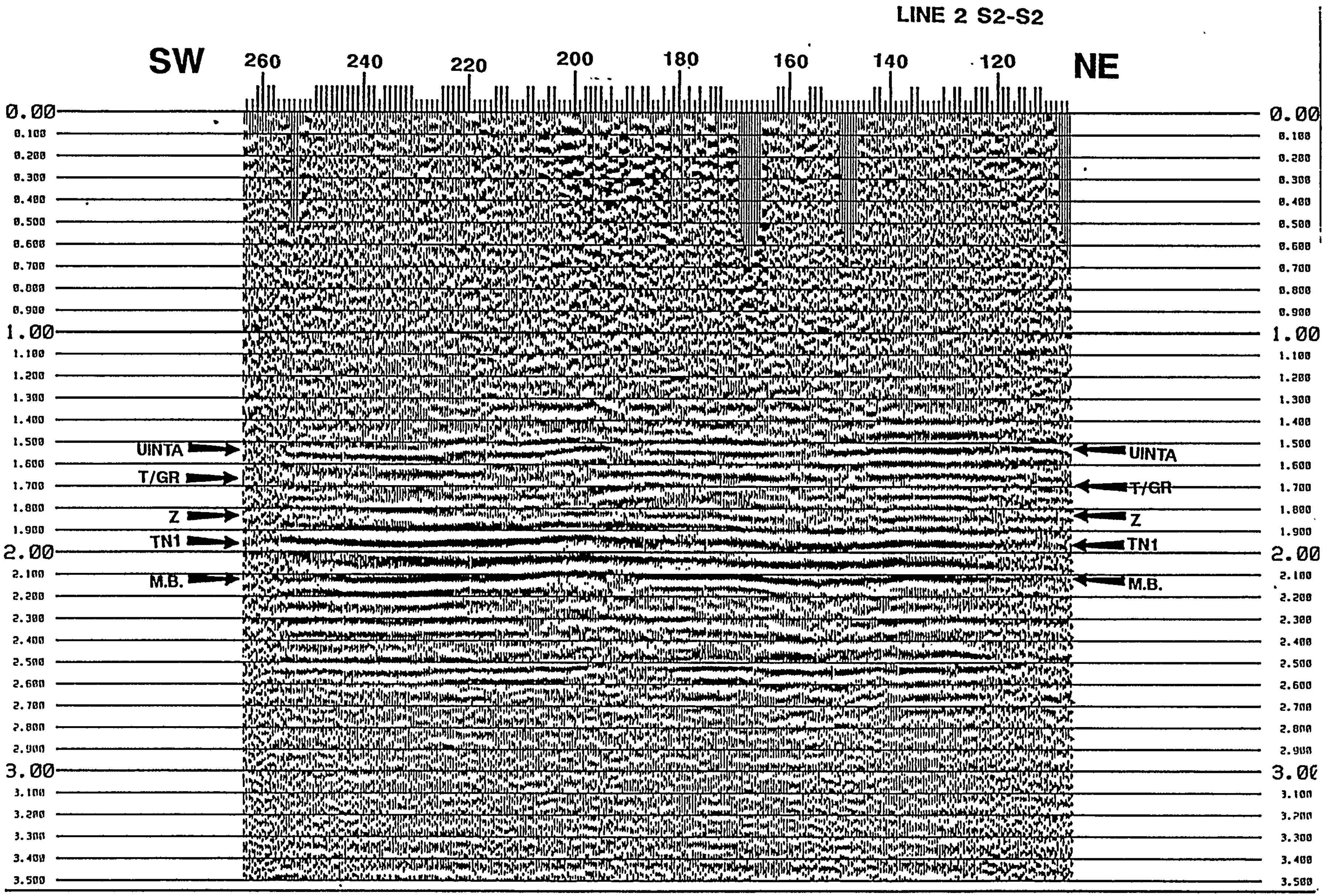

LINE 2 S2-S2

FIGURE 7–18

S-wave Line 2 final stack, post-rotation S2 component (slow S-wave).

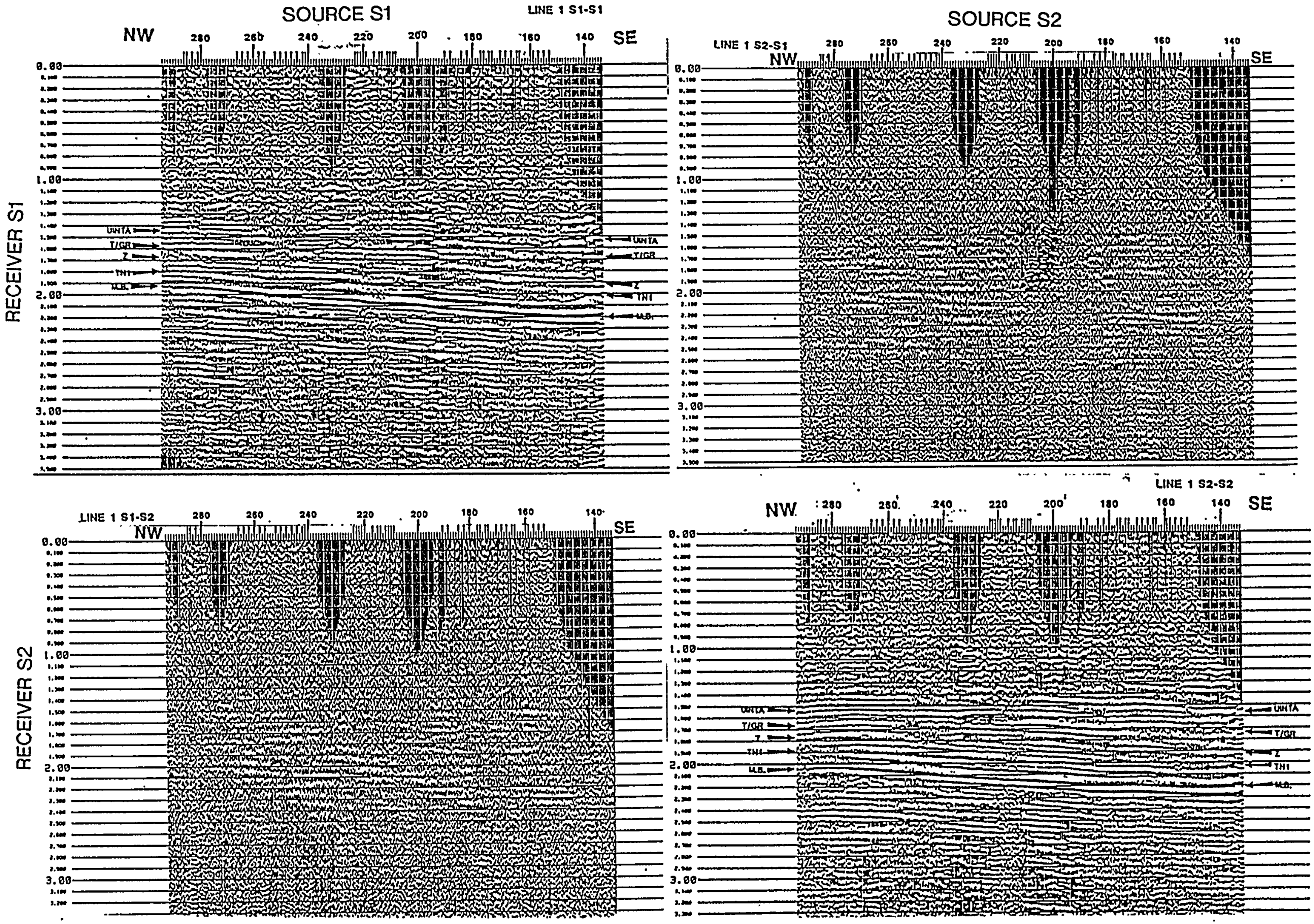

Matrix display of rotated sections. Columns are source components, rows are receiver components

FIGURE 7-19

7.2.2.3 S-wave Stacking Velocities

Methodology

The stacking velocity function for each S-wave component on each line were compared at the line intersection. Figure 7-20 shows the stacking velocity function at the tie point for L1-S1, L1-S2, L2-S1, L2-S2. These stacking velocities are the final ones, posted on the filmed sections. See Appendix B for tabulated values.

7.2.2.4 Observations

For the interval of interest, from 1500 msec to 2500 msec, we observe,

(1) on Line 1, Vstk S1 > Vstk S2, but for Line 2, Vstk S2 > Vstk S1 (where Vstk is the stacking velocity).

Line 1 is about 20° away from parallel to the dominant NW fracture orientation, while Line 2 is about 20° from perpendicular to the fractures. This is a special case in which the post-rotation S1 and S2 components are close to the pre-rotation inline (SV) and crossline (SH) acquisition components, and it is useful in this case to refer to these pre-rotation components when comparing normal moveout velocities. Also, there is a time-variant mistie at the tie point between S1 and S2, which is interpreted to indicate the presence of NW-trending cracks. It is noted that

on Line 1, SV (inline) ~ S1 and SH (crossline) ~ S2, while

on Line 2, SH (x-line) ~ S1 and SV (inline) ~ S2.

Therefore, observation (1) may also be written as

(2) on both Line 1 and Line 2, Vstk SV > Vstk SH, in the good data zone from 1.3 to 2.3 sec.

7.2.2.5 Layer Anisotropy

The predicted S1 and S2 vertical velocities (average velocities using the well depths measured from KB at the tie point) are posted next to the S1 and S2 seismic picks in Tables 7-4. The observed stacking velocities are approximately 11% increased over the vertical velocity. The method used to calculate the percent difference is (Vstk-Vvert)/Vstk.

The difference between SV and SH stacking velocities is ~2% to ~3% (Figure 7-20, 1.5-2.3 sec). The divergence between SH and SV is small (to about 1.6 sec), and then increases with increasing time to the reflector. Since the first reliable velocity pick is the Uinta reflector at about 1.4 sec, no reliable information about Vstk can be gained above the Uinta.

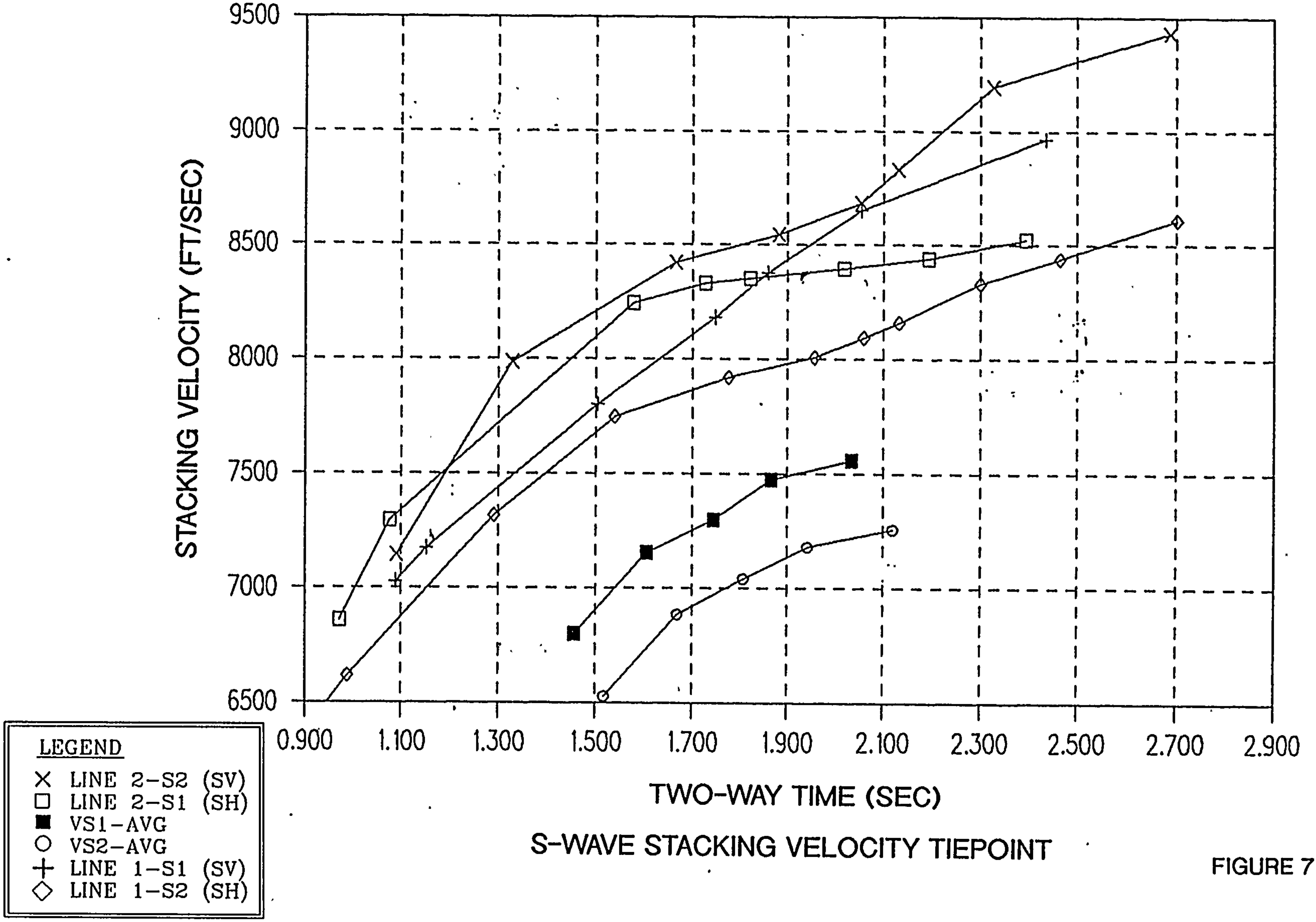

FIGURE 7-20

S-wave stacking velocity functions at line tie point, showing on Line 1 (parallel to the cracks), $V_{STK}S1 > V_{STK}S2$; but on Line 2 (perpendicular to the cracks), $V_{STK}S2 > V_{STK}S1$.

The predicted P-wave vertical velocities range between 11,805 ft/s to 13,273 ft/s (Table 7-5a). The observed P-wave stacking velocities 13,000 ft/sec to 15,000 ft/sec are 6-8% higher for Uinta through the MB reflectors, respectively (Figure 7-13, P-wave Stacking Velocities). The layer anisotropy effect decreases with increasing depth to reflector, as expected. The reason that the apparent layer anisotropy decreases with depth is that the angles of incidence become more nearly vertical with greater reflector depth for a given maximum offset. Thus, near vertical velocity is measured with increasing depth. Tables 7-5a, 7-5b, and 7-5c list the velocities, times, and depths.

Table 7-4a
S-wave Stacking Velocity (Vstk) Analysis at Tie Point
Seis. Datum = 5000 ft ASL K.B. = 5798 ft ASL

Depth Ref. K.B. ft	Formation Name	Depth Ref. Seis. Dat. ft.	Two-Way Time sec		Vert. V-Avg S1 ft./sec	Vstk S1 ft/sec	Vert. V-Avg S2 ft/sec	Vstk S2 ft/sec
			Line 1					
			S1	S2				
5750	Uinta	4952	1.456	1.517	6802	7710	6529	7720
6543	T/UGR	5745	1.606	1.669	7154	7960	6884	7860
7161	Z	6363	1.744	1.808	7297	8150	7039	7940
7770	TN1	6972	1.866	1.942	7473	8380	7180	8005
8483	M.B.	7685	2.034	2.118	7557	8590	7257	8140

Table 7-4b
Line 1 VP Stack at Tie Point

Time sec	Vstk ft/sec
0.000	5600
0.264	9185
0.357	11351
0.434	12263
0.614	12947
0.866	13517
1.181	14087
1.788	14600
0.000	5600
0.250	8387
0.347	10667
0.449	12035
0.619	12947
0.866	13517
1.016	13916
1.206	14315
1.409	14771
1.967	14942
2.360	15227

Table 7-5a
P-wave Vertical Velocity (Vvert) Analysis at Tie Point
Seis. Datum = 5000 ft ASL K.B. = 5798 ft ASL

Depth Ref K.B. ft	Formation Name	Depth Ref S.D. ft	Time P	V-Avg P VP-vert
5750	Uinta	4952	0.839	11805
6543	T/UGR	5245	0.921	12476
7161	Z	6363	0.995	12790
7770	TN1	6972	1.067	13068
8483	M.B.	7685	1.158	13273

Table 7-5b
P-wave V-Vert vs. Vstk % Difference

Formation	T_0	V-vert	L1 Vstk	L2 Vstk	% Difference	
					L1	L2
Uinta	.839	11805	13420	13420	12.1	12.0
T/UGR	.921	12476	13958	13645	8.3	8.6
Z	.955	12790	13760	13850	7.1	7.65
TN1	1.067	13068	13775	13880	5.1	5.9
Mahogany Bench	1.158	13273	13980	14110	5.1	5.9

Table 7-5c

Line 1 VP Stack at Tie Point		Line 2 VP Stack at Tie Point	
Time sec	Vstk ft/sec	Time sec	Vstk ft/sec
0.000	5600	0.000	5600
0.264	9185	0.250	8387
0.357	11351	0.347	10667
0.434	12263	0.449	12035
0.614	12947	0.619	12947
0.866	13517	0.866	13517
1.181	14087	1.016	13916
1.788	14600	1.206	14315
		1.409	14771
		1.967	14942
		2.360	15227

7.2.2.6 Discussion: Crack Anisotropy

The observed inequalities of stacking velocities, while perhaps not intuitively obvious, are predicted by theory (Thomsen, 1988). For an azimuthally anisotropic medium, characterized by transverse isotropy with a horizontal symmetry axis (TIH), the line with source-receivers parallel to the cracks (Line 1) is predicted to have the inline moveout greater than the crossline moveout velocity, because there is no angular variation of velocity for this geometry. On the shear wave seismic line with sources and receivers perpendicular to the fracture strike (Line 2), the crossline (SH) moveout velocity Vnmo is predicted to be less than the inline (SV) moveout velocity.

The observed relationships among the S1 and S2 stacking velocities conform to Thomsen's (1988) prediction for stacking velocities of shear wave in azimuthally anisotropic media. The interval of difference among the stacking velocities includes the fractured gas reservoir interval (Upper Green River). Furthermore, the relationships for the S1 and S2 stacking velocities are in accordance with the presence of dominant open NW-trending fractures. The NW-trending cracks are the dominant open crack set in-situ because the shear waves polarized N30W have the minimum travel time (S1), and the N70E polarized shear waves exhibit the greater travel time (S2).

7.2.2.7 Layer Anisotropy

The stratigraphic column at the Bluebell-Altamont area is composed of many thin layers, which results in layer anisotropy, or transverse isotropy with a vertical axis (TIV). Goodway and Mayo (1994) have reported that the inline (SV) moveout in TIV media is 10-20% faster, based on the velocity scans, than the crossline (SH) moveout, irrespective of line orientation. In the presence of layer-anisotropy alone, their field data showed SV always to be faster than SH. This finding is similar to the Bluebell-Altamont field data shown here, although here the SV stacking velocity is only about 2% faster than SH.

The difference between V_{nmo} and V_{vert} is about 11% for S-wave [(Vstk-Vavg)/(Vstk)]; for P-wave, about 6-8%. The effective horizontal velocities are thus greater than the vertical velocities, which is a well-known phenomenon. The stacking velocities exhibit the effects associated with significant layer anisotropy, in accordance with the thin-layer appearance of the wireline logs. The crack anisotropy observed in the shear wave stacks also influences the effective moveout velocities. The effective crack anisotropies range from about 2-3% in the first 2800 ft, to about 1% to 6,500 ft (T/UGR), to ~10-15% in high-fracture-density anomalous intervals, or ~1-3% for background "normal" anisotropies. The effect of the layer anisotropy is entangled with the crack anisotropy in the stacking velocities, and insufficient techniques are available to separate the two.

8.0 SEISMIC INTERPRETATION

8.1 A. Nine-Component VSP

Figure 8-1 shows the sonic and density logs from the 9C VSP well together with the P-wave synthetic seismogram (from sonic and density) with the S1 and S2 corridor stacks from the two shear wave VSPs (550 ft west of the borehole, and 1,121 ft east). The figure shows that the P and S reflectors correlate very well. The S-corridor stacks were played out with a VP/VS of 1.82 on the plot scale to match the zone of interest (6,650 ft-8,850 ft). This good match between P and S reflectors is attributed to the low-porosity regime of this area. The lower the porosity, the more the P wave and S wave reflectors resemble each other. The greater the porosity, the less the P wave and S wave reflectors resemble each other. This is because the P-waves are sensitive to both rock frame matrix, pore geometry, and pore constituents; while the S-waves are sensitive primarily to rock frame matrix, and relatively insensitive to pore constituents. Split shear waves can give information about the pore geometry. As the porosity decreases, one approaches the end point of solid rock, at which point the P-wave and S-wave would both be responding to the rock frame matrix alone.

It should also be noted from Figure 8-1 is that the T/UGR reflector is bright for S1 and dim for S2 on the 550 ft west offset, coupled with a significant S2 time delay to the Z reflector. This is interpreted as indicating that to the west of the 9C VSP well, going updip onto structure, there is significant open crack density (about 5% or more). However, the 1,121 ft east offset shows more equivalent amplitudes on the S2 and S1 T/UGR reflectors and no significant S2 time delay to the Z reflector. This situation implies that going downdip offstructure to the east, there is not a significant crack density. The production data for these zones adjacent to the 9C VSP well agrees with this interpretation.

In the 550 ft west offset, the S1 and S2 corridor stacks show no significant difference above the T/UGR trough through the Uinta. Below the T/UGR to the MB, there is significant travel time anisotropy. A different situation appears to exist in the 1,121 ft east offset. From the Uinta through the T/UGR, a greater travel time of 10 msec is seen in S2, and much less shear-wave birefringence is seen to the MB reflection. This indicates that the Uinta-T/UGR is birefringent (contains a crack anisotropy), while the T/UGR-MB interval is less anisotropic. We interpret this as an indication of heterogeneity, that is, different geologic conditions downdip from the 9C VSP (off-structure), than updip (on-structure).

Figure 8-2 shows the sonic, density and gamma ray logs from the well, the P-wave synthetic seismogram generated from sonic and density logs, and the P and S1 VSP 550 ft west corridor stacks. The bandpass filter for the P and S was set by the VSP data, not the reflection seismic data. The filters used were 10-80 hz (P), and 6-48 hz (S). The good correlation of reflection events from synthetic

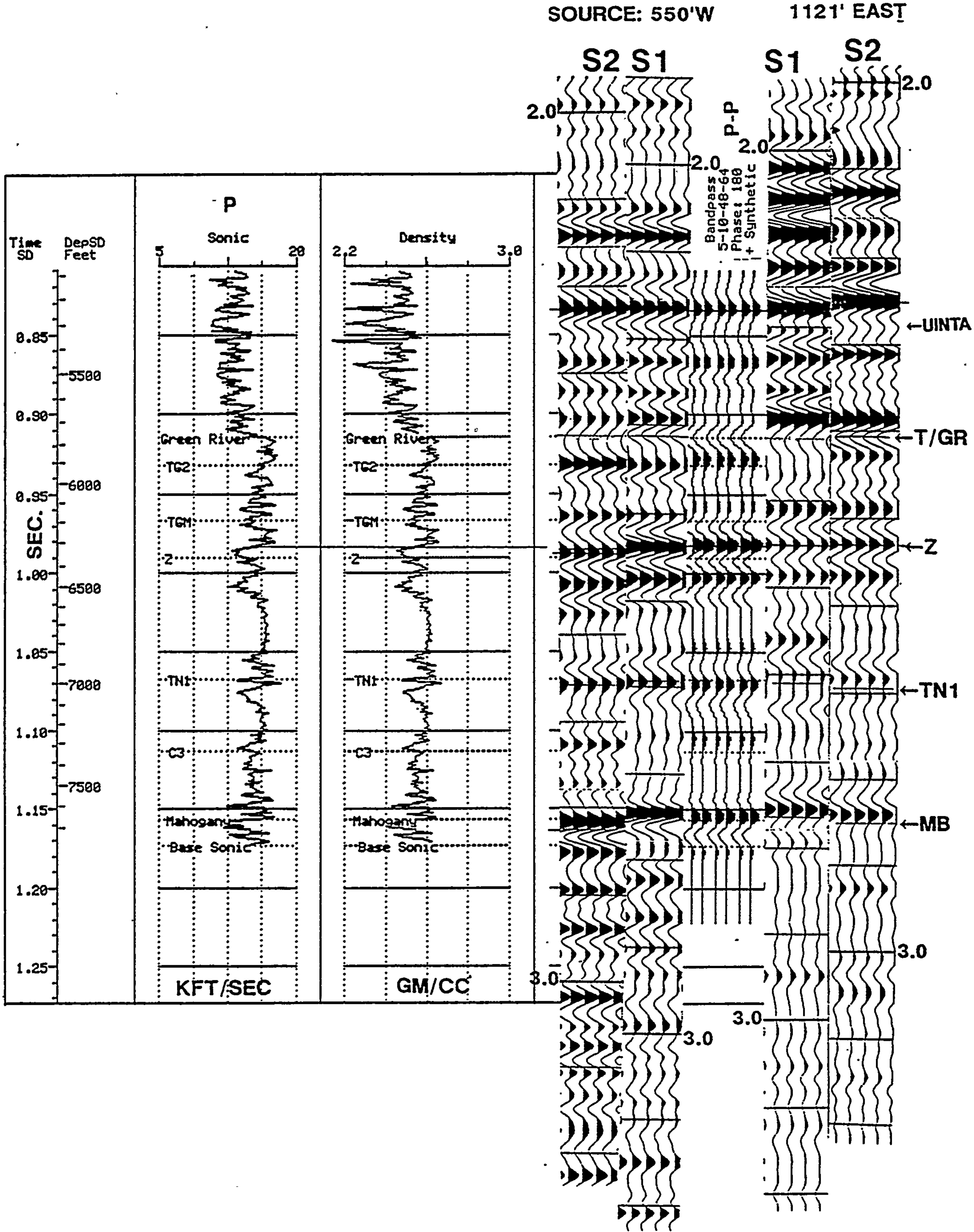

Sonic and density logs for the 9C VSP well. Also shown are S2 and S1 corridor stacks for the 550 ft. west offset source VSP, the P-wave synthetic seismogram from sonic and density logs, and S1 and S2 corridor stacks for the 1121 ft. east offset source VSP. Similarity between P-wave and S-wave reflections is due to low-porosity rocks. Differences in amplitude of T/GR reflection package are noted on 550 ft. west source (S2 is dim, S1 is bright). These differences are not observed on the 1121 ft. east source VSP; the change is interpreted to represent less fracturing in the T/GR towards the east. VP/VS 1.82 for plot scale.

FIGURE 8-1

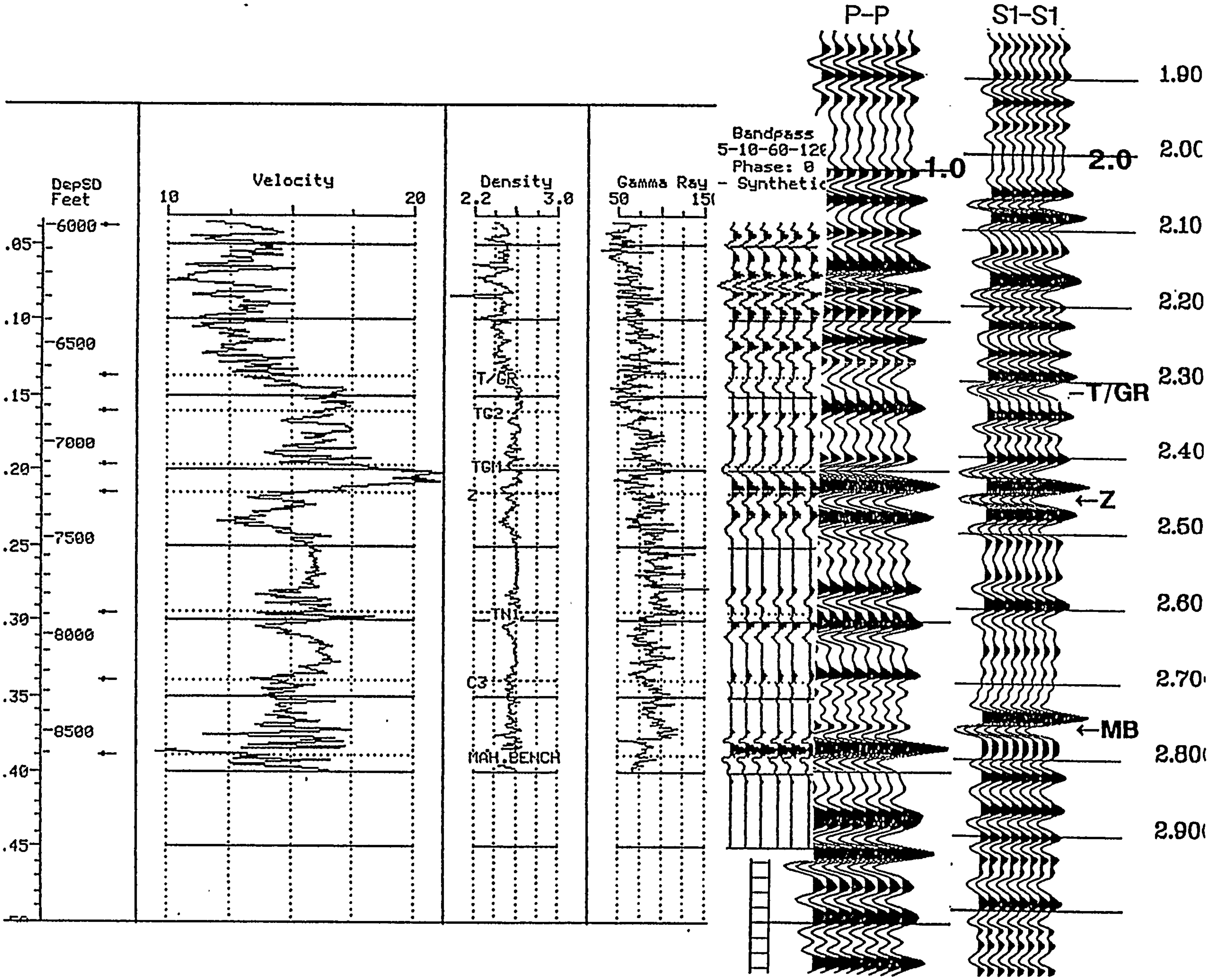

Sonic, density and gamma ray logs, P-wave synthetic, and P and S1 corridor stacks for the 9C VSP well. An excellent correlation of seismic events is observed.

FIGURE 8-2

seismogram to corridor stacks is evident. The VSP provides invaluable depth to time (P, S1, S2) data for reflection identification.

Establishing the depth to time correlation for the S-wave surface reflection data was accomplished using the VSP results for each post-rotation component (S1, S2). Figure 8-3 shows the S1 VSP display with depth on the horizontal axis and one-way time on the vertical axis. The S1 corridor stack is plotted twice on the right of the time-depth display, once unfiltered and once filtered back to 6-16 hz passband to match the surface seismic data. The VSP two-way time is shifted to tie the surface seismic, according to the previous discussion. Depth to time correlation was done in the same manner for the S2 component.

The P-wave VSP is tied to the P-wave Line 2 at the well location in Figure 8-4, which also displays the synthetic seismogram from the wireline log data. An excellent match is observed with the key reflectors easily identified.

Correlation of the interpreted horizons from the VSP to the surface reflection seismic was straightforward on the S1 and S2 components also, due to the good signal to noise of both the surface seismic and the VSP data sets. The S1 VSP corridor stack to surface reflection line tie is shown in Figure 8-5, and the S2 corridor stack tie is shown in Figure 8-6.

8.1.1 B. Nine-Component Reflection Seismic Data

After final processing, the P-wave and two S-wave components S1 and S2 of the surface reflection seismic data were interpreted for geologic significance. Special attention was paid to indicators of fracture characteristics and gas saturation. The interpretation included: 1) stratigraphic modeling, 2) S-wave anisotropy analysis, and 3) P-wave amplitude variation with offset (AVO) analyses. Each of these efforts was directed toward obtaining specific knowledge of the reservoir.

Stratigraphic variations influence all seismic reflection components, so the first step for interpreting the surface seismic data was to model the stratigraphy. The cross-sectional modeling that was done to aid in identifying reflectors, and interpreting stratigraphy along the lines was used for both the P-wave and S-wave sections.

Shear waves reveal information about the internal structure of the rock, so the difference in travel times through defined intervals for the two shear components S1 and S2 were compared to obtain the S-wave anisotropy. This gives an indication of the fracture density within specific intervals.

P-waves are influenced by both the rock structure and its fluid saturant, so the P-wave data were analyzed for amplitude variation with offset that could indicate gas saturation.

The seismic interpretation was calibrated to well production data at the many well locations near the seismic lines. Table 8-1 is a summary of the seismic

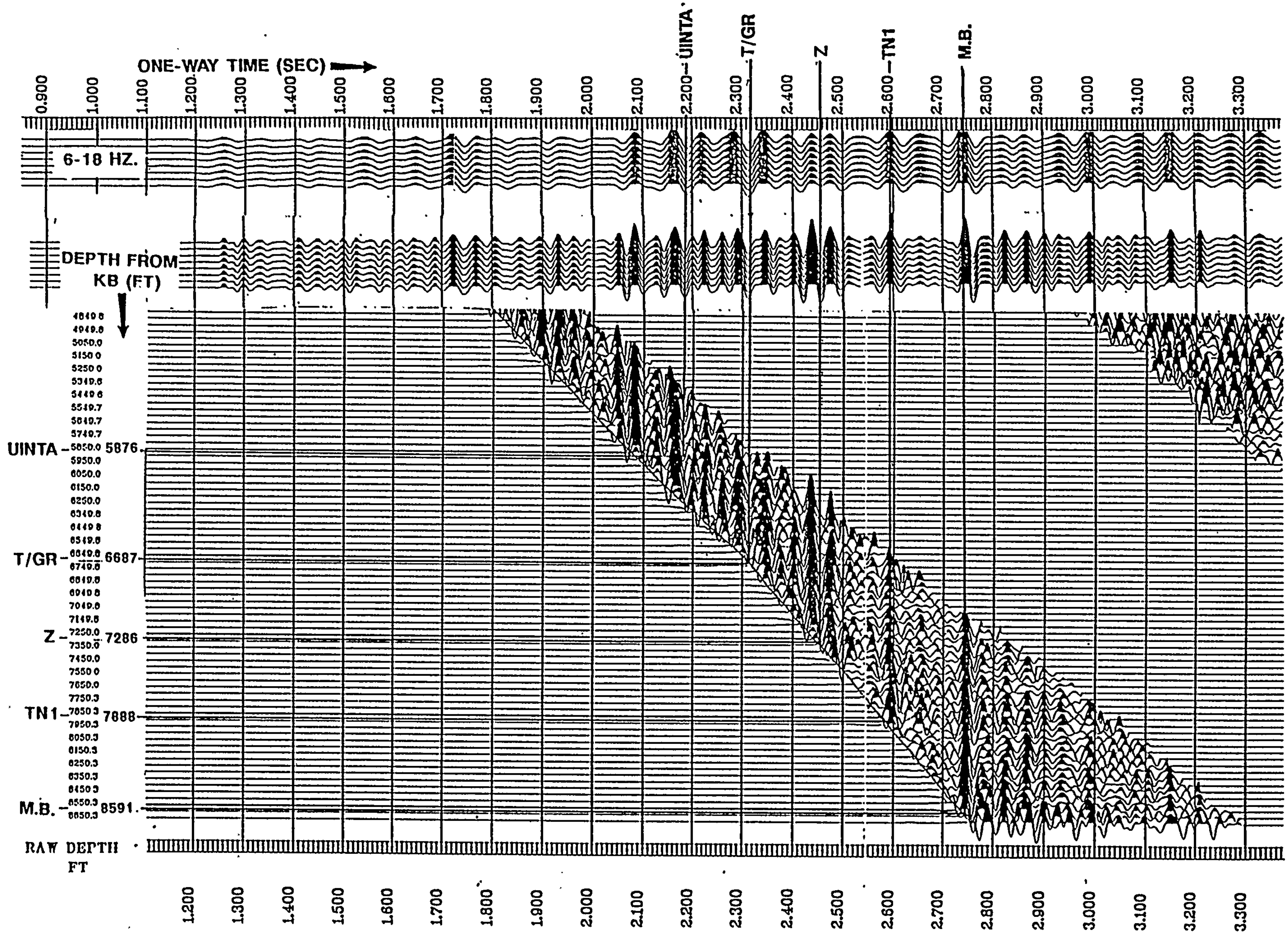

9C VSP display showing depth to time correlation for the S1 component.

FIGURE 8-3

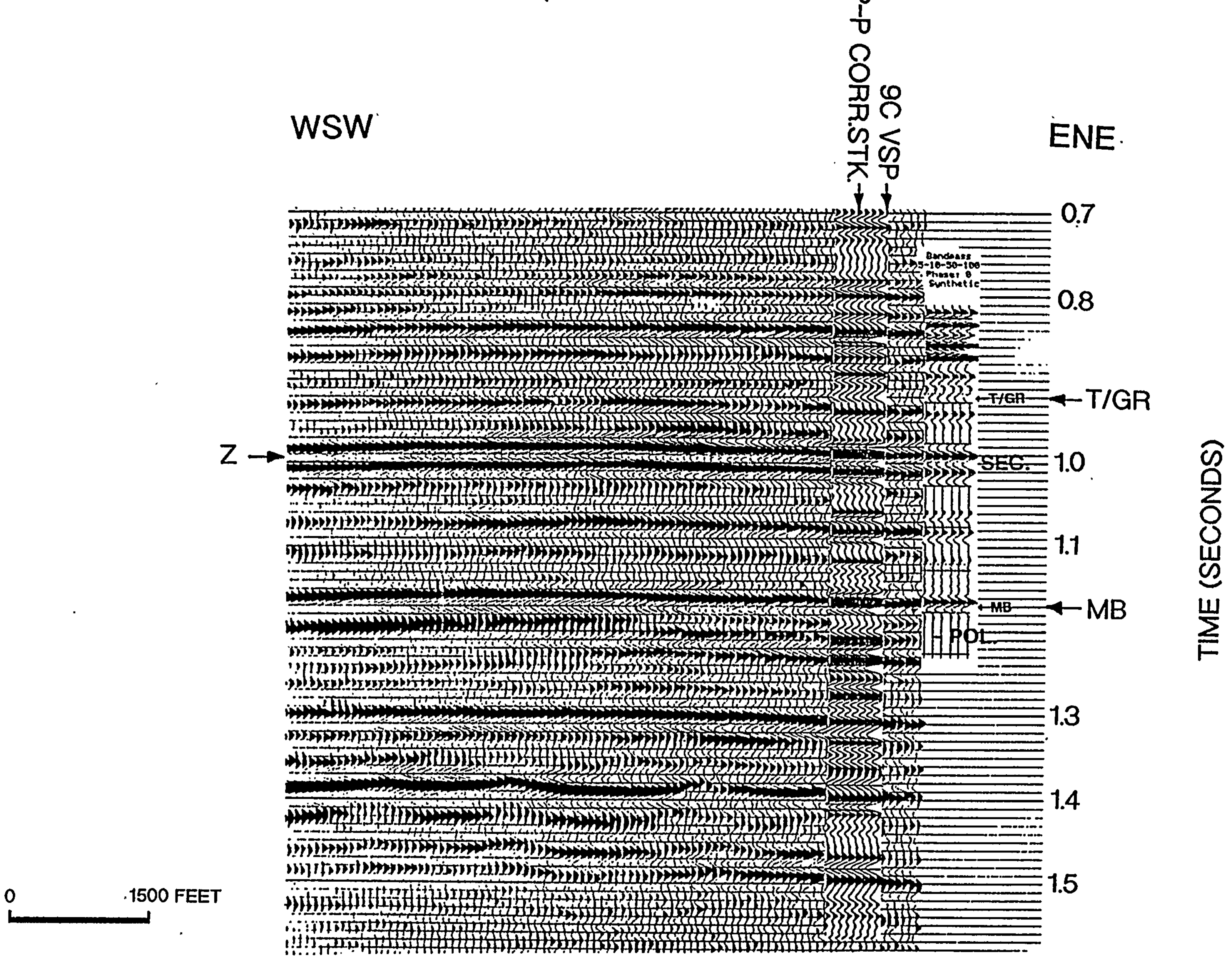

9C VSP P-wave corridor stack tied to P-wave surface reflection seismic Line 2 at the well location, showing excellent correlation of seismic events.

FIGURE 8-4

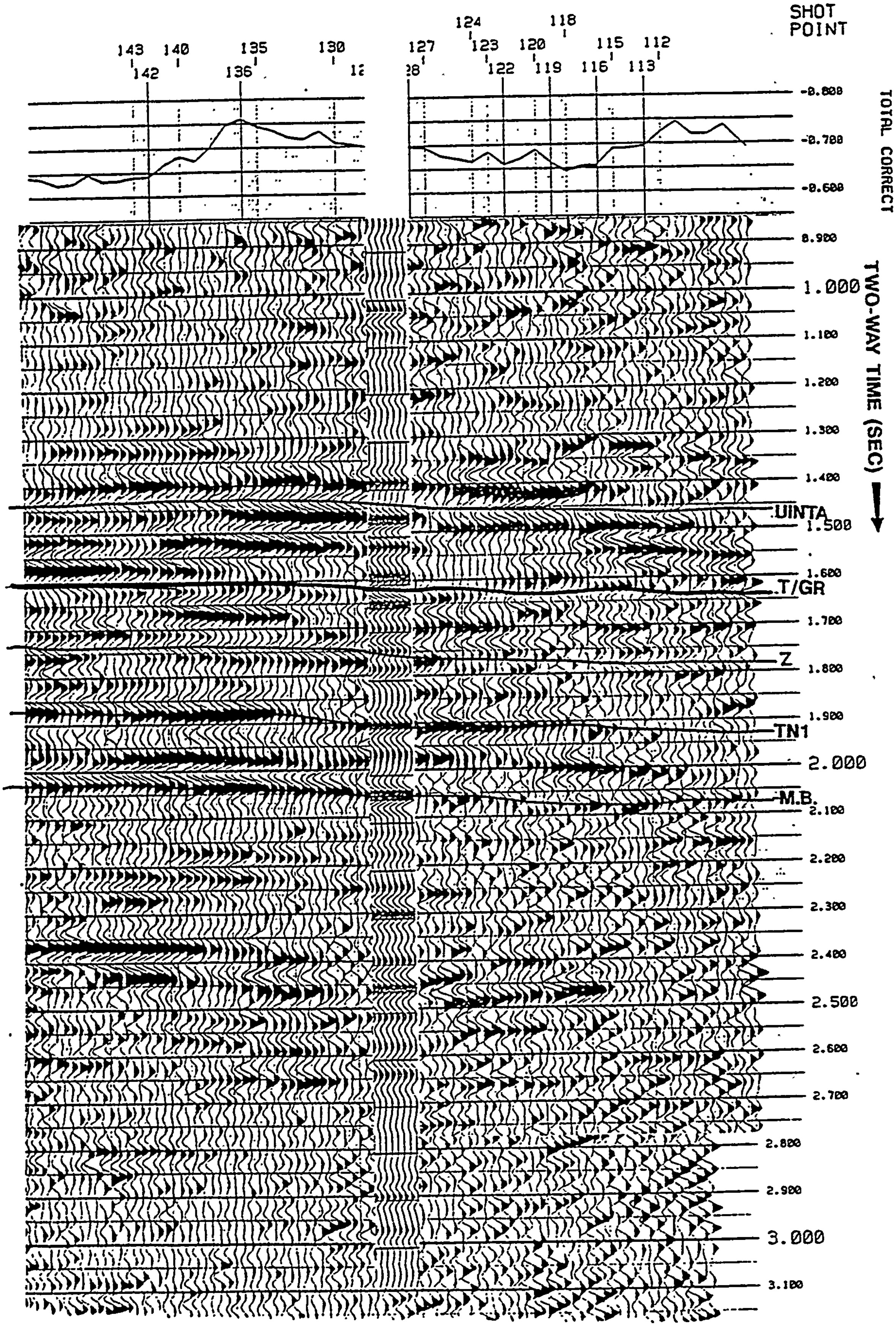

9C VSP S1 corridor stack tied to S1 surface reflection section shows good correlation of interpreted horizons.

FIGURE 8-5

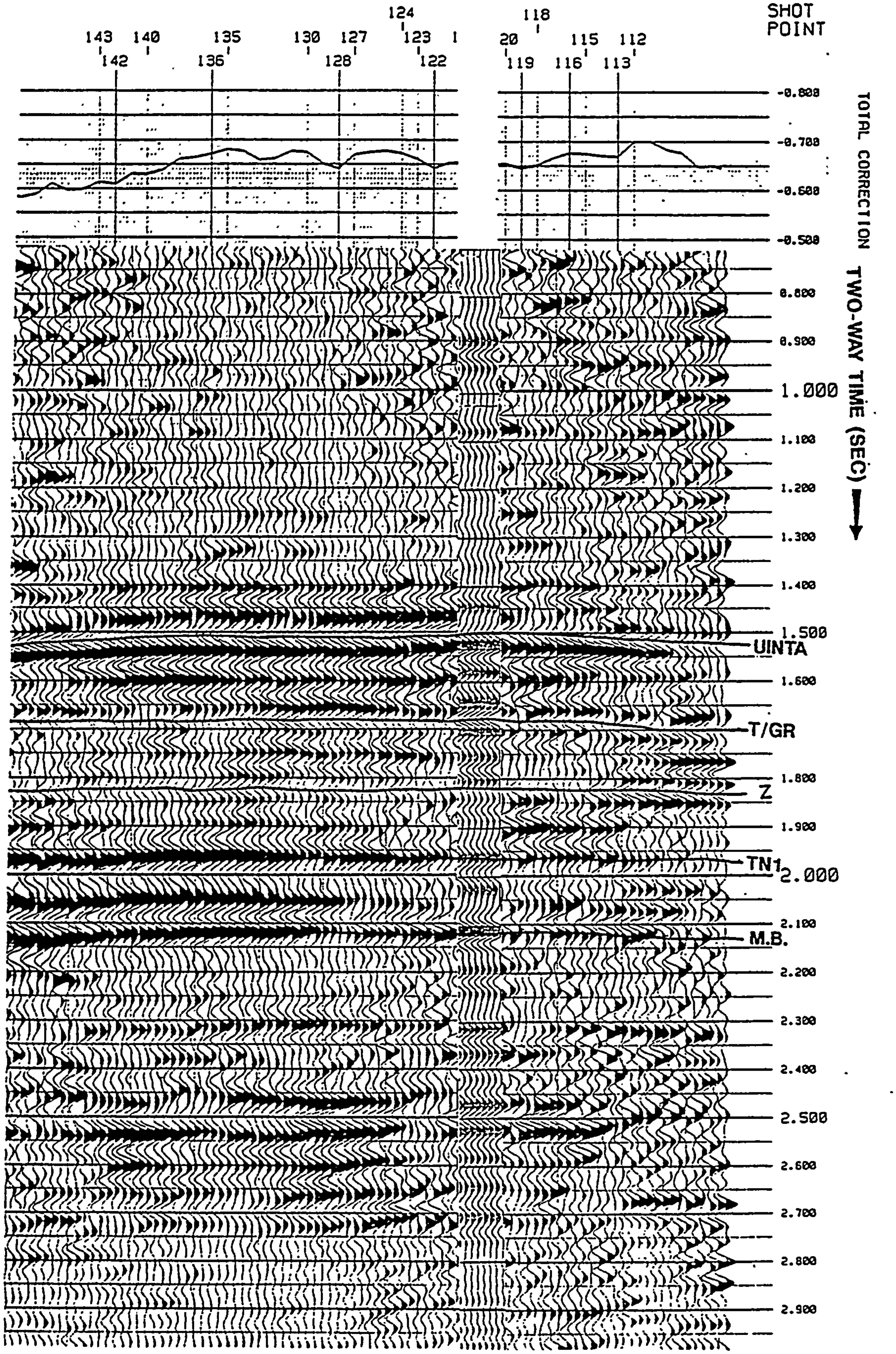

9C VSP S2 corridor stack tied to S2 surface reflection section shows good correlation of interpreted horizons.

FIGURE 8-6

analyses performed at locations corresponding to wells near the seismic reflection lines. The correlation of P-wave and S-wave analyses with well production were considered valid for wells located 1,050 ft (2 - 2-1/2 wavelengths) or less from the seismic lines.

Table 8-1
Seismic Analyses at Wells Near Multi-component Seismic Lines

Well	Dist/Az. From Line	Analysis Included		Upper Green River (UGR) Production
		P-wave	S-wave	
A	2000 ft/SW L.2	----	----	None
B	1250 ft/SE L.2	----	----	None
B2	550 ft/NE L.2	Figure 8-47	Figure 8-13	None; tar shows
C	1800 ft/SE L.2	----	----	None
D	150 ft/SE L.2	Figures 8-41-8.45	Figures 8-14-8-19	Good DSTs in UGR
E	<100 ft/ L.2	Figure 8-42	Figure 8-15	Blowout well; previous producer
F	1500 ft/NW L.2	----	----	None; gas kick while drilling
G	<100 ft/ L.2	Figure 8-36	Figure 8-16	Cumulative production 2.1 BCF gas.
H	200 ft/SE L.2	Figure 8-39	Figure 8-17	None; gas kick while drilling
I	100 ft/SE L.2	Figure 8-38	Figures 7-8, 7-10	None; 9-C VSP well
J	500 ft/NE L.1	----	----	None
K	680 ft/SW L.1	Figure 8-37	Figure 8-18	Cumulative production 421 MMCF gas
L	2200 ft/NE L.1	----	----	Cumulative production 195 MMCF
M	2150 ft/NE L.1	----	----	None
N	1050 ft/SW L.1	Figure 8-47	Figure 8-20	None
O	1800 ft/SW L.1	----	----	None
P	2750 ft/NE L.1	----	----	None

8.2 Cross-sectional Modeling

Inspection of the seismic lines revealed that lateral changes in stratigraphy have first-order effects on the seismic response. The three seismic components P, S1 and S2 all showed similar lateral changes within the Upper Green River section, which were attributable to stratigraphy. The depositional model for the Upper Green River has individual sands of 5 - 20 ft thick, changing rapidly with respect to the shoreline of the paleo-lake throughout Eocene times. In general, the Upper Green River formation becomes thicker and shalier towards the south, or basinward. These changes are seen both on P-wave seismic Line 1 which is oriented NW-SE, approximately a dip line (see basemap, Figure 8-7), and on Line 2, the SW-NE or approximate strike line. Since the major goal of this project is an evaluation of the influence of vertical, oriented fractures on the seismic response, it is important to be able to differentiate between the effects of

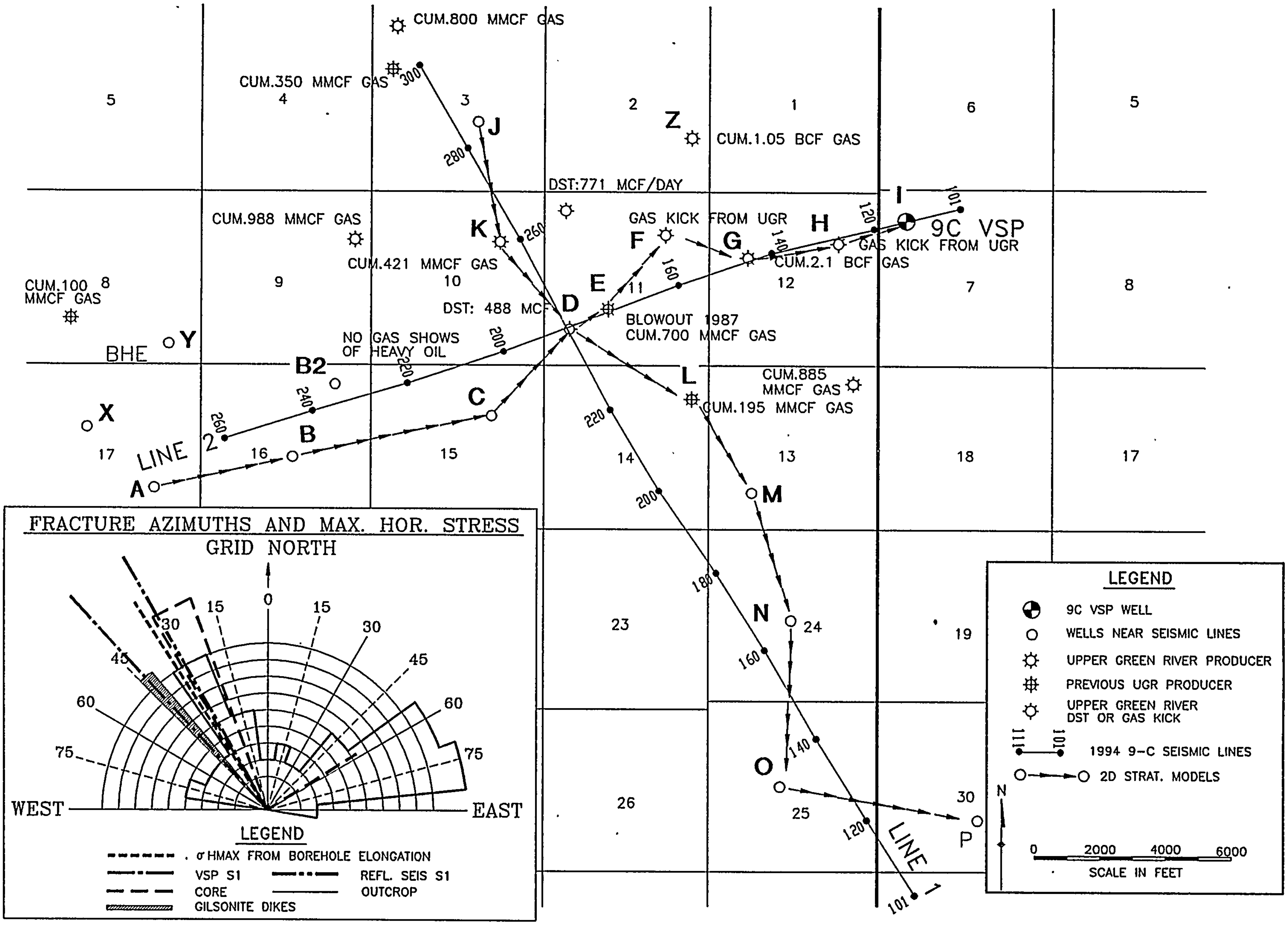

Basemap showing cross-sectional models and surface reflection seismic lines.

FIGURE 8-7

stratigraphy on the data and the effects of the fractures on the data. That is, to first account for the stratigraphy, leaving the remaining response to be explained by other features such as the fractures. Knowledge of the stratigraphy also allows the precise correlations from the wells to the seismic that are necessary for accurate time measurements of the P-wave and S-wave seismic reflectors. It is these time measurements that are the basis of subsequent anisotropy analyses.

8.2.1 Method

An interval approximately 2,000 ft thick in the Upper Green River formation (from approx. 6,500 ft to 8,500 ft) was modeled using 17 wells, 9 wells along the east-west line and 8 wells along the north-south line. The MIRA software package was used for all sonic modeling.

The models consist of 2-D zero-offset synthetic seismograms, created from the sonic logs from individual wells. The top of the models was 350 ft above the T/UGR, to ensure a full seismic wavelength above the section of interest.

Structural cross sections were created from the sonic logs, using the correlations provided by Pennzoil (Tables 8-2 and 8-3). These cross sections were the depth models used to create the 2-D synthetic seismograms that were compared to the seismic data. The sonic log cross section for Line 1 (NW-SE) is displayed in Figure 8-8a, showing the five correlated Upper Green River markers. Figure 8-8b shows the interpolated sonic log section created from the well sonic logs. The interpolated sonic log section is shown again in Figure 8-8c as a shaded interval velocity display. P-wave reflection coefficients were calculated from the sonic logs with a constant density assumption. In order to assess the influence of stratigraphic variation on the seismic data, the models were converted to 2-way time and filtered to match the seismic data on lines 1 and 2. It is these filtered synthetic seismic sections that are compared to the actual seismic lines 1 and 2 (limited offsets from 0-6,000 ft).

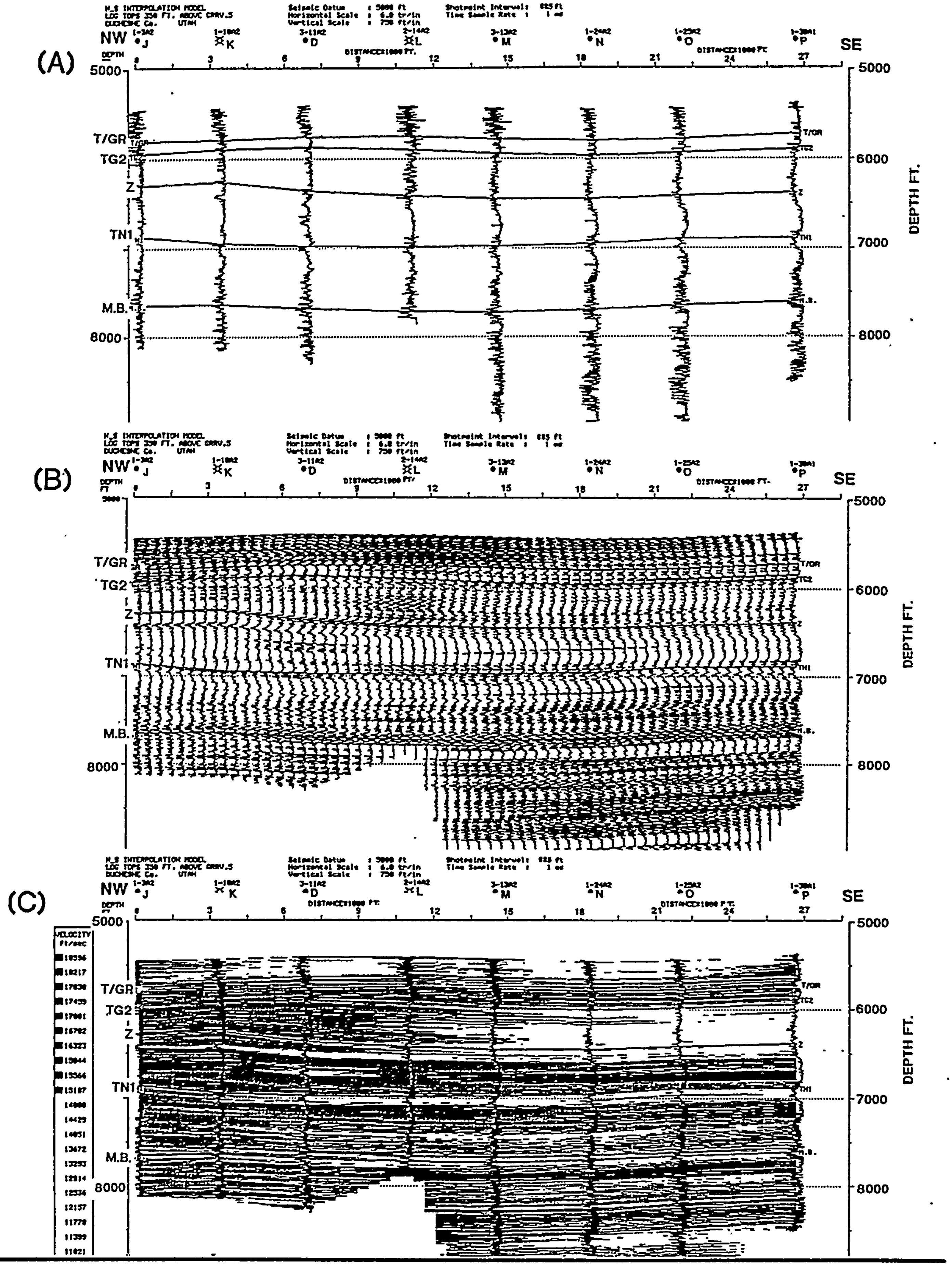

(A) SW-NE model, sonic log cross section as shown on basemap, figure 8-7. Apparent thinning of T/GR-Z interval at well F due to slightly off-structure position of this well. (In general the T/GR-Z interval thickens on structure).
(B) SW-NE model, interpolated sonic log section, showing lateral consistency in sonic character of marker horizons.
(C) SW-NE model, sonic interval velocity section. Low-velocity units marked by TN1 and M.B. become thicker and slower in velocity off-structure (to west).

FIGURE 8-8

Table 8-2
Stratigraphic Correlations in The Upper Green River
Northwest-Southeast Cross Section

WELL	J	K	D	L	M	N	O	P
KB*	5863	5850	5798	5696	5669	5576	5500	5488
UINTA†	5885	5818	5750	N.P.	N.P.	5507	5386	5276
T/UGR†	6665	6632	6543	6441	6441	6369	6275	6205
TG2†	6804	6743	6662	6592	6608	6537	6436	6378
Z†	7156	7106	7161	7116	7112	7025	6917	6871
TN1†	7726	7795	7770	7679	7643	7530	7392	7372
M.B.†	8512	8488	8483	8413	9399	8274	8149	8090

* Depth in feet above sea level
† Logged depth below K.B.

Table 8-3
Stratigraphic Correlations in The Upper Green River
Southwest-Northeast Cross Section

WELL	A	B	C	D	E	F	G	H	I
KB*	5992	5808	5771	5798	5786	5933	5879	5925	5917
UINTA†	6029	5903	5758	5750	5756	5867	5791	5842	5876
T/UGR†	5856	5726	6556	6543	6533	6669	6609	6666	6687
TG2†	7000	6857	6685	6662	6647	6785	6731	6801	6827
Z†	7515	7349	7195	7161	7135	7197	7212	7281	7286
TN1†	8081	7927	7761	7770	7766	7873	7841	7892	7888
M.B.†	8860	8700	8501	8483	8465	8571	8535	8595	8591

* Depth in feet above sea level
† Logged depth below K.B.

8.2.2 Northwest-Southeast Model

The sonic log cross section (Figure 8-8a) shows thickening of the Upper Green River between the T/UGR and Z markers towards the south, reflecting the basinward progradation of the marginal lacustrine facies. In Figure 8-8b, the interpolated sonic log section, a marked change in sonic character is seen at the

T/UGR, marking the boundary between the overlying Uinta Formation which is alluvial, and the marginal lacustrine Green River Formation. The alluvial Uinta appears erratic and relatively slow in sonic velocity, compared to the more uniform, high sonic velocity character of the Upper Green River below. The remaining four horizons indicated on the figure mark low-velocity units embedded in the predominantly fast Upper Green River formation. Comparison of the depth model (the sonic log cross section) with the time section shows a velocity gradient towards the south: Figure 8-8, in depth, shows a dip reversal on the T/UGR horizon: the lowest point is Well location N; whereas on the reflection coefficient (R.C.) time section, Figure 8-9a upper, the T/UGR marker, as well as the other markers, continues to dip to the southeast across the entire line. This is probably due to slower interval velocities within the Uinta formation, above the T/UGR marker, towards the southeastern end of the line. Unfortunately, insufficient log data available above the T/UGR marker meant that the slow velocities causing the time pull-down in this model could not be demonstrated. Figure 8-8c can be used for lithological interpretation: in the upper part of the Upper Green River formation, between T/UGR and Z, there is a gradual decrease in interval velocity from north to south, which is interpreted as a lithologic change from sands to shales towards the basin. Between the Z and TN1 markers, the interval velocities increase gradually basinward, possibly indicating more carbonates deposited towards the deeper basin.

The filtered reflection coefficient (RC) section in Figure 8-9a shows lateral changes in amplitude which can be interpreted by referring to the Figure 8-8c, the interval velocity display. The Z horizon, at 0.98 sec at the northern end of the model, increases in amplitude over the crest of the structure and then decreases gradually to the south. The velocity display shows this marker to be a thin, low-velocity unit, whose contrast in interval velocity with the overlying unit becomes greater towards the south. From Well D south, the Z unit thickens and becomes slower. However, as the entire Upper Green River section is decreasing in velocity towards the south, the contrast between the Z and the overlying unit is also decreased, causing the smaller R.C. on the southern half of the model. The TN1 unit, at 1.05 sec. on the north end of the model, is similar to the Z in that it also becomes slower and thicker to the south. The nature of the contact at the top TN1 shows a change, from an abrupt sonic velocity change at the D well, where the R.C. has highest amplitude, to a more gradual change in sonic velocity towards the south, where the R.C. is lowest. This probably indicates that deposition within the basin changed more gradually here than on the north flank. Likewise, the thin low-velocity unit corresponding to the M.B. marker, at 1,140 sec. at the north end of the model becomes thicker and slower towards the south, showing a continual and gradual increase in R.C. amplitude corresponding with the continual and gradual decrease in interval velocity of the MB oil shale unit.

The variations in thicknesses and amplitudes described above on the model can also be seen on the actual seismic data on Line 1. Figure 8-9b shows the 8

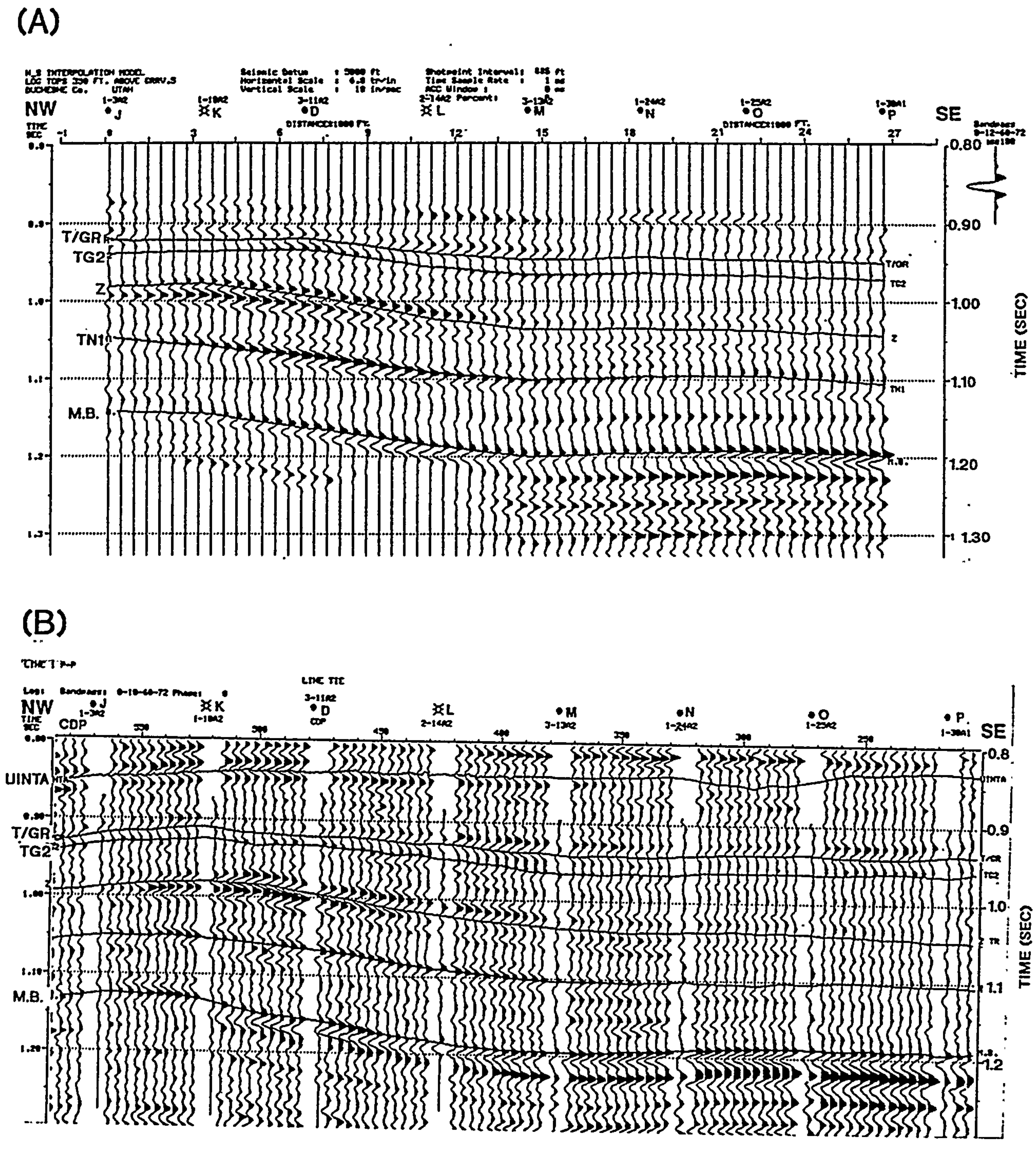

(A) SW-NE model, filtered R.C. section. Note that T/GR-TG2 reflection pair shows increased amplitude at well F.
(B) Migrated, near-offset stack of line 2, SW-NE, shows overall good match to model data (upper). Amplitude of T/GR-TG2 reflector pair does not diminish from well F to the east end of line as on model.

FIGURE 8-9

synthetic seismograms used in the model, spliced into the migrated, near-offset (less than 6000 ft) stack of Line 1. The synthetic seismograms along Line 1 are considered a good match to the seismic data of the Upper Green River, both in two-way time and in relative amplitude.

8.2.3 Southwest-Northeast Model

This model suggests that there is little variation in stratigraphy in the east-west direction, which is approximately along depositional and structural strike. However, the migrated near-offset stacked display of Line 2 shows some variations that are not seen in the model, which suggests that these variations are caused by factors other than isotropic velocity changes as recorded by the sonic logs. Figure 8-10a, the southwest to northeast sonic log cross section, shows conformable layers across the model. Slight variations in thicknesses occur because the sonic log traverse is not exactly coincident with the axial crest of the anticline. Figure 8-10b, the interpolated sonic log section, shows a sonic character similar to that of the north-south model: the marker horizons TG2, Z, TN1 and M.B. are manifest by low interval velocity units within the overall fast Upper Green River section. As on the NW-SE model, thickening and decrease in interval velocities off-structure can be seen in several intervals. For example, on Figure 8-10c, the shaded interval velocity section, the TN1 and M.B. units become gradually thicker and slower off-structure towards the west. The filtered R.C. section, Figure 8-11a, shows the reflector pair T/UGR and TG2 increasing in amplitude from SW to NE, with maximum amplitude at Well F, then decreasing to the northeastern end of the model. However, the actual seismic data on Figure 8-11b shows the maximum amplitude of the reflector pair further to the east. The real seismic data show that the amplitude increases over the crest of the structure, with the maximum amplitude at the well that produces gas from the T/UGR - TG2 interval, Well G. There are differences in the amplitudes of this reflector pair between the model and the real data; the real data have slightly lower amplitudes than the models, at the current and previously producing wells over the field structure, which may be an indication that some effects other than stratigraphy are controlling the amplitude of this reflection, even with offsets only to 6,000 ft. The well showing the biggest discrepancy between model and real seismic amplitude is Well F, which is projected a distance of 1,500 ft onto the line. It is significant that the differences between the model and real data at the top Upper Green River reflection, for those wells lying very close to the lines, are observed on Line 2 and not on Line 1, because Line 2 is oriented ENE, perpendicular to the strike of the open vertical aligned fractures, and these fractures contribute the majority of the porosity in the reservoir. Seismic P-waves propagating <u>across</u> the open fractures may sense fracture porosity not sensed by the P-waves propagating in the direction <u>along</u> the open fractures.

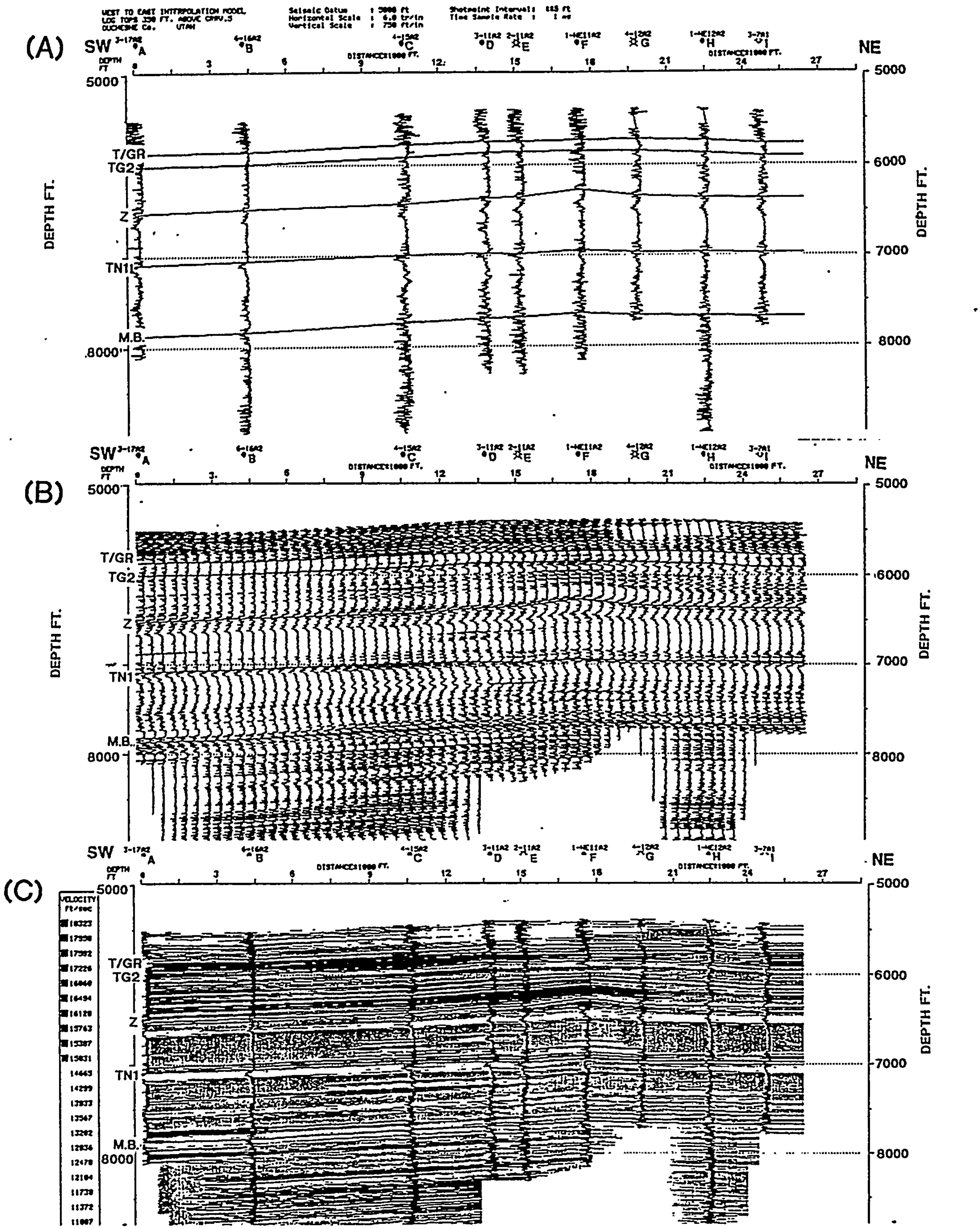

(A) NW-SE model, sonic log cross section (in depth) showing correlation upper Green River markers. T/Green River is top of high velocity unit. Z, TN1 and M.B. mark low-velocity formations.

(B) NW-SE model, interpolated sonic log section (in depth). Note abrupt change in sonic character at the T/Green River, and laterally consistent low-velocity characterizing Z, TN1 and M.B. markers.

(C) NW-SE model, sonic interval velocity section (in depth). Gradual decrease in interval velocity toward SE within T/GR-Z markers shows lithologic change basinward from sandier to shalier rocks. Between Z and TN1, sonic velocities increase basinward, possibly reflecting more carbonate deposition.

FIGURE 8-10

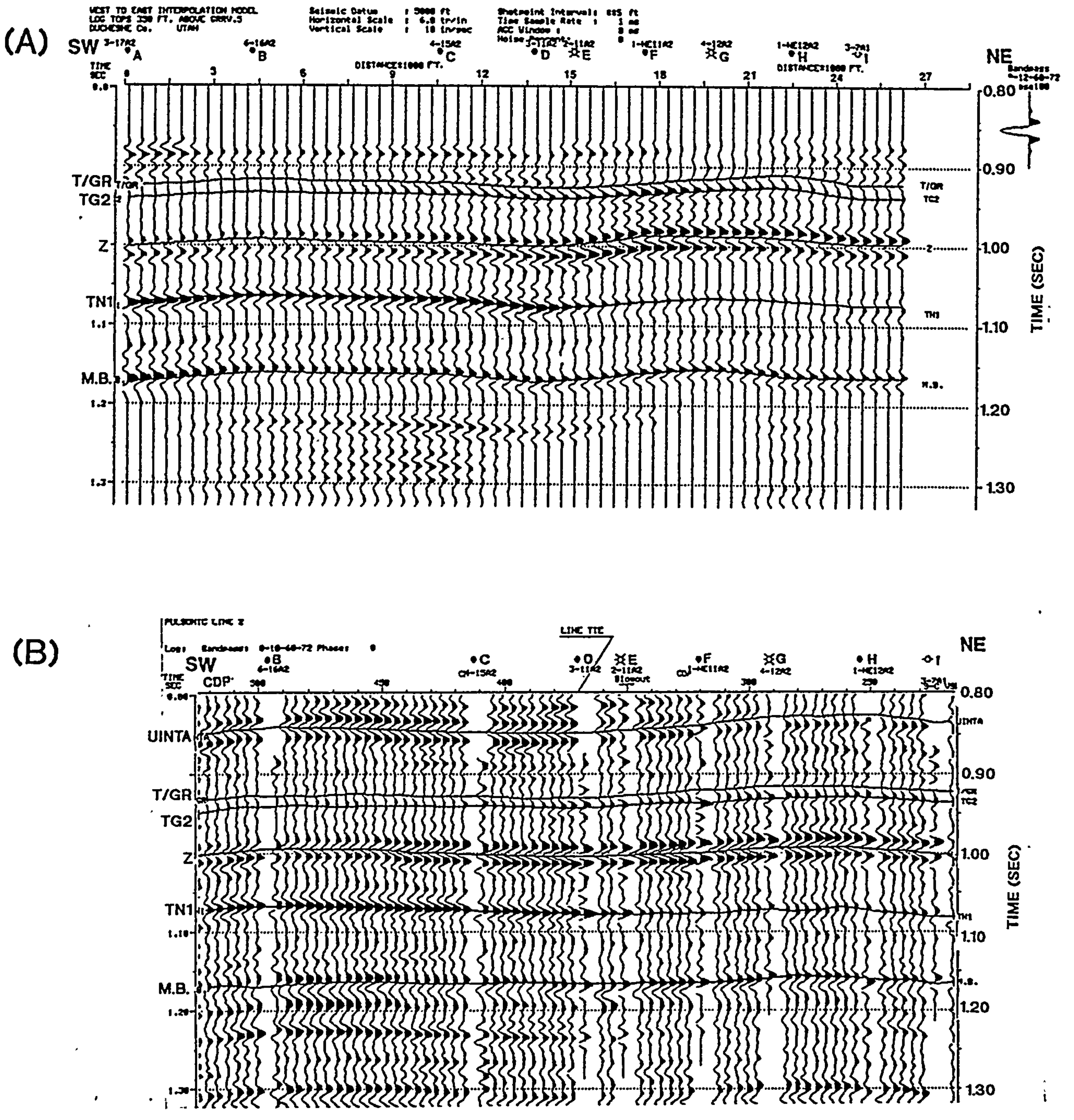

(A) NW-SE model, filtered reflection coefficient section (in time) shows lateral amplitude variations due to changes in stratigraphy.

(B) Field data for line 1 (migrated, near-offset stack) shows lateral amplitude changes similar to model data (upper).

FIGURE 8-11

8.2.4 Conclusions

In general, the match between the synthetic model data and the real seismic data along both Lines 1 and 2 is considered quite good. The P-wave near-offset migrated sections are not expected to show great differences from the model data, because the near traces have nearly vertical P-wave propagation and are not greatly influenced by vertical fractures. Therefore, it is necessary to analyze the far-offset P-wave data in order to detect seismic variations due to vertical fractures. The overall good match between the model and real seismic data facilitates the next phase of interpretation of the multi-component seismic data, that of the anisotropic effects produced by the vertical, aligned fractures. The value of the 2-D stratigraphic models is that they represent a "baseline case" showing principally stratigraphic variations. They were used to identify and interpret the main reflecting horizons on all components of the reflection seismic data.

8.3 S-wave Reflection Data

The final shear wave reflection sections were migrated Dip Moveout (DMO) sections, with source-receiver offsets limited to 6,000 ft. S-wave offsets to 10,000 ft were recorded, and some of the far-offsets contain reflection signal: however, in this study, only the near-vertical travel paths (offsets to 6,000 ft) were used to avoid complications associated with far offset data.. The same reflection events that were interpreted on the P-wave sections were interpreted on the S1 and S2 sections, in order to extract geologic meaning from the differences between the components, within a given stratigraphic interval. Reflection events on the S1 and S2 sections were identified by correlation with the events on the P-wave sections, which had been analyzed using 2-D modeling, discussed above, and by the S-wave corridor stacks (also discussed above). A shallow reflector within the Uinta formation (approx. 5,800 ft log depth) was also interpreted so as to include an interval above the T/UGR reservoir. Five P-wave reflectors bracketing the reservoir section were identified on the S-wave sections. S-wave travel times were picked manually to be consistent with P-wave ties.

Because even the thickest stacks of sands (~80 ft) in the Upper Green River are very thin with respect to seismic wavelengths (approx. 300-500 ft for P- and S-waves), we do not have discrete reflectors for individual sand units. Our seismic analysis is restricted to intervals larger than these wavelengths (see Table 8-4).

TABLE 8-4 Intervals Used for S-wave Anisotropy Measurements	
Interval	**Average Thickness**
Datum (5,000 ft ASL)-Uinta	5,755 ft
Uinta-T/UGR	800 ft
T/UGR-Z	590 ft
Z-Trona	590 ft
Trona-MB	730 ft

The analysis of the S-wave sections was based on interpretations of travel time anisotropy within the stratigraphic intervals between the mapped horizons. This travel time anisotropy is equivalent to the interval velocity anisotropy within the interval. It was computed as the difference in interval travel times between the S1 and S2 components, divided by the interval travel time of the S1 component, or (DtS2 - DtS1)/DtS1. This assumes that the interpreted horizons represent exactly the same stratigraphic events on the two components.

The travel time anisotropy is interpreted to be caused by the presence of vertically aligned fractures, striking in the direction of S1 and with fracture density approximately equal to the percent travel time anisotropy. Crampin (1994) has asserted that for fluid-filled cracks (water-filled), the split shear-wave velocity anisotropy is approximately equal to the crack density $\in$, defined as Na^3/v, where N is the number of cracks of radius *a* in volume v. This definition assumes that the seismic wavelengths are much larger than the crack dimensions.

The disadvantage of this analysis technique is that it is performed on time intervals rather than on discrete reflections, and, therefore, there is an associated reduction in resolution as compared with analysis techniques which rely on direct measurements of seismic attributes. However, the advantages of the travel time anisotropy technique are that the reflection time measurements are precise but the exact velocities do not have to be known. The only assumption is that of exactly equivalent stratigraphic intervals being compared on S1 and S2. Therefore, the technique is more robust.

In general, the very good data quality of both the P-wave and the S-wave sections resulted in straightforward identification of marker horizons and correlation between the 3 components of the seismic data. The seismic character ties are shown at locations corresponding to selected wells along each line, in Figures 8-13 through 8-20. For each well location discussed, there is a display showing the character correlation of the S1 to P to S2 components, and a display showing the S1 to S2 correlation. These Figures are included to show that the assumption of correlation of the same stratigraphic intervals on the P-wave and the two S-wave sections is satisfied. Figures 8-21 and 8-22 show the tie between the same shear wave component for the two lines, at the line intersection. Reference should be made to Figure 8-12 for the map locations of these correlation displays. In addition, Figures 8-23 and 8-24 show the shear wave anisotropy graphically for each stratigraphic interval along the lines. The interpretation at each well location along the lines is discussed below and presented in Tables 8-5a and 8-5b at the end of the Section 8. Finally, the two maps in Figures 8-49 and 8-50 show the combined interpretation of P-wave AVO anomalies and S-wave anisotropy for the two Upper Green River intervals, T/UGR-Z and Z-TN1.

8.3.1 Well B2 (Line 2)

At the location of Well B2, Figure 8-13a shows a good correlation between the S-wave and the P sections for each marked event, although differences in frequency content between P and S-wave sections are apparent, especially at the Z and the T/UGR markers. The S1-S2 correlation (Figure 8-13b) shows increased travel time within the T/UGR-Z interval on the S2 section, indicating velocity anisotropy between the two shear waves over this interval. The seismic picks at this location are considered very good, and interpretation here can be made with confidence. Although the velocity anisotropy suggests significant fracturing at this location (15 percent fracture density; see Figure 8-23), the P-wave AVO did not show a gas response here (refer to Figure 8-46). Therefore, it is concluded that there are NW-trending fractures in the T/UGR-Z reservoir interval, but they are <u>not</u> gas-filled. There were no shows of gas in the Upper Green River in this well, which was drilled for deeper Wasatch oil pay. S-wave travel times were picked manually to be consistent with P-wave ties.

8.3.2 Well D (Line 2)

At the location of Well D which is also the line intersection, on Line 2, Figure 8-14a shows that the 5 marker horizons are identifiable on the 3 components S1-P-S2, but there are significant amplitude variations between the components. Of particular interest is the Z marker, which has very high amplitude on the P-wave section, lower amplitude on S1, and very low amplitude on S2. This dimming of the reflector on S2 is interpreted as an indication of the lower S2 velocity at the Z marker caused by dense fracturing. This phenomenon has been documented by Mueller (1991) in the Austin Chalk, where high fracture density zones were linked with oil production. The upper peak of the Z marker is the seismic event showing a large P-wave AVO anomaly, discussed in the next section. This upper Z peak on the P-wave section is due to a 55 foot-thick low-impedance clastic layer, which is too thin to be fully resolved by the S-wave data. (The S-wave data at this depth have a vertical limit of resolution of about 100 ft bed thickness). The coincidence of the P-wave AVO anomaly, which responds to a lowered Poisson's ratio (often associated with gas) in the medium below the reflector, and the S-wave amplitude anomaly at this location, suggest both dense

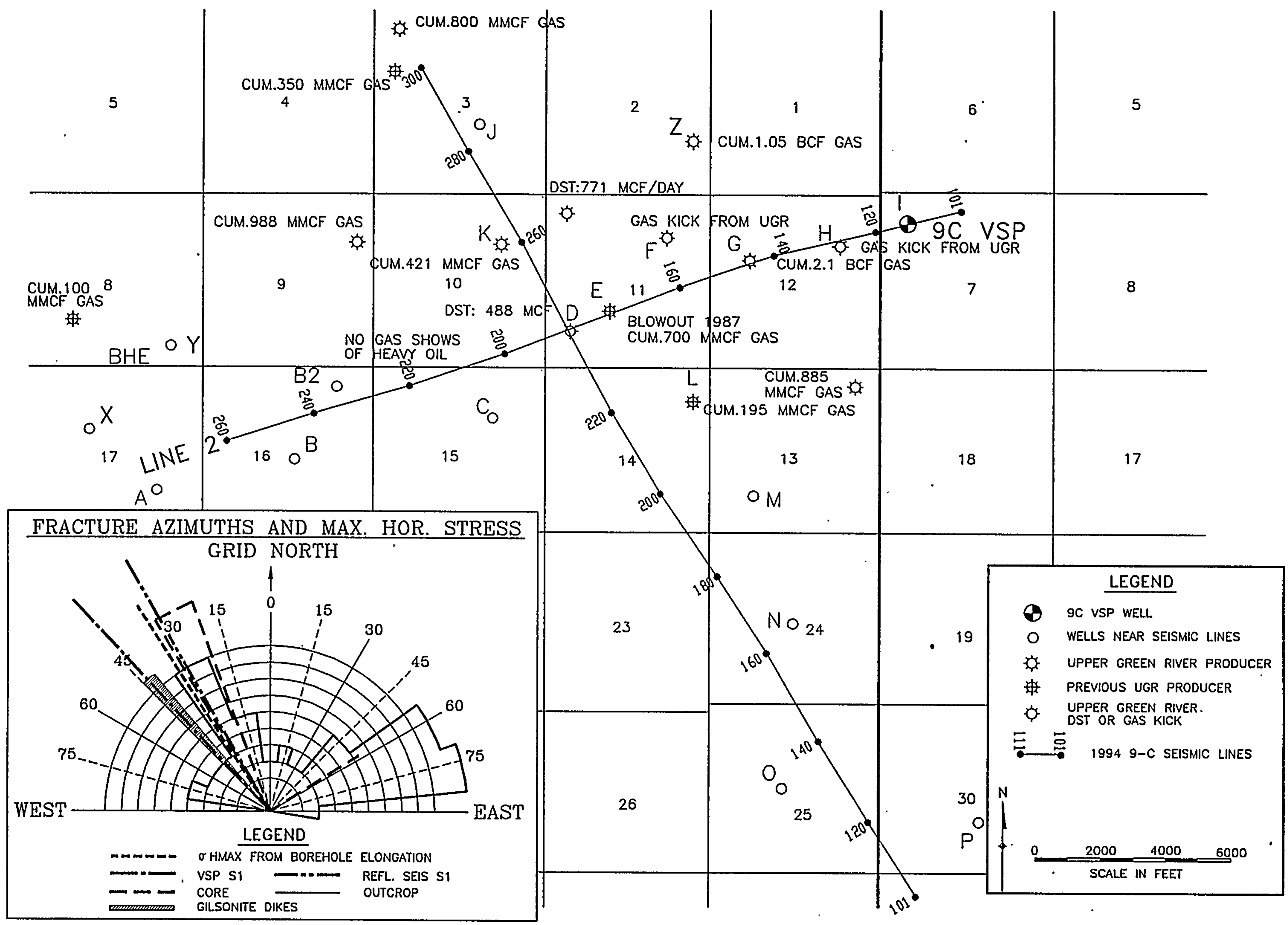

Seismic basemap showing locations of wells near seismic lines used to calibrate S-wave anisotropy to known geology and Upper Green River gas production.

FIGURE 8-12

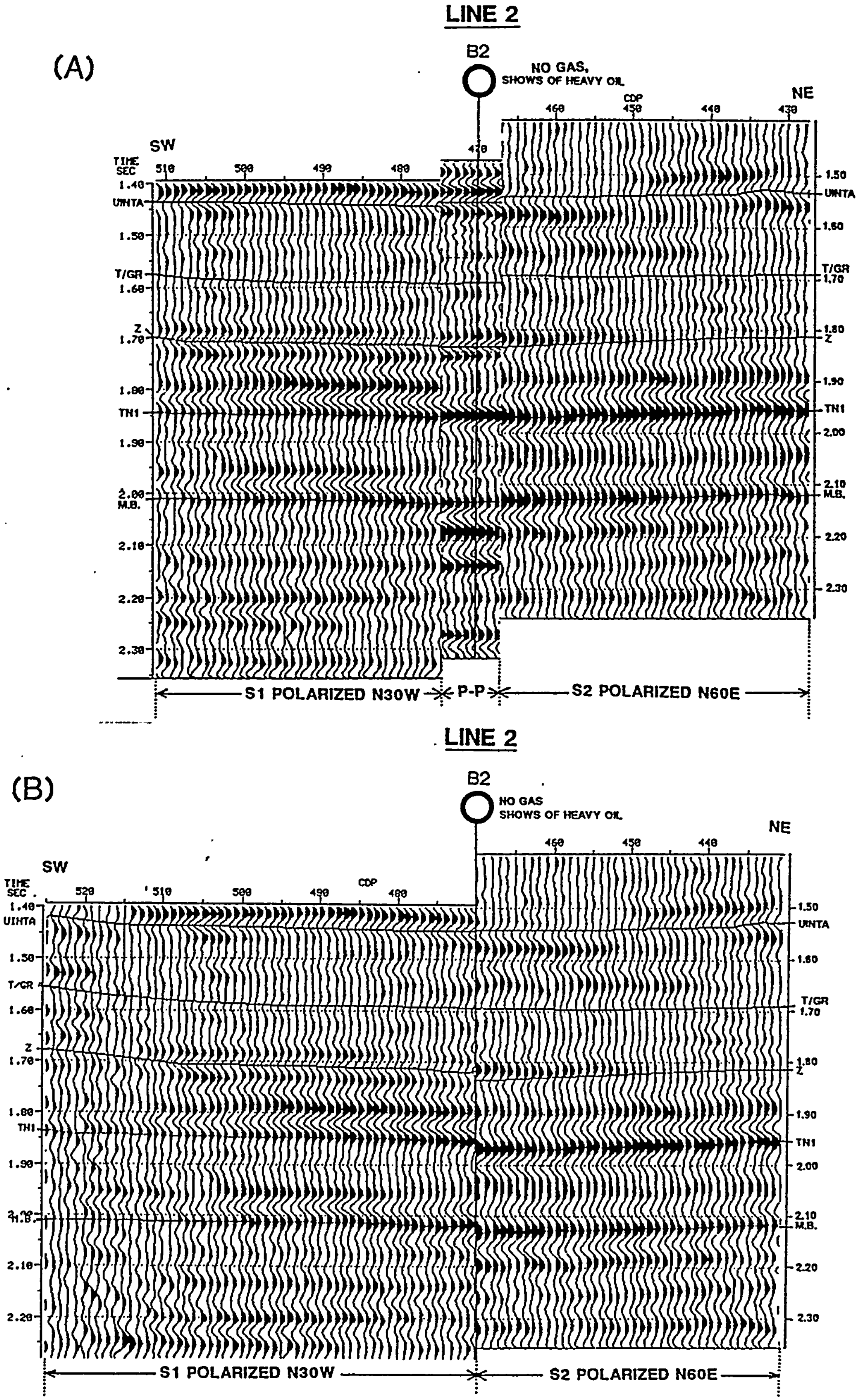

(A) S1-P-S2 composite section Line 2, centered at well **B2**, showing correlation of 3 marked horizons on the 3 seismic components.

(B) Line 2, well **B2** location: correlation between S1 and S2 sections. Increased travel time through T/GR-Z interval S2 indicates NW-trending fractures in this interval.

FIGURE 8-13

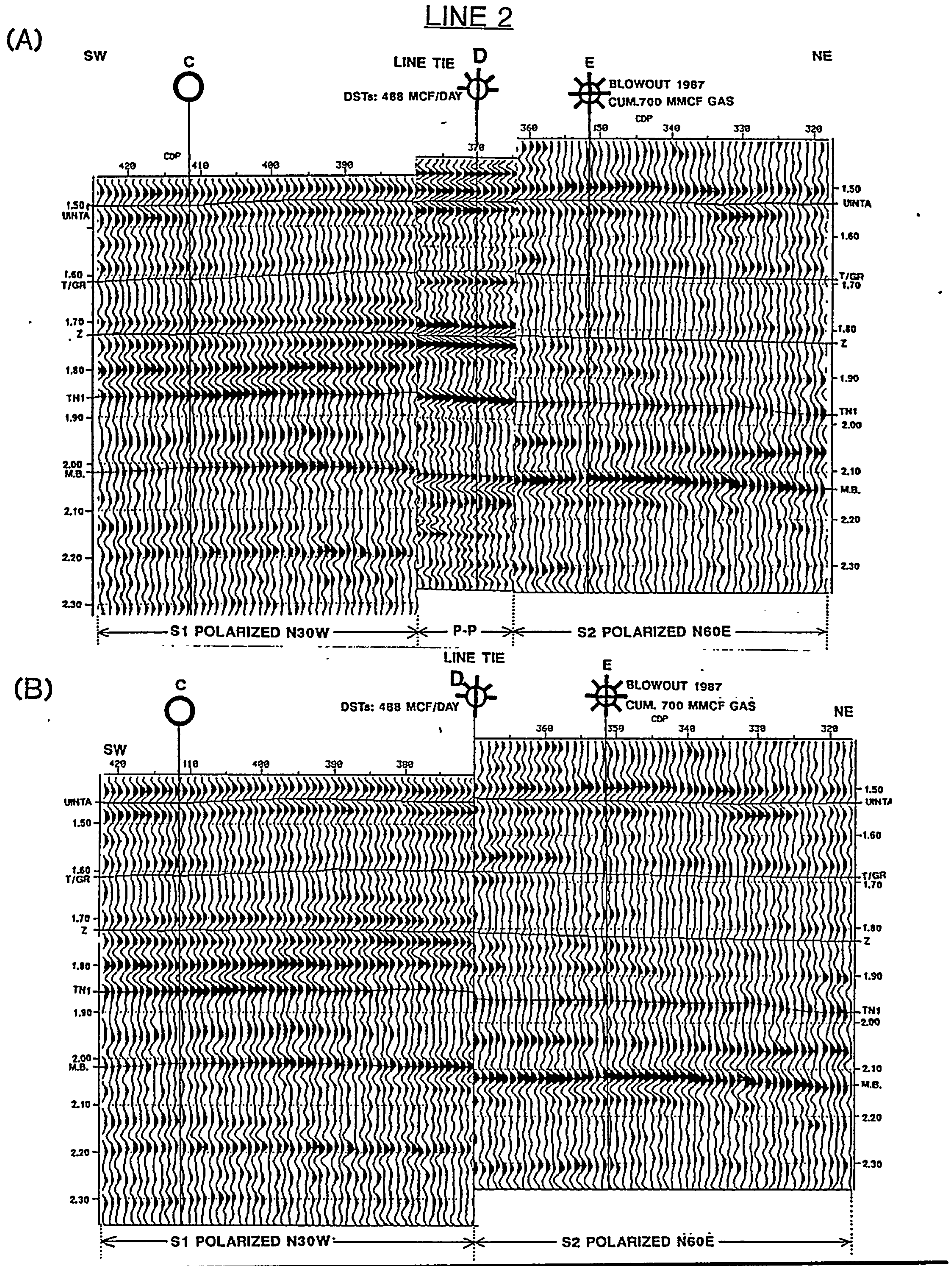

(A) S1-P-S2 composite section Line 2, centered at well **D** (line tie), shows consistency of siesmic character on 3 components.

(B) S1-S2 correlation at line 2, well **D** (line tie). Amplitude dimming on S2 at Z marker and increased S2 travel time through Z-TN1 interval indicate NW-trending fractures within Z-TN1.

FIGURE 8-14

fracturing and gas saturation within the Z-TN1 interval. In addition, there is an anomalously high degree of S-wave velocity anisotropy (14%) in the interval Z-TN1, as evidenced by the increased S2 travel time in that interval (Figure 8-14b). The anomalous positive S-wave anisotropy is also evident in Figure 8-24, (S-wave anisotropy, Line 2, Z-Trona interval), indicating a high density of NW-trending fractures within the interval Z-TN1.

There were two drill stem tests (DST) which flowed gas in the uppermost Green River, within the T/UGR-Z interval. The seismic events corresponding to these DST'd intervals showed a P-wave AVO response suggesting gas saturation, but the S-wave data do not show velocity anisotropy within the T/UGR-Z interval. There are two possible explanations to fit these observations: either the gas which flowed on test came from matrix porosity (and thus also azimuthally isotropic rock), or there could be open fractures in both NW and NE trends (and thus azimuthally isotropic rock). The core analysis performed on Wells D, X, and Z concluded that the T/UGR reservoirs in these wells are not highly fractured. Therefore, the gas in matrix porosity is considered the most likely explanation of the concurrence of a P-wave AVO gas response and negligible S-wave anisotropy at the T/UGR.

8.3.3 Well E (Line 2)

Well E is located on Line 2, approximately 1,350 ft east-northeast of the tie point. The S1-P-S2 display, Figure 8-15a, shows that the marker horizons can be correlated with confidence on all three sections. The S1-S2 display (Figure 8-15b) shows that there are character changes between the S1 and S2 sections which are significant in light of the well's production history. This well can be considered the gas discovery well in the field, when it blew out in 1987. Prior to the blowout, unassociated gas had not been produced from the Upper Green River. The exact interval that blew out is not known, but it is thought to be between the T/UGR and the Z markers. Figure 8-15 shows the character changes between S1 and S2 within the interval from T/UGR to the Z marker which includes dimming/polarity reversal at the T/UGR through the next sequence of events, and dimming and diminished frequency at the Z. The S1 section can be considered as representing the seismic response of the closed fractures or unfractured matrix rock; the very different appearance of the S2 section at this well location is interpreted by the presence of fractures within this Upper Green River interval. Velocity anisotropy of 6%, indicating NW-trending fractures, is observed in the T/UGR-Z interval. Since there are several reflectors showing significant amplitude variations between S1 and S2 in the interval between the T/UGR and the Z markers, it is inferred that there are several zones of fracturing at this location.

There is also velocity anisotropy in the Z-TN1 interval, of 4%. The strong P-wave AVO anomaly at the Z reflector extends from Well D to this well, a distance of 1,300 ft. From the seismic evidence, it is postulated that the blowout may

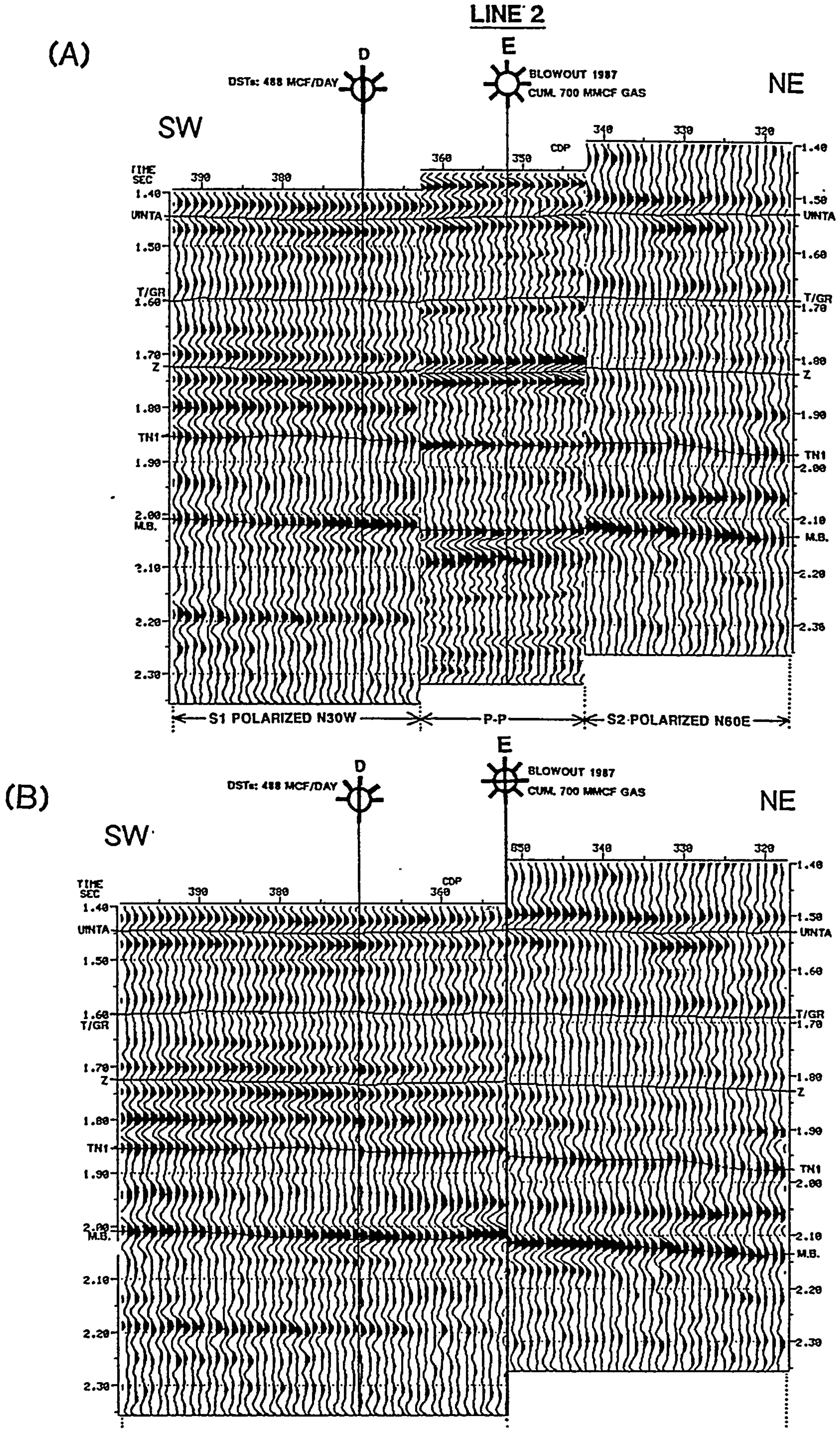

(A) S1-P-S2 composite section Line 2, centered at well E.

(B) Line 2: S1-S2 sections spliced together at well E. Note dimming of T/GR reflection on S2 and loss of higher frequencies on S2 between T/GR and Z markers. Velocity anisotropy suggesting NW fracturing is observed within T/GR-Z and Z-TN1 intervals.

FIGURE 8–15

have occurred from the upper Z peak (within the Green River TGM.7 interval at about 7,120 ft log depth). Inspection of Figure 8-24 (S-wave anisotropy, Line 2 Z-TN1 interval) reveals that the positive S-wave anisotropy falls off rapidly from Well D toward Well E. This is interpreted as a possible indication of pressure relief at the E location. The P-wave AVO anomaly is present as a positive AVO gradient at the two well locations, suggesting gas saturation at both locations (refer to Figure 8-41), but the S-wave anisotropy (Figure 8-24) is diminished at Well E (+4%) from Well D (+14%). The following interpretation is suggested: Open, gas-filled NW-trending fractures within the Z peak interval (base GRTGM.7) existed in a lateral zone encompassing both Wells D and E before 1987 when the well blew out. Once the high pore-fluid pressure associated with the gas saturation was decreased by the blowout, the open NW fractures have begun to close. This infers that high- pressure gas saturation helps to hold the fractures open. P-wave AVO cannot distinguish between a few percent and very high gas saturation, since the drop in P-wave velocity and Poisson's ratio, responsible for the AVO gas response, occurs with the few percent gas saturation. Therefore, the combined P-wave AVO anomaly and S-wave anisotropy variations along Line 2 from Well D to Well E are interpreted as indicating high gas saturation in the Z peak marker within an increased fracture density zone at the D well, and lower gas saturation due to a lower NW-trending open fracture density at the E well.

8.3.4 Well G (Line 2)

Well G, located at SP 145.5 on Line 2, has produced 2.1 BCF of gas from two intervals in the uppermost Green River. Figure 8-16a shows the S1-P-S2 character ties at this location, and figure 8-16b shows the S1-S2 correlation, aligned at the T/UGR marker. An increase in interval time from T/UGR to Z with coincident amplitude dimming at the T/UGR reflection is seen on the S2 section. The T/UGR-Z interval time difference of 7 msec. between S1 and S2 is equivalent to 5.5 percent azimuthal anisotropy, with NW polarized S1, or along fracture strike direction. Figure 8-24 shows a slightly higher value for the S-wave anisotropy). The P-wave AVO response at the T/UGR reflector at this well location is a positive AVO gradient (see Figure 8-34), which is predicted by theory and modeling for a shale/gas sand interface.

8.3.5 Well H (Line 2)

The data quality at the Well H location suffers from noise, but Figure 8-17a shows the S1-P-S2 section, where it is possible to correlate the marker horizons. Figure 8-17b, the S1-S2 display, shows a large travel time increase in the T/UGR-Z interval on S2, equivalent to 16 percent (+/- 3 percent) azimuthal anisotropy, among the highest amount of anisotropy observed in any interval in this study. Despite the noisy data quality, the interpretation of anomalous anisotropy within the T/UGR-Z interval at this location is considered valid. The

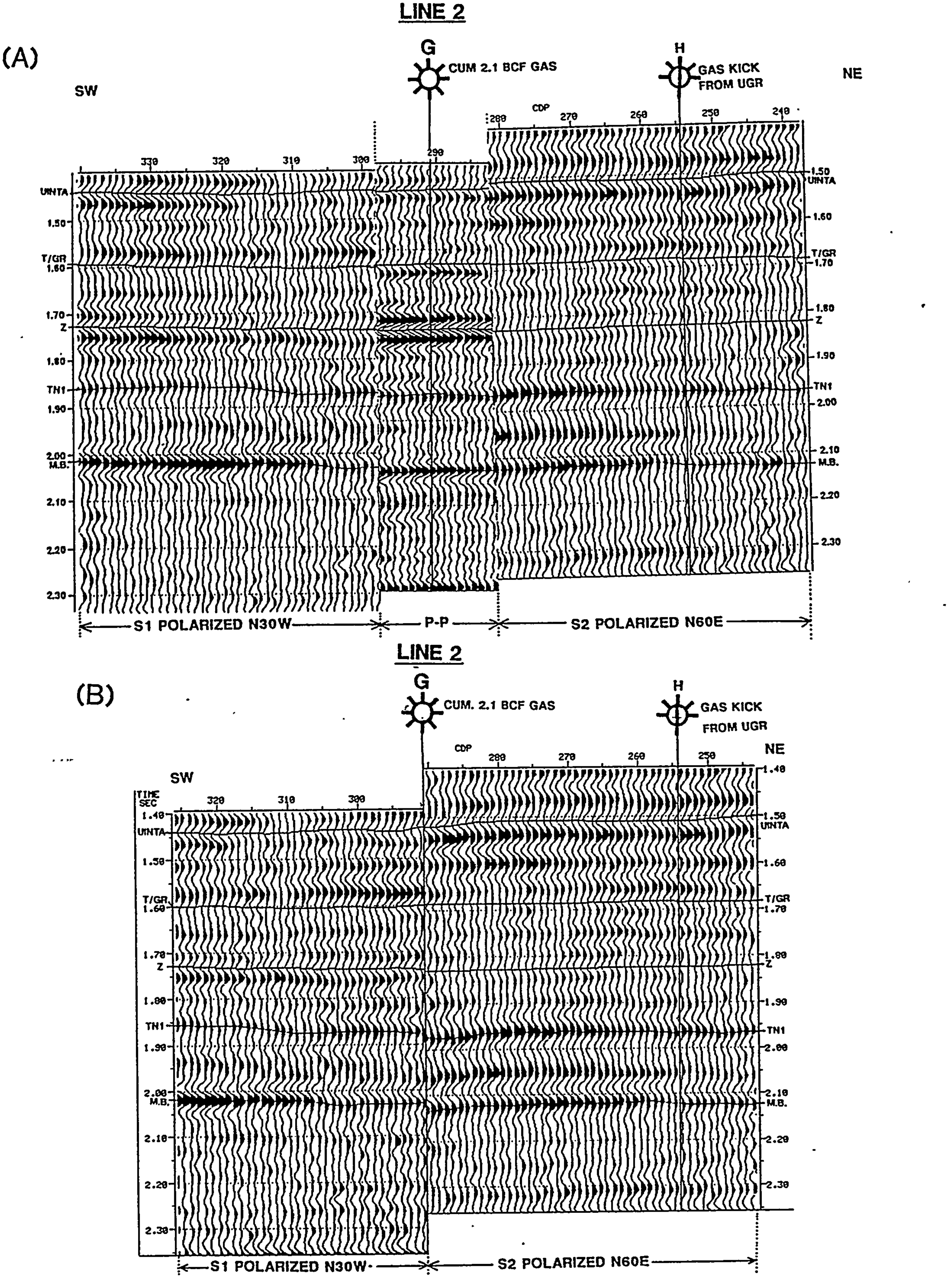

(A) S1-P-S2 composite section Line 2, centered at well **G**.

(B) S1-S2 correlation at Line 2, well **G**, showing S2 increased travel time in T/GR-Z interval. Cause of dimming of T/GR reflection on S2 interpreted as S2 velocity reduction due to fracturing within T/GR-Z.

FIGURE 8-16

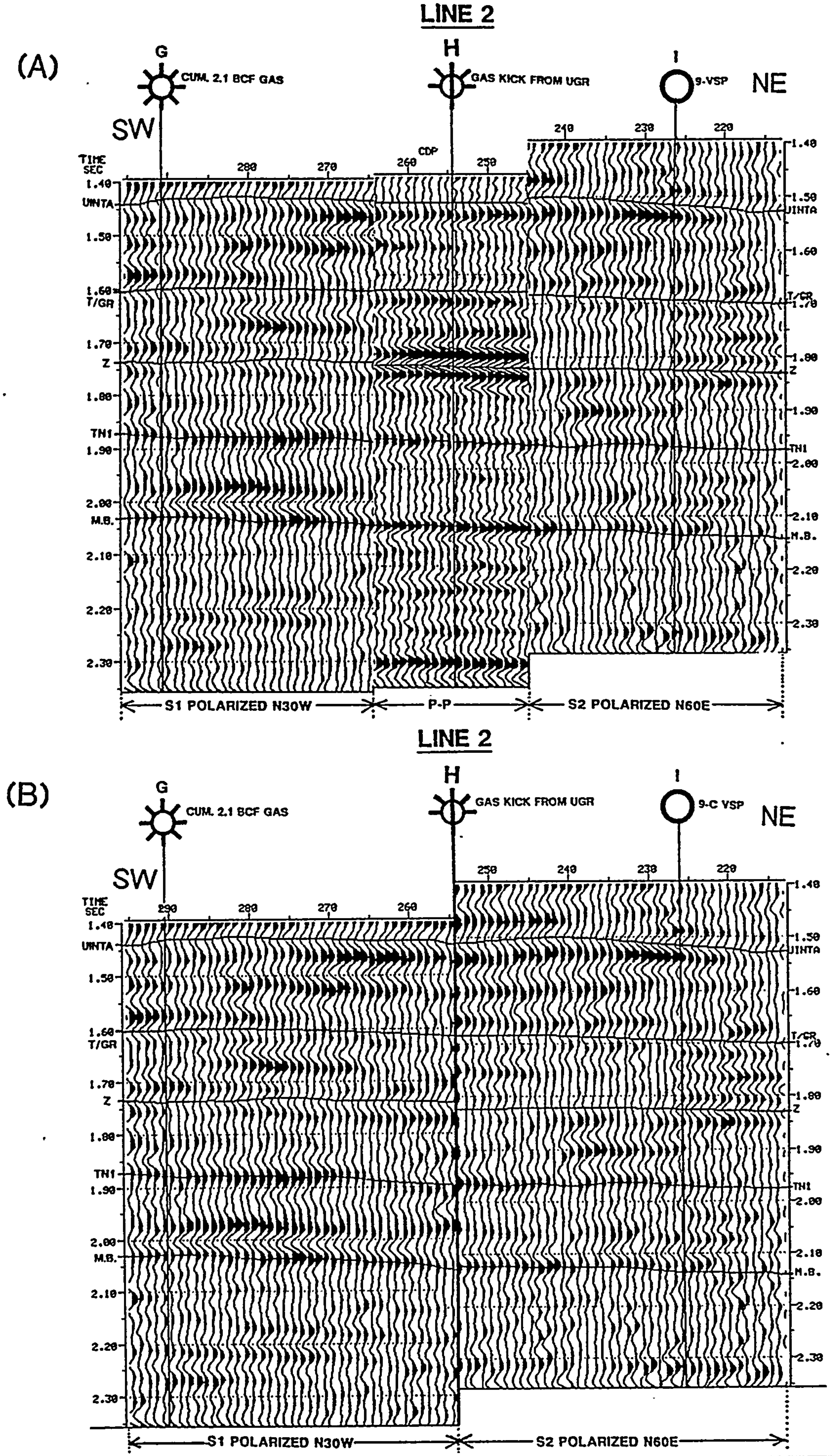

(A) S1-P-S2 composite section Line 2, centered at well H.

(B) Line 2: S1-S2 sections spliced at well H location. Anomalously high S-wave anisotropy, indicative of increased NW-trending fracture density within T/GR-Z interval evidenced by increased S2 travel time.

FIGURE 8-17

anisotropy represents a fracture density of 13 to 19 percent within the interval T/UGR-Z. This is also the location of positive P-wave AVO anomalies at both the T/UGR and the second shale/sand interface below the T/UGR suggesting the presence of gas in the northwest-trending fractures between the T/UGR and Z horizons. The well was not tested in the Upper Green River, although the mud log recorded several gas "kicks" during drilling of the well.

8.3.6 Well I (Line 2)

Well I, the nine-component VSP, is located very near the northeast end of Line 2. The stacked S-wave components at the end of the line are reduced to 10 to 12 fold, which lowers the signal/noise ratio. Interpretation of the marker horizons here is questionable due to the poor data quality. The shear wave data recorded in the VSP at this location, however, are of excellent quality, and, therefore, more confidence is placed in the interpretation of the shear wave data in the VSP than in the surface reflection seismic at this location. Consequently, the reader is referred to the Section 8-1.

8.3.7 Well K (Line 1)

The character correlation between S1-P-S2 at Well K (Line 1 SP 261) is shown in Figure 8-18a. Figure 8-18b, the S1-S2 tie at this location, shows an incremental time difference beginning with the T/UGR-Z interval, clearly establishing the S1 or NW-polarized section as the faster-traveling polarization.

This well has produced a cumulative total of 421 MMCF gas from the uppermost Green River (between the T/UGR and Z markers). The shear velocity anisotropy (+7%) within the T/UGR-Z interval indicates that the open fractures trend NW here. We interpret that the produced gas came from the NW-trending fractures. The S-wave anisotropy in this interval increases to a maximum of +13 % at CDP 506, 1,300 ft southeast of Well K (Figure 8-23), suggesting additional potential for fractured gas production. It is observed that the two Upper Green River gas producing wells which lie close to the seismic lines, Wells G on Line 2 and Well K on Line 1, both exhibit positive anisotropy. This suggests that NW-trending fractures are more likely to contain producible gas, than the orthogonal NE trending fractures. No producing well had S-wave anisotropy indicating NE-trending cracks. Positive S-wave anisotropy, implying NW-trending fractures, also implies that P-wave AVO will be ineffective on Line 1, which has source-receivers aligned NW. Therefore, it is not possible to make an interpretation of the fluid within S-wave interpreted NW fractures on Line 1, except at well locations where it is known from production data.

8.3.8 Well D (Line 1)

The S-wave interpretation at Well D at the line tie on Line 1, is shown in Figures 8-19a and b which can be compared to the same well location on Line 2 (Figures

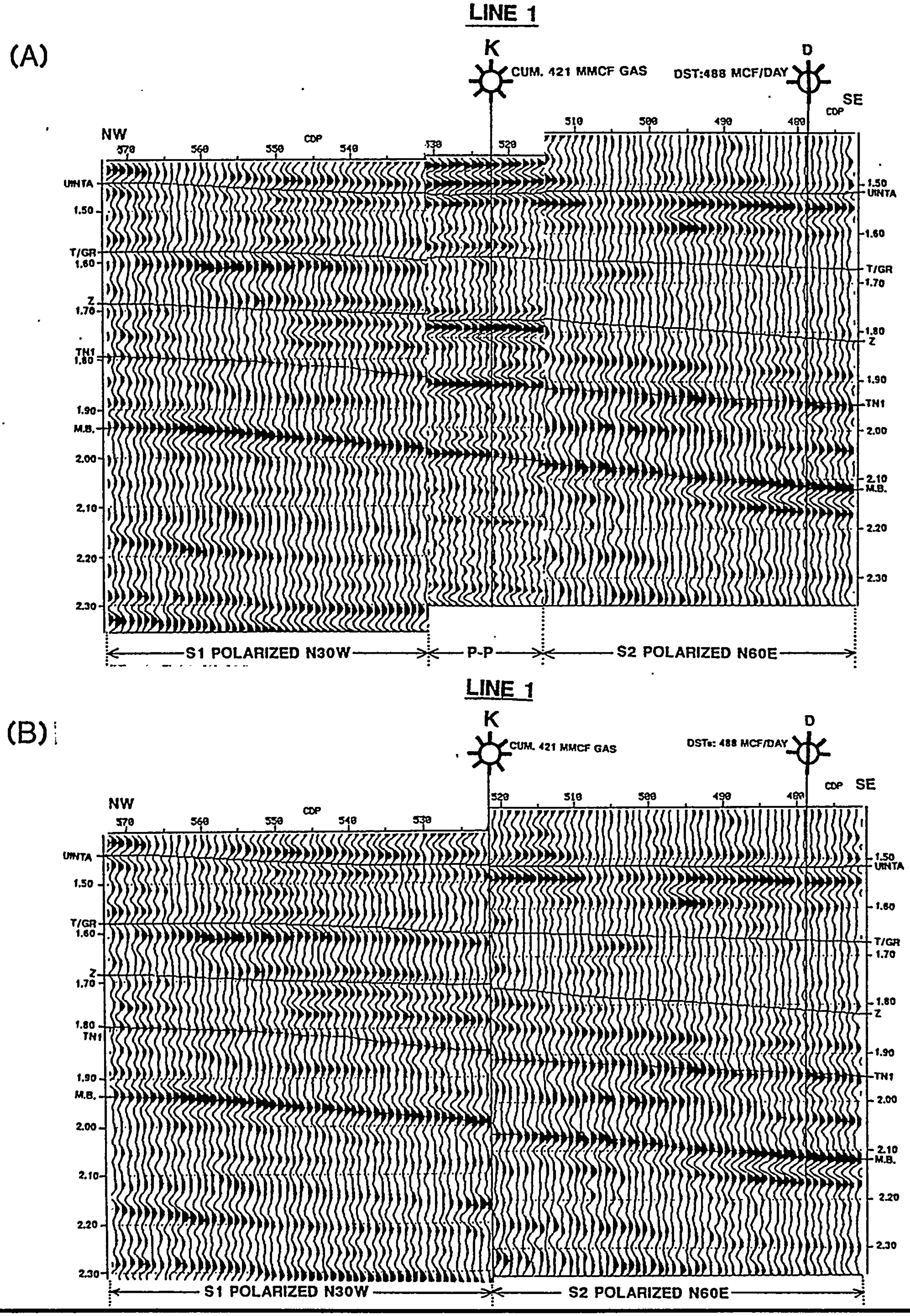

(A) S1-P-S2 composite section Line 1, centered at well K.

(B) Line 1: S1-S2 sections spliced at well K location showing increased S2 travel time within T/GR-Z interval. Incremental time difference continues to M.B. marker, indicating NW cracks are present throughout upper Green River section. Gas production from T/GR-z interval.

FIGURE 8-18

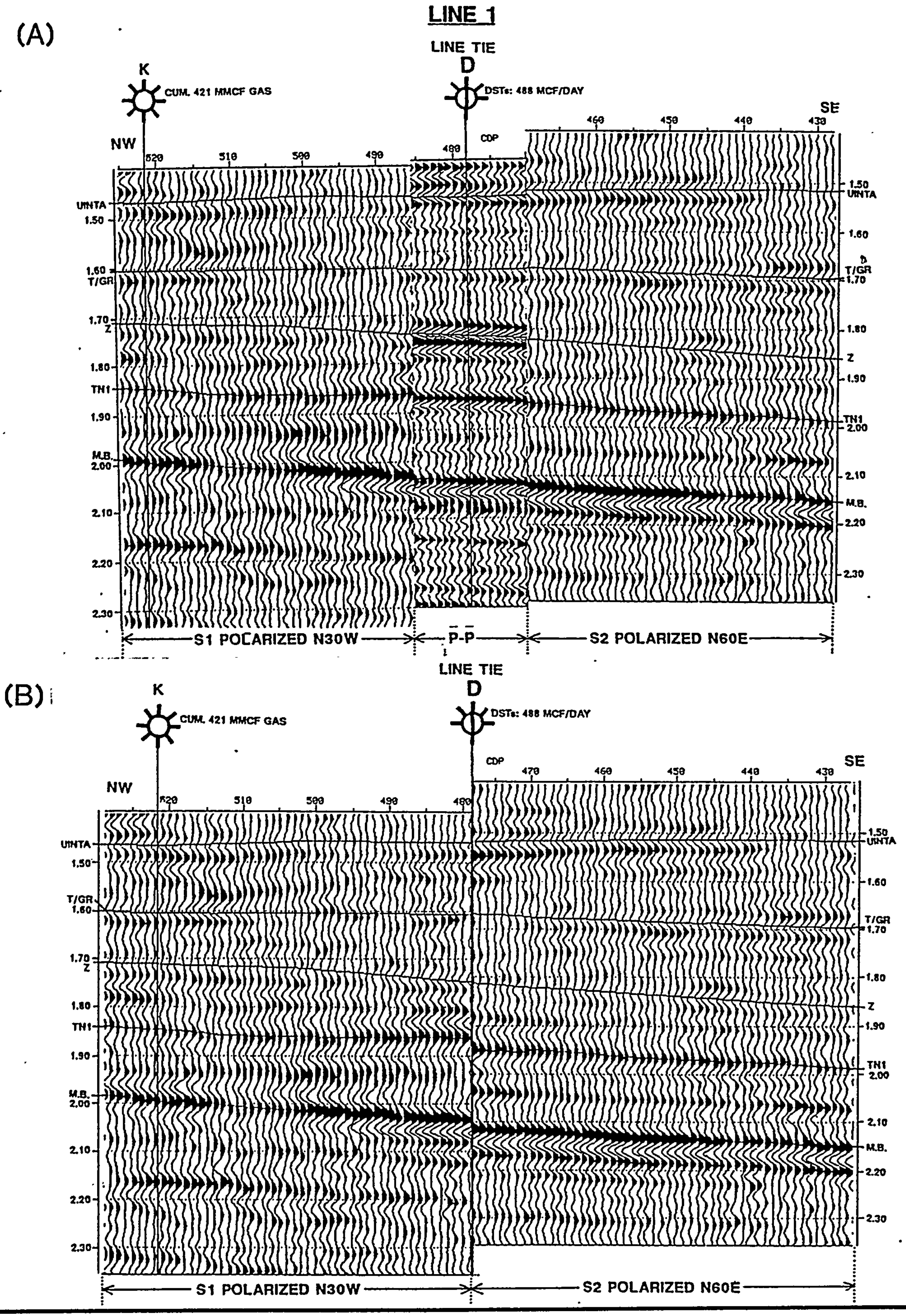

(A) S1-P-S2 composite section Line 1, centered at well **D** (line tie).

(B) Line 1: S1-S2 sections spliced at well **D** (line tie) showing anomalously high S-wave anisotropy in Z-TN1 interval. Amplitude change of Z marker on S2 interpreted as effect of NW-trending fractures at top Z-TN1 interval.

FIGURE 8-19

8-13a and b). On Line 1, the character ties are very similar to those on Line 2, with the very apparent decrease in S2 amplitude at the Z marker perhaps better seen on Line 2 than on Line 1. The velocity anisotropy is very low (3%) from the Uinta to Z markers, and is anomalously high (12%) from Z-TN1 as seen by the increase in S2 time in that interval, again suggesting that the gas response at the Z peak which is seen only on Line 2 on the P-wave AVO section (Figure 8-41) at this location is due to open, gas-filled, NW-trending fractures.

8.3.9 Well N (Line 1)

Well N is located in a downdip position at S.P. 162 on Line 1. It is included in order to compare the response of a non-producer to a gas producer on Line 1. The data at this location show a change in the average VP/VS ratio to 1.94. In order to accommodate this ratio, Figures 8-20a and b are plotted at 5.15 inches per second. The increase in average VP/VS ratio is interpreted to be caused by an increased proportion of shale to sand in this stratigraphically basinward position. Figure 8-20a shows that the MB marker has a very consistent seismic character on all three components, but the shallower markers can not be traced across the composite section. This is interpreted to be due partly to the change in frequency content (loss of high frequencies) on the S-wave sections compared to the P-wave section, and partly to the VP/VS ratio changing with depth, which causes differences in the time intervals between the S-wave and P-wave sections.

The S1-S2 correlation in Figure 8-20b shows increased travel time on S2 within the Z-TN1 interval, interpreted as NW-trending fractures with fracture density estimated at 7 percent. The amplitude of the Z reflector package on S2 appears to be diminished, indicating a decrease in velocity associated with the fractures. There is no P-wave AVO anomaly at this location which would indicate a potential for gas fill in the fractures. Based on the seismic data shown and the downdip structural position of this well at the T/UGR level, it is postulated that there are NW-trending open fractures that are water filled. The well was drilled for deeper oil pay.

8.3.10 Post-Rotation S-wave Component ties: Reflection Amplitudes

The stacked migrated shear wave amplitudes at the tie point for the two lines were compared. The relative differences between S1 and S2 on Line 1 were not present on Line 2. For example, at the Uinta (the first mappable reflector, above the target) the following anomalies were observed:

Line 2	S1 (SH): brighter	S2 (SV): dimmer
Line 1	S1 (SV): dimmer	S2 (SH): brighter

These relationships can be seen in Figures 8-21 through 8-22. The reflection coefficient series for S1 and S2, as determined by the column of rock within the

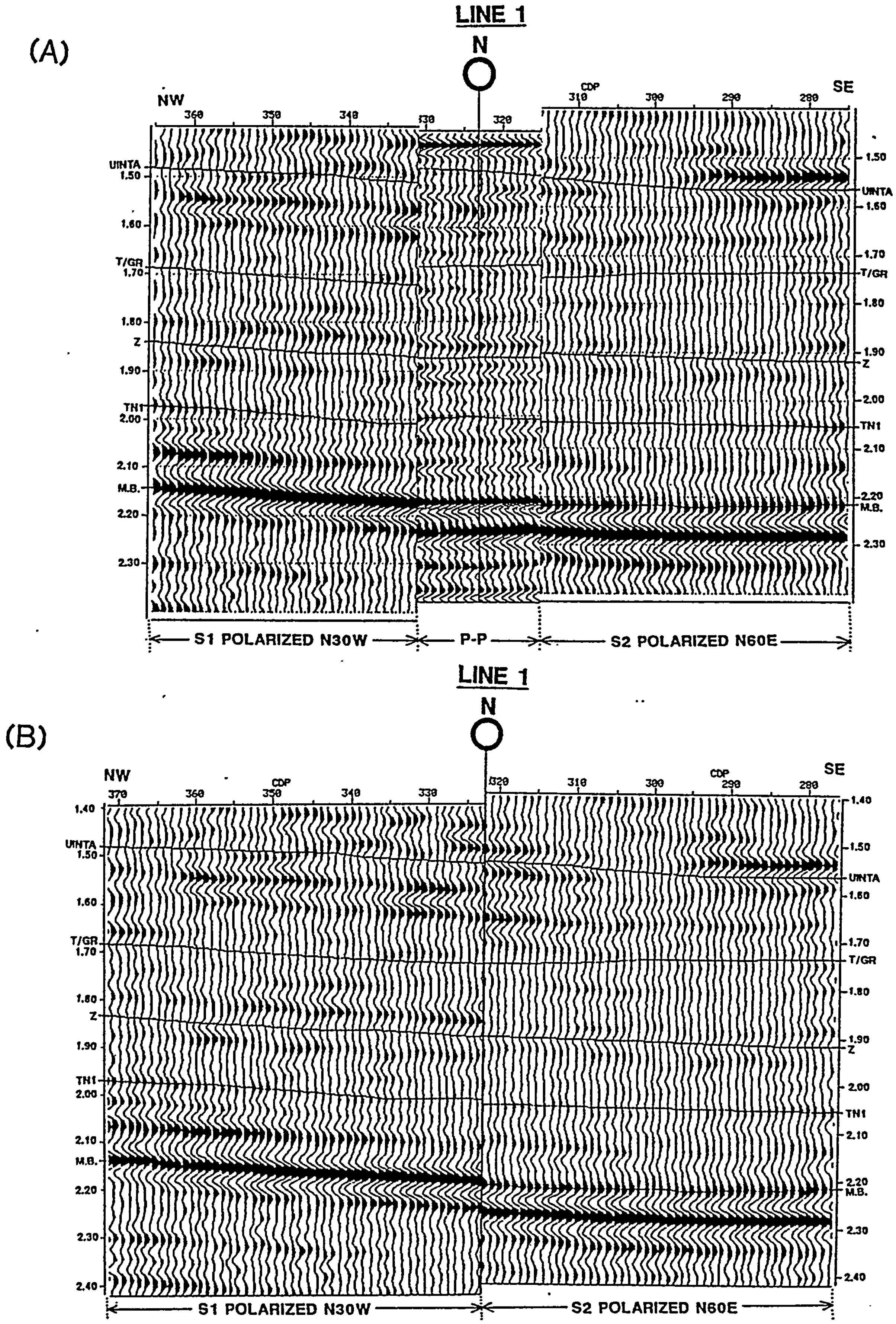

(A) Line 1 composite S1-P-S2 section centered at well N, showing low-frequency M.B. event has consistent character but shallow higher-frequency events show marked character changes. Variation in VP/VS ratio successive intervals cause apparent miscorrelation of time picks.

(B) Line 1: S1-S2 sections spliced at well N location. S-wave anisotropy in Z-TN1 interval apparent from increased S2 time and S2 dimming of Z amplitude.

FIGURE 8-20

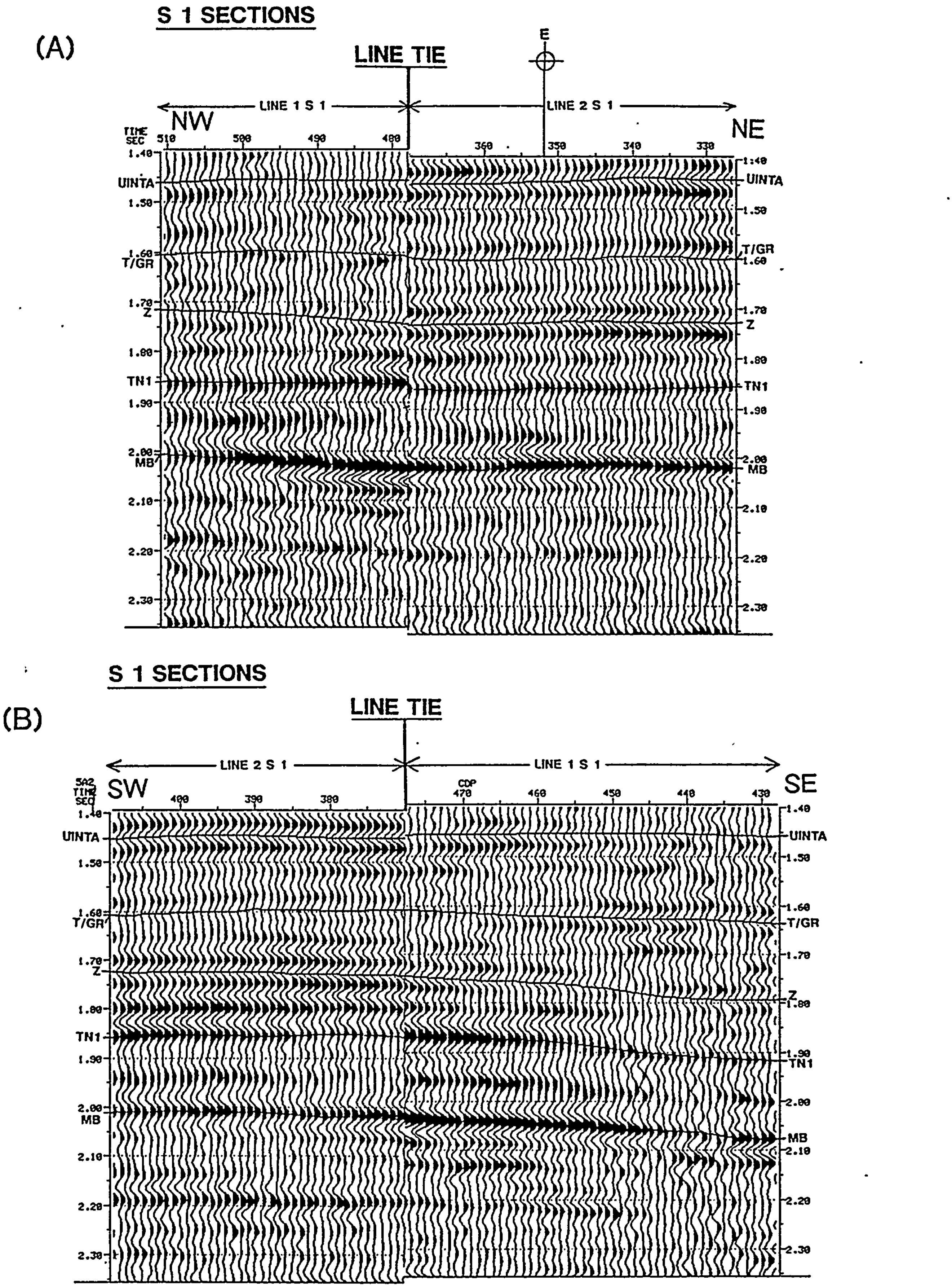

(A) S1 sections for Line 1 (left) and Line 2 (right) spliced at line tie, show difference in amplitudes of T/GR and Z events attributed to SH and SV (source and receiver polarization) considerations.
(B) S1 sections for Line 2 (left) and Line 1 (right) spliced at line tie, show difference in amplitudes of T/GR and Z events attributed to SH and SV (source and receiver polarization) considerations.

FIGURE 8-21

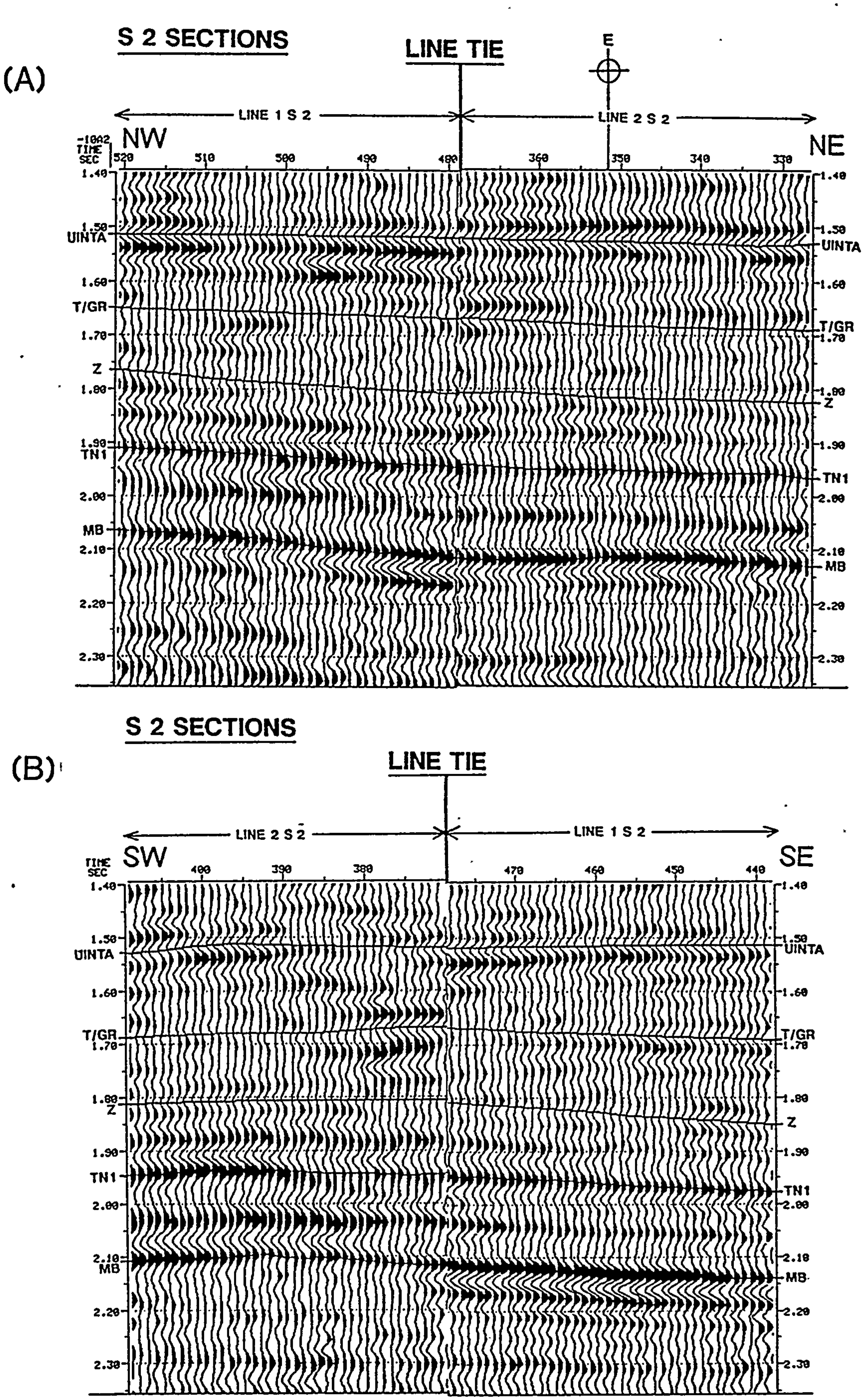

(A) S2 sections for Line 1 (left) and Line 2 (right) spliced at line tie, amplitude differences are less apparent on S2 sections than on S1 sections.

(B) S2 sections for Line 2 (left) and Line 1 (right) spliced at line tie, amplitude differences are less apparent on S2 sections than on S1 sections.

FIGURE 8–22

Fresnel zone, is line-independent. However, other factors are also dependent on line direction. For example, the transmission effects, the near-surface effects, and the source-generated noise. In particular, crossline (SH) field acquisition is well-known to yield better S/N data than inline (SV) field acquisition. This is partly due to the loss of shear-wave energy from mode-conversion that SV undergoes. Moreover, the source-generated noise is different for SH than for SV.

The nearly pure-mode recording of the shear wave surface reflection lines could place a bias on the interpretation of S1 and S2 amplitudes because of the differences between SH and SV recording. Most SH wave data have better S/N than most SV wave data, due to the nature of the source-generated coherent noise on the field records. However, the nearly pure-mode recording was required to render the P-wave AVO analysis interpretable, and the P-wave AVO was considered more important to the overall project than the shear wave amplitudes. The shear wave amplitude variations, therefore, warrant further study beyond the scope of this project.

8.3.11 S-wave Anisotropy Graphs

On the S-wave anisotropy graphs, Figures 8-23 through 8-24, positive anisotropy indicates that the S1 or N30W-polarized wave is the first-arriving shear wave component. Positive S-wave anisotropy suggests the presence of NW-trending fractures, with an average fracture density approximately equal to the percentage of anisotropy. Negative anisotropy indicates that the S1 or N30W-polarized wave arrives later in time than the S2 or N60E-polarized wave, suggesting a NE trend of open cracks with fracture density equivalent to the percentage anisotropy. The crack density is defined (Crampin, 1984) to be Na^3/v,

where N = the number of cracks of radius *a* in volume v

The S-wave anisotropy within the Upper Green River section varied from -10 percent to +19 percent. This degree of lateral variation is not uncommon in shear wave studies. The reversals in the sign of the anisotropy can be due to many factors or combinations of factors, including changes in the stress field and/or pore geometry or open fracture azimuth at depth and/or stress field.

For all of the S-wave anisotropy graphs, the uncertainty in picking the time is estimated at +/- 2 msec. for S1 and S2 individually, or +/- 3% for anisotropy within the Uinta-MB intervals. In the datum-Uinta interval, the maximum cumulative error, with the same time picking uncertainty of +/- 2 msec, is +/- 0.65 percent.

Because the S-wave anisotropy in the reservoir intervals typically showed great lateral variation, a very mild smoothing operator (7-point or 500 ft moving average) was applied to the graphs displayed in Figures 8-23- and 8-24.

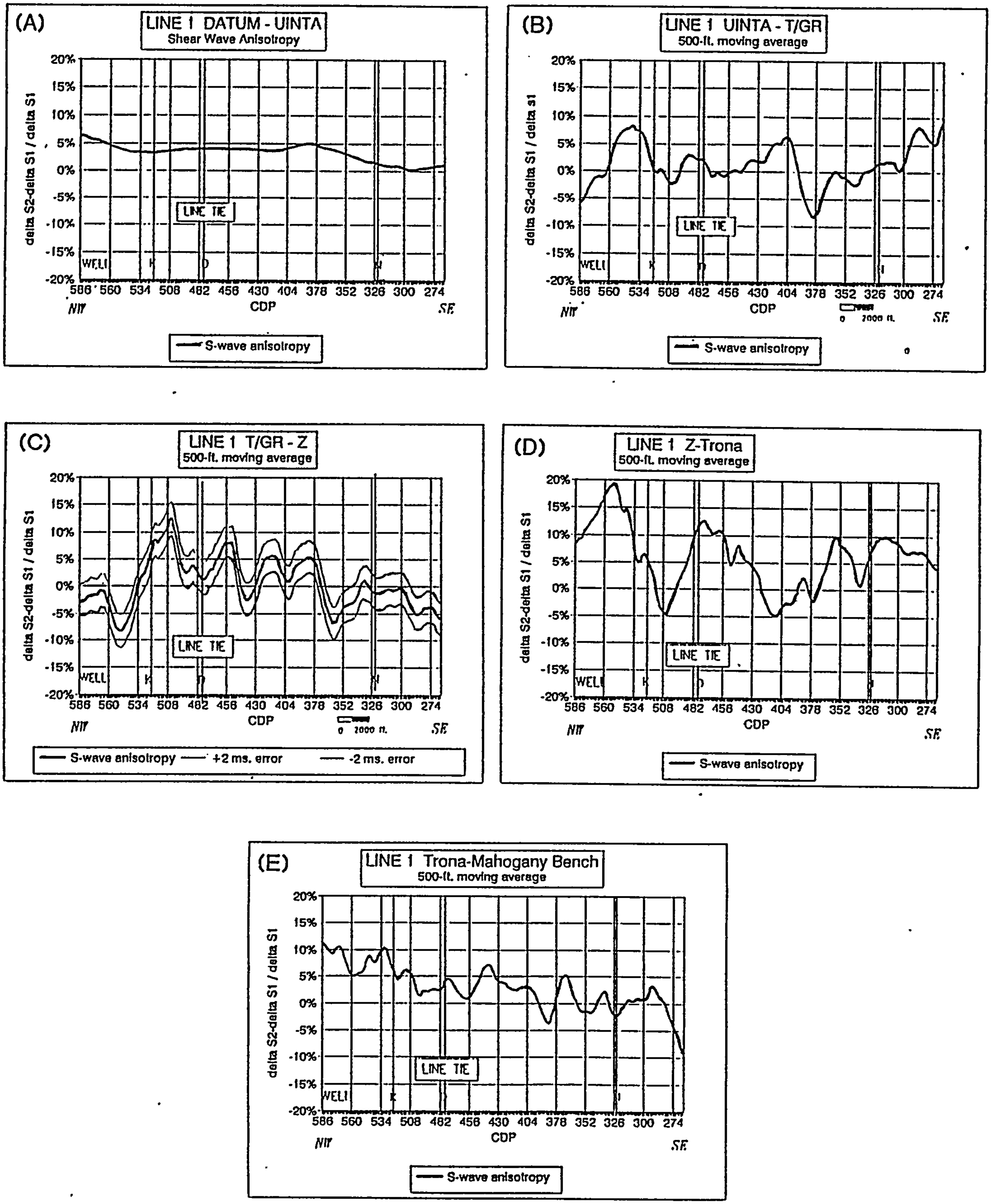

Line 1: Average S-wave anisotropy within the five stratigraphic intervals analyzed for Line 1. These show the variation in percent S-wave anisotropy, which can be taken as equivalent to the average fracture density within the interval. Positive values indicate S1 polarized N30W is the first-arriving S-wave (NW-trending fractures); negative values indicate S2 polarized N60E arrived first (NE-trending fractures). All graphs have smoothing of 500 ft. moving average applied. Error range plotted on T/GR-Z applies to all intervals.

FIGURE 8–23

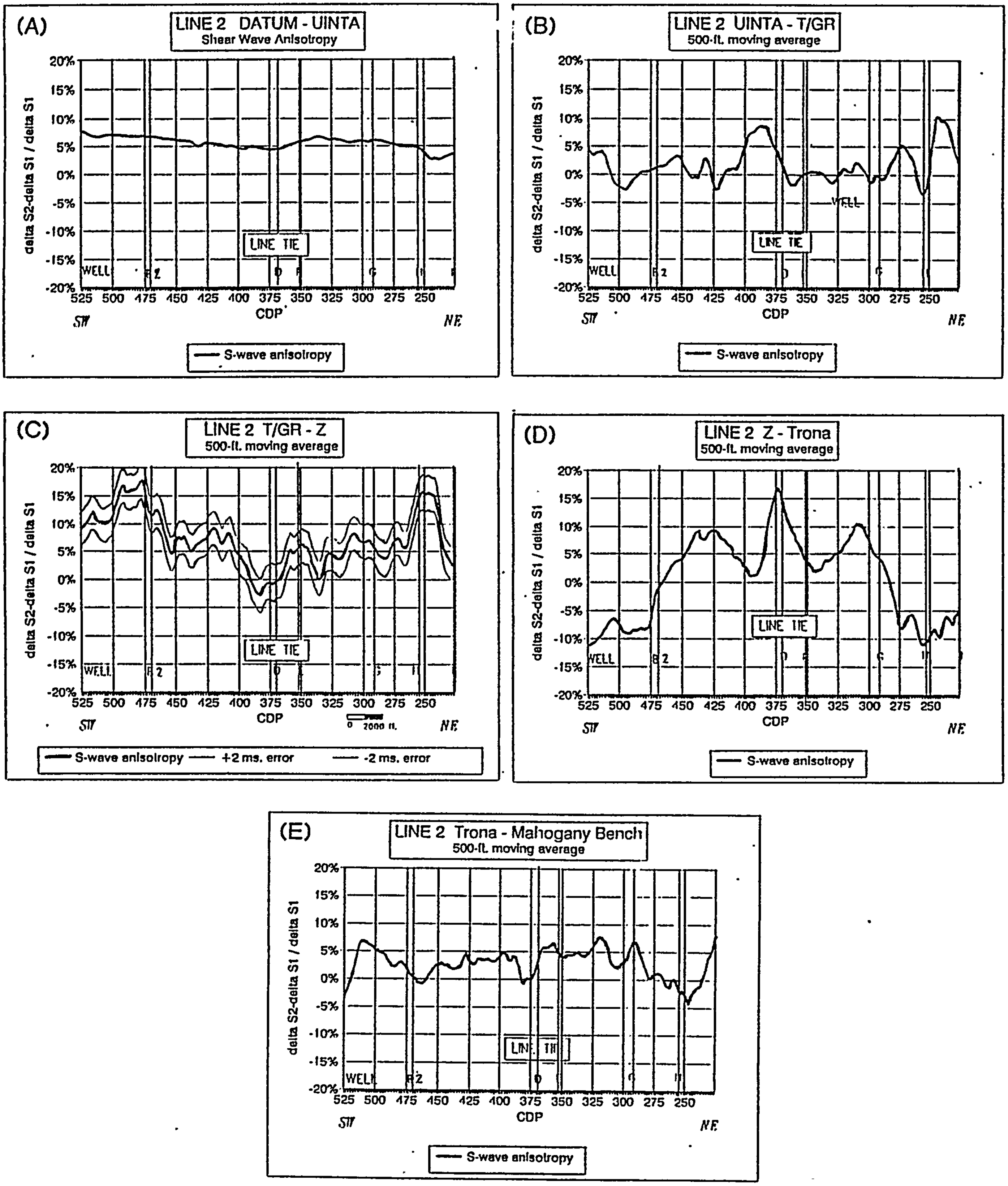

Line 2: Average S-wave anisotropy within the five stratigraphic intervals analyzed for Line 2. These show the variation in percent S-wave anisotropy, which can be taken as equivalent to the average fracture density within the interval. Positive values indicate S1 polarized N30W is the first-arriving S-wave (NW-trending fractures); negative values indicate S2 polarized N60E arrived first (NE-trending fractures). All graphs have smoothing of 500 ft. moving average applied. Error range plotted on T/GR-Z applies to all intervals.

FIGURE 8-24

8.3.12 VP/VS Ratio

The VP/VS1 and VP/VS2 ratios were computed for the five stratigraphic intervals from the measured interval travel time ratios VS1/VP and VS2/VP. These are shown in Figures 8-25 through 8-27. The velocity ratio VP/VS is often used as a lithology indicator. However, there are many other factors which influence VP/VS, among them, degree of compaction, pore shape and gas saturation. By analyzing the change in VP/VS with these various factors, it is hoped to draw some conclusions about the significance of the VP/VS ratios in the Upper Green River intervals analyzed, or to add support to interpretations made from data presented previously.

In the interval T/UGR-Z, the VP/VS ratios on both Line 1 and Line 2 are lowest within the survey where the greatest percentage of sandstone is interpreted, i.e., over the crest of the structure (Figures 8-25 and 8-26). This is also the place where gas is currently produced and where the azimuthal anisotropy is greatest. Figure 8-28 shows the relation between VP/VS and various rock properties. Since an increase in sandstone percentage, an introduction of gas into the rock and a decrease in aspect ratio (in gas-saturated rocks) all act to decrease the VP/VS, a low VP/VS is expected in these locations. Note also that the VP/VS1 and VP/VS2 show the most separation where the azimuthal anisotropy is greatest. (Compare Figures 8-25-8-26 with Figures 8-23-8-24). VP/VS2 is greater than VP/VS1 when the anisotropy is positive (NW-trending cracks) and the VP/VS1 is the greater of the two when the anisotropy is negative (NE-trending cracks). The two curves are widely separated with high values if the fractures are water-filled (as at Well B2, Line 2 T/UGR-Z interval) and widely separated with low values when the cracks are gas-filled (as at Well H, Line 2 T/UGR-Z interval and Well D, Z-Trona interval). The conclusion thus reached is that the VP/VS ratio can be used as a tool to help discriminate between prospective and non-prospective intervals, in gas exploration.

8.4 P-wave Reflection Data

AVO (Amplitude Variation with Offset)

AVO analysis was used as the primary interpretation tool for the P-wave reflection data, based on the observation of amplitude differences in reflections on the far offsets of the two P-wave lines at their tie point. Figure 7-13 showed a comparison of "supergathers" of 9 summed CDPs on each line, centered on the tie point, where clear differences in amplitude are seen on the Z and MB marker horizons. The amplitude differences on the two lines are observed on far offsets from approximately 5,989 ft to 9,000 ft. 5,989 ft was used as the dividing offset between near-offset stacks and far-offset stacks. Figures 8-29 and 8-30 compare the near offset stacks, which show an excellent tie at the line

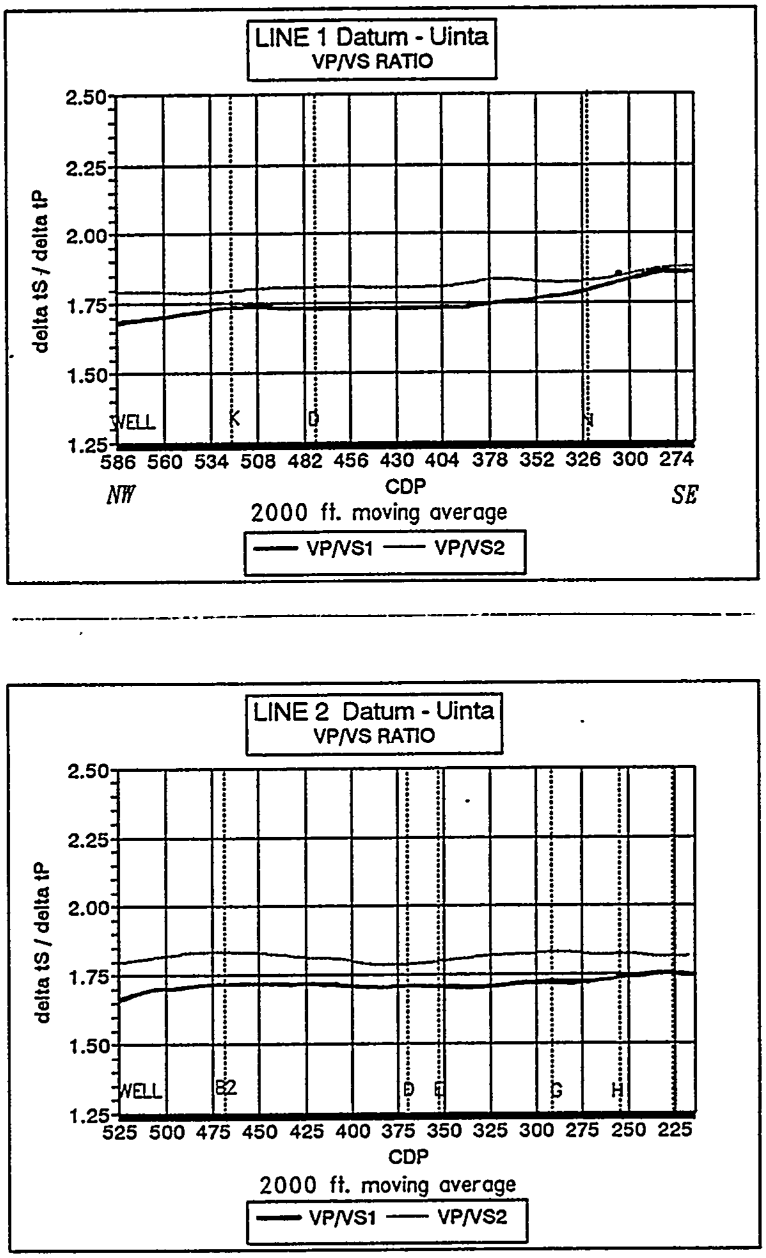

VP/VS ratios for Line 1 and Line 2, datum to Uinta interval (uppermost interval). On Line 1, VP/VS1 and VP/VS2 are separated at the NW end of the line, indicating azimuthal anisotropy, but come together at the SE end of the line, where azimuthal anisotropy is greatly reduced. This is discussed under S-wave Refraction Statics in the section on Data Processing.

FIGURE 8-25

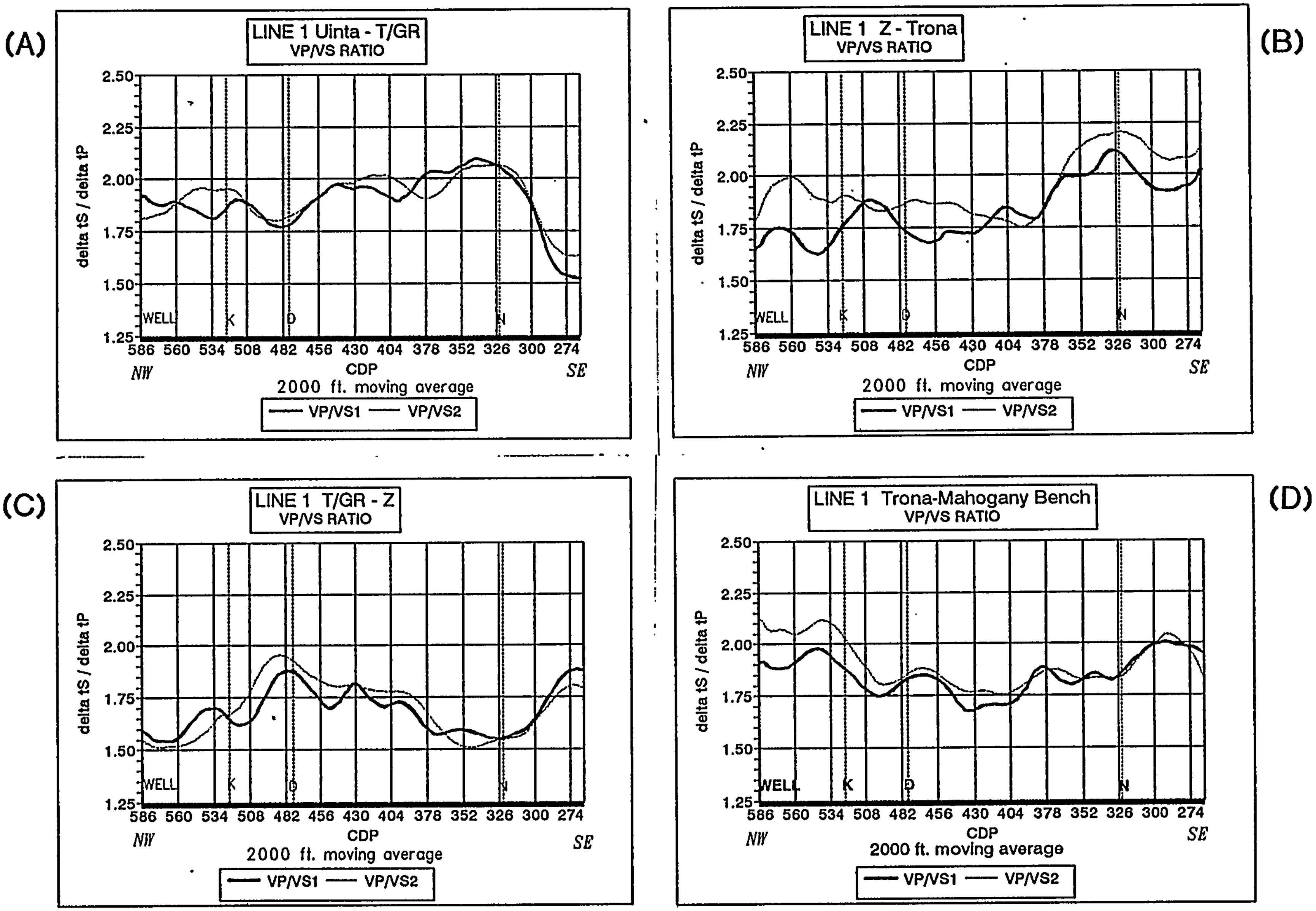

VP/VS ratios for four stratigraphic intervals from Uinta-M.B., Line 1.

FIGURE 8–26

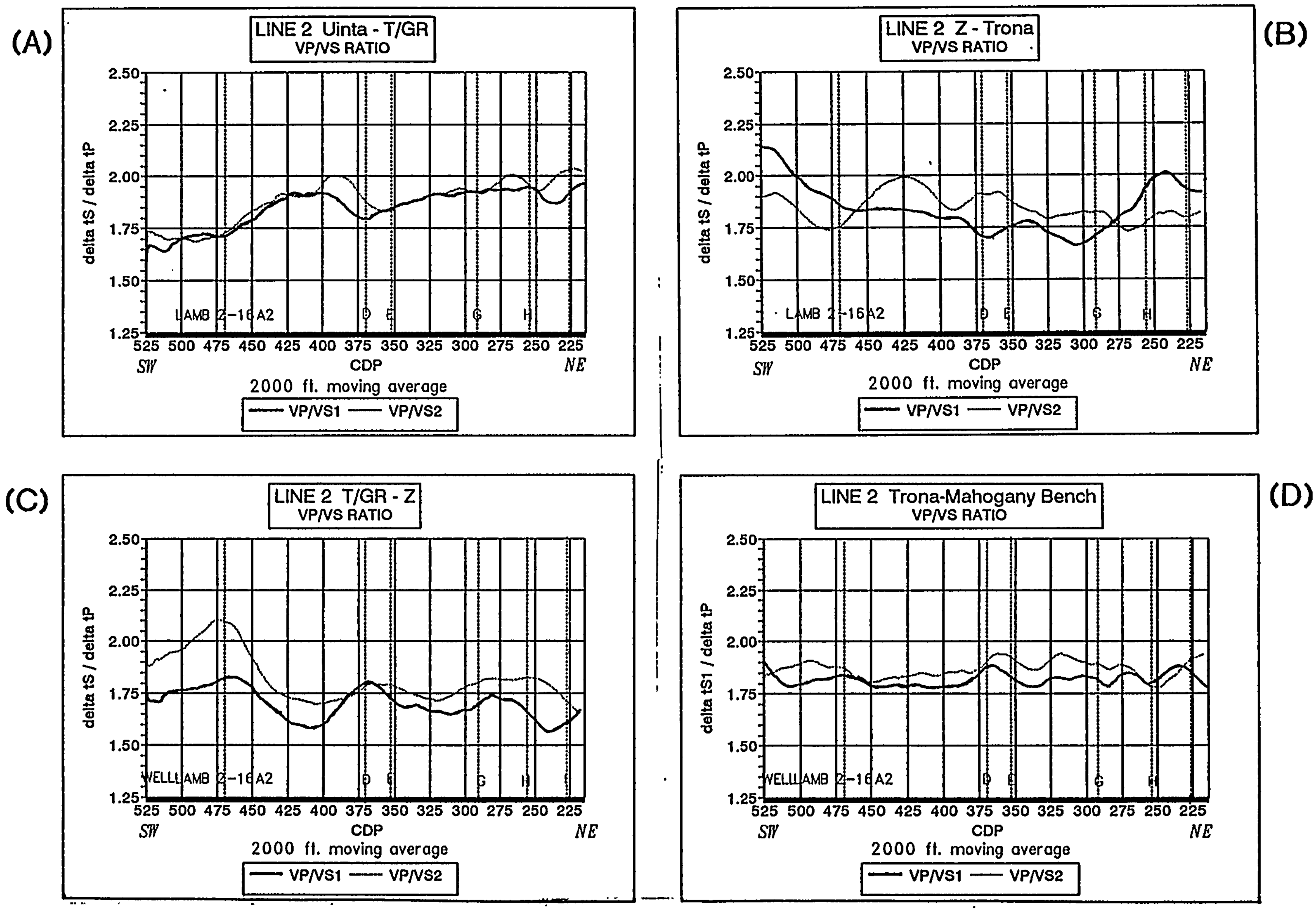

VP/VS ratios for four stratigraphic intervals from Uinta-M.B., Line 2.

FIGURE 8-27

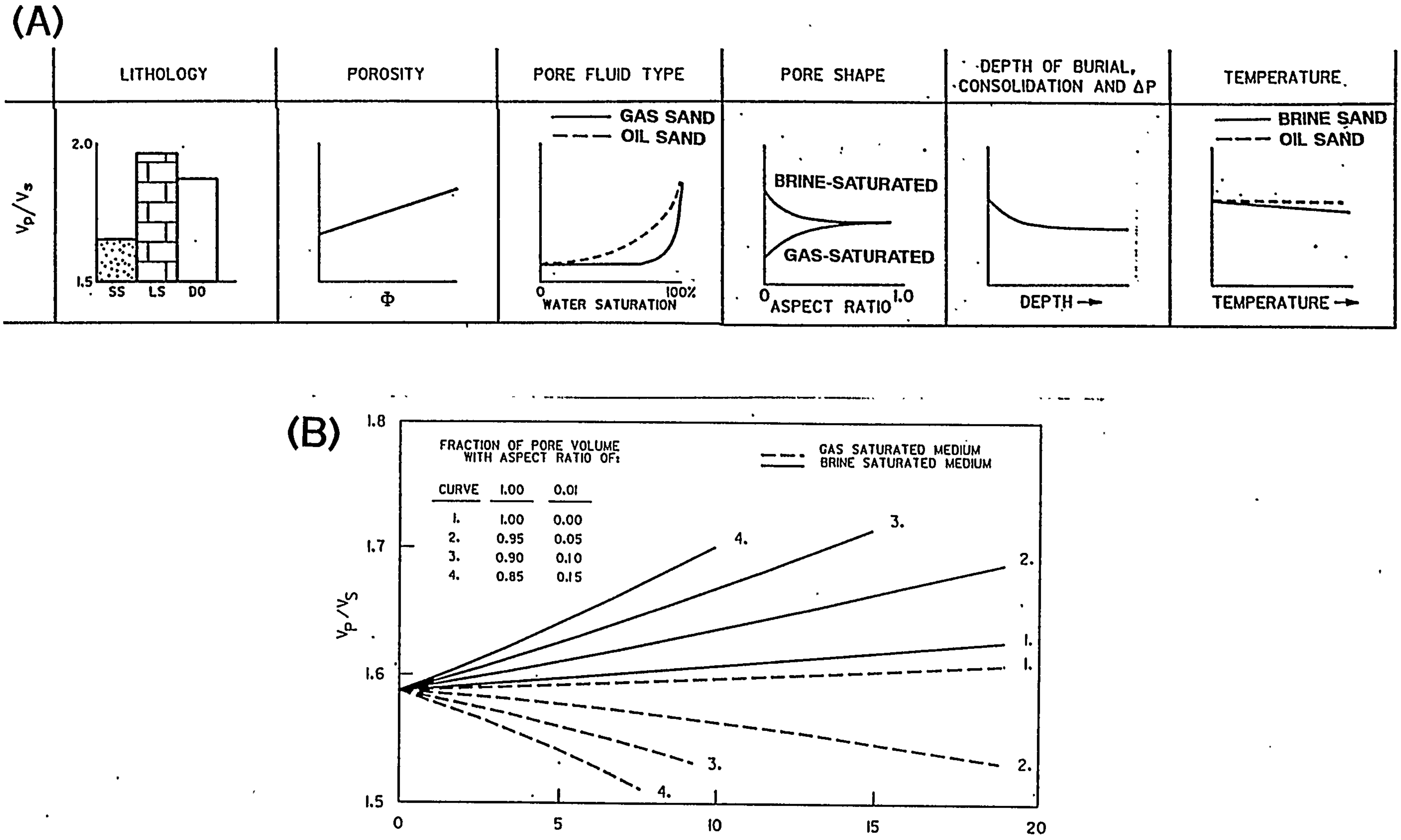

(A) Variation of VP/VS with rock properties. Increase in sand percentage, introduction of gas, and increase in depth of burial all cause decrease in VP/VS. (From Tatham and McCormack, 1991).
(B) Calculated values of VP/VS versus porosity for gas and brine saturated solids with four different proportions of spherical pores (aspect ratio 1.0), and flat cracks (aspect ratio of 0.01). (From Tatham and McCormack, 1991).
For gas-saturated rock, VP/VS decreases with increased percentage of flat cracks.

FIGURE 8–28

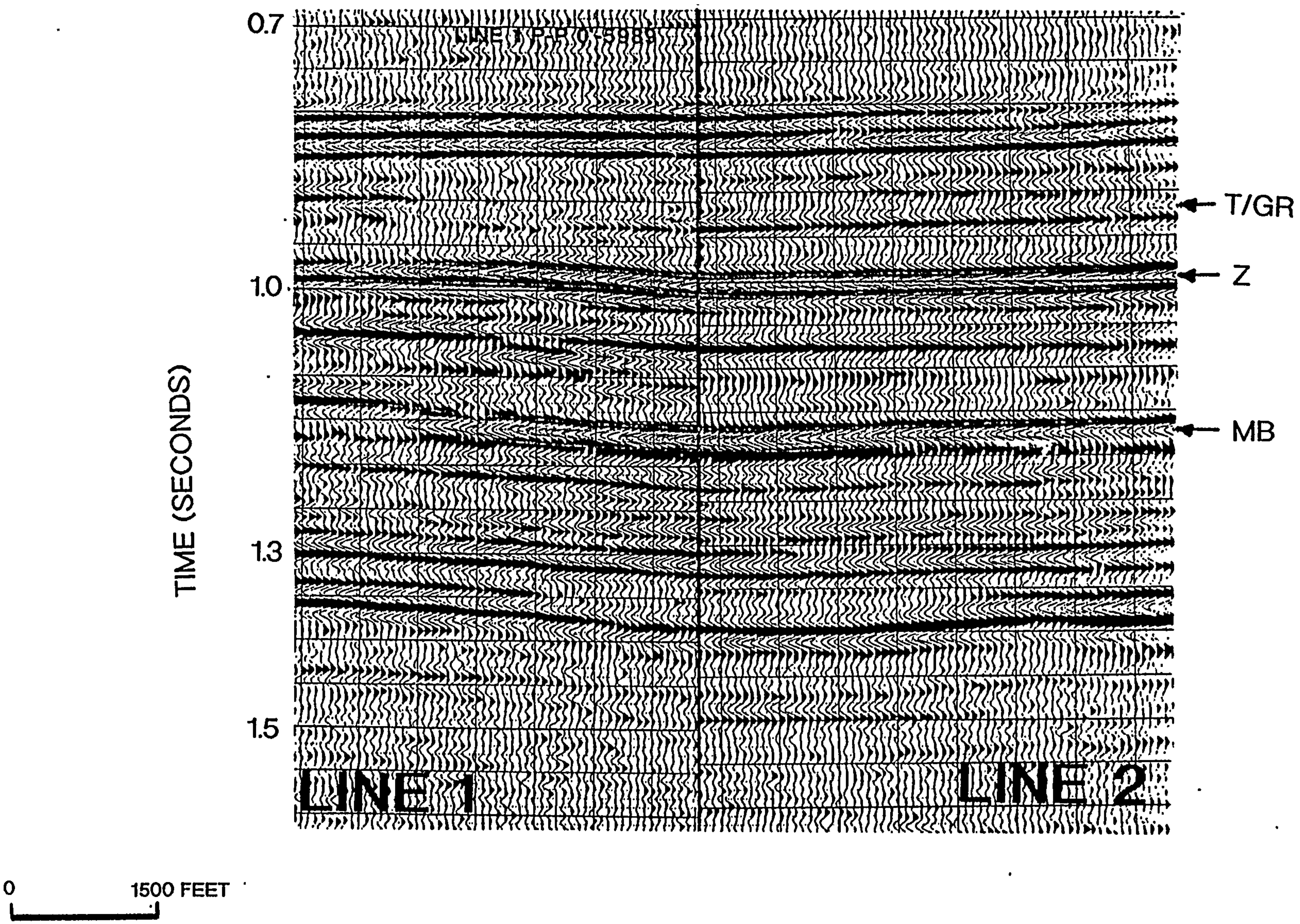

Comparison of near stacks (offset less than 5989 ft.) of Line 1 and Line 2 at tiepoint, shows very close similarity in reflector amplitudes on the two lines.

FIGURE 8–29

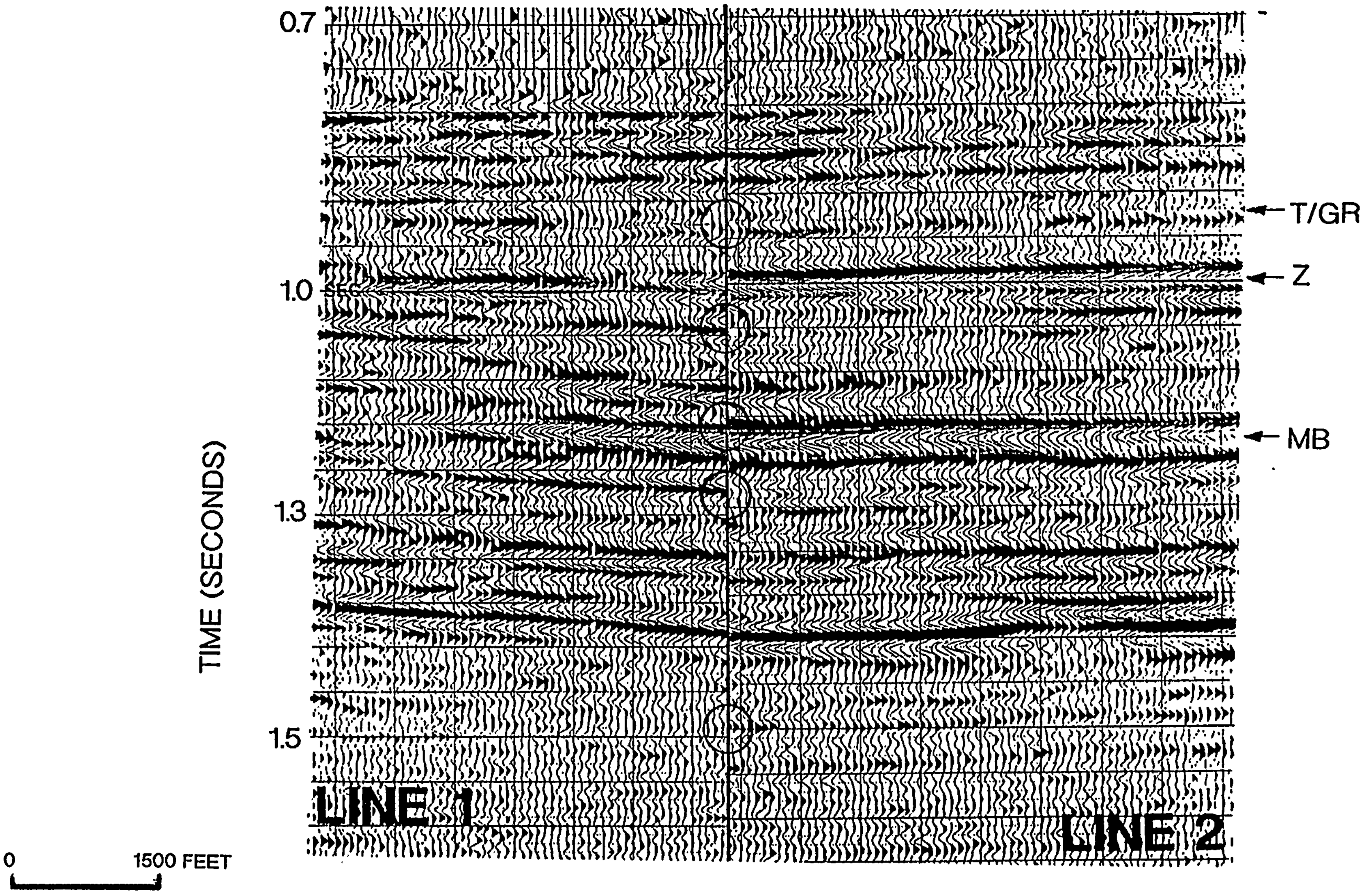

Comparison of far-offset stacks (offset greater than 5989 ft.) of line 1 and line 2 at tiepoint, shows differences in reflector amplitudes on the two lines at far offsets, indicating an azimuthal difference in AVO response.

FIGURE 8–30

intersection, and the far-offset stacks, which show significant differences in amplitude on the Z, MB, and other markers.

The AVO gradient, or linear variation in reflectivity with $\sin^2 q$, where q is the P-wave angle of incidence, is proportional to the change in Poisson's ratio across the reflecting interface (Shuey, 1985). Since the effect of gas in the pore spaces of a rock is to decrease the rock's Poisson's ratio, AVO is an appropriate method for gas detection. The sensitivity of P-waves to gas saturation is enhanced by the presence of cracks (Nur, 1971), as implied by the variation of P-wave velocity relative to crack alignment, so a significant AVO anomaly is expected in this fractured gas reservoir.

Using examples from different basins, Rutherford and Williams (1989) classified gas-bearing sandstones into three broad categories according to their impedance relative to an overlying shale:

- Class I, shows impedance substantially higher than the overlying shale;
- Class II, demonstrated nearly the same impedance as the overlying shale; and,
- Class III, impedances were substantially lower than the overlying shale.

With Rutherford and Williams' polarity, a shale to gas sand boundary is linked to a negative AVO gradient (Figure 8-31a), and a low-to-high impedance contrast is a peak. The Bluebell-Altamont data polarity is reverse to Rutherford and Williams' nomenclature. The Bluebell-Altamont seismic lines were processed and displayed using Society of Exploration Geophysicists (SEG) "normal" polarity, that is, low-to-high impedance across a reflecting boundary gives a trough, or negative number. Because the AVO gradient responds to the Poisson's ratio and since the Poisson's ratio (like the P-wave velocity and the VP/VS ratio) decreases dramatically for the first 10 percent gas saturation, it cannot distinguish between commercial and non-commercial gas accumulations. Figure 8-32 shows the variation of P-wave velocity, S-wave velocity, Poisson's ratio, and VP/VS ratio with gas saturation (from Ostrander, 1984).

In order to interpret the AVO response of the Bluebell-Altamont P-wave lines, the AVO response for the isotropic case of varying thicknesses of gas sands at the T/UGR was first compared to the case with no gas. Subsequently, the AVO gradients at locations corresponding to known gas production were examined and used as "AVO signatures." The Castagna Parameter was used to evaluate AVO signatures and is discussed in Appendix A.

8.4.1 AVO Modeling of the Top of Green River

The 9-C VSP well, Duncan 3-7A1, located at the northeastern end of Line 2, provided the starting information (Poisson's ratio from the linear parametric

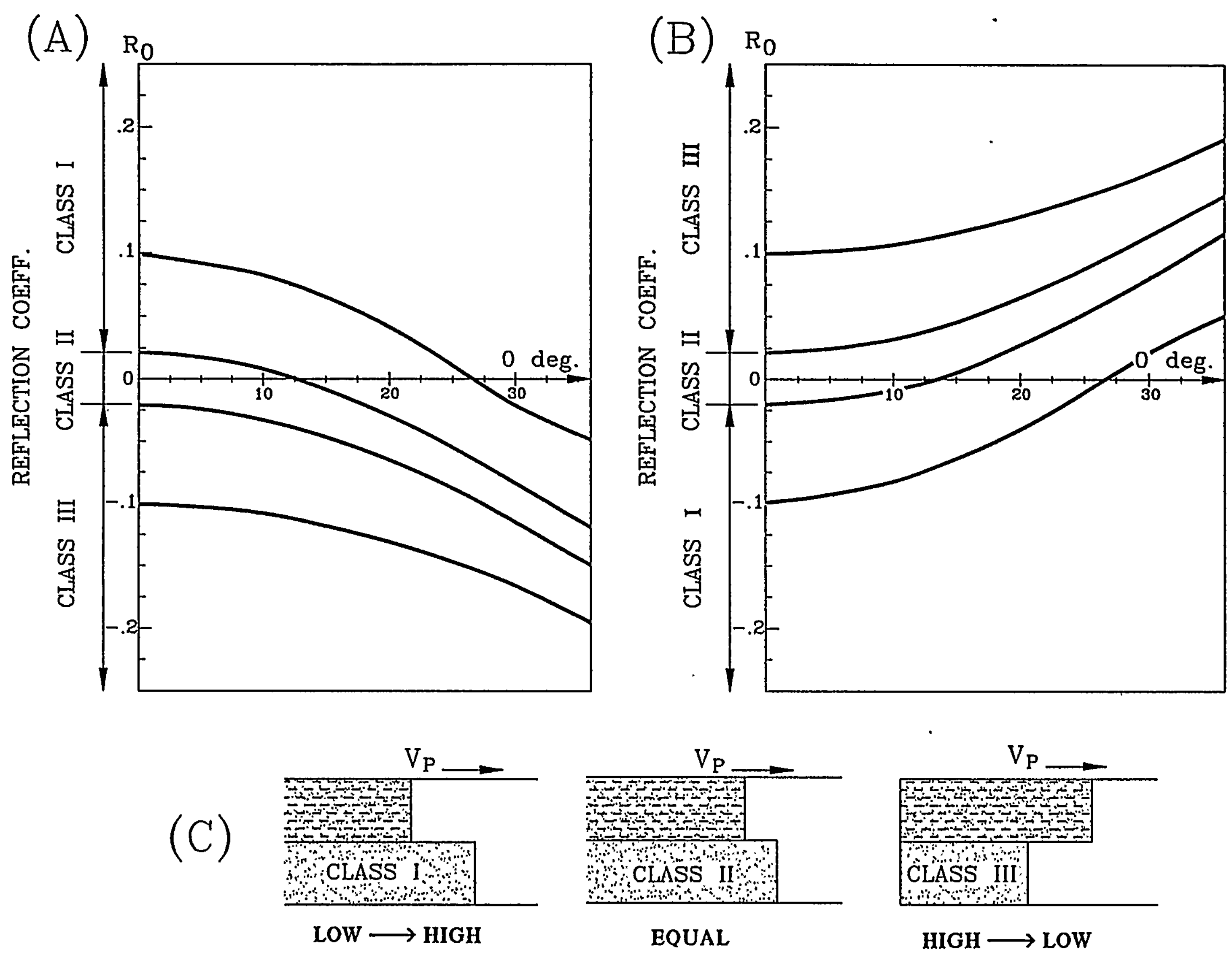

(A) Reproduced from Rutherford and Williams, 1989. Zoeppritz P-Wave reflection coefficients for a shale -gas sand interface for a range of R_0 values. The Poisson's ratio and density of the shale were assumed to be 0.38 and 2.4 g/cm^3 , respectively. The Poisson's ratio and density of the gas sand were assumed to be 0.15 and 2.0 g/cm^3, respectively.
(B) Relative position of curves from figure (A) when SEG "normal" polarity seismic data amplitudes are used as reflectivity. This is the polarity of the Bluebell- Altamont multi-component seismic data. The sign of R_0 and the slope of the curves are reversed from figure (A).
(C) Class I, II and III shale- gas sand interface.

FIGURE 8–31

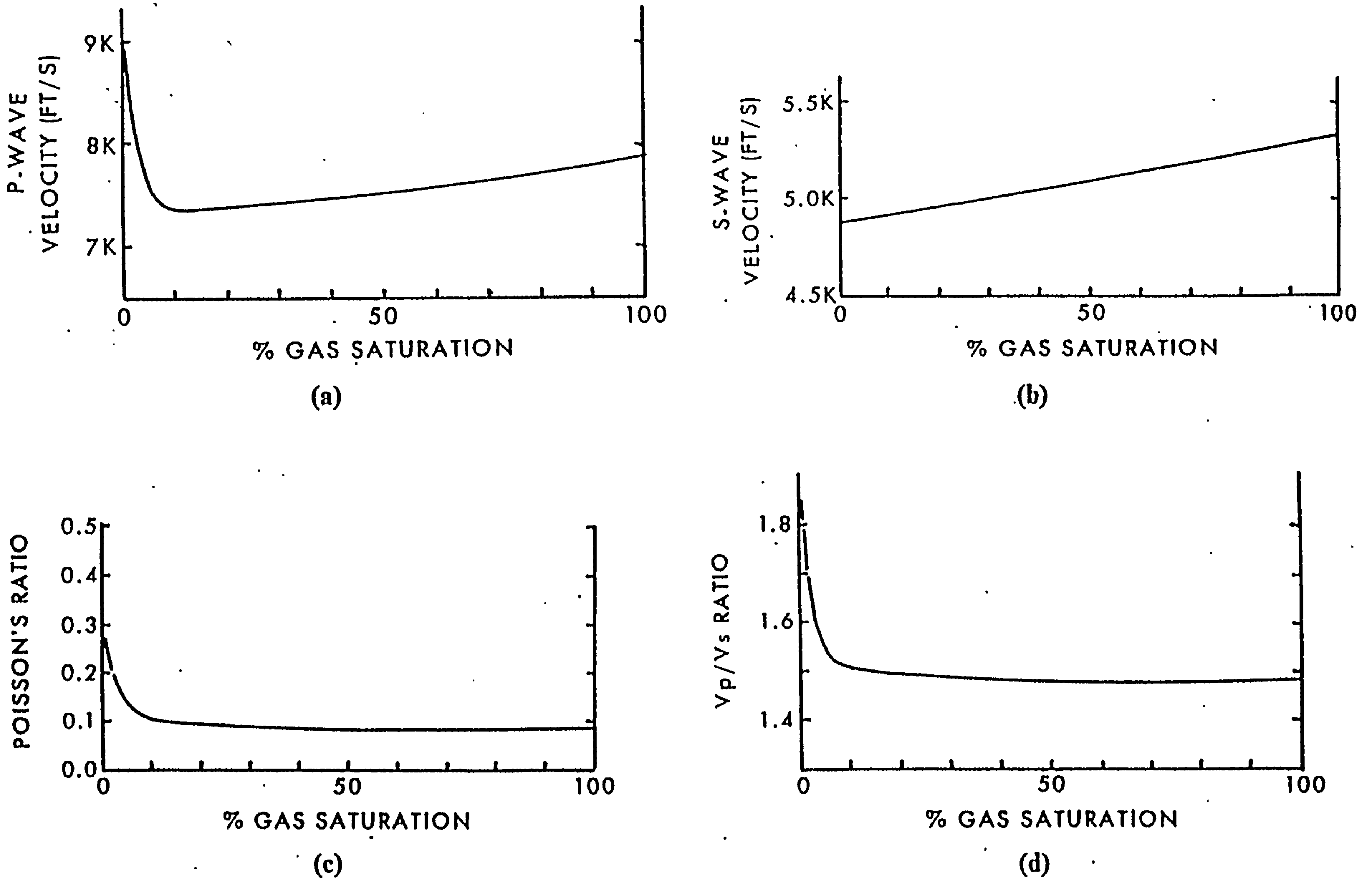

Plots of (a) *P-wave* velocity, (b) *S-wave* velocity, (c) Poisson's ratio, and (d) *Vp/Vs* ratio as a function of gas saturation. (After Ostrander, 1984)

FIGURE 8–32

inversion) to model the AVO response at the T/UGR. Also in this well, an S-wave interval velocity model was derived from the wireline log suite. Logs in this well did not indicate gas in the Upper Green River section, and a model CDP gather using the derived shear log, showed reflector amplitudes decreasing slightly with offset, which would be expected if no gas were present (Figure 8-33).

Figure 8-34a shows an isotropic-case synthetic CDP gather produced from a no-gas model for the T/UGR. This can be compared to the synthetic CDP gather for a 100 ft gas-sand model in the Figure 8-34b. The T/UGR corresponds to a Class I to Class II sand (using Rutherford and Williams', 1989, nomenclature) as seen by the increase in acoustic impedance at the marker. The no-gas model CDP gather shows a slight monotonic decrease in reflector magnitude with offset, but the 100 ft thick gas sand model shows a strong decrease, with polarity reversal of the T/UGR event apparent at about 6,000 ft offset.

It should be noted that the no-gas case is not a 100 ft thick wet sand, but the actual lithology of thinly-bedded sands, shales and limestones found in the well (none of which contained gas), so the comparison is not exact. The shear velocity was increased within the 100 ft gas sand model interval, rather than decreasing the P-wave velocity, which would have been more realistic. Since the <u>ratio</u> of the two velocities is responsible for the AVO effect, the synthetic CDP result is not changed. The P-wave velocities in the T/UGR are very fast, and in general, the faster sands are the cleaner sands (less clay content), which produce the gas. Geologists working the field used contoured sonic log interval velocity maps as a tool to help differentiate between potential productive and dry areas, using approximately 15,000 ft/sec. sonic interval velocity as a cut-off. The influence of gas is to decrease the P-wave velocity, however the shoaling of the sands produces very clean and, therefore, higher velocity sands. Dimming of the amplitude of the P-wave reflection at the T/UGR, which would be expected if the presence of gas significantly slowed down the velocities, has not been observed in the P-wave data.

This AVO modeling was done for the isotropic case (the gas in approximately round and evenly distributed pores). Although this isotropic model is not thought to be representative of the fractured Upper Green River, knowledge of the isotropic case is important as a base for further anisotropic modeling. Furthermore, this isotropic modeling used an arbitrary source-receiver direction, and modeled only AVO variation with offset, not with azimuth.

The model-generated CDPs were sorted by angle for input to regression analysis, in order to determine the AVO gradient. Figure 8-35 shows AVO regression displays for the two models where there is more than an order of magnitude difference between the AVO gradients for the no-gas case (AVO grad. = 520) and the 100 ft gas sand case (AVO grad. = 6776). Since the maximum thickness of stacked sands in the Upper Green River at Bluebell-Altamont tends to be about 80-110 ft, these models represent end-member

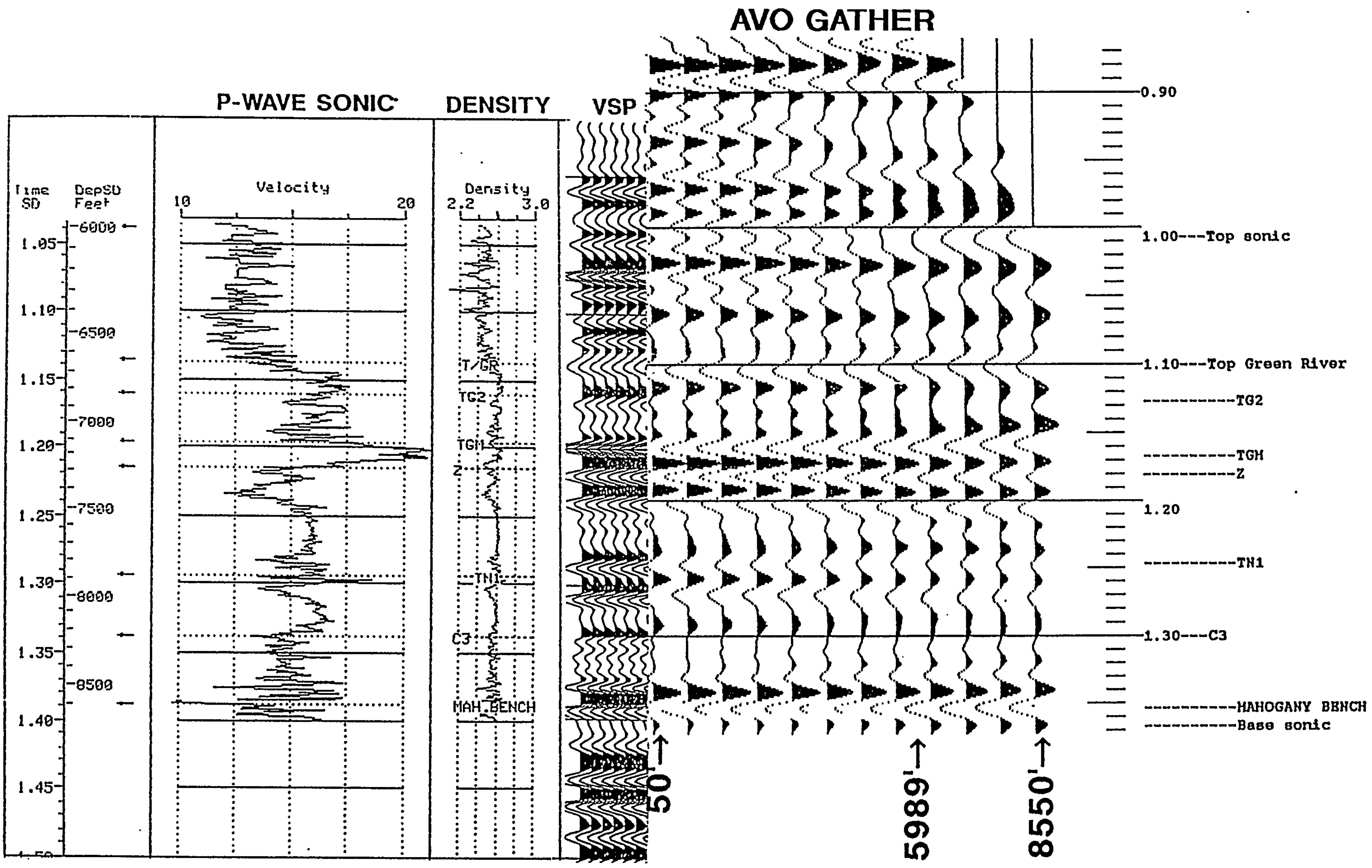

Synthetic AVO gather showing minor decrease of upper Green River reflector amplitudes with offset, indicating no gas. Produced by Associated Geophysical Analysts, Denver, from pseudo-shear log of well I (9-C VSP well) which was derived from full wireline suite.

FIGURE 8-33

AVO MODEL: NO GAS AT T/GR (A)

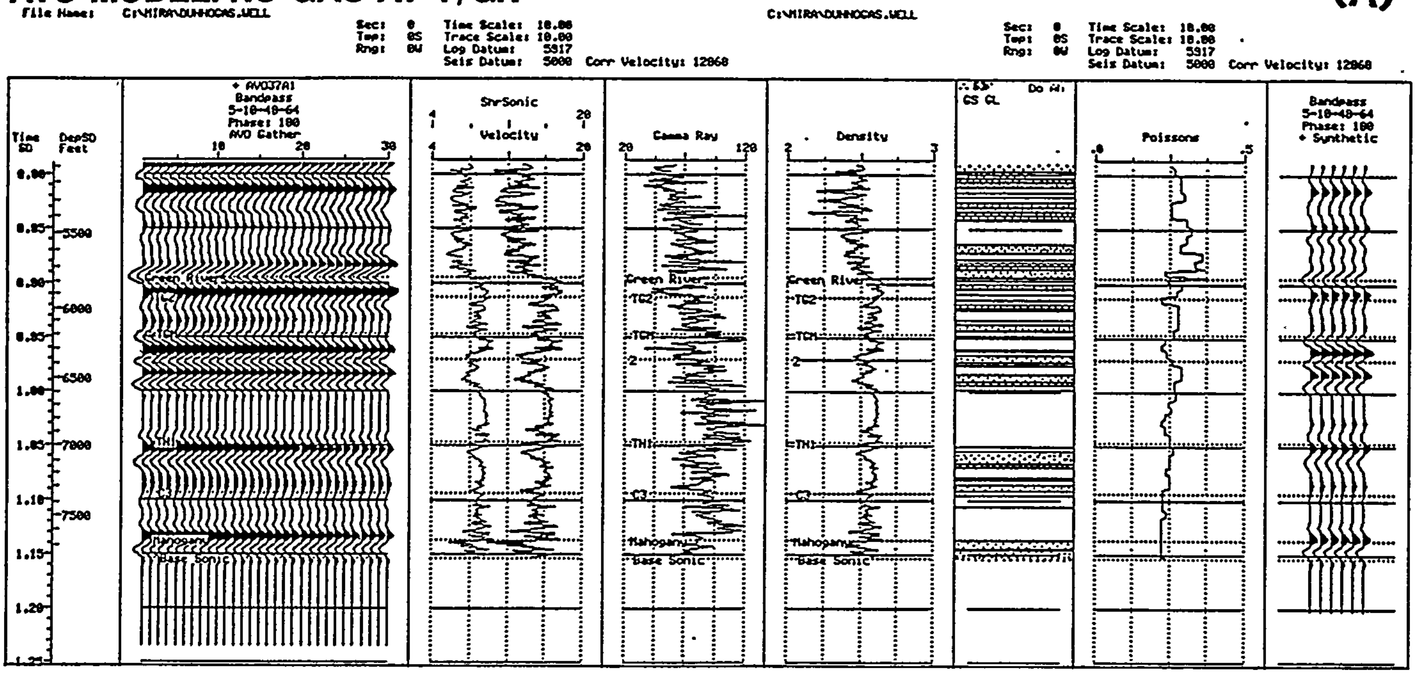

AVO MODEL: 100 FT. THICK GAS SAND AT T/GR (B)

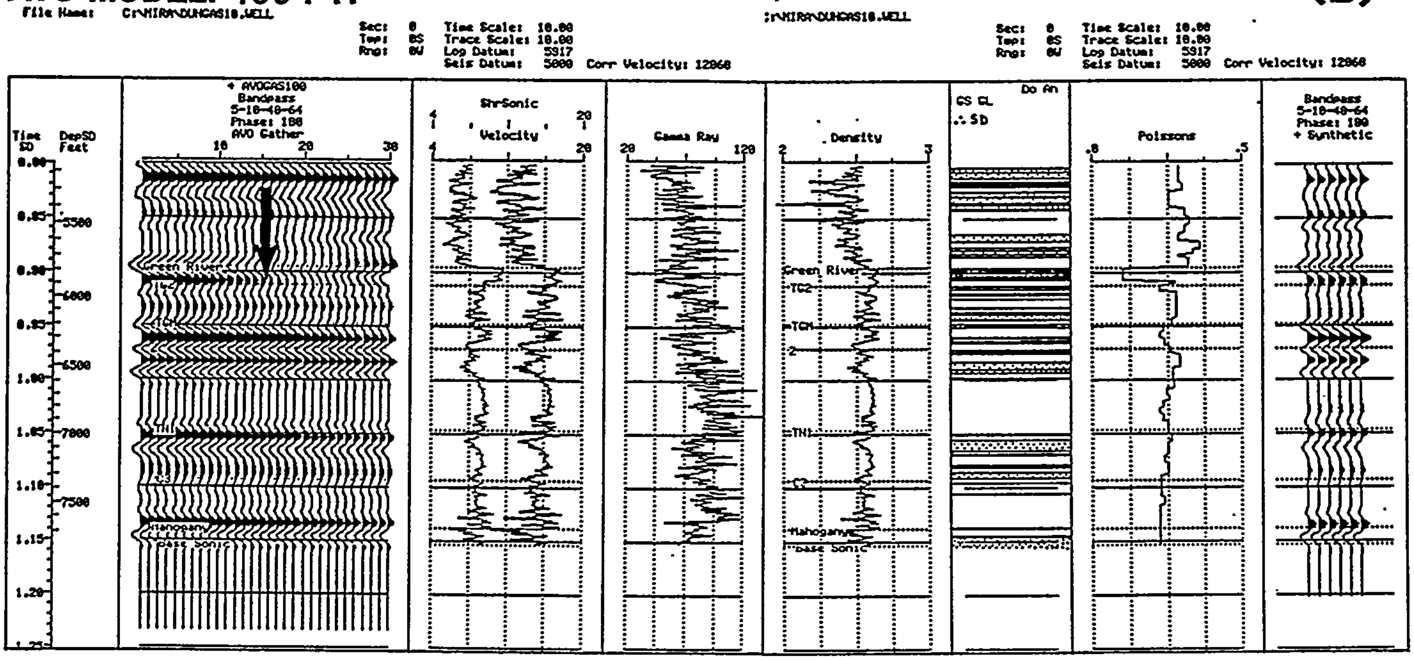

FIGURE 8–34

(A) Synthetic AVO gather and input model including P and S velocity logs (pseudo-shear log generated by AGA, Denver), gamma ray, density and lithology. Poisson's ratio curve modified from linear parametric inversion of VSP data. Very little change in amplitude of T/UGR reflector from 0-7,500 ft offset.
(B) Synthetic AVO gather and input model as in above, with model altered for the case of 100 ft thick gas sand at T/UGR. Poisson's ratio of 0.1 input for gas sand. Note T/UGR reflector amplitude polarity change at approx. 6,000 ft. offset.

P-WAVE AVO REGRESSION ANALYSIS

NO GAS MODEL
T/GR REFLECTOR

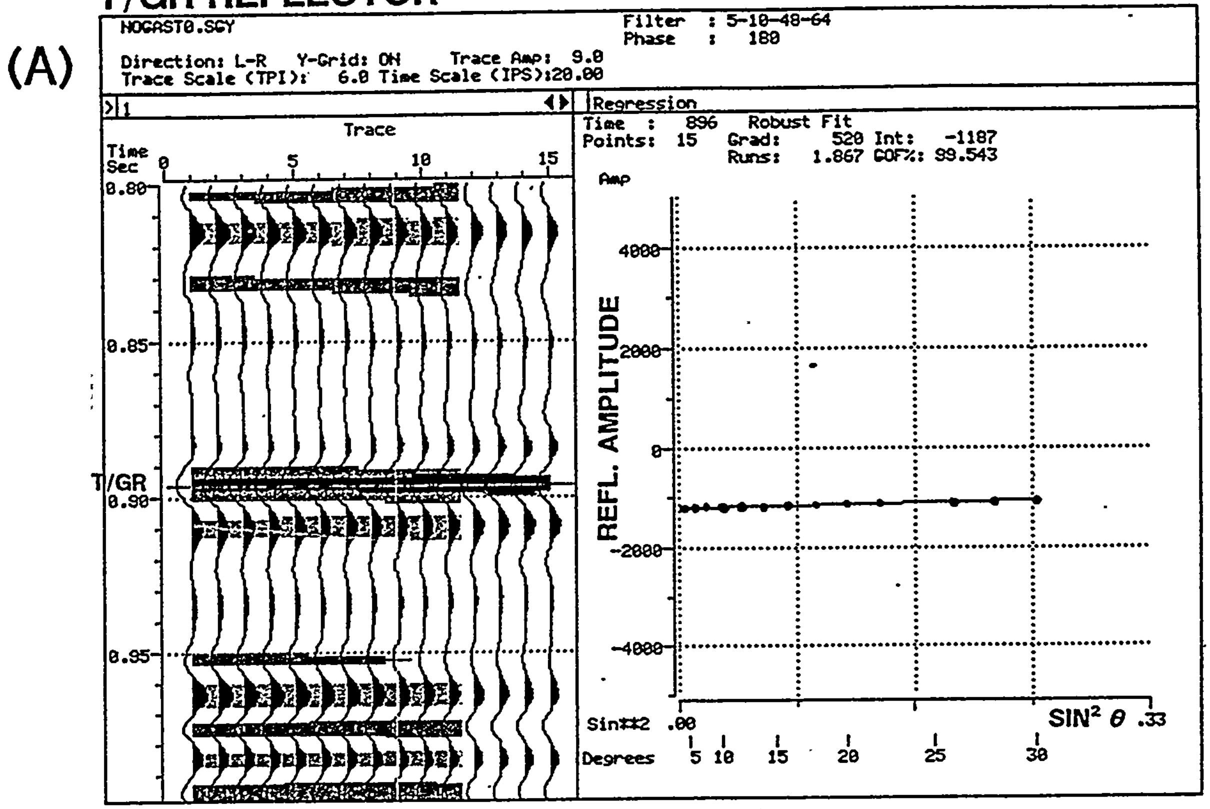
(A)

NOGAST0.SGY
Filter : 5-10-48-64
Phase : 180
Direction: L-R Y-Grid: ON Trace Amp: 9.0
Trace Scale (TPI): 6.0 Time Scale (IPS):20.00

Regression
Time : 896 Robust Fit
Points: 15 Grad: 520 Int: -1187
Runs: 1.867 GOF%: 99.543

100 FT. GAS SAND MODEL

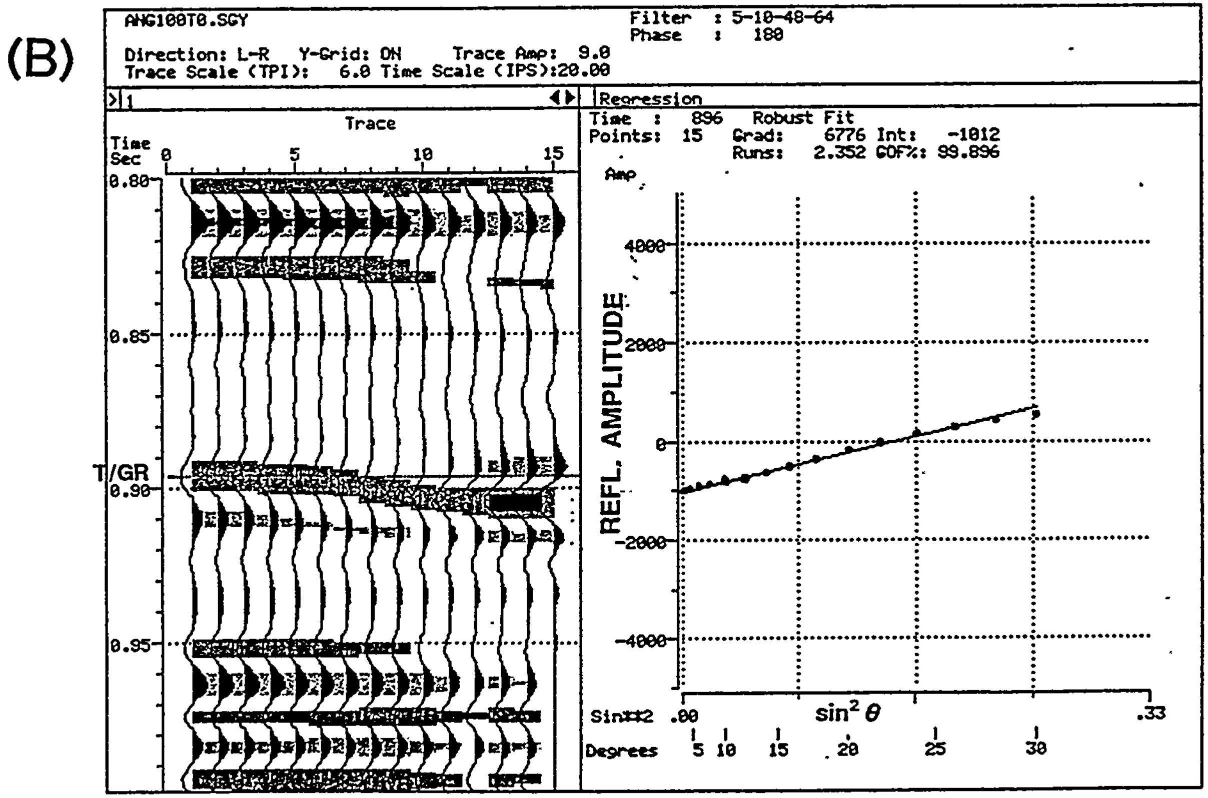
(B)

ANG100T0.SGY
Filter : 5-10-48-64
Phase : 180
Direction: L-R Y-Grid: ON Trace Amp: 9.0
Trace Scale (TPI): 6.0 Time Scale (IPS):20.00

Regression
Time : 896 Robust Fit
Points: 15 Grad: 6776 Int: -1012
Runs: 2.352 GOF%: 99.896

AVO regression plots for the two models in Figure 8-34, showing linearized reflection amplitude of T/UGR reflector with $\sin^2\theta$. The AVO gradient differs by more than an order of magnitude for the two models.

FIGURE 8-35

cases. The AVO responses for various thicknesses of gas-saturated sand at the T/UGR were modeled, with results which indicated that: 1) the positive AVO gradient increased in proportion to increasing gas sand thickness; 2) the AVO gradient for gas sand thicknesses below about 50 ft was undifferentiable between that for zero gas sand thickness; and 3) the AVO gradient at the T/UGR reflector was similar between a 66 ft thick gas-saturated sand at the T/UGR (AVO grad.=4069), and a series of 5 to 15 ft thick gas-saturated sands totaling 66 ft, interspersed with shales within a 140 ft thick interval (AVO grad.=4976). From this last observation it is expected that thinly-layered gas sands, such as those found at the T/UGR, if gas-saturated, will produce a positive AVO gradient.

8.4.2 AVO Signatures of Gas Producing Zones

The AVO gradients were calculated at locations corresponding to wells nearest the seismic lines. On the AVO gradient plots in this report, the "goodness of fit" shown by GOF% above each graph, is a statistical indication of the goodness of the linear regression. A high GOF (80 or above) is considered a good fit, 60 - 80, a fair fit, and a GOF of 60 or below is a poor fit.

8.4.2.1 Top of Upper Green River: Well G

Well G, which produces gas from two intervals near the T/UGR, is located at SP 145.5 (CDP 291) on Line 2. The sonic log for this well, Figure 8-36a, shows that the sandy interval from T/UGR - TG2, or T/UGR, corresponds to a Class I to II sand; its impedance (sonic velocity) is higher than that of the overlying rock. The AVO gradients of the reflections corresponding to the gas-producing zones are positive, as seen in Figure 8-34 (AVO regression analyses, CDP 291, upper and lower gas zones).

Well K

This well produces from the Upper Green River (sonic log showing productive interval, Figure 8-37a). This well is located at SP 261.5 (CDP 523) on Line 1. The AVO gradient of the reflector at the top gas zone at this location, Figure 8-37b does not resemble the AVO gradient of the Well G on Line 2, in Figure 8-36: the slope at Well K is reversed (a negative gradient). Although the gather at the K location in Figure 8-37 is arguably noisier than those at the G well location, the difference in AVO signature between the two wells is interpreted to indicate an anisotropic response on the two lines due to open, gas-filled vertical fractures striking parallel to Line 1. All known gas-productive zones located on Line 2 had similar (positive gradient) AVO signatures, which differed from those of zones known not to flow. The AVO signature of the known gas zone in the K well, on Line 1, does not agree with the Line 2 gas zones. The gas zone in Well K corresponds to the same seismic reflector as the lower gas zone in Well G. It is, therefore, concluded that the azimuthally anisotropic P-wave AVO response is dependent on the line source-receiver azimuth with respect to the fracture strike.

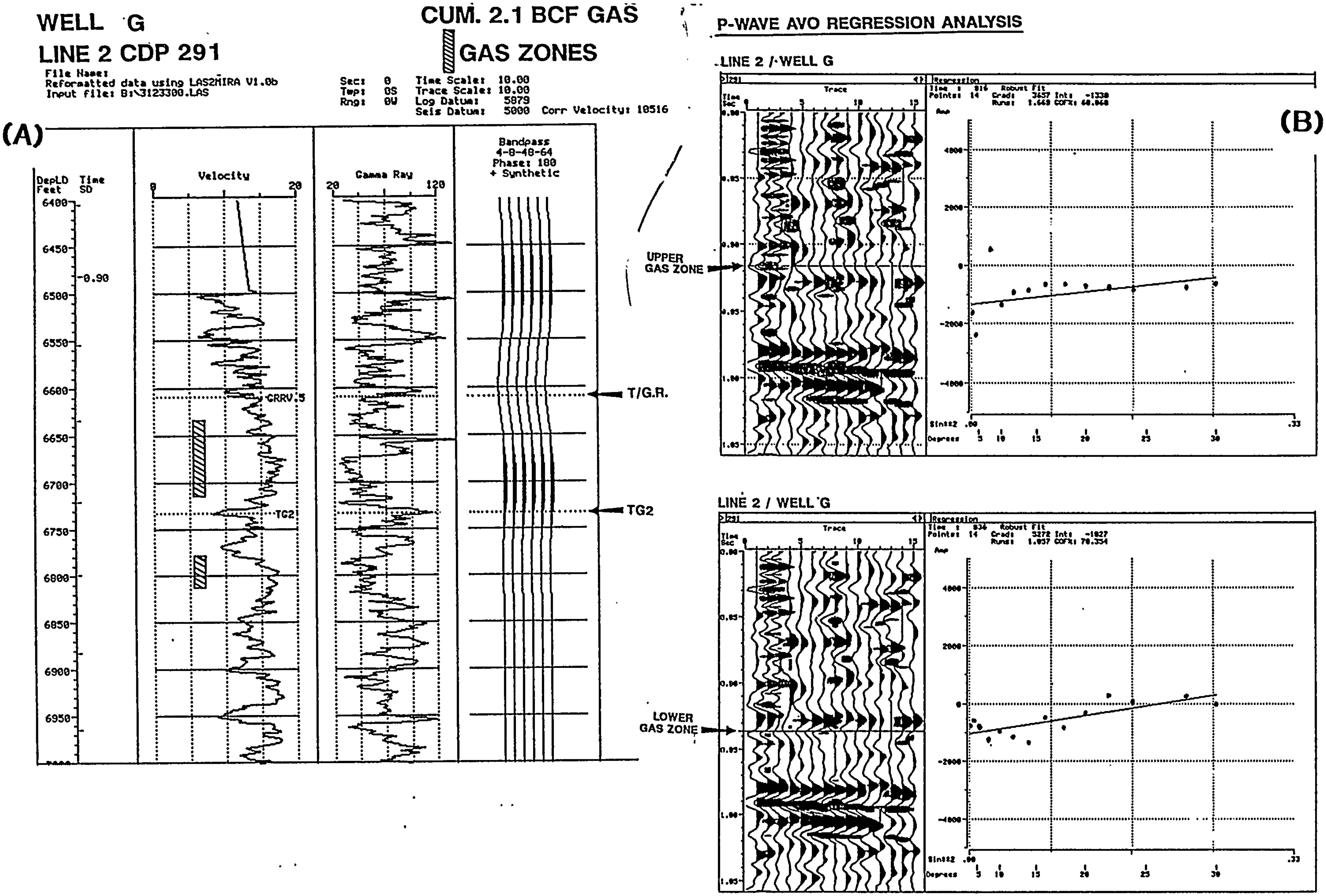

(A) Sonic and gamma ray logs for well G showing productive intervals below T/GR and below TG2.

(B) Positive AVO gradients (3657 and 5272) at line 2, CDP 291, well G location, corresponding to upper and lower gas zones indicated at left (arrows). GOFs are 68.07% and 78.35%, considered fair fits.

FIGURE 8–36

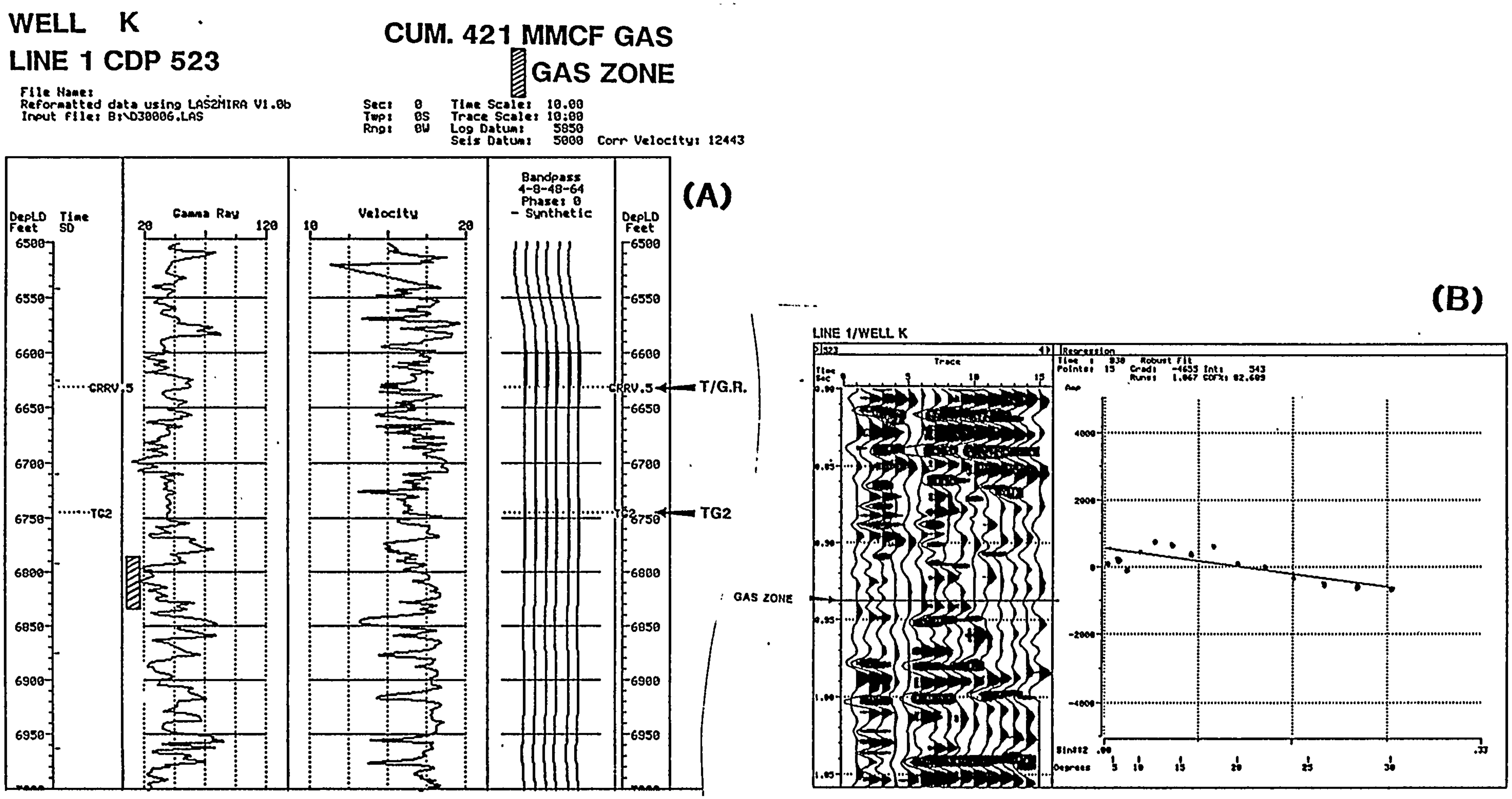

(A) · Sonic and gamma ray logs for well K showing productive interval below TG2.

(B) Negative AVO gradient (-4655) at line 1, CDPs 523, well K location, time 0.938 sec., top gas producing zone. GOF is 82.69% (a good fit).

FIGURE 8–37

Well I

The 9-C VSP well, Well I is located at the extreme eastern end of Line 2, which does not have enough long offsets to perform a valid AVO analysis at the well. Nonetheless, 600 ft to the west of the well location (CDP 234) incorporates angles up to 25 degrees. The AVO gradient plot at this location (Figure 8-38a), shows a steep positive gradient, which may be interpreted as a gas indicator, by comparison with the other known gas intervals along Line 2. This interpretation is supported by the parametric inversions of the nine-component VSP run in the Duncan 3-7A1 well, which indicate a very low Poisson's ratio for the T/UGR (Figure 8-38b). Updip to the west on Line 2, the T/UGR again shows a positive gradient starting at SP 120 (CDP 240), which extends laterally to SP 128 (CDP 256), a distance of 1,200 ft (Figure 8-39).

Well D

A direct comparison of the AVO response with azimuth, for any particular reflector, is possible only at the intersection of the two lines. Well D is located at the line intersection and provides a calibration point for both lines. The sonic and gamma ray logs at the T/UGR in this well are shown in Figure 8-40. The T/UGR reflector shows minor differences in AVO gradient magnitude at the line tie; here both lines show a positive slope that is very limited in lateral extent. Figure 8-41a shows the AVO gradient at Line 1, 1 CDP north of the tie point , and the tie point CDP. Figure 8-41b shows the gradient for Line 2, 1 CDP east of the tie point , and the tie point CDP. A DST in this zone in the D well, located at the line tie, tested flow of 319 MCF gas/day. Because the AVO response shows essentially the same positive AVO gradient on both lines, we interpret either no significant anisotropy and thus no significant fracturing in this Upper Green River zone, *or*, equally well-developed NW and NE open fracture trends. As discussed under S-wave Seismic Interpretation (Section 8-3), the most reasonable explanation is considered to be the presence of matrix porosity in the T/UGR. The DST results indicate gas is present, and the positive AVO gradient on both lines agrees with the modeled response for gas saturation. The core analysis has indicated that matrix porosity may have been underestimated in this interval. If the gas were in NW-striking aligned fractures, then the fracture porosity sensed by P-waves traveling in the directions parallel and perpendicular to the open fractures might have resulted in different AVO gradients for the reflector on Line 1 and Line 2, such as those observed at the top gas zone reflector on Wells G (Line 2) and K (Line 1). The shear wave reflection data at the line tie showed no azimuthal anisotropy in the interval T/UGR-Z, consistent with the interpretation of azimuthal isotropy and of matrix porosity in the T/UGR at the tie point.

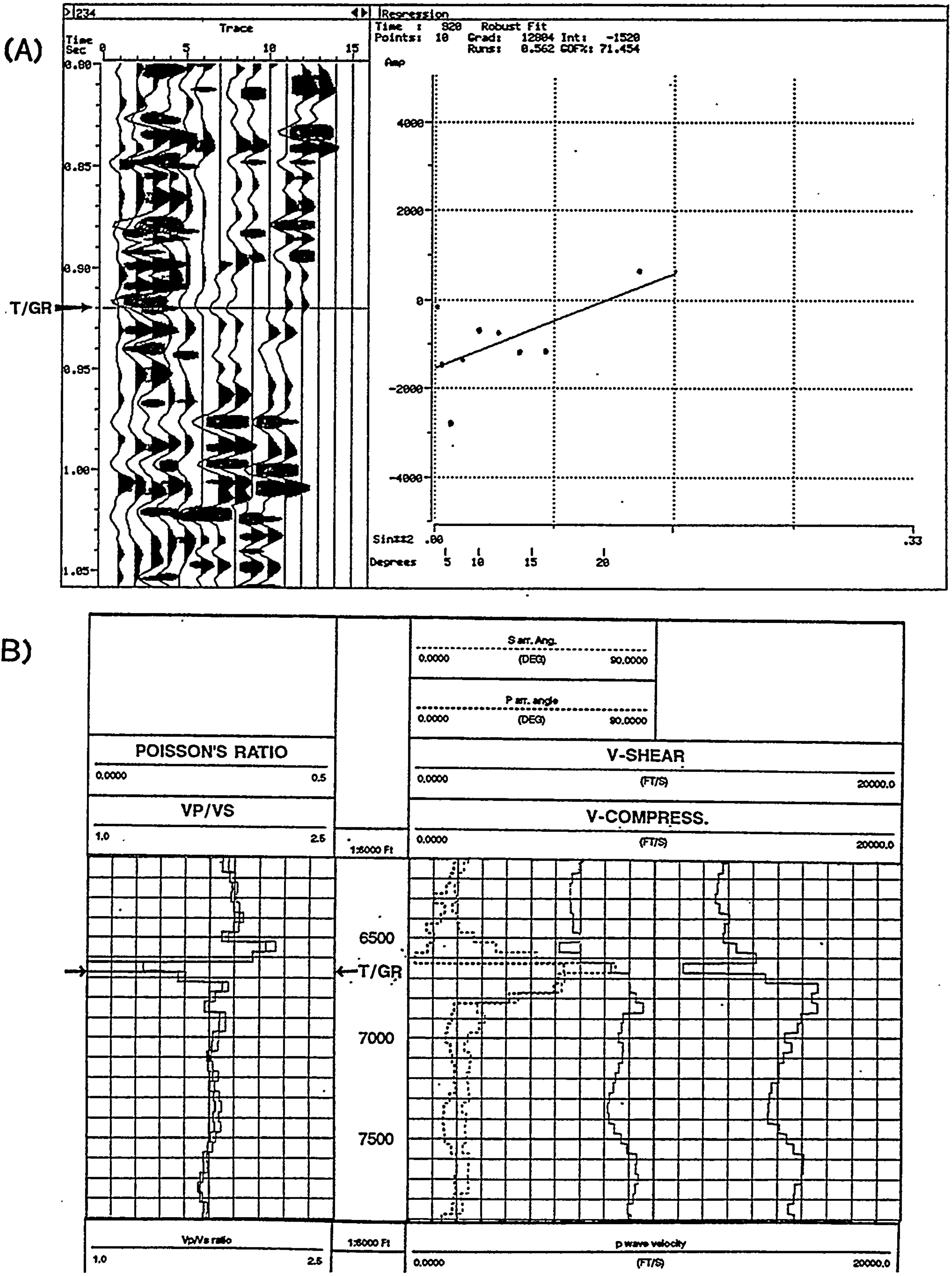

(A) Strong positive AVO gradient (12804) at line 2, CDP 234, time 0.920 sec. (T/Green River), 8 CDPs (600 ft) west of well I location. GOF is 71.45% (a fair fit). This is the nearest CDP to the well location containing sufficient offsets for AVO analysis.

(B) Portion of parametric inversion display from 9-component VSP in well I. Poisson's ratio, calculated from P and S-wave velocities from the VSP taken with a P-wave source offset 3050 ft. to the west, is extremely low at the top Upper Green River.

FIGURE 8-38

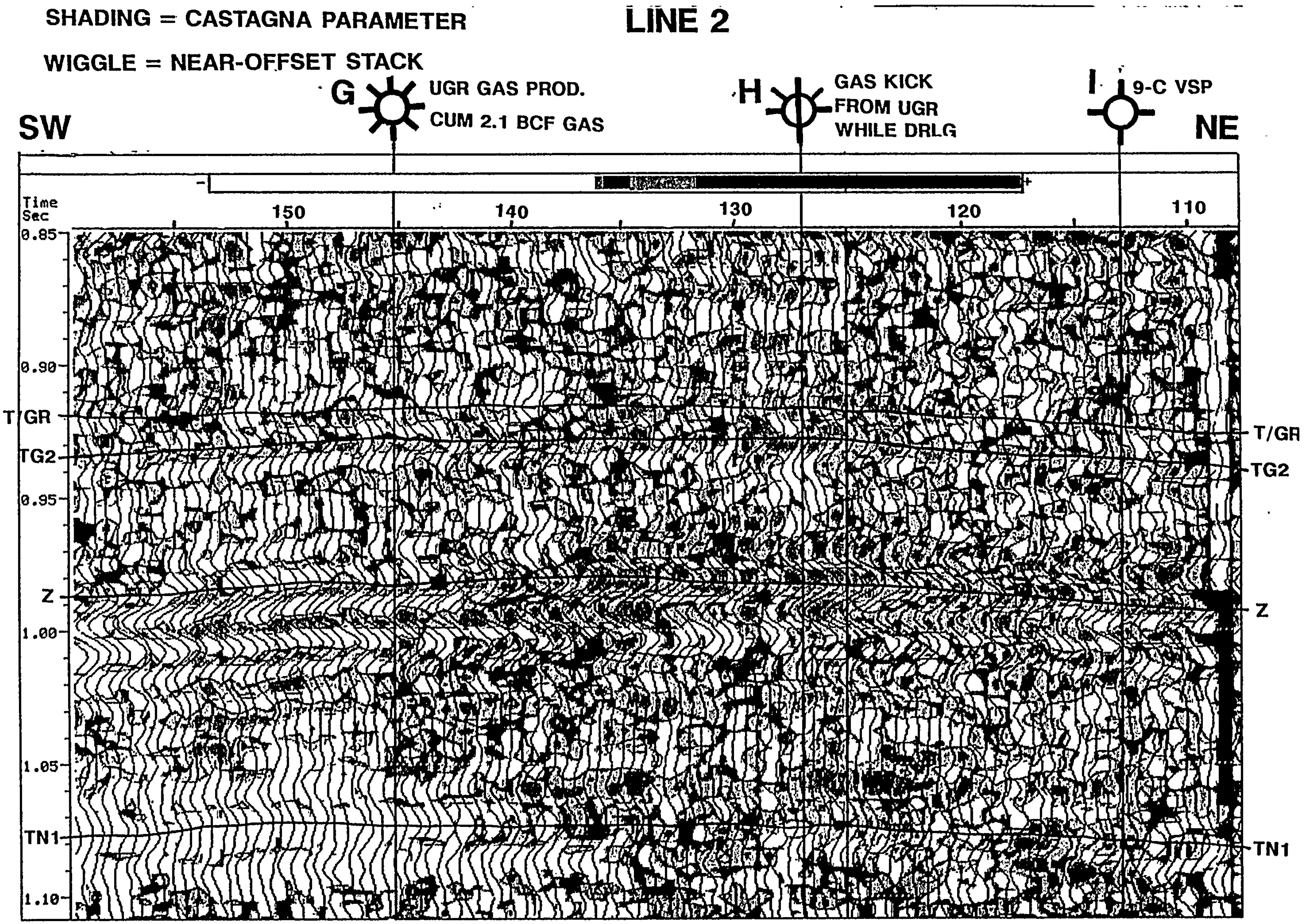

Castanga Parameter (AVO gradient + AVO intercept 12, see Appendix A) display for Line 2 showing positive AVO anomaly west of Well I.

FIGURE 8-39

▨ DST: 6553-6620 319 MCF/DAY T/GR

▨ DST: 6663-6761 169 MCF/DAY TG2

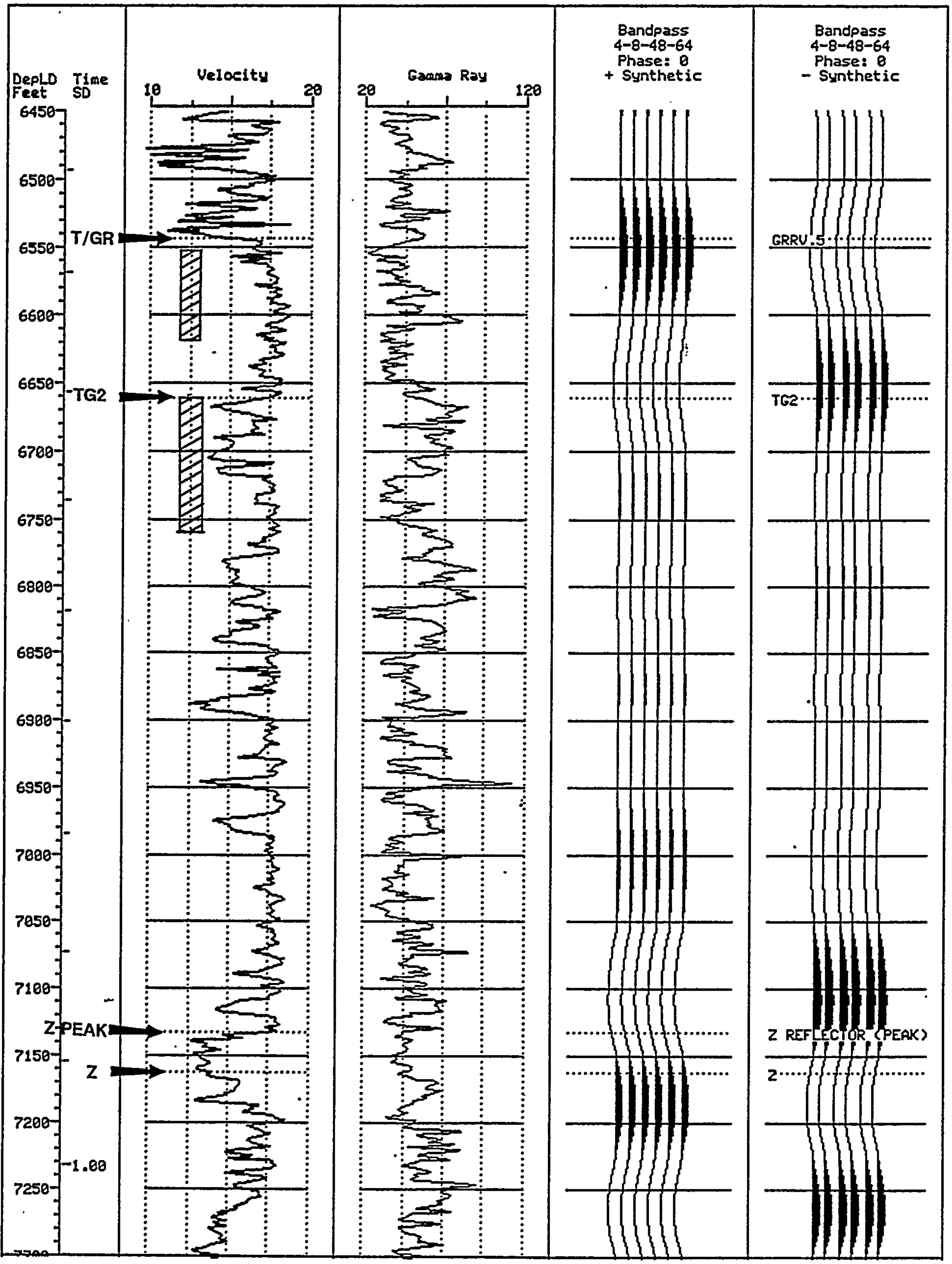

FIGURE 8-40

Sonic and gamma ray logs for Well D located at tie point, showing DST'd intervals near the T/UGR.

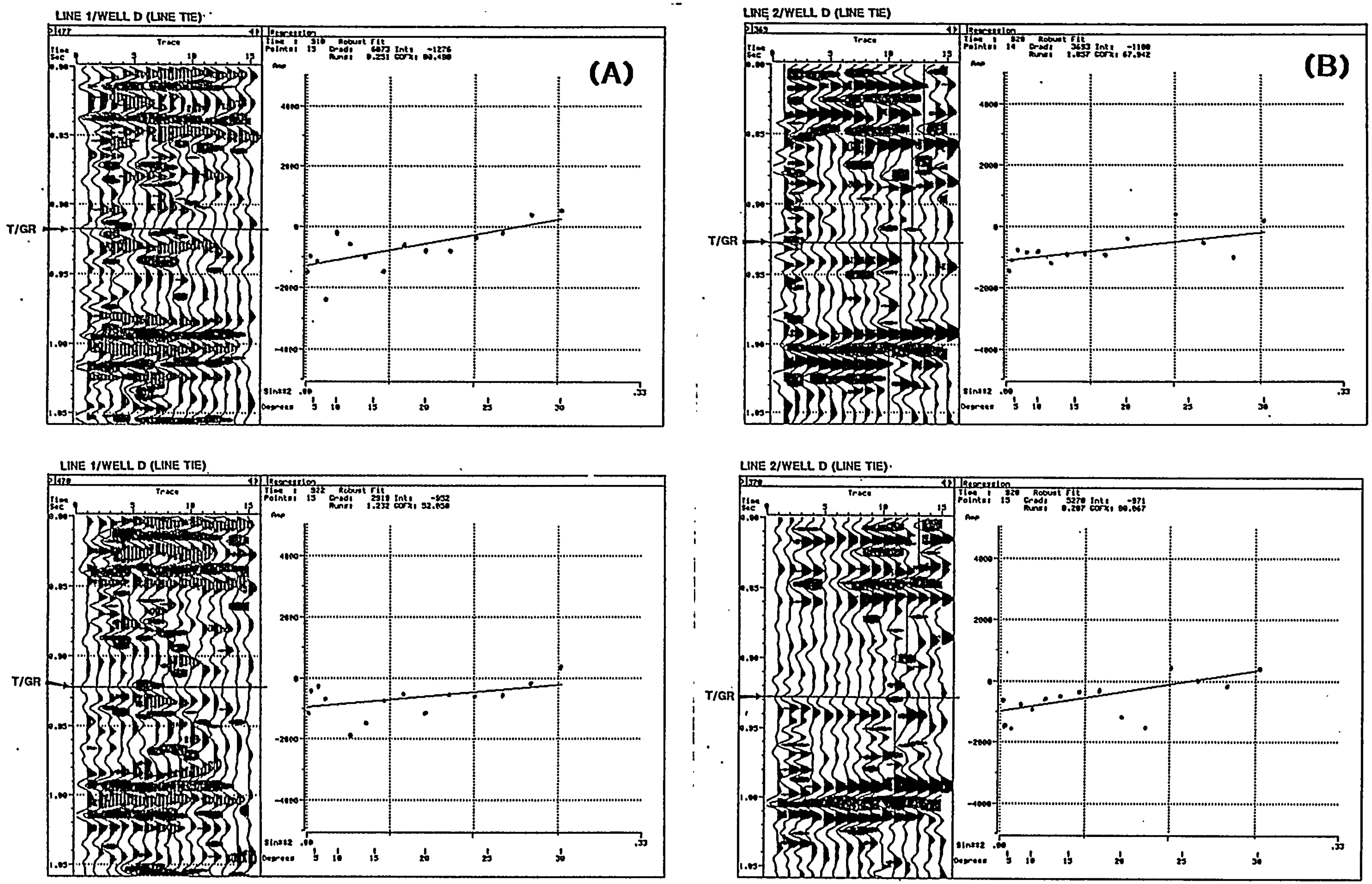

(A) Positive AVO gradients (+6073 and +2919) at Line 1, CDPs 477 and 478, line tie and 1 CDP south, time .918 and .922, T/UGR gas sand.

(B) Positive AVO gradients (+3693 and +5270) at Line 2, CDPs 369 and 370, line tie and 1 CDP west, time .928, T/UGR gas sand. Positive AVO gradients on both lines indicate an isotropic AVO response to the interval which flowed gas on DST. (Note: there is a static shift of 10 msec. between the gathers of the two lines, which was corrected for after stack).

FIGURE 8-41

8.4.2.2 Z Reflector: Well D

The Z reflector corresponds to a relatively low-velocity unit, as shown in Figure 8-40, sonic and gamma ray logs for Well D, which is situated at the intersection of the two lines. The lithological interpretation of the interface is a change from highly calcareous sand above to thinly laminated sandstones, siltstones and shales below. The low-velocity unit is laterally continuous and widespread, interpreted to thicken and become shalier in more stratigraphically basinward positions. Because the zero-offset reflection coefficient for this reflector is negative (a peak on SEG-polarity data) its seismic response is analogous to the Class III sand category in Figure 8-31b: there is no polarity reversal with offset for gas saturation, instead, the peak at zero offset becomes a higher-amplitude peak at far offsets. The AVO response at the Z marker is compared for azimuthal differences in Figure 8-42, showing the Castagna Parameter (an AVO parameter similar to the AVO gradient; see Appendix A) at the line tie. On Line 2 (right side), the AVO gradient is positive (shown as shading), while on Line 1 (left) it is negative. This is the most prominent AVOA anomaly in the P-wave data. The near-offset stack traces, shown as the wiggle trace overlay, are the same for both lines at the tie point. These figures also show the lateral extent of the anomaly (from Well D to Well E, a distance of 1,350 ft). AVO gradient plots for two CDPs at the tie point for both lines are shown in Figure 8-43, where the increase in amplitude with offset of the reflector on Line 2 (Figure 8-43b) is clearly seen, in contrast to the decrease in amplitude with offset on Line 1 (Figure 8-43a). These results are interpreted by the presence of northwest trending gas-filled fractures within the Z low-velocity clastic unit.

There is no current gas production from the vicinity of the Z reflector, and, therefore, the AVO response cannot be calibrated to known gas, as in the T/UGR - TG2 interval. However, the entire Upper Green River formation is considered potentially gas-bearing, and DSTs have recovered gas from sands within the Z unit in two wells, neither of which, unfortunately, are near the 1994 seismic lines.

The fact that the AVO response of the Z reflector in Figures 8-42 and 8-43 is strongly anisotropic indicates that it is likely to be caused by gas-filled fractures, striking parallel to Line 1 in the relatively low-velocity clastic. P-waves recorded on the long offsets of Line 2 would have traveled across these gas-filled fractures, lowering the effective Poisson's ratio in the medium. Along Line 1, the P-waves would propagate along the fractures, not sensing them. This sensitivity to aligned fractures with line direction is illustrated schematically in Figure 8-44.

8.4.2.3 Mahogany Bench Reflector: Well D

This reflector is similar to the Z reflector described above, in that it is the top of a low-velocity unit occurring throughout the basin, which is known as the "Mahogany Bench" (MB) or "Mahogany Oil-Shale." Lithologically it is interpreted

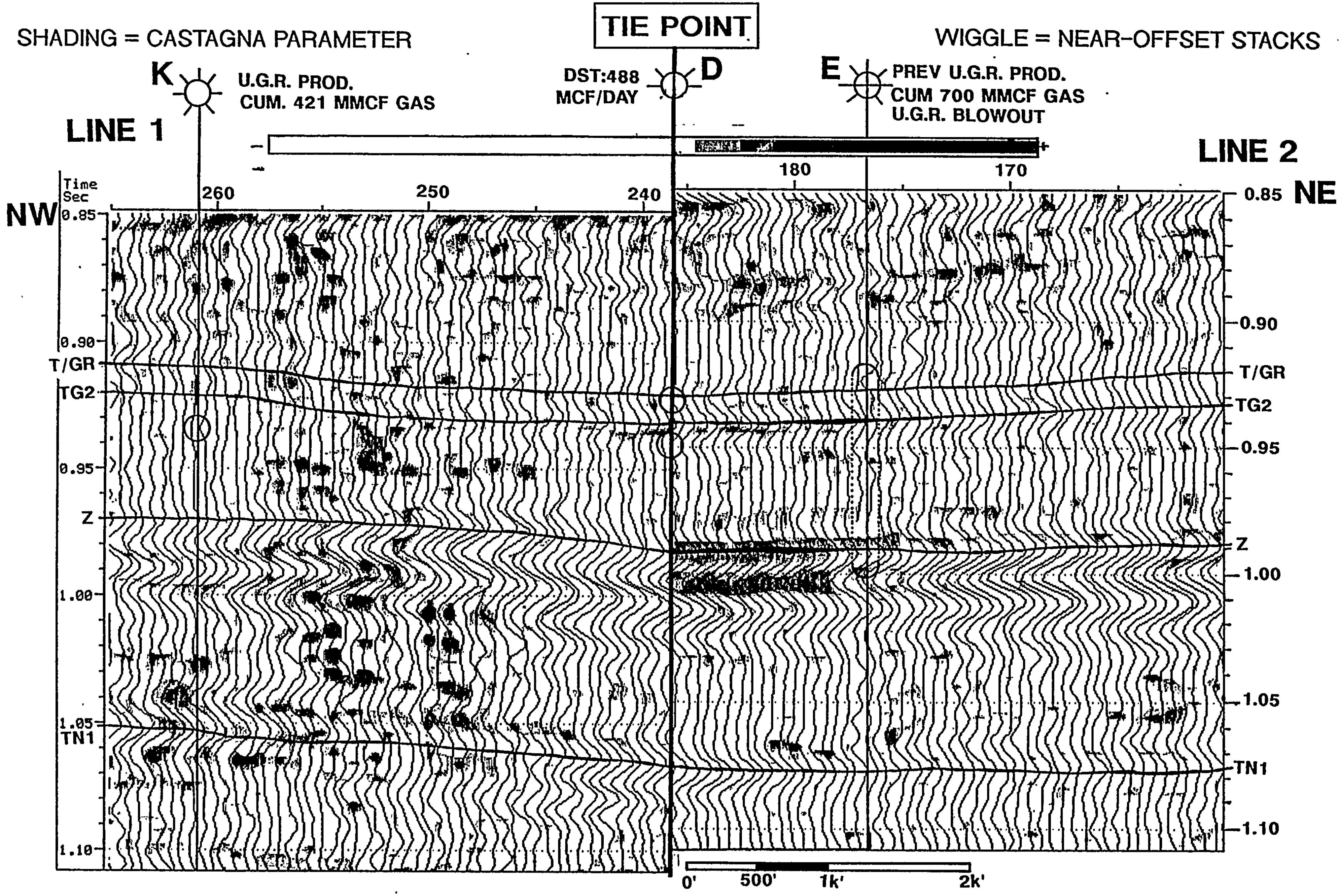

AVO response of line 1 (left) and line 2 (right), spliced together at line tie. Shading is Castagna Parameter [(AVO Gradient + AVO Intercept)/2] where positive values only are shaded; wiggle trace is near-offset stack. Note difference at Z reflector; the cause of the anisotropic AVO response is interpreted as NW-trending gas-filled fractures.

FIGURE 8-42

P-WAVE AVO REGRESSION ANALYSIS

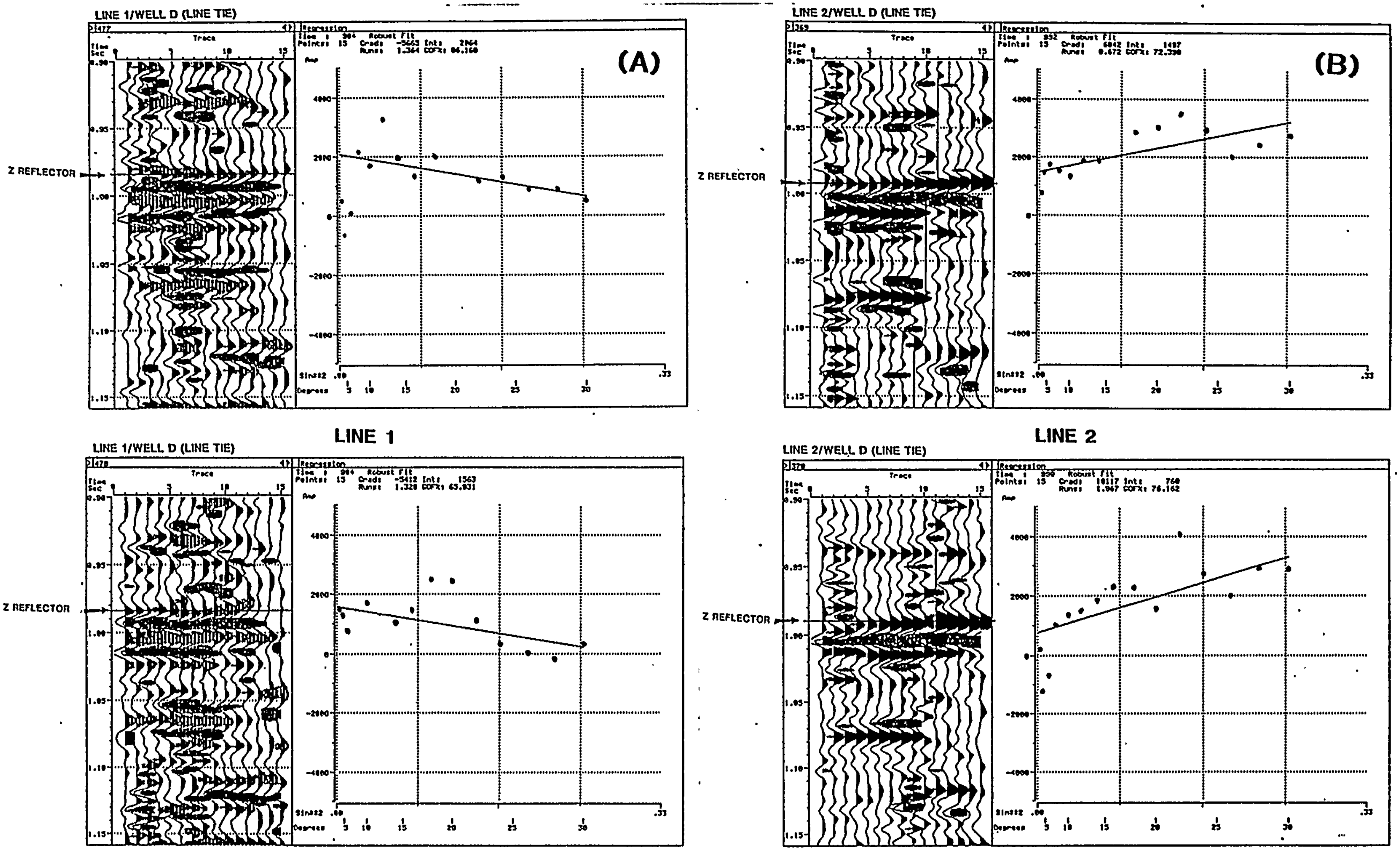

(A) Negative AVO gradients (-5665 and -5412) at line 1, CDPs 477 and 478, 1 CDP south of line tie and line tie location, time .984 sec., Z reflector.

(B) Positive AVO gradients (+6842 and +10117) at line 2, CDPs 369 and 370, 1 CDP (75ft) east of line and line tie location, time .992 and .990 sec., Z reflector. AVO gradients of opposite signs on lines 1 and 2 show dependence of AVO gradient on line direction.

FIGURE 8-43

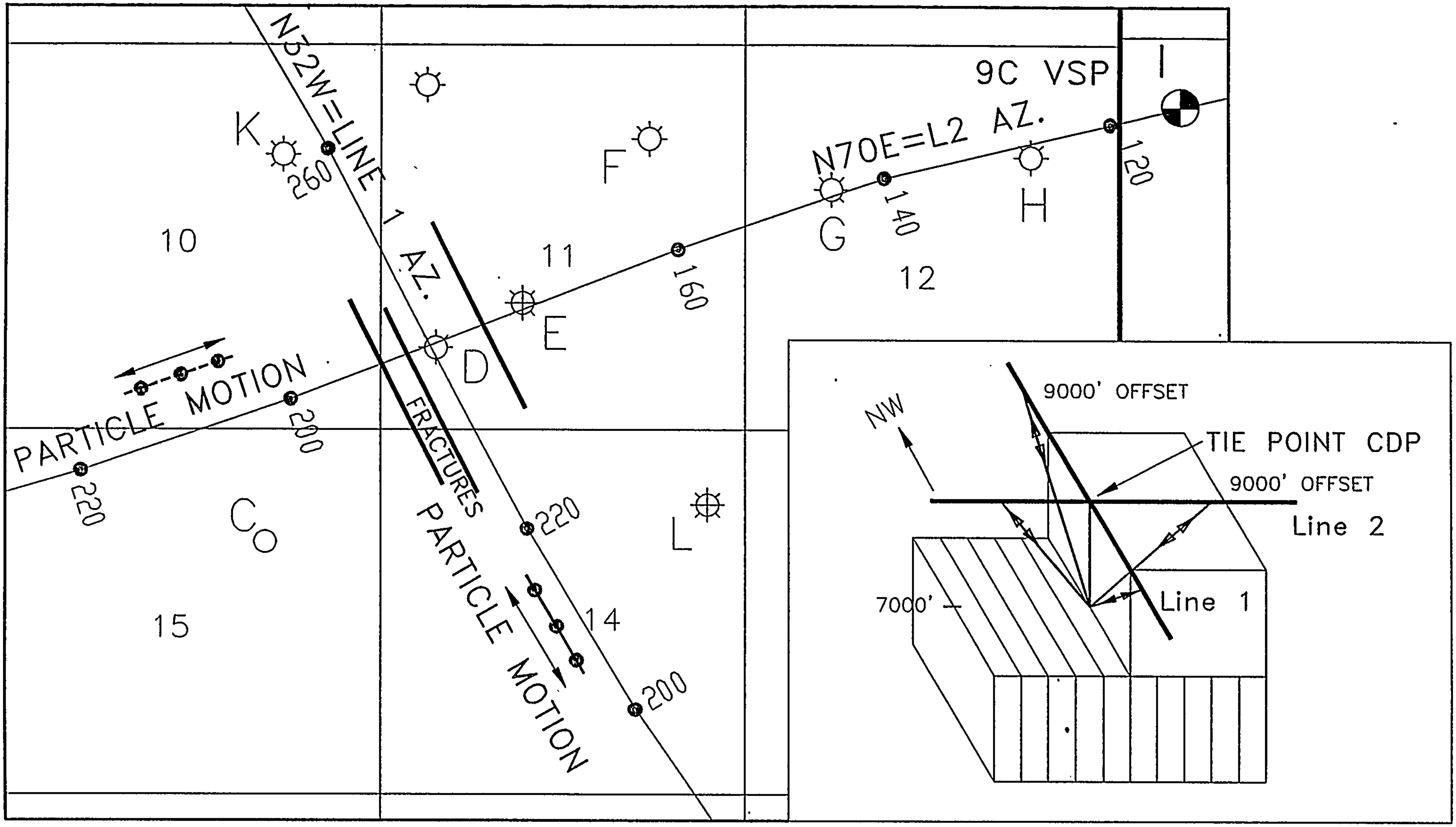

FIGURE 8-44

Schematic representation of anisotropic AVO response, showing P-wave particle motion on Lines 1 and 2 with respect to dominant NW fracture trend: P-waves on Line 1 are insensitive to fractures because source to receiver raypaths are parallel to fractures, while P-waves on Line 2 have raypaths which cross the fractures and do sense the fractures and their fluid or gas fill.

Figures 8-46a and 8-46b as calcareous shale at the line tie location. AVO gradient plots for two CDPs at the tie point for both lines are shown in Figure 8-45. The AVO gradient at this reflector is positive on Line 2, while it fluctuates from negative to positive on Line 1, once again showing a dependence on azimuth, although not as clearly as the dependence on azimuth seen at the Z marker.

8.4.2.4 Non-flow Intervals: Well G

The mud logs and production test history files of wells near the seismic lines were examined for zones within the Upper Green River which were drillstem tested and did not flow. The AVO gradients corresponding to these zones were near-zero and negative, consistent with the absence of gas in these intervals. For example, Well G was tested in the interval corresponding to the Z reflector with a result of no flow. The sonic and gamma ray logs for this zone and the corresponding AVO gradient are displayed in Figure 8-46.

8.4.2.5 Water-wet Intervals:

The AVO response at the T/UGR reflector at locations corresponding to downdip wells on both lines was investigated.

Well N

On Line 1, Well N, located at CDP 325, is structurally downdip and had no gas shows in the Upper Green River. The AVO regressions at Line 1 CDPs 324 and 325 show negative gradients for the T/UGR reflector (Figure 8-47a). If the T/UGR interval at this location were known to have NW-trending fractures, then, based on the examples cited previously, a negative AVO gradient on Line 1 would be inconclusive as regards gas saturation, since far offsets on Line 1, parallel to the fractures, would not sense the open fractures. However, since the S-wave reflection seismic showed near zero S-wave anisotropy (Figure 8-25), a near-zero fracture density or nearly isotropic rock at the T/UGR is interpreted. Thus for these conditions, the P-wave AVO gradient is interpreted to be valid for any azimuth (the negative AVO gradients represent an increase in Poisson's ratio, not consistent with the presence of gas, at this interface).

Well B2

Well B2 on Line 2, CDP 469, is also in a structurally low position. This well had no shows of gas, but did have traces of heavy oil reported in the mud logs. The AVO regressions for Line 2 CDPs 468 and 469, Figure 8-47b, show near-zero AVO gradients, both negative and positive. The weak positive AVO gradient for the T/UGR at CDP 468 is 42% smaller than the smallest Line 2 positive AVO gradient which is associated with gas production or DSTs in this study. The zero-intercept is also much closer to zero than for any gas sand reflector,

P-WAVE AVO REGRESSION ANALYSIS

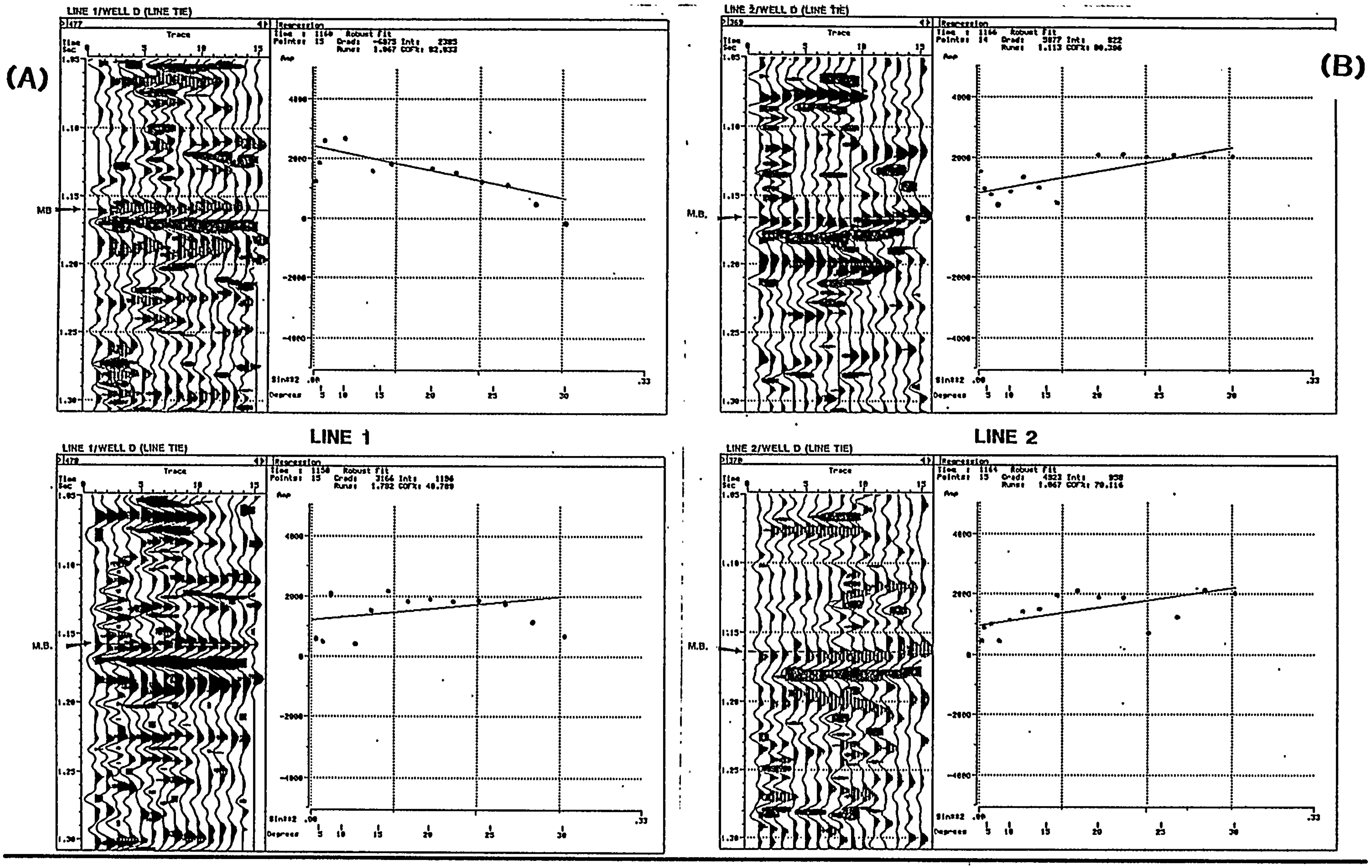

(A) Negative (-6975) and Positive (+3166) AVO gradients at line 1, CDPs 477 and 478, 1 CDP south of line tie and line tie location, time 1.160 and 1.158 sec., M.B. reflector.

(B) Positive AVO gradients (+5977 and +4923) at line 2, CDPs 369 and 370, 1 CDP east of line tie and line tie location, time 1.166 and 1.164 sec., M.B. reflector. Positive AVO gradients correspond to low Poisson's ratio in the medium below the M.B. reflector. Different AVO gradients on line 1 and line 2 indicate variation with line direction, although line 1 AVO gradient fluctuates near the line tie location.

FIGURE 8–45

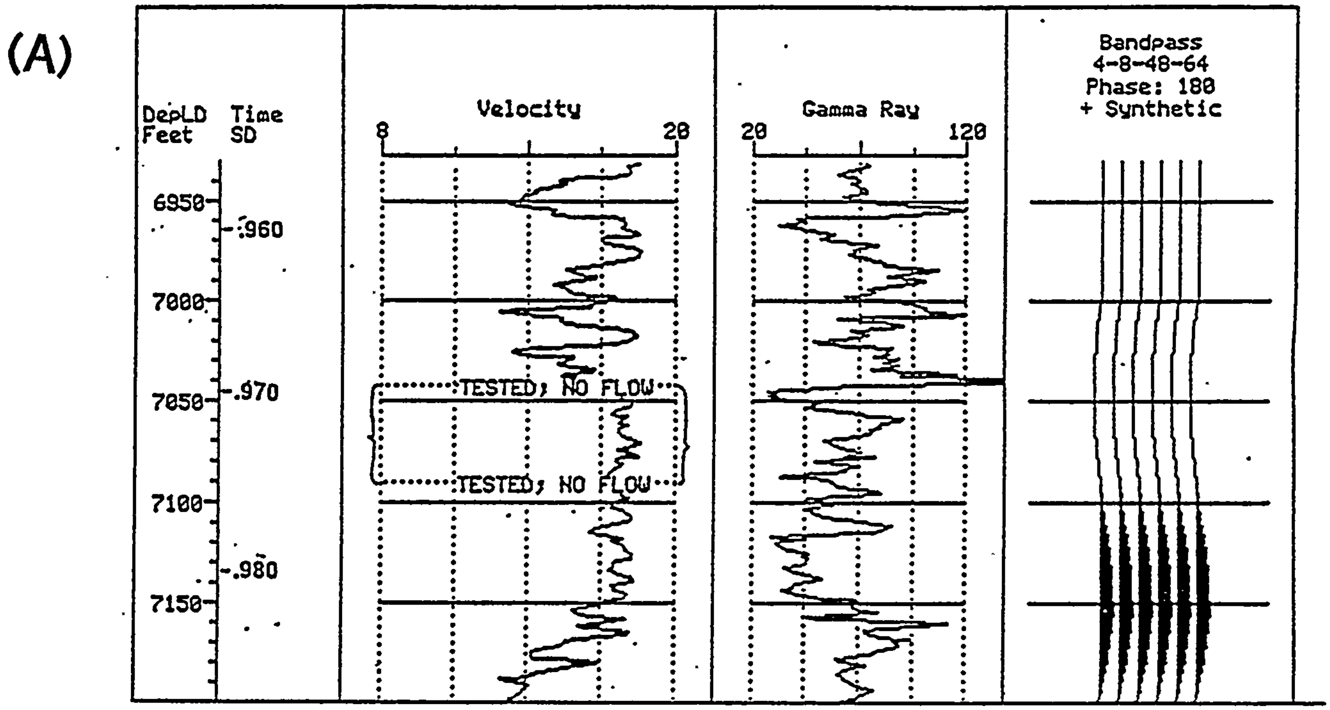

WELL G

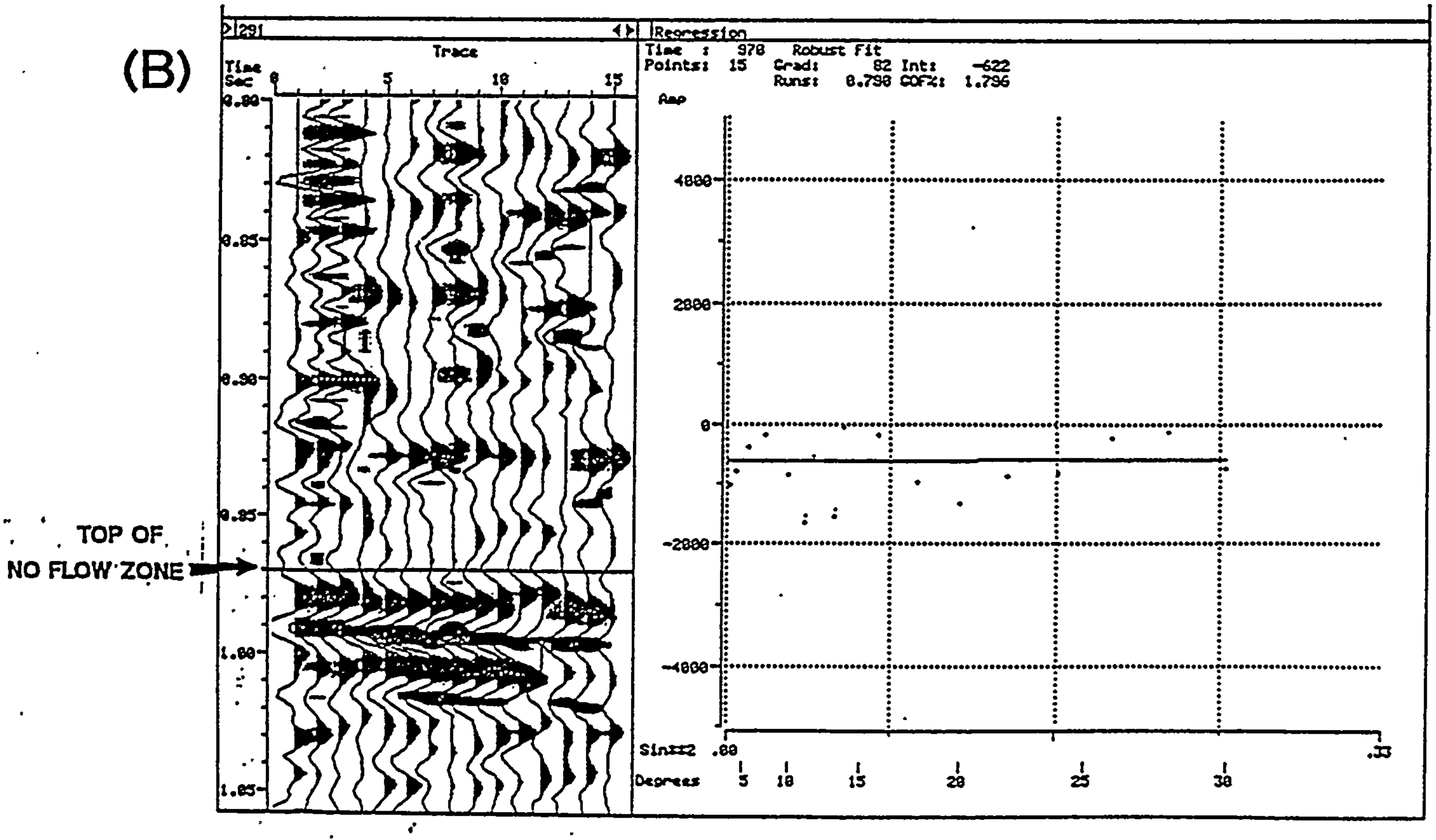

P-WAVE AVO-REGRESSION ANALYSIS

(A) Sonic and gamma ray logs over portion of well G where DST test did not flow.

(B) Flat AVO gradient (+82) corresponding to top sand at left.

FIGURE 8-46

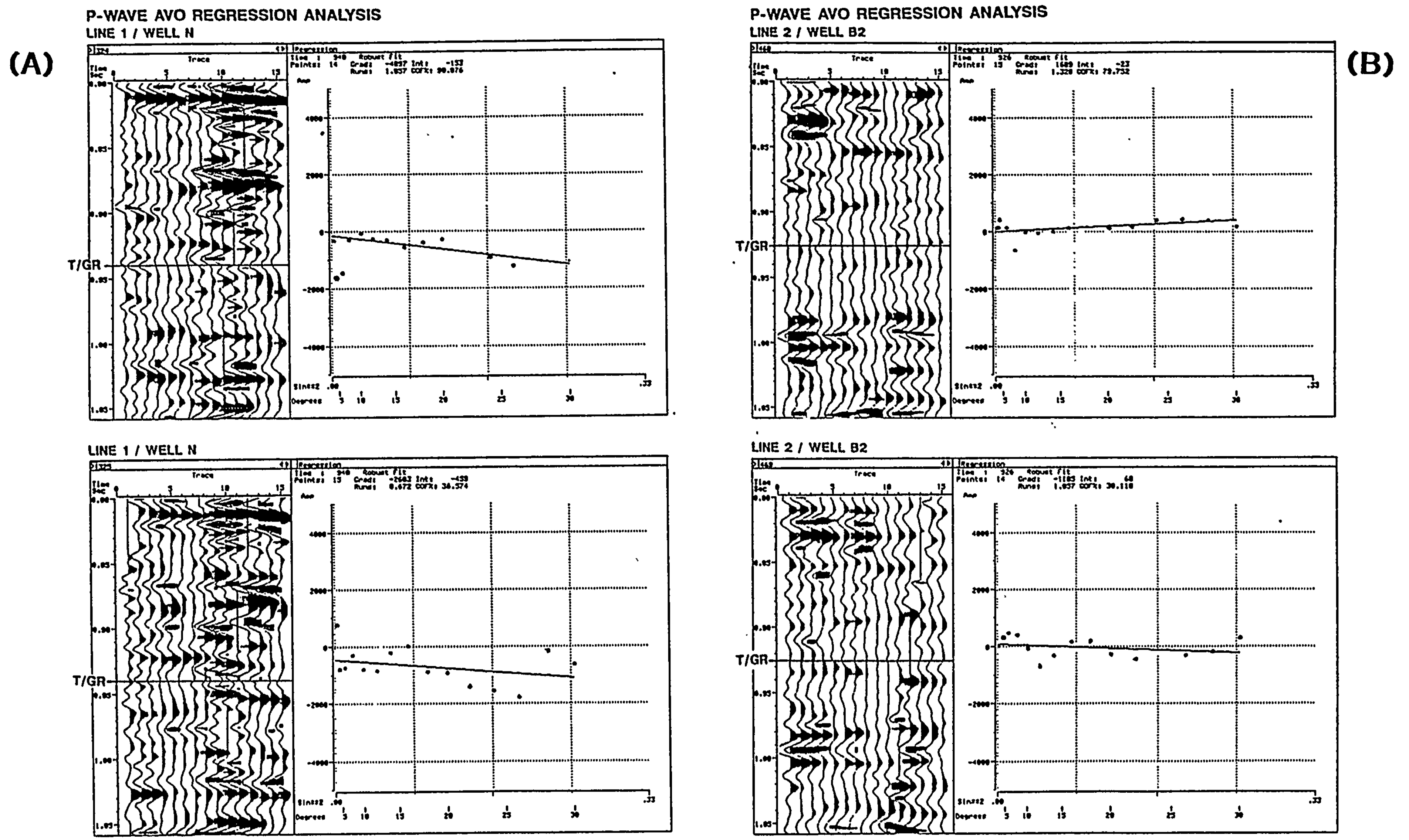

(A) Negative AVO gradients (-4097 and -2603) at line 1, CDPs 324 and 325, 1 CDP south of well N and well N location, time .940 sec., T/GR reflector. Negative gradients represent increase in Poisson's ratio beneath reflector. The top Green River is water-wet in this well.

(B) Near-zero AVO gradients (+1689 and -1185) at line 2, CDPs 468 and 469, 1 CDP east of well B2 and B2 location, time .926 sec., T/Green River reflector. The top Green River is water-wet in this well.

FIGURE 8-47

probably indicating a siltier sand at this location which would decrease the velocity. The S-wave anisotropy from the S-wave reflection seismic at this location is anomalously high, indicating NW-trending fractures within the interval T/UGR - Z, but the absence of a positive AVO gradient leads to the conclusion of the presence of water-filled fractures at this location, which is consistent with the lack of any gas indications in the mud log or wireline logs.

The observation of near-zero AVO gradients for both water-wet and no-flow intervals permits the calibration of AVO gradients on Line 2 into ranges for gas versus no-gas AVO response at the T/UGR, as shown in Figure 8-48. AVO gradients for reflectors corresponding to the tops of gas sands are clearly separated from those corresponding to non-gas sands on Line 2. On Line 1, gas pay zones are associated with negative AVO gradients, except for one case at the T/UGR at the tie point well, where matrix porosity was interpreted. With additional data, it is conceivable that the AVO gradient could be calibrated into discrete gradient bands corresponding to cases of gas and water saturation, for a specific reservoir reflector, on the line perpendicular to the dominant open fracture trend.

8.4.3 Elastic Modeling

The data recorded in this project match those of Allen and Peddy's (1993) model data (see Figure 4-5b) after the polarities are reviewed. With the polarity reversal, Allen and Peddy's <u>trough</u> reflection from a low-to-high acoustic impedance contrast exhibits a positive AVO gradient (becomes less troughy) on the line <u>perpendicular</u> to the gas-filled open cracks, thus indicating the presence of a low Poisson's ratio interval. On the line <u>parallel</u> to the cracks, Allen and Peddy's trough reflector appears constant in amplitude for angles out to 30°, past the angles contained in our data, thus exhibiting an approximately flat AVO gradient.

8.5 Conclusions

A summary of the interpretations is given in Figures 8-47 and 8-48, and Tables 8-5a and 8-5b with conclusion listed below:

1. Analysis of the AVO response of several Upper Green River reflectors showed that all known gas-productive intervals are associated with positive AVO gradients for seismic data <u>on Line 2</u>. However, gas producing intervals <u>on Line 1</u> display negative gradients, except for one case at the T/UGR at Well D. The oppositely signed gradients for known gas-producing intervals on Line 2 and Line 1 indicate the presence of gas-filled northwest-striking fractures at depth. These fractures have set the S1 azimuth as N45W in the 9-C VSP (in well I), and are seen in outcrop, core, and FMS data.

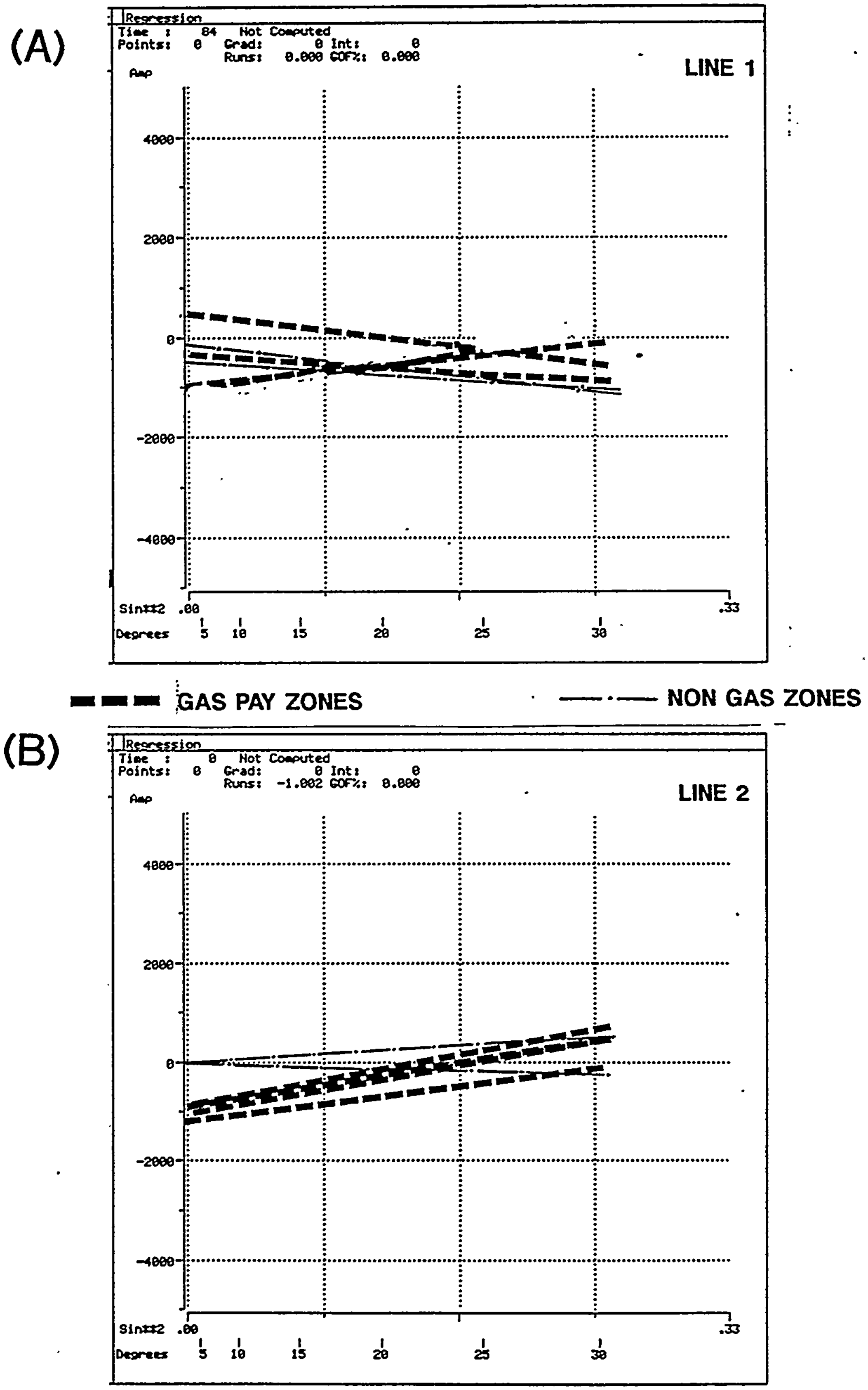

Range of AVO gradients observed on line 1(A) and line 2(B) gas-producing sands and non-gas sands in upper Green River, calibrated to wells closest to line. Gas pay and non-pay sands show overlap in AVO gradients and intercepts for line 1 and distinct separation for line 2.

FIGURE 8–48

2. Known non-productive intervals are associated with near-zero AVO gradients on Line 2. Since the range of AVO gradients observed at the T/UGR showed clear separation between gas and non-gas sands on Line 2, but no such separation was seen on Line 1, it is concluded that P-wave AVO is of most significant value only on lines nearly perpendicular to the dominant open fracture trend.
3. The Z and MB reflectors, which mark the tops of relatively low-velocity clastic units, show positive AVO gradients on Line 2 and negative gradients on Line 1 at the line tie point; this is attributed to gas within NW-striking fractures in the low-velocity units.
4. Based on the T/UGR AVO signature, it is postulated that there are also gas-filled fractures in the uppermost Green River at a location 600 ft west of the Well I.
5. The AVO parameter [(A + B)/2] published by Castagna and Smith (1994) was found to be useful for clarifying displays of the gas effect within the uppermost Green River, where the signal to noise ratio is sometimes poor and the AVO gradient alone gave inconclusive results.
6. Since the Poisson's ratio is greatly reduced within the first few percent of gas saturation, AVO techniques cannot distinguish between fully gas-saturated rocks and rocks with only low gas saturation.
7. At the line intersection, where there were DSTs which recovered 488 MCF/day in the uppermost Green River, considered as potential commercial pay, the AVO gradients were positive on both Lines 1 and 2. This suggests either the presence of gas in the matrix of the rocks, or equally well-developed gas-filled open fracture trends in both NW and NE directions.

Since the presence of a dominantly aligned fracture trend appears to limit the effectiveness of the AVO method to lines nearly perpendicular to the open fracture strike (from 2. above), then for AVO purposes, P-wave seismic should be acquired with as many lines as possible in the direction perpendicular to the fracture trend, or, as a multi-azimuth 3-D survey, as discussed in Lynn et al., 1995a.

Table 8-5a
Results Of Seismic Analysis At Wells Near Seismic Lines

Well	Production	S-wave Analysis	P-wave Analysis	S-wave Seismic Interpretation	P-wave Seismic Interpretation
T/UGR-Z Interval					
B2	Not tested; deep oil production	+12% anisotropy	Near-0 AVO gradient	12% fracture density, NW-trending fractures	Water in fractures
D	DSTs (potential gas production)	0 anisotropy	Positive AVO gradients at top DST'd sands on Lines 1 and 2	Matrix porosity in isotropic distribution of open fractures	Gas in matrix porosity in both crack sets
E	Blowout? cum. 700 MMCF?	+6% anisotropy	+ AVO gradient at T/UGR	NW-trending fractures	Low P.R. suggesting gas in fractures
G	cum 2.1 BCF	+5% anisotropy	+ AVO gradient at T/UGR	NW-trending fractures	Low P.R. suggesting gas in fractures
H	Not tested	+15% anisotropy	+ AVO gradient at T/UGR and lower sand	High density of NW-trending fractures	Low P.R. Þ gas in fractures
I	Not tested 9-C VSP well	+3% anisotropy +4% anisotropy (VSP)	Insufficient offsets for AVO at well location	NW-trending fractures (VSP)	600 ft west of well low P.R. suggesting gas
K	421 MMCF	+5% anisotropy	- AVO gradient at T/UGR	NW-trending fractures	AVO inconclusive (line 1 ½ cracks)
N	Not tested	0 anisotropy	- AVO gradient at T/UGR	No fractures	No gas

Table 8-5b
Results Of Seismic Analysis At Wells Near Seismic Lines

Well	Production	S-wave Analysis	P-wave Analysis	S-wave Seismic Interpretation	P-wave Seismic Interpretation
Z-TN1 Interval					
D	Not tested	+14% anisotropy	Line-dependent AVO: Line 1 -AVO gradient Line 2 +AVO gradient	High density of NW-trending fractures	Low P.R. suggesting gas in fractures
E	Blowout? cum 700 MMCF?	+4% anisotropy	+AVO gradient at upper Z peak	NW-trending fractures	Little remaining gas in fractures
N	Not tested; deep oil production	+7% anisotropy	-AVO gradient at T/UGR	7% fracture density NW-trending fractures	Water in fractures

Tables 8-5a and 8-5b summarize the results of the interpretation of the multi-component surface seismic data within the two reservoir intervals that have shown both potential for gas production and the most significant seismic anomalies associated with fractures and gas. The anomalously high S-wave anisotropy and the P-wave AVO anomalies are also shown in map form in Figures 8-49 and 8-50.

8.6 Cost-benefit Analysis

The 33 trillion cubic feet (TCF) of the technically recoverable natural gas resources in the lower 48 states has been identified as reserve growth potential from currently discovered tight gas sand reservoirs. Precise mapping of fractured reservoirs is, therefore, critical to the reserve growth potential. Economical production of natural gas from tight reservoirs can be achieved in zones that have been adequately fractured by geologic processes. The desired information from this project is: 1) seismic detection of relative fracture density in the subsurface target formation; and 2) seismic detection of fracture azimuth.

While shear wave seismic techniques offer the most conclusive evidence for relative fracture density and fracture orientation, P-wave AVOA (amplitude variation with offset and azimuth) was identified in the bid proposal as a possible low cost-high benefit technique for detecting high fracture density and fracture azimuth.

A cost evaluation of the techniques used in this project is given below. Figure 8-51 presents the percents of costs for site selection, 9C-VSP, P-wave reflection seismic, S-wave reflection seismic, and supporting geologic analysis (core

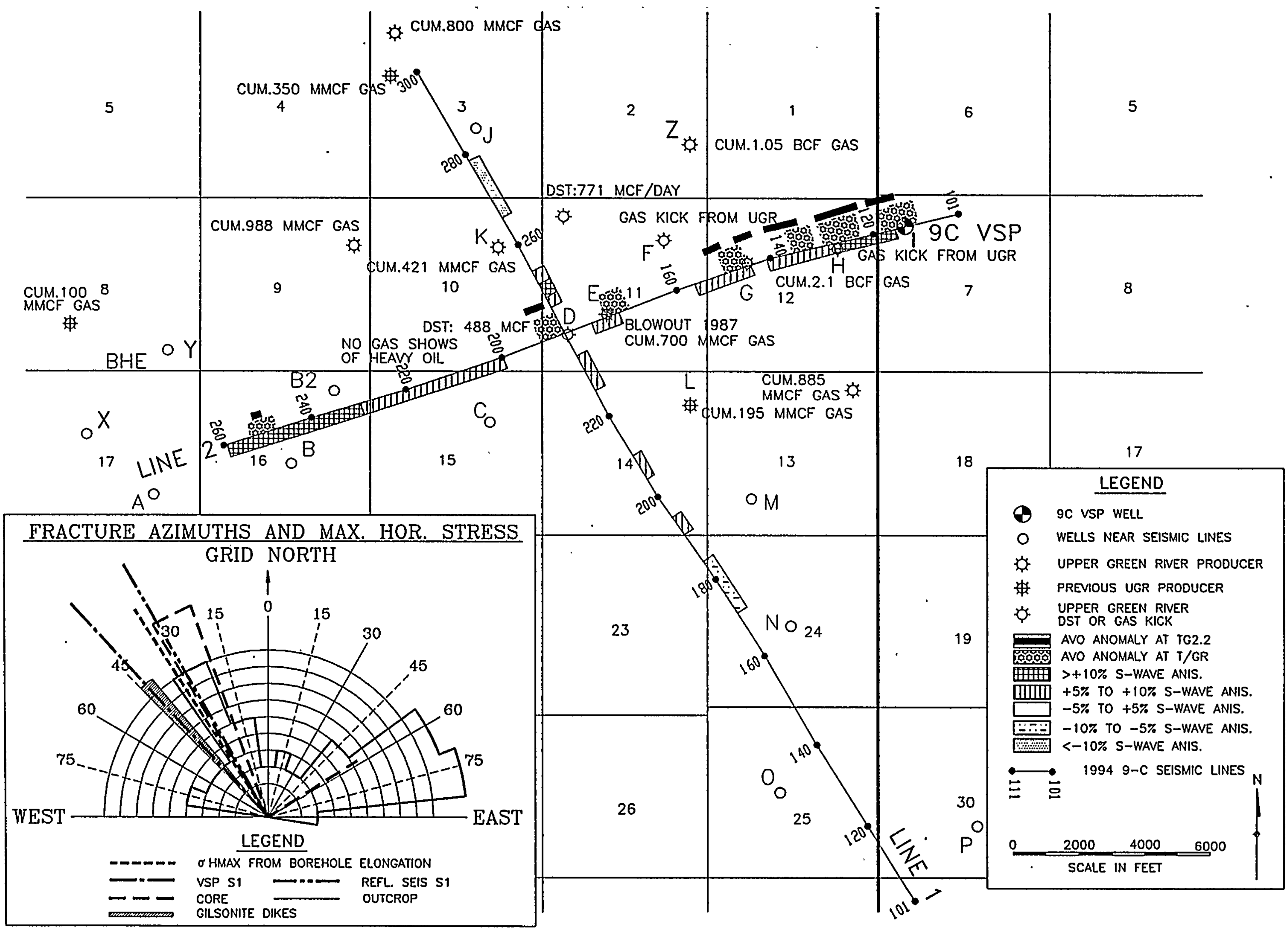

Composite Anomaly Map, T/GR - Z Interval: P-wave AVO anomalies: stars denote positive AVO gradient at T/GR shale/sand interface; (▬) denote positive AVO gradient at second upper Green River shale/sand reflection (sand in TG2.2-TG2.3). S-wave anisotropy shown by density orientation of line shading.

FIGURE 8-49

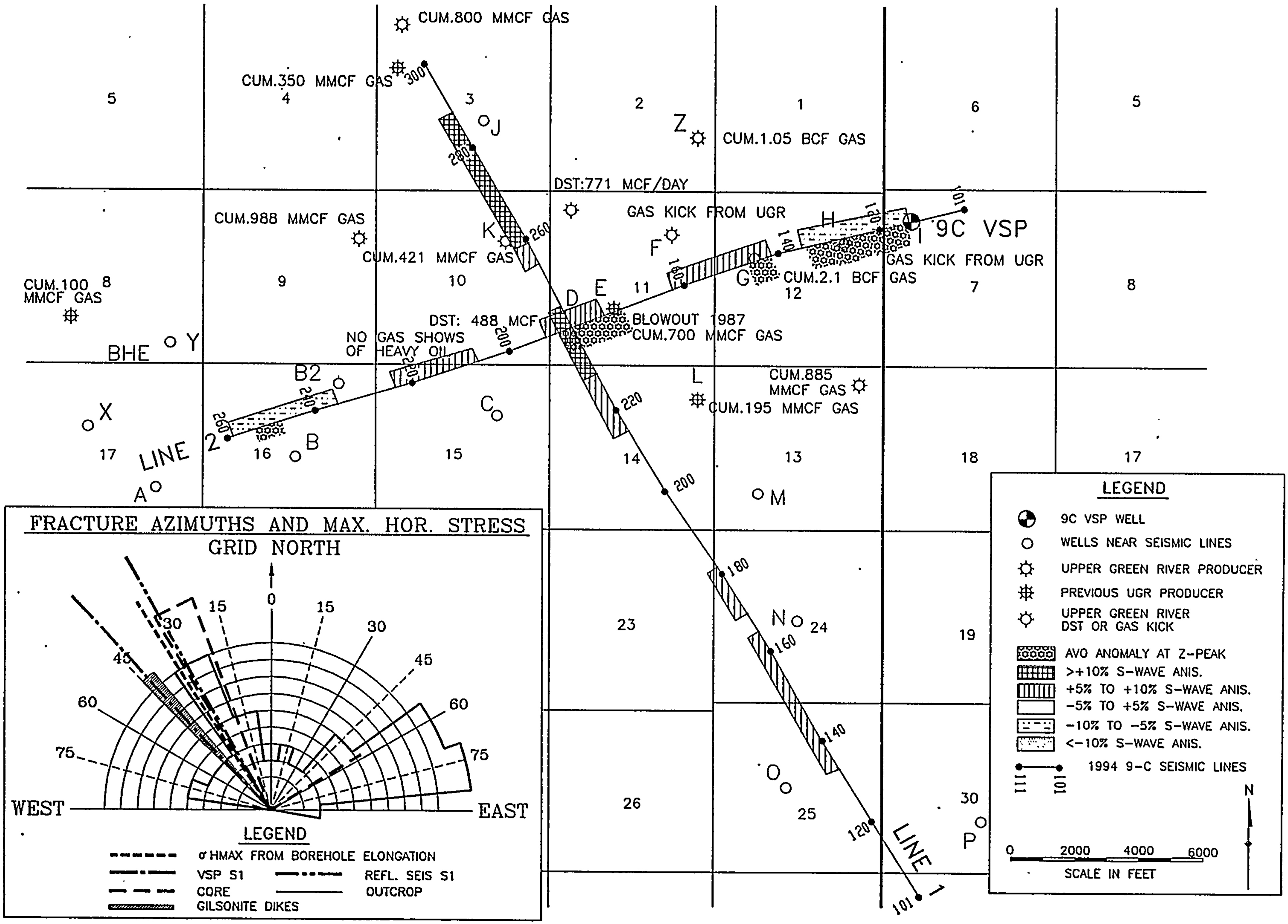

Composite Anomaly Map, Z - TN1 Interval: P-wave AVO anomalies at Z-Peak denoted by stars; S-wave anisotropy shown by density/orientation of line shading.

FIGURE 8-50

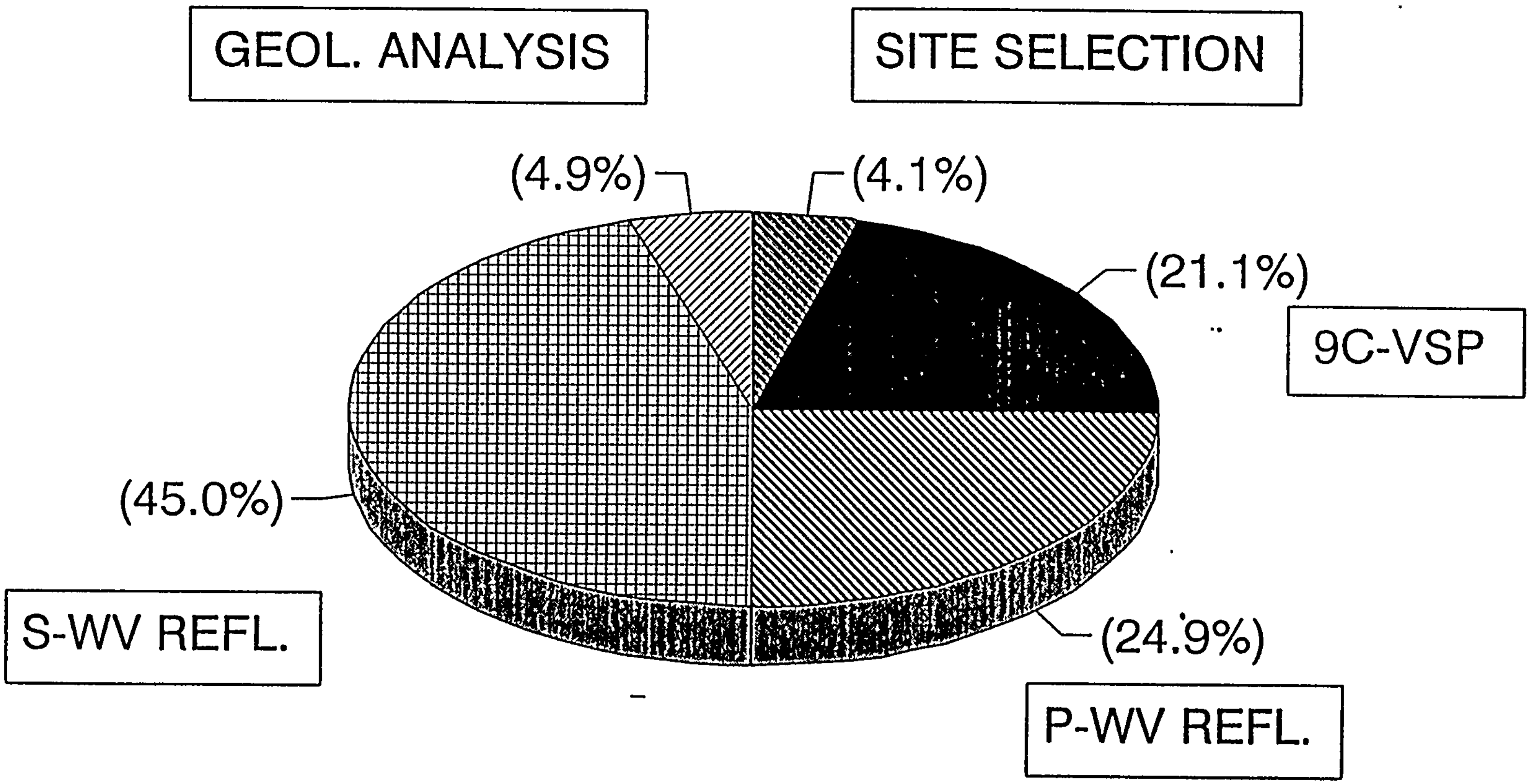

FIGURE 8–51

Cost in percent of each facet of the project.

studies, seismic modeling). The total cost of the project was approximately $943,800. Figure 8-52 shows the dollar amounts among these four categories, with further breakdown into acquisition (including planning), processing, and interpretation. The S-wave reflection costs comprise 45% of the total cost of the project.

8.6.1 9C VSP

The benefits of the 9C VSP are:

1. Identification of the S-wave reflectors, key to the project, for calculating interval S1 and S2 traveltimes in zones of interest.
2. Identification of the S1 azimuth with depth.
3. Identification of the azimuthal anisotropy (crack anisotropy) with depth: the reservoir unit showed the dramatic increase in shear wave splitting;
4. The reflection coefficients (corridor stacks) of the S1 and S2: the S2 dimmed while the S1 was bright at the velocity increase at the T/UGR.
5. Identification of the P-wave reflectors.
6. VP/VS of the intervals of interest.

8.6.2 P-wave Surface Seismics

The benefits of the P-wave reflection data are:

1. P-wave AVOA at the tie point; key to the project was the P-wave AVO response at the gas-producing well on the line parallel the cracks (no gas-response) and the P-wave AVO response at the gas producing well on the line perpendicular the cracks (gas-response).
2. P-wave stratigraphic seismic response.
3. P-wave structural (time) setting.

8.6.3 S-wave Surface Seismics

The benefits of the S-wave reflection data are:

1. Percent shear wave anisotropy along the lines for the intervals of interest: this documents the relative crack density along the line and the open fracture azimuth - key to the project.
2. Documentation that the P-wave AVOA anomaly at the tie point is associated with an interval showing a 15% shear-wave anisotropy anomaly (zones having produced ~2 BCF gas show 5% shear wave anisotropy; zones with virgin gas pressures show 15% shear wave anisotropy).

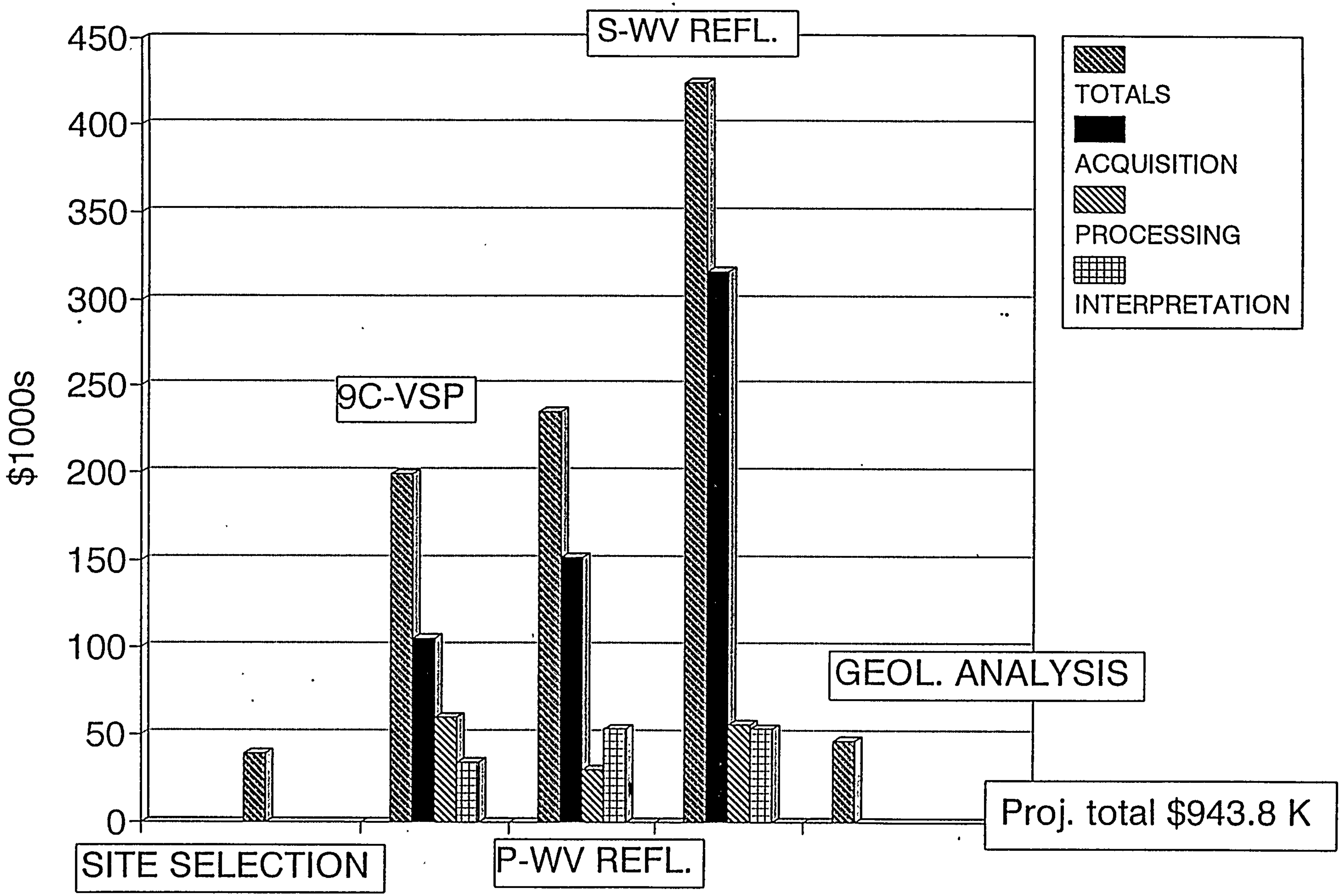

Cost in dollars of each facet of the projects, showing breakdown of each facet into acquisition, processing and interpretation.

FIGURE 8–52

3. VP/VS ratio along the lines for the intervals of interest. This is useful for stratigraphy and for gas detection.

8.6.4 Geologic Analysis

The benefits of the geologic analysis (core analysis and seismic modeling) are the integration of the seismic with the geology - a necessary piece of the project.

8.7 Summary and Recommendations

Each of the above aspects is a necessary part of this project, to demonstrate the relationship between P-wave AVO analysis, shear wave anisotropy, fractures, in-situ stress, and horizontal permeability anisotropy. Due to plant, well and operational difficulties, no two adjacent wells were on line at a useable time in order to investigate the communication between wells, and thus there was no documentation of the horizontal permeability anisotropy. When the site-specific relationship between shear wave anisotropy and fractures with depth is established, multi-azimuth P-wave AVO analysis can be used on previously acquired P-wave data sets (of proper orientation). Either 2-D or 3-D P-wave data sets, properly acquired and properly processed, may be re-interpreted for relative fracture density using similar techniques to those documented in this project.

The recommendation for subsequent work is that multi-azimuth P-wave data be analyzed to investigate P-wave AVOA. This work would necessitate local calibration with a 9C VSP of the time-depth-velocity function of S1 and S2, as well as the S1 azimuth and percent anisotropy. Local calibration with mode-converted seismic (P-S) using 3-component phones and P-wave sources would also allow a space-variant, well-by-well analysis of the relationship between shear wave anisotropy and P-wave AVOA.

9.0 CONCLUSIONS

Two lines of nine-component (9C) surface seismic reflection data, and two 9C Vertical Seismic Profiles, were acquired in Upper Green River gas reservoirs of the Bluebell-Altamont field, in northeastern Utah. The work is one of four projects sponsored by the U.S. Department of Energy, to demonstrate how exploration for and reservoir characterization of naturally fractured gas reservoirs can be more effective with the use of seismic technologies. This multi-disciplinary project integrated the seismic response (both P-wave and S-wave) with the geologic setting (including stratigraphic changes, structural setting, stress field) and changes in fracture density and orientation. Evidence of fractures was obtained from geologic sources, and production data, including information on preferred flow direction in the reservoirs (maximum horizontal permeability).

Gas production in Bluebell-Altamont field is from numerous sandstones and carbonates in the Tertiary Upper Green River formation, at depths of approximately 6,500 ft to 8,500 ft. The local geologic setting is one of very gentle anticlinal relief (<50 ft), which was an important consideration in the design of the project. This area is considered appropriate for 2-D seismic. Other areas require 3-D seismic, due to structural complexity. Matrix porosity in the reservoir rocks is generally low (between 2-10%). Permeabilities are also low, such that fracturing yields substantially higher commercial production rates. Consequently, seismic detection of fracturing is a potentially important aid to field development of the reservoir.

In this project, both P-wave and S-wave data were used, because both types of seismic waves respond, in different ways, to vertical, aligned, gas-filled fractures. The P-wave response observed at Bluebell-Altamont is an azimuthal variation of AVO signature (AVOA), which is seen to depend on source-receiver azimuth relative to fracture strike. This observation is consistent with modeling work of Allen and Peddy (1993). Analysis of azimuthal P-wave AVO variation has been successfully used to position gas wells in a naturally fractured reservoir by Johnson (1995).

S-wave polarizations in VSP data have been found to be a reliable indicator of the stiff and compliant directions in the rock. The stiff direction is usually parallel to the open fracture orientation and/or the maximum horizontal stress direction (Crampin, 1985), and the compliant direction in the rock is usually perpendicular to the open dominant open fracture orientation. For vertically propagating shear waves in flat-layered media containing vertically aligned fractures, the fast shear wave, S1, is polarized parallel to the stiff direction of the rock, and carries information about the rock matrix. The slow shear wave, S2, is polarized in the compliant direction, and carries information about the fracture density. Mueller (1991) used reflection S-wave data as fracture azimuth and density indicators. In this project, both the 9C VSPs and S-wave reflection data were used to explain the P-wave AVO results. Local seismic calibration using a 9C VSP is essential for this type of work.

Direct evidence of vertical fractures from cores, and fractures mapped on outcrops were used to orient the surface seismic lines in the field. The in-situ stress field was estimated from various sources including published maps and borehole elongation observed in four-arm caliper logs in two adjacent wells. The geologic, engineering and production data were integrated to understand how the seismic anisotropy relates to the fracture network, the in-situ stress field, and ultimately the preferred reservoir flow direction. The hypothesis is offered that the maximum horizontal permeability direction is consistent with the S1 azimuth, in that the open fractures dominating the seismic response are flow conduits.

The seismic reflection lines were oriented to be nearly parallel and perpendicular to the dominant fracture azimuth, as identified from regional studies, outcrop mapping and core analysis. The normal incidence, isotropic P-wave reflection seismic response was modeled from sonic logs and the resultant P-wave synthetic data used as a reference for further work. The P-wave surface seismic data showed azimuthal variations in AVO response at the tie point of the seismic lines, interpreted to indicate vertical, aligned, gas-filled fractures. The 9C VSP documented the fast shear (S1) and slow shear (S2) polarizations, S1 and S2 reflection characters, and travel time anisotropy in the fractured Upper Green River. The S-wave reflection seismic lines displayed travel time and amplitude anomalies consistent with the geologic evidence of the dominant open fracture azimuth (N40W). The S-wave data were interpreted for fracture orientation and relative fracture density along the lines. The consistency between the P-wave AVO and the S-wave anisotropy interpretations provided confidence in the use of P-wave pre-stack data to correctly characterize the fractures in this naturally fractured reservoir.

9.1 P-WAVE AVO ANALYSIS

The most significant conclusion from the P-wave AVO analysis is the dependence of AVO response on line azimuth, indicating that the AVO gradient is azimuthally anisotropic in this fractured gas reservoir. Figure 9-1 shows the anisotropic AVO response of the Z reflector (roughly at the middle of the gas-producing Upper Green River formation) at the line tie.

AVO gradients were calculated along the two seismic lines which were oriented approximately parallel and perpendicular to the presumed dominant fracture direction as determined from core analyses and outcrop mapping. The hypothesis to be tested was that the AVO response would be different when source-receivers were parallel or perpendicular to the dominant gas filled fracture direction. The AVO gradients were calculated using Shuey's simplification of the Zoeppritz equations (Shuey, 1985). The AVO signatures for the reflection from the T/UGR reservoir sand (a Class II sand, using Rutherford

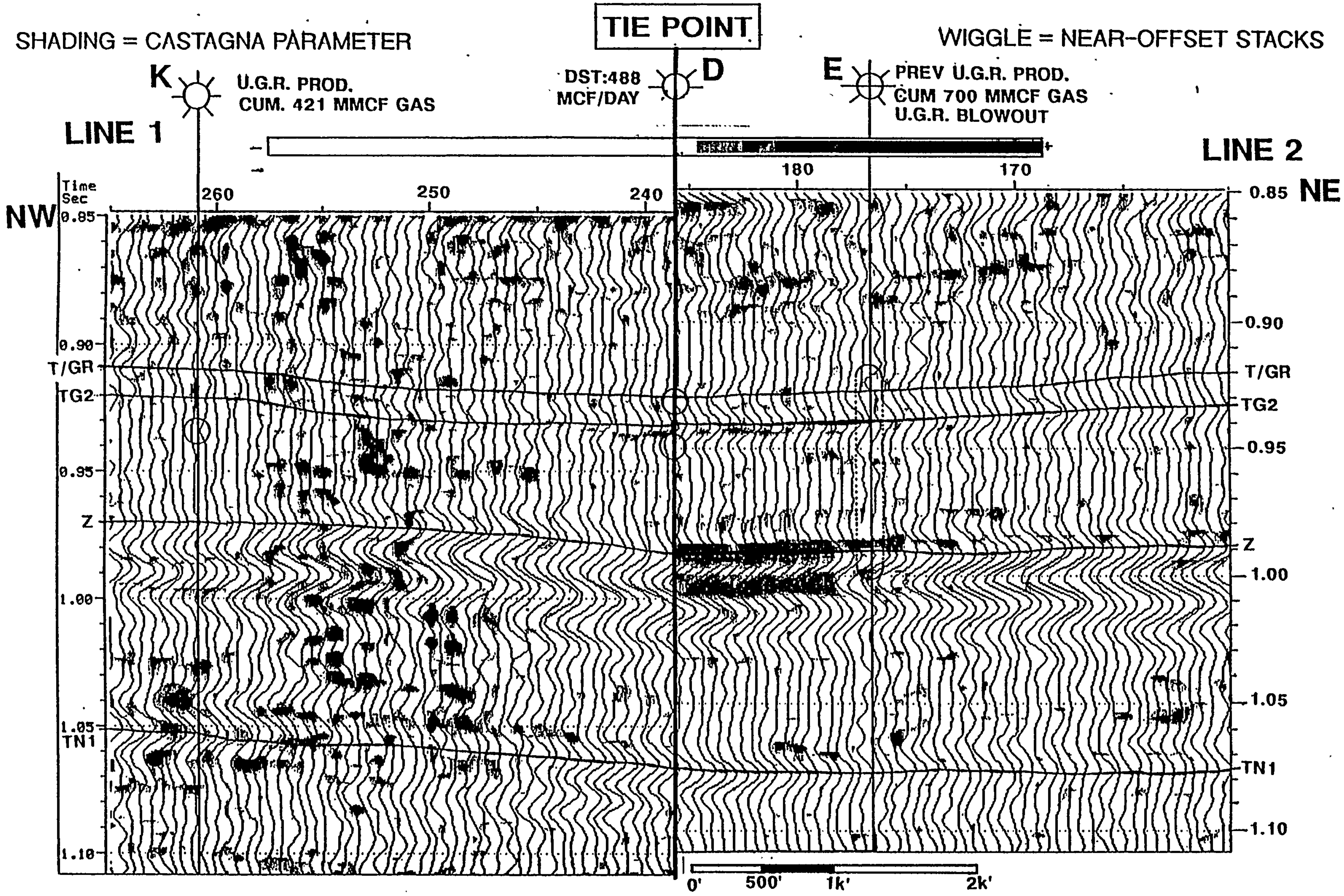

The anisotropic AVO response of the Z reflector (roughly at the middle of the gas-producing Upper Green River Formation) at the line tie.

FIGURE 9-1

and Williams', 1989, nomenclature) on the lines parallel and perpendicular to the open, gas filled fractures were compared and were different. The seismic response of the SEG normal polarity data was that the line *perpendicular* to the NW open fractures showed a positive AVO gradient at the producing interval in a well with high cumulative gas production. However, gas production from a different well on the line *parallel* to the open fractures was characterized by a negative AVO gradient at the same gas-producing interval. The conclusion drawn from this observation was that the far offsets of the line perpendicular to the open fractures sense a low Poisson's ratio in the fractured gas interval, because the P-waves have traveled across the fractures and sensed the extra compliance within the rock, while on the line parallel to the open fractures, the P-waves have propagated through the matrix, sensing neither the cracks nor their contained gas.

At the top gas zone in a well located at the line intersection, the AVO gradient showed a similar positive slope on both lines. This was interpreted as indicating the presence of significant matrix porosity, since gas in matrix porosity causes an isotropic AVO response. This is in contrast to the different AVO gradient response observed in the producing wells on the two lines, described above, which was attributed to gas in NW-trending open fractures. The S-wave reflection data at the line intersection supported the interpretation of matrix porosity, not fracture porosity, for this interval.

Other reflectors at the line intersection, and most notably the Z reflector, show anisotropic AVO responses, where the line perpendicular to the dominant open fracture direction shows the positive AVO gradient associated with a low Poisson's ratio (and gas), but the line parallel to the open fracture trend shows the negative AVO gradient associated with no gas. Based on the expected AVO signature for a gas sand, and the anisotropic AVO gradient responses, the interpretation was made of the presence of low Poisson ratio-intervals, sensed only by the line perpendicular to the fractures. These low Poisson-ratio intervals may be caused by NW-trending fractures with only a few percent gas saturation, since the variation in Poisson's ratio detected by the AVO analysis occurs within the first few percent gas saturation. The S-wave reflection data indicated anomalously high (15%) S-wave anisotropy in the zone under the AVOA anomaly at the Z reflector: this supported the interpretation of NW-trending fractures. A summary of the interpretation is found in Lynn et al (1995c).

9.2 S-WAVE ANISOTROPY

9.2.1 VSPs

The two most important conclusions from the VSP S-wave analysis were 1) that the polarization direction of the S1 wave, N43W, does not change with depth, and 2) that the S-wave anisotropy increases abruptly from background (1%) to anomalously high levels (5-12%) at the T/UGR, the top fractured gas reservoir interval (Figure 9-2).

Analysis of the polarization direction of the S1 wave from the VSP revealed a uniform polarization of N43W S1, from 2,850 ft to 8,650 ft, which suggests that the fracture orientation is also uniform over this depth range, at this location. The top 2,850 ft exhibit a 3% S-wave velocity anisotropy. The beginning of the anomalously high S-wave velocity anisotropy (7%), or time delay differential between downgoing fast and slow S-waves, is at the top of the reservoir interval, which is consistent with the S-wave amplitude anomaly. Parametric inversion (Esmersoy, 1990) of the far-offset P-wave VSP, recorded with source-receiver azimuth SW-NE, or perpendicular to the fractures, revealed that the fractured gas reservoir section has an anomalously low Poisson's ratio. The P-wave AVO response 600 ft west of this 9C VSP well, the closest location at which far offset data are available, shows a positive gradient in the interval of interest, suggesting the presence of gas (interpreted to be contained in NW trending fractures). A bright S1 and a dim S2 reflection at the top fractured reservoir interval on the S1 and S2 corridor stacks are interpreted as relating to the presence of gas-filled fractures in the interval corresponding to production in adjacent wells.

9.2.2 Surface Reflection Data

The S-wave anisotropy computed from the interval time analysis of the multi-component reflection data was used to interpret the relative fracture density and fracture azimuth along the lines which, together with the P-wave AVO results, could be incorporated into an overall interpretation of potential for gas production in this reservoir. Figure 9-3 is a map of such a composite interpretation for the upper gas reservoir interval in the field.

Using S1 and S2 sections time-aligned for the upper marker horizon at the T/UGR Formation in the zone of interest, the fastest traveling S-wave was usually polarized NW, but occasionally was NE. However, at all locations corresponding to wells with current gas production, S1 is polarized N30W within the gas-productive interval. This is consistent with the interpretation of dominant open NW fracture orientation from the 9C VSP and P-wave AVO analysis.

In summary, azimuthally dependent P-wave AVO responses are interpreted to be related to fracture orientation and relative fracture density, as deduced by commercial pay intervals. S-wave data, which are more diagnostic of internal rock structure, are consistent with the P-wave interpretation. VSP S-wave data show the first-arriving S-wave polarized N30W throughout most of the data set, which is consistent with the dominant fracture orientations seen in outcrops and cores. Surface reflection S-wave data at all producing well locations on both seismic lines show that the fast S-wave is the wave polarized N30W, thus indicating the open gas-filled fractures are N30W.

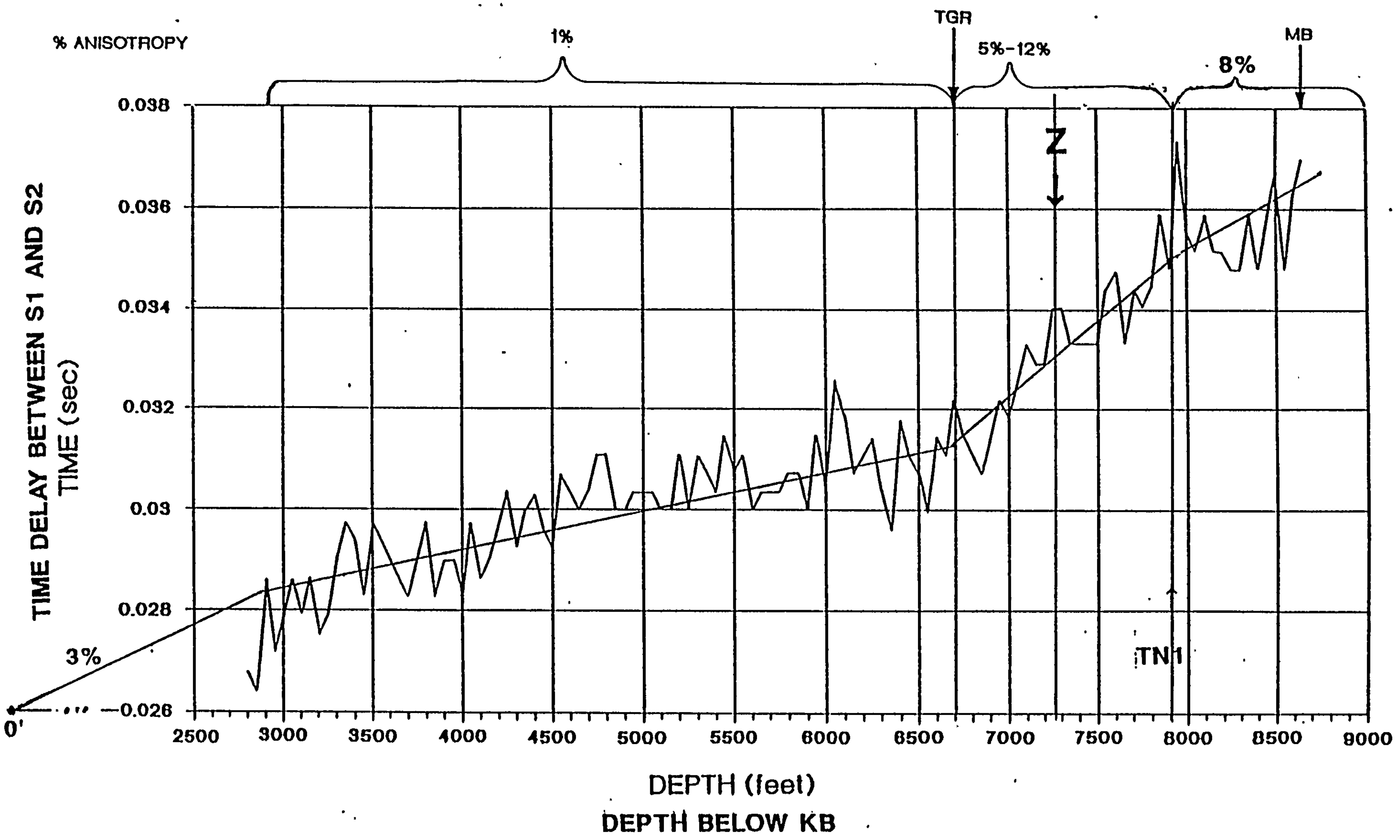

The S1-S2 time delay, representing the percent anisotropy, with depth.

FIGURE 9-2

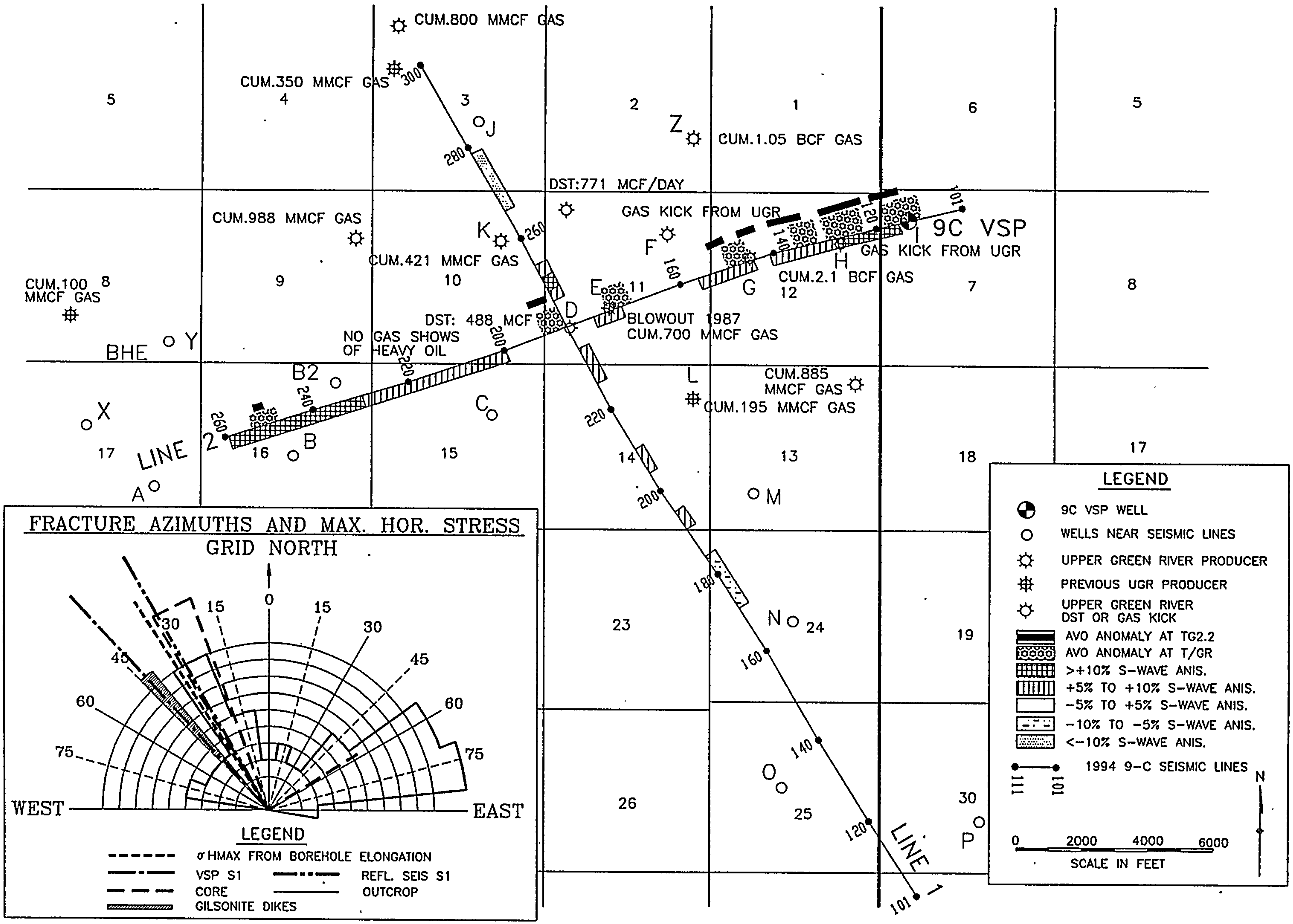

Map of the composite interpretation for upper gas reservoir interval in the field.

FIGURE 9-3

This work indicates that azimuthal variations in the P-wave AVO response are found in association with gas-filled fractures, and that the azimuth of the source-receiver direction with respect to fracture orientation governs the AVO response. In the present interpretation, confidence in P-wave AVO fracture indicators is increased by consistency with the anisotropy observed in S-wave seismic data. The extension of this work (Lynn et al, 1995a) is in 3-D multi-azimuth P-wave seismic.

REFERENCES

Allen, J.L. and C.P. Peddy, 1993, AVO Frontiers, in *Amplitude Variation with Offset: Gulf Coast Case Studies*, Geophysical Development Series, vol. 4, SEG 117-124.

Bredehoeft, J.D., Wesley, J.B., and T.D. Fouch, 1994, Simulations of the origin of fluid pressure, fracture generation, and the movement of fluids in the Uinta Basin, Utah, Amer. Assn. Petrol. Geol., **78**, 1729-1747.

Castagna, J.P. and Smith, S.W., 1994, Comparison of AVO indicators: A modeling study: Geophysics, **59**, 1849-1855.

Crampin, S., 1984, Effective anisotropic elastic-constants for wave propagation through a cracked solid: polarization as a possible dilatancy diagnostic: Geophy. J. Roy. Astr. Soc., 53, 467-496.

Crampin, S., 1985, Evaluation of anisotropy by shear-wave splitting, Geophysics, **50**, 142-152.

Crampin, S. and H. Lynn, 1989, Shear-wave VSPs: A powerful new tool for fracture and reservoir description, Journal of Petroleum Technology, p. 283- 288.

Crampin, S. 1994, The Fracture Coiticality of Coastal Rocks Geophysics, J. Int., Blackwell Science Ltd. 118, 428-438.

Domenico, S.N., 1976, Effect of brine-gas mixture on velocity in an unconsolidated sand reservoir, Geophysics, **41**, 882-894.

Esmersoy, C., 1990, Split-shear inversion for fracture evaluation, SEG Expanded Abs., 1400-1403.

Fouch, T., V. Nuccio, J. Osmond, L. MacMillan, W. Cashion and C. Wandrey, 1992, Oil and gas in the uppermost Cretaceous and Tertiary rock, Uinta Basin, UT, in Hydrocarbon and Mineral Resources of the Uinta Basin, UT and CO, UT Geol. Assn. Guidebook 20, Fouch, Nuccio and Chidsey, eds., publ. by UT Geol. Assn., Salt Lake City, UT.

Garotta, R., 1989, Detection of azimuthal anisotropy, 1989 SEG Annual Meeting Expanded Abstracts, pp. 861-863.

Gelinsky, S., and S. A. Shapiro, 1995, Low frequency anisotropy of layered media, as presented orally at the 1995 EAEG conference, Glasgow, Scotland.

Goodway, W.N., and L. Mayo, 1994, Multi-component seismic and borehole experiment to establish and identify the cause of anisotropy in the 2nd White Specs at Garrington, Alberta, 1994, Canadian SEG Expanded Abstracts, p. 254-255.

Gough, D.I., and Bell, J.S., 1982, Stress orientation from borehole wall fractures with examples from Colorado, east Texas, and northern Canada, Can. J. Earth Sci. 19, p. 1358-1370.

Harthill, N., and Bates, C.R., 1995, Uinta Basin: Fracture detection: Blackhawk Geosciences.

Heffer, K.J. and Dowokpor, A.B., 1990, Relationship between azimuths of flood anisotropy and local earth stresses in oil reservoirs: North Sea Oil and Gas Reservoirs-II, The Norwegian Institute of Technology, Graham & Trotman, publ.

Johnson, W.E., 1995, Direct detection of gas in pre-Tertiary sediments?, Leading Edge, 1995, **14**, no. 2, 119-122.

Lucas, P.T., and J.M. Drexler, 1976, Altamont-Bluebell, a major naturally fractured stratigraphic trap, Uinta basin, Utah, in North American oil and gas fields, AAPG Mem. 24, p. 121-135.

Lynn, H.B., 1986, Seismic detection of oriented fractures, Oil and Gas Journal, p. 54-55.

Lynn, H.B., 1989, Shear waves, multi-component seismic, and anisotropy: What information about the earth can we extract? presented at "Geophysics and Computers: A Look to the Future", a symposium held on April 28, 1989, at Houston Area Research Center, 9 p. Proceedings of the workshop may be obtained by writing Geotechnology Research Institute, 4802 Research Forest Dr., The Woodlands, TX 77381.

Lynn, H.B., and L.A. Thomsen, Reflection shear-wave data collected near the principal axes of azimuthal anisotropy, Geophysics, **55**, 147-156.

Lynn, H.B., C.R. Bates, K.M. Simon, R. Van Dok, 1995a, The effects of azimuthal anisotropy in P-wave 3-D seismic, SEG Expanded Abs. 65th Ann. Mtg.

Lynn, H.B., C.R. Bates, M. Layman, and M. Jones, 1995b, Natural fracture characterization using P-wave reflection seismic data, VSP, Borehole imaging logs, and the in-situ stress field determination, SPE paper 29595, presented at the SPE Rocky Mtn. Regional Symposium, March 1995.

Lynn, H.B., K.M. Simon, C.R. Bates, M. Layman, R. Schneider, and M. Jones, 1995c, Use of anisotropy in P-wave and S-wave data for fracture characterization in a naturally fractured gas reservoir: The Leading Edge, **14**, 887-893.

Mallick, S., and L.N. Frazer, 1991, Reflection/transmission coefficients and azimuthal anisotropy in marine seismic studies, Geophys. J. Int., **105**, 241-252.

Mueller, M.C., 1991, Prediction of lateral variability in fracture intensity using multi-component shear-wave surface seismic as a precursor to horizontal drilling in the Austin Chalk, Geophys. J. Int., **107**, p. 409-415.

Narr, W., and J.B. Currie, 1982, Origin of fracture porosity--example from Altamont Field, Utah, Amer. Assn. of Petr. Geol., **66**, 1231-1247.

Nur, A., 1971, Effects of stress on velocity anisotropy in rocks with cracks: J. Geophys. Research, **76**, 2022-2034.

Nur, A. and Simmons, G., 1969, Stress-induced velocity anisotropy in rock: An experimental study, J. Geophys. Res., **74**, 6667-6674.

Ostrander, W.J., 1984, Plane-wave reflection coefficients for gas sands at non-normal angles of incidence: Geophysics, **49**, 1637-1648.

Queen, J.H., and W.D. Rizer, 1990, An integrated study of seismic anisotropy and the natural fracture system at the Conoco Borehole Test Facility, Kay County, Oklahoma, J. Geophys. Res., **95**, B7, 11,255-11,274.

Rutherford, S.R. and Williams, R.H., 1989, Amplitude-versus-offset variations in gas sands: Geophysics, **54**, 680-688.

Shuey, R.T., 1985, A simplification of the Zoeppritz equations: Geophysics, **50**,609-614

Tatham, R.H. and McCormack, M.D., 1991, Multi-component Seismology in Petroleum Exploration: Society of Exploration Geophysicists.

Thomsen, L.A., 1986, Weak elastic anisotropy, Geophysics, **51**, 1954-1966.

Thomsen, L.A., 1988, Reflection seismology over azimuthally anisotropic media, Geophysics, **53**, no. 3, p. 304-313.

Zoback, M.L. and M.D. Zoback, Tectonic stress field of the continental United States, in Pakiser, L.C., and Mooney, W.D., Geophysical framework of the continental United States, Boulder CO, **Geol. Soc. of Amer. Memoir 172**, p. 523-539.

Zoback, M.D., Moos, D., Mastin, L., 1985, Well bore breakouts and in situ stress, Jour. of Geophys. Research, Vol. 90, p. 5523-5530.

Appendix A: The "Castagna Parameter" Amplitude Variation With Offset

Castagna and Smith (1994) proposed an AVO parameter that they concluded to be more robust as a gas indicator than the AVO gradient or the sometimes used "product gradient", (gradient times zero-intercept). This parameter is a linear combination of the gradient and intercept, (A + B)/ 2 , where

A = AVO intercept (reflection coefficient at normal incidence); and,

B = AVO gradient.

Their work was based on studies of velocity measurements of many brine and gas sands which fell into all three Rutherford & Williams classes. These brine sands and gas sands had many possibilities of overlying shales. They found that a direct gas indicator that works universally, regardless of the gas-sand impedance, is $R_P - R_S$, where

R_P = P-wave reflection coefficient at normal incidence; and,

R_S = S-wave reflection coefficient at normal incidence.

In their analysis, they demonstrated that this normal incidence reflection coefficient difference $R_P - R_S$, is well-approximated by the parameter (A + B)/ 2. It is noteworthy that this parameter works for all classes of sands, unlike other AVO indicators like the "product gradient", which, they point out, effectively masks gas responses from Class I sands of the type present at Bluebell-Altamont.

On the basis of Castagna and Smith's work, plots of (A + B)/ 2 were generated, which are referred to as the "Castagna Parameter" displays along Lines 1 and 2. These were used in conjunction with classic AVO regression plots, to analyze the data. As with the AVO gradient, this parameter is positive for gas sands in data of SEG-normal polarity. Castagna and Smith's conclusion that the parameter is more sensitive than the gradient alone, for bringing out small differences due to gas is supported with this work.

Appendix B: Stacking Velocity Functions at Tie Point

Line 1 S1 (SV)

0.848	6282
1.088	7026
1.153	7173
1.749	8177
1.859	8377
2.053	8652
2.434	8969
3.487	9925

Line 2 S1 (SH)

Time (sec)	Vstk (ft/sec)
0.973	6860
1.076	7292
1.578	8242
1.728	8329
1.822	8350
2.018	8394
2.192	8437
2.394	8523
3.103	8631
3.980	8890

Line 1 S2 (SH)

Time (sec)	Vstk (ft/sec)
0.909	6398
0.989	6618
1.292	7314
1.539	7746
1.777	7918
1.956	8005
2.058	8091
2.131	8156
2.300	8329
2.465	8437
2.703	8610
2.945	8739
3.062	8989
3.433	9228
3.997	9551

Line 2 S2 (SV)

Time (sec)	Vstk (ft/sec)
1.090	7141
1.329	7983
1.665	8420
1.882	8545
2.954	8684
2.130	8830
2.327	9194
2.689	9430
3.993	9955

APPENDIC C: 550 FT. WEST VSP TIME-DEPTH-VELOCITY VALUES

Depth Kb below	Vert. P- travel Time [ms]	S 1 Time [ms]	S 2 Time [ms]	Delta VP/ VS1	Delta Z	% ANIS	VS1 int.	VS2 int.	MSEC DIFF S2-S1	INT VP	P- wave 2 way T ref: seis	avg p vel datum
2800	288	626	653								0.355	9735
2850	292	634	661	1.73	100	5.6%	6614	6246			0.364	9760
2900	296	641	669	1.89	100	1.3%	6452	6369		12180	0.373	9785
2950	300	649	676	1.93	200	2.7%	6513	6335	1	12188	0.380	9826
3000	305	657	684	1.85	200	0.5%	6481	6450	0	12587	0.389	9850
3050	308	664	692	1.96	200	1.8%	6598	6477	1	12210	0.397	9889
3100	312	672	700	1.85	200	2.2%	6817	6669	1	13046	0.405	9928
3150	317	679	707	1.87	200	0.5%	6782	6750	0	13072	0.413	9950
3200	320	686	714	2.02	200	2.9%	6859	6662	1	13080	0.420	10003
3250	324	694	722	1.95	200	4.4%	7082	6773	1	14045	0.427	10040
3300	328	701	730	1.95	200	0.7%	6787	6741	0	12658	0.435	10075
3350	331	708	737	1.79	200	2.0%	6897	6759	1	13106	0.442	10126
3400	336	716	744	1.86	200	0.6%	6976	6937	0	13115	0.451	10128
3450	339	723	751	1.98	200	-1.1%	6857	6930	-0	13110	0.458	10178
3500	343	730	759	1.97	200	0.4%	7085	7055	0	13601	0.466	10210
3550	346	737	766	1.86	200	-7.7%	6863	7391	-2	13132	0.472	10257
3600	350	744	772	1.86	200	2.9%	7339	7125	1	13158	0.481	10274
3650	354	752	778	1.73	200	3.5%	7382	7127	1	12735	0.488	10305
3700	358	757	787	1.58	200	2.0%	7266	7118	1	14151	0.496	10335
3750	362	764	794	2.20	200	7.3%	7360	6823	2	13645	0.504	10365
3800	365	772	801	2.15	200	-2.8%	6855	7046	-1	14157	0.509	10424
3850	369	779	808	1.94	200	-2.2%	7012	7165	-1	14167	0.518	10438
3900	372	786	815	1.89	200	-3.6%	7022	7273	-1	12747	0.524	10481
3950	376	792	821	1.69	200	0.9%	7469	7403	0	14170	0.532	10508
4000	380	800	828	1.90	200	1.6%	7585	7464	0	13666	0.540	10520

4050	383	806	835	1.94	200	-0.5%	7444	7483	-0	14190	0.546	10575
4100	387	813	842	1.91	200	4.7%	7783	7419	1	14756	0.553	10601
4150	390	819	848	1.86	200	2.5%	7657	7465	1	14215	0.560	10641
4200	394	826	855	1.81	200	1.2%	7715	7621	0	14228	0.568	10666
4250	397	832	861	1.83	200	1.5%	7814	7700	0	13702	0.574	10704
4300	401	839	868	1.71	200	1.5%	7647	7535	0	13711	0.582	10728
4350	405	845	874	1.76	200	-0.1%	7336	7341	-0	13248	0.589	10751
4400	408	852	882	1.91	200	0.2%	7794	7779	0	14235	0.597	10774
4450	412	859	889	1.90	200	2.2%	7013	6859	1	13250	0.604	10797
4500	415	864	894	1.87	200	-1.1%	7026	7100	-0	13723	0.610	10847
4550	420	873	903	1.99	200	-0.3%	7406	7430	-0	13723	0.619	10841
4600	423	880	910	1.83	200	2.5%	7058	6878	1	13250	0.626	10876
4650	427	886	916	1.74	200	-0.9%	7698	7770	-0	14815	0.633	10897
4700	430	893	923	2.02	200	3.7%	8258	7956	1	15452	0.640	10931
4750	433	899	929	2.02	200	0.9%	8007	7934	0	15452	0.646	10965
4800	436	905	935	1.84	200	-2.5%	7783	7978	-1	14844	0.652	11012
4850	440	911	941	1.82	200	1.0%	7998	7918	0	14293	0.659	11031
4900	443	918	948	1.75	200	-2.4%	7734	7918	-1	13755	0.667	11050
4950	447	924	954	1.74	200	1.0%	7802	7727	0	14863	0.674	11069
5000	450	931	960	2.11	200	-0.4%	7954	7986	-0	14863	0.681	11101
5050	453	937	967	2.01	200	-1.7%	8155	8290	-0	15471	0.686	11145
5100	457	944	973	1.72	200	0.7%	7863	7808	0	15483	0.694	11163
5150	460	949	978	1.93	200	-1.1%	7990	8081	-0	14296	0.700	11193
5200	463	956	986	1.86	200	4.0%	8209	7882	1	14844	0.707	11223
5250	467	962	992	1.70	200	1.8%	7762	7626	0	14844	0.714	11240
5300	470	968	998	1.97	200	0.4%	8067	8031	0	14281	0.721	11268
5350	474	975	1005	1.84	200	3.2%	7932	7676	1	14844	0.727	11297
5400	477	981	1011	1.78	200	-1.2%	7890	7981	-0	14881	0.735	11312
5450	481	987	1018	1.93	200	-1.6%	7954	8083	-0	14885	0.741	11340
5500	484	993	1023	1.97	200	-0.4%	7986	8021	-0	14885	0.748	11368
5550	487	1000	1029	1.80	200	-2.5%	8112	8315	-1	15508	0.754	11396
5600	491	1006	1036	1.85	200	-0.4%	7821	7851	-0	14885	0.762	11410
5650	493	1012	1042	2.02	200	1.1%	8197	8107	0	14316	0.767	11449

5700	497	1019	1049	1.65	200	0.5%	7707	7671	0	14914	0.774	11463
5750	501	1024	1054	1.86	200	-0.5%	7564	7604	-0	13814	0.782	11477
5800	504	1032	1062	2.01	200	-1.8%	7722	7861	-0	14348	0.788	11504
5850	508	1038	1068	1.86	200	1.9%	7257	7118	1	13833	0.796	11517
5900	511	1045	1074	1.81	200	-1.8%	7315	7449	-0	13316	0.802	11542
5950	515	1052	1082	1.79	200	1.8%	7477	7345	0	13822	0.811	11543
6000	519	1059	1089	1.89	200	2.5%	7020	6842	1	13316	0.818	11556
6050	522	1065	1095	2.02	200	-1.0%	7087	7161	-0	13324	0.825	11581
6100	526	1073	1103	1.87	200	2.8%	7297	7090	1	13822	0.832	11593
6150	530	1080	1110	1.78	200	0.7%	6757	6707	0	12438	0.841	11594
6200	534	1087	1117	1.81	200	-1.8%	6544	6662	-1	12444	0.847	11617
6250	539	1095	1125	2.01	200	-1.6%	6633	6738	-0	12852	0.857	11606
6300	542	1104	1133	2.07	200	0.5%	6506	6476	0	12436	0.865	11618
6350	546	1110	1140	1.80	200	-2.2%	6393	6535	-1	12860	0.872	11630
6400	550	1117	1148	1.96	200	1.0%	7042	6971	0	13822	0.880	11641
6450	554	1126	1156	2.14	200	-0.8%	6433	6485	-0	12887	0.888	11641
6500	557	1132	1162	2.05	200	-6.8%	6638	7090	-2	12878	0.893	11675
6550	562	1141	1171	1.78	200	1.0%	7125	7055	0	13831	0.903	11664
6600	565	1147	1176	1.82	200	2.3%	7120	6959	1	12453	0.911	11675
6650	569	1154	1184	1.72	200	3.1%	8197	7946	1	15528	0.917	11697
6700	573	1160	1191	1.98	200	6.7%	8826	8230	2	15540	0.926	11697
6750	574	1166	1196	1.82	200	0.6%	9412	9359	0	16207	0.926	11751
6800	578	1170	1200	1.48	200	0.9%	9547	9461	0	17730	0.936	11761
6850	581	1175	1205	1.89	200	4.0%	9537	9158	1	15540	0.942	11793
6900	584	1181	1212	1.78	200	3.4%	8807	8503	1	16949	0.948	11814
6950	587	1187	1218	1.96	200	4.7%	8791	8382	1	15552	0.955	11834
7000	590	1193	1224	1.76	200	6.8%	9443	8803	2	15564	0.960	11865
7050	594	1198	1229	1.39	200	1.1%	8177	8091	0	14937	0.967	11874
7100	597	1202	1235	1.89	200	3.7%	8735	8412	1	14951	0.974	11894
7150	601	1211	1242	2.07	200	6.0%	9146	8600	1	16237	0.981	11903
7200	603	1216	1247	1.63	200	-0.5%	7805	7842	-0	15568	0.987	11934
7250	606	1220	1252	1.92	200	5.4%	8735	8266	1	15580	0.992	11963
7300	610	1228	1260	1.89	200	6.0%	8917	8379	1	14937	1.000	11972

7350	614	1234	1267	1.45	200	-1.1%	7657	7740	-0	14368	1.007	11980
7400	617	1238	1271	1.86	200	2.8%	8613	8372	1	15552	1.013	11999
7450	620	1246	1278	2.23	200	1.0%	8760	8669	0	14937	1.020	12017
7500	623	1251	1284	1.56	200	0.7%	8368	8313	0	14937	1.025	12046
7550	627	1257	1290	1.43	200	4.8%	9443	8989	1	15564	1.034	12043
7600	630	1262	1295	1.75	200	0.6%	9243	9184	0	15558	1.040	12061
7650	633	1267	1301	2.04	200	0.6%	9556	9502	0	16989	1.046	12089
7700	635	1273	1306	1.81	200	-0.5%	9230	9273	-0	16989	1.051	12117
7750	639	1278	1311	1.67	200	1.3%	8867	8751	0	16258	1.057	12135
7800	642	1284	1317	1.86	200	2.2%	9005	8811	0	15576	1.064	12152
7850	645	1290	1323	1.78	200	8.0%	9191	8452	2	16239	1.070	12169
7900	648	1295	1329	1.67	200	6.1%	9095	8543	1	16239	1.077	12186
7950	651	1300	1334	2.00	200	1.9%	9145	8972	0	15569	1.082	12212
8000	654	1306	1340	1.73	200	2.1%	8787	8605	0	15556	1.088	12229
8050	658	1312	1346	1.76	200	-1.3%	8576	8688	-0	15576	1.096	12235
8100	661	1318	1352	1.92	200	-1.5%	9110	9244	-0	15568	1.102	12251
8150	664	1323	1357	1.65	200	0.2%	8991	8971	0	16982	1.108	12277
8200	667	1328	1362	1.86	200	2.1%	9262	9068	0	15568	1.114	12293
8250	670	1334	1368	1.71	200	5.1%	9081	8619	1	14951	1.119	12319
8300	674	1339	1374	1.48	200	2.3%	8584	8386	1	14959	1.128	12315
8350	677	1345	1381	1.78	200	4.2%	9692	9287	1	14375	1.134	12330
8400	680	1351	1386	1.49	200	1.4%	8645	8523	0	16256	1.141	12345
8450	684	1354	1390	1.99	200	-4.0%	8408	8747	-1	14385	1.147	12360
8500	686	1363	1397	1.90	200	3.0%	9244	8966	1	14955	1.153	12385
8550	691	1369	1403	1.33	200	0.9%	7686	7619	0	13850	1.162	12371
8600	694	1373	1408	1.70	100	3.9%	8475	8143	0	14368	1.168	12396
8650	698	1380	1416	1.86	100	3.9%	8475	8143	0	14368	1.176	12391

Depth below Kb	Vert. P-Travel Time [ms]	S 1 Time [ms]	S 2 Time [ms]	Inter-val Delta Z thick-ness	% ANIS	VS1 int.	VS2 int.	AVG. VS1	AVG. VS2
2800	288	626	653					4472	4290
2850	292	634	661	100	5.6%	6614	6246	4498	4315
2900	296	641	669	100	1.3%	6452	6369	4522	4337
2950	300	649	676	200	2.7%	6513	6335	4545	4362
3000	305	657	684	200	0.5%	6481	6450	4566	4383
3050	308	664	692	200	1.8%	6598	6477	4591	4407
3100	312	672	700	200	2.2%	6817	6669	4612	4431
3150	317	679	707	200	0.5%	6782	6750	4636	4455
3200	320	686	714	200	2.9%	6859	6662	4662	4479
3250	324	694	722	200	4.4%	7082	6773	4684	4503
3300	328	701	730	200	0.7%	6787	6741	4706	4523
3350	331	708	737	200	2.0%	6897	6759	4734	4547
3400	336	716	744	200	0.6%	6976	6937	4749	4569
3450	339	723	751	200	-1.1%	6857	6930	4773	4592
3500	343	730	759	200	0.4%	7085	7055	4795	4614
3550	346	737	766	200	-7.7%	6863	7391	4818	4637
3600	350	744	772	200	2.9%	7339	7125	4838	4660
3650	354	752	778	200	3.5%	7382	7127	4854	4689
3700	358	757	787	200	2.0%	7266	7118	4886	4704
3750	362	764	794	200	7.3%	7360	6823	4909	4725
3800	365	772	801	200	-2.8%	6855	7046	4924	4746
3850	369	779	808	200	-2.2%	7012	7165	4941	4766
3900	372	786	815	200	-3.6%	7022	7273	4959	4786
3950	376	792	821	200	0.9%	7469	7403	4984	4808
4000	380	800	828	200	1.6%	7585	7464	4999	4830

4050	383	806	835	200	-0.5%	7444	7483	5025	4852
4100	387	813	842	200	4.7%	7783	7419	5044	4871
4150	390	819	848	200	2.5%	7657	7465	5065	4892
4200	394	826	855	200	1.2%	7715	7621	5086	4912
4250	397	832	861	200	1.5%	7814	7700	5108	4933
4300	401	839	868	200	1.5%	7647	7535	5127	4954
4350	405	845	874	200	-0.1%	7336	7341	5148	4976
4400	408	852	882	200	0.2%	7794	7779	5164	4991
4450	412	859	889	200	2.2%	7013	6859	5179	5007
4500	415	864	894	200	-1.1%	7026	7100	5206	5035
4550	420	873	903	200	-0.3%	7406	7430	5209	5037
4600	423	880	910	200	2.5%	7058	6878	5224	5056
4650	427	886	916	200	-0.9%	7698	7770	5246	5078
4700	430	893	923	200	3.7%	8258	7956	5265	5093
4750	433	899	929	200	0.9%	8007	7934	5281	5112
4800	436	905	935	200	-2.5%	7783	7978	5306	5134
4850	440	911	941	200	1.0%	7998	7918	5322	5155
4900	443	918	948	200	-2.4%	7734	7918	5335	5170
4950	447	924	954	200	1.0%	7802	7727	5355	5187
5000	450	931	960	200	-0.4%	7954	7986	5373	5207
5050	453	937	967	200	-1.7%	8155	8290	5390	5224
5100	457	944	973	200	0.7%	7863	7808	5405	5242
5150	460	949	978	200	-1.1%	7990	8081	5427	5263
5200	463	956	986	200	4.0%	8209	7882	5440	5275
5250	467	962	992	200	1.8%	7762	7626	5458	5295
5300	470	968	998	200	0.4%	8067	8031	5476	5309
5350	474	975	1005	200	3.2%	7932	7676	5489	5325
5400	477	981	1011	200	-1.2%	7890	7981	5506	5343
5450	481	987	1018	200	-1.6%	7954	8083	5521	5356
5500	484	993	1023	200	-0.4%	7986	8021	5537	5375
5550	487	1000	1029	200	-2.5%	8112	8315	5551	5391
5600	491	1006	1036	200	-0.4%	7821	7851	5568	5407
5650	493	1012	1042	200	1.1%	8197	8107	5584	5424

5700	497	1019	1049	200	0.5%	7707	7671	5595	5435
5750	501	1024	1054	200	-0.5%	7564	7604	5614	5455
5800	504	1032	1062	200	-1.8%	7722	7861	5622	5463
5850	508	1038	1068	200	1.9%	7257	7118	5634	5478
5900	511	1045	1074	200	-1.8%	7315	7449	5648	5492
5950	515	1052	1082	200	1.8%	7477	7345	5657	5498
6000	519	1059	1089	200	2.5%	7020	6842	5665	5512
6050	522	1065	1095	200	-1.0%	7087	7161	5681	5524
6100	526	1073	1103	200	2.8%	7297	7090	5684	5528
6150	530	1080	1110	200	0.7%	6757	6707	5694	5540
6200	534	1087	1117	200	-1.8%	6544	6662	5706	5552
6250	539	1095	1125	200	-1.6%	6633	6738	5710	5556
6300	542	1104	1133	200	0.5%	6506	6476	5708	5558
6350	546	1110	1140	200	-2.2%	6393	6535	5720	5571
6400	550	1117	1148	200	1.0%	7042	6971	5728	5577
6450	554	1126	1156	200	-0.8%	6433	6485	5729	5582
6500	557	1132	1162	200	-6.8%	6638	7090	5741	5593
6550	562	1141	1171	200	1.0%	7125	7055	5739	5595
6600	565	1147	1176	200	2.3%	7120	6959	5752	5613
6650	569	1154	1184	200	3.1%	8197	7946	5763	5617
6700	573	1160	1191	200	6.7%	8826	8230	5775	5626
6750	574	1166	1196	200	0.6%	9412	9359	5791	5645
6800	578	1170	1200	200	0.9%	9547	9461	5812	5666
6850	581	1175	1205	200	4.0%	9537	9158	5829	5683
6900	584	1181	1212	200	3.4%	8807	8503	5841	5693
6950	587	1187	1218	200	4.7%	8791	8382	5857	5708
7000	590	1193	1224	200	6.8%	9443	8803	5869	5721
7050	594	1198	1229	200	1.1%	8177	8091	5885	5736
7100	597	1202	1235	200	3.7%	8735	8412	5905	5750
7150	601	1211	1242	200	6.0%	9146	8600	5904	5755
7200	603	1216	1247	200	-0.5%	7805	7842	5923	5772
7250	606	1220	1252	200	5.4%	8735	8266	5943	5789
7300	610	1228	1260	200	6.0%	8917	8379	5945	5792

7350	614	1234	1267	200	-1.1%	7657	7740	5956	5803
7400	617	1238	1271	200	-2.8%	8613	8372	5977	5821
7450	620	1246	1278	200	1.0%	8760	8669	5979	5828
7500	623	1251	1284	200	0.7%	8368	8313	5994	5840
7550	627	1257	1290	200	4.8%	9443	8989	6007	5854
7600	630	1262	1295	200	0.6%	9243	9184	6022	5867
7650	633	1267	1301	200	0.6%	9556	9502	6037	5882
7700	635	1273	1306	200	-0.5%	9230	9273	6049	5896
7750	639	1278	1311	200	1.3%	8867	8751	6065	5913
7800	642	1284	1317	200	2.2%	9005	8811	6077	5923
7850	645	1290	1323	200	8.0%	9191	8452	6087	5932
7900	648	1295	1329	200	6.1%	9095	8543	6100	5946
7950	651	1300	1334	200	1.9%	9145	8972	6118	5958
8000	654	1306	1340	200	2.1%	8787	8605	6127	5969
8050	658	1312	1346	200	-1.3%	8576	8688	6138	5982
8100	661	1318	1352	200	-1.5%	9110	9244	6147	5992
8150	664	1323	1357	200	0.2%	8991	8971	6161	6004
8200	667	1328	1362	200	2.1%	9262	9068	6177	6021
8250	670	1334	1368	200	5.1%	9081	8619	6185	6031
8300	674	1339	1374	200	2.3%	8584	8386	6197	6041
8350	677	1345	1381	200	4.2%	9692	9287	6209	6048
8400	680	1351	1386	200	1.4%	8645	8523	6218	6062
8450	684	1354	1390	200	-4.0%	8408	8747	6239	6081
8500	686	1363	1397	200	3.0%	9244	8966	6238	6083
8550	691	1369	1403	200	0.9%	7686	7619	6247	6092
8600	694	1373	1408	100	3.9%	8475	8143	6266	6108
8650	698	1380	1416	100	3.9%	8475	8143	6266	6110